A DFT study of the interaction of O_x with Pt nanorod edge sites:

A model for the ORR activity on Pt nanoparticle edges

Thesis submitted in partial fulfilment for the degree of Master of Science in Engineering in Chemical Engineering at the University of Cape Town

By

Gorden Thobani Gambu

BSc Chemical Engineering (UCT)

Supervisors

Prof E van Steen

Dr M Petersen

October 2015

Centre for Catalysis Research

Department of Chemical Engineering

University of Cape Town

Private Bag X3

Rondebosch, 7701

South Africa

Declaration

"I know the meaning of plagiarism and declare that all the work in the document, save for which is properly acknowledge is my own"

G. Thobani Gambu
14/10/2015

.....

Abstract

Proton exchange membrane fuel cells (PEMFCs) are an attractive energy conversion technology, this due to their high theoretical fuel utilization efficiencies compared to Carnot engines. However, due to potential losses, the operational efficiencies achieved in state-of-the-art PEMFCs are only between 45% and 55%. The slow kinetics of the oxygen reduction reaction (ORR) over a platinum based electrode accounts for ca. 70% of the potential losses. As a result of the sluggish ORR kinetics, high platinum loadings are required. The high cost of platinum has made it crucial to improve the ORR activity and hence reduce platinum loading. The surface-area-specific ORR activity has been reported to decrease with platinum particle size. This places a limitation to the degree to which platinum loading can be reduced by increasing metal dispersion.

To understand the origin of this behaviour, experimental studies have measured the ORR activity over different single crystalline surfaces and used model nanoparticle shapes to elucidate the overall ORR activity. Theoretical studies use density functional theory (DFT) to investigate the ORR activity on various site-types present on assumed model particle shapes. Thermodynamically, the exposed surface terminations aught to be predominantly Pt{111} and Pt{100} separated by edges and corners. It has been postulated that the overall ORR activity can be calculated as a weighted average of the activity of exposed surface terminations.

Using DFT calculations and nanorod models the above postulations are tested for the edge sites between a Pt(111) and Pt(100) surface. A rhombic nanorod model is used due to its computational efficiency compared to model nanoparticle clusters which are generally large and computationally expensive models. Furthermore, the use of rhombic nanorod model enables the investigation of the connection and communication between the Pt(111) and Pt(100) facets, this is difficult to investigate with stepped-surface models. It is argued that if, (i) the edge has insubstantial effect on the adsorption strength of adsorbed ORR intermediates as a function of distance from the edge and (ii) the diffusion of ORR intermediates between adjacent surface planes is limited, then the above postulation does hold.
Using atomic O and O_2 it was observed that the edge effect is a local phenomenon with adsorption involving only edge atoms being stronger than on extended surfaces. The adsorption of both atomic O and O_2 was weaker on the Pt(111) nanorod terrace sites compared to the adsorption on equivalent sites on extended Pt(111) slabs. These effects were not observed for adsorption on Pt(100) nanorod terrace sites.

The diffusion of atomic O from the Pt(100) nanorod terrace bridge sites towards the Pt(111) nanorod terrace fcc sites (across the edge) was investigated. It was observed that whilst at lower coverage the diffusion of atomic O is limited with an overall hopping frequency of 1.88×10^{-2} s^{-1} (at T = 85 °C and P = 1 bar), at a higher coverage, the diffusion of atomic O across the edge is facile (overall hopping frequency of 1.12×10^{5} s^{-1}). At a higher coverage limit and current density of 100 mA/cm^2 (an arbitrary current density in the activation polarization region), the hopping frequency of atomic O was determined to be three orders of magnitude higher than the turnover frequency for H_2O production. Hence at high coverage, the first condition (i.e. edge effect is localised) is satisfied, but the second condition (i.e. limited diffusion of atomic O from one facet to the other facet) can not be ruled out. Therefore, the assumption necessary for the evaluation of the overall ORR activity as a weighted average of individual activity, can be questioned.

Acknowledgements

I would like to acknowledge the following individuals and institutions whose guidance and support has been of paramount importance to the success of this project:

Professor Eric van Steen, you have been a great teacher and mentor to me—you continue to be. "After bashing my head against the wall a few times, you have always been the one person who can make me see another set of questions". This relationship has been the basis of the evolution of this thesis and my growth over the past two years. Without your guidance and support much of what was achieved in this project would not have been possible. I am grateful to have had you as a principal supervisor

Dr Melissa Petersen, your knowledge and background in computational chemistry has enriched my learning. You often quoted that apples and pear are not to be compared, no matter how trivial it may have seemed, this has been particularly difficult in the present study. Thank you for making time to discuss some of the more computationally difficult calculations. Your guidance is greatly appreciated and valued.

The often long weekly group meetings have truly been educational and important to my growth. I am greatly indebted to both of you for much that I have learned. Also to the rest of the molecular modelling collogues, Molefi Matsutsu and Tracey van Heerden, I have enjoyed and learned a lot from our frequent discussions over the past two years. Also to Mr Graham Inggs, thank you for all the technical support and your help in getting me acquainted with a number of available software and scripts. Further acknowledgement is made to Jan-Albert van den Berg for supplying data processing scripts.

Financial support from Johnson Matthey (JM) and the National Research Foundation (NRF)—Free-standing scholarship—is greatly acknowledge. Without the financial assistance from both JM and NRF, I would not have been able to enjoy the great experience of finding things out. Further thanks to Dr Glenn Jones and JM for an annual opportunity to present my work at their student meetings, this has been greatly appreciated.

Last but not least, I acknowledge the computational resources provided by the University of Cape Town's ICTS High Performance Computing facility and the Council for Scientific and Industrial Research's Centre for High Performance Computing (CHPC). Computational resources have been the only tool by which this study was conducted, access to these resources is greatly acknowledge.

Opinions expressed and conclusions arrived at, are those of the author and are not necessarily to be attributed to the NRF.

Contents

Glossary

Polarization:	Decrease in cell potential with increasing current density
Stepped-surfaces:	Surfaces with periodic steps which form a discontinuation of a given surface
Lateral interactions:	Interactions between closely adsorbed species which result in a decrease or increase in the adsorption energy
Hopping frequency:	The rate at which an adsorbate, e.g. atomic O, jumps from one adsorption site to the next
Turnover frequency:	The rate at which a given reaction occurs per active site
Coverage:	A fraction based on the number of adsorbed species per total number of surface atoms
Integral Gibbs free energy:	Change in the Gibbs free energy over a time period
Differential Gibbs free energy:	Instantaneous Gibbs free energy at a given time
Exergonic process:	A process which overall release energy to the surroundings
Endergonic process:	A process which overall absorbs energy from the surroundings

Abbreviations

CO-TPD	: Carbon monoxide Temperature-Programmed Desorption
CV	: Cyclic Voltammetry
DFT	: Density Functional Theory
EELS	: Electron Energy Loss Spectroscopy
FS	: Final state
GGA	: Generalized Gradient Approximation
IS	: Initial state
LSV	: Linear Sweep Voltammetry
mNR	: modified nanorod
NR	: Nanorod
ORR	: Oxygen Reduction Reaction
PAW	: Projected Augmented Wave
PBE	: Perdew, Burke and Ernzerhof
pDOS	: projected Density of States
PEMFC	: Proton Exchange Membrane Fuel Cell
PES	: Potential Energy Eurface
PW91	: Perdew-Wang from 1991
RHE	: Reversible Hydrogen Electrode
RPBE	: Revised Perdew, Burke and Ernzerhof
RRDE	: Rotating Ring Disk Electrode
SHE	: Standard Hydrogen Electrode
TS	: Transition state
UHV	: Ultra High Vacuum
USPP	: Ultra-soft Pseudopotential
VASP	: Vienna *Ab-initio* Simulation Package
XPS	: X-ray Photoelectron Spectroscopy
ZPE	: Zero point energy

Nomenclature

S	: Entropy
H	: Enthalpy
E_a	: Activation energy
ΔX	: Change in any property X
$\Delta G^{\ddagger}_{ACT}$	: Diffusion Gibbs free energy barrier
E^0	: Standard electrode potential at 25 °C
E_0	: Ground state electronic energy
ε_{dc}	: d-band center energy
ε_f	: Fermi-level energy
E^{vac}	: Vacuum potential
Φ	: Workfunction
υ	: Vibrational model
d_{O-O}	: Bond distance between two oxygen atoms
d_{Pt-O}	: Bond distance between a platinum atom and an oxygen atom
d_{Pt-Pt}	: Bond distance between two platinum atoms
Δd_{h1}	: Perpendicular height above the surface of an adsorbed atom
θ	: Angle between the Pt(111) nanorod facet normal vector and the bond axis of atomic O and O_2
β	: Angle between the Pt(100) nanorod facet normal vector and the bond axis of atomic O and O_2
α_{O-O}	: Angle between the O-O bond axis and the surface plane on which O_2 is adsorbed
k_B	: Boltzmann constant
h	: Planck constant
r_{H_2O}	: Rate of water production

List of Tables

List of Figures

Chapter 1

Introduction and Literature Review

1.1 Context

The cost and negative environmental impact of fossil fuel use has resulted in the need for improved utilization efficiencies of these fuels. Whilst the thermodynamic efficiency of both heat engines and fuel cells is limited thermodynamically (Lutz *et al.*, 2002; Wright, 2004), the fuel utilization efficiency in fuel cells is still much higher than that achieved by heat engines at practical temperatures (Yuan & Wang, 2008; Gewirth & Thorum, 2010). The Carnot efficiency limit (η_{Carnot}) for heat engines increases with temperature at which the heat is received, T_H, according to equation 1.1,

$$\eta_{Carnot} = 1 - \frac{T_L}{T_H} \tag{1.1}$$

where T_L and T_H are temperatures of the Carnot cycle at which the heat is being given off and recovered, respectively. Temperatures as high as 300 °C are required to achieve appreciable (ca. 50%) Carnot efficiencies if the heat is being given off at ca. 25 °C (Yuan & Wang, 2008). The fuel cell theoretical efficiency (η_{FC}) is given by equation 1.2,

$$\eta_{FC} = 1 - T \cdot \frac{\Delta S_R}{\Delta H_R} \tag{1.2}$$

where ΔH_R and ΔS_R are the enthalpy and entropy of reaction, respectively. Fuel cell efficiency decreases with increasing temperature. As a result higher efficiencies can be achieved at moderate temperatures (Gewirth & Thorum, 2010). As an example the theoretical efficiency of a fuel cell operating at 25 °C is 83% (Yuan & Wang, 2008). Figure 1.1 presents a comparison of efficiency limits of the Carnot cycle and fuel cell.

Proton exchange membrane fuel cells (PEMFCs), also known as hydrogen fuel cells, are an attractive technology for application in the automotive industry (Gasteiger *et al.*, 2010; Gewirth & Thorum, 2010). PEMFCs can operate at low temperatures and pressures, i.e. 65 - 85 °C and 1 - 2 bar. They have the potential to achieve high efficiencies and can be utilized over a wide range of applications. State-of-the-art PEMFCs can however only achieve efficiencies between 45% and 55% due to polarization losses at the cathode and anode electrodes (Gewirth & Thorum, 2010).

1.2 Proton exchange membrane fuel cells

The operating principle of PEMFCs is based on the oxidation and reduction of hydrogen and oxygen, respectively. The device consists of two spatially separated electrodes, the anode and cathode, where oxidation and reduction takes place. The cathode and anode are separated by a solid polymer electrolyte membrane as illustrated in Figure 1.2. Hydrogen is introduced at the anode side where it splits into protons and electrons over a platinum-based catalyst. The electrons are conducted via an external circuit whilst protons diffuse through a polymer electrolyte membrane. The electrons pass through an external load, where electrical work is done, to the cathode electrode where proton-coupled

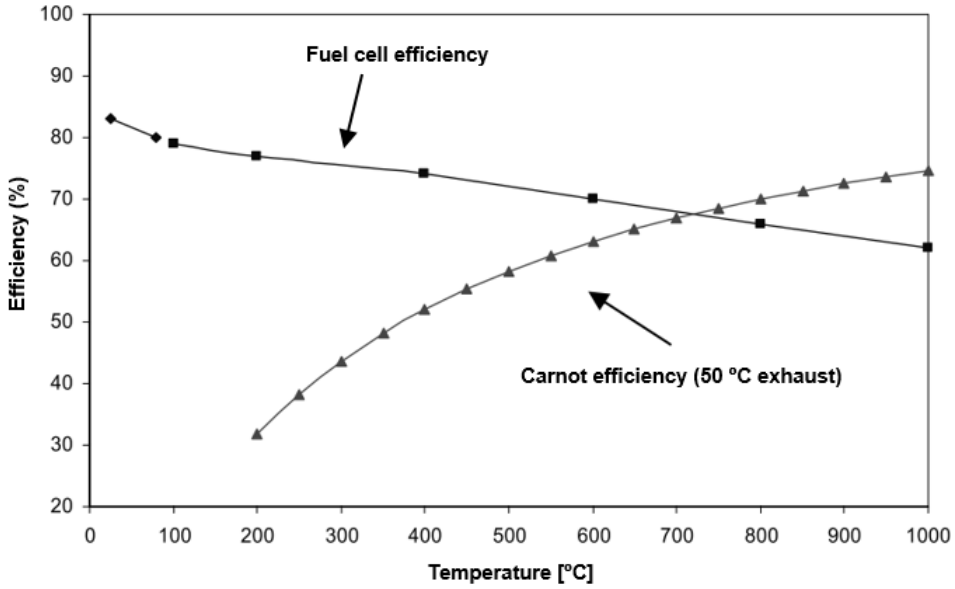

Figure 1.1: Comparison of the theoretical efficiencies of a hydrogen fuel cell (at 1 bar using the higher heating value of hydrogen) and the Carnot cycle (Yuan & Wang, 2008).

electron transfer occurs, resulting in the reduction of oxygen to water (Janik *et al.*, 2009; Qi & Li, 2012; Hansen *et al.*, 2014). The half-cell reactions occurring at the anode and cathode electrodes are presented by equations 1.3 and 1.4, respectively, whilst equation 1.5 is the overall PEMFC reaction equation.

$$H_2(g) \longrightarrow 2H^+(aq) + 2e^- \qquad E^0 = 0.0V \ \ at \ \ T = 25\,^\circ C \tag{1.3}$$

$$O_2(g) + 4e^- + 4H^+(aq) \longrightarrow 2H_2O \qquad E^0 = 1.23V \ \ at \ \ T = 25\,^\circ C \tag{1.4}$$

$$H_2 + \frac{1}{2}O_2 \longrightarrow H_2O \qquad \Delta E = 1.23V \ \ at \ \ T = 25\,^\circ C \tag{1.5}$$

ΔE is the theoretical cell potential relative to the standard hydrogen electrode (SHE). Since power is directly proportional to both current density and cell potential, it is desirable to operate at a high cell potential and a high current density. However this is not practically possible, since the cell potential decreases with increasing current density. Although the theoretically equilibrium fuel cell potential at 80°C and 1 bar is 1.169 V, lower potentials are achieved at appreciable current densities due to reaction activation, proton-electron transport resistance and gas transport losses (Gasteiger *et al.*, 2005; Yuan & Wang, 2008; Gewirth & Thorum, 2010). A benchmark study by Gasteiger *et al.* (2005) showed that over 70% of the potential loss is due to kinetic losses which have mostly been ascribed to the sluggish kinetics of the oxygen reduction reaction (ORR) (Yuan & Wang, 2008). Figure 1.3 illustrates the different potential polarization behaviour observed in a typical PEMFC. As a result of these polarization phenomena, PEMFC devices are operated at lower potentials, i.e. between 0.65 and 0.95 V per cell. These potentials correspond to lower fuel cell efficiencies than theoretically possible (83% at 25°C and 1 bar). Since over 70% of the potential loss has been reported to be due to sluggish kinetics of the ORR (Gasteiger *et al.*, 2005), improved kinetics of this reaction can lead to direct increases in the fuel cell efficiency.

Platinum-based catalysts have been shown to be highly active for the ORR (Gasteiger *et al.*, 2010), however the cost and stability of these catalysts is still one of the factors that hinders the commercial viability of this technology. To make this technology commercially viable for application in the automotive industry, a four- to ten-fold reduction in platinum loading is required without decreasing the power density (Gasteiger *et al.*, 2010). Therefore to make fuel cells commercially viable, fuel cell efficiencies need to be improved by finding more active catalysts that utilize less platinum per device. This can in part be achieved by developing catalysts that are more active for the ORR (Gasteiger *et al.*, 2010).

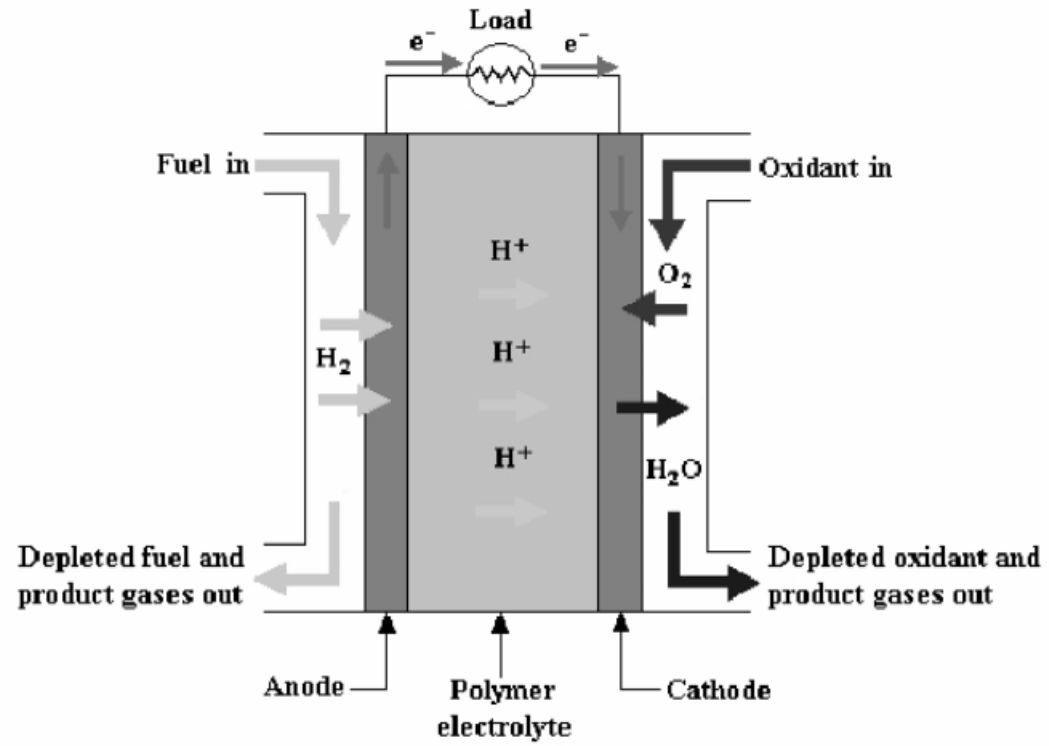

Figure 1.2: Schematic representation of a proton exchange membrane fuel cell (PEMFC) (Yuan & Wang, 2008).

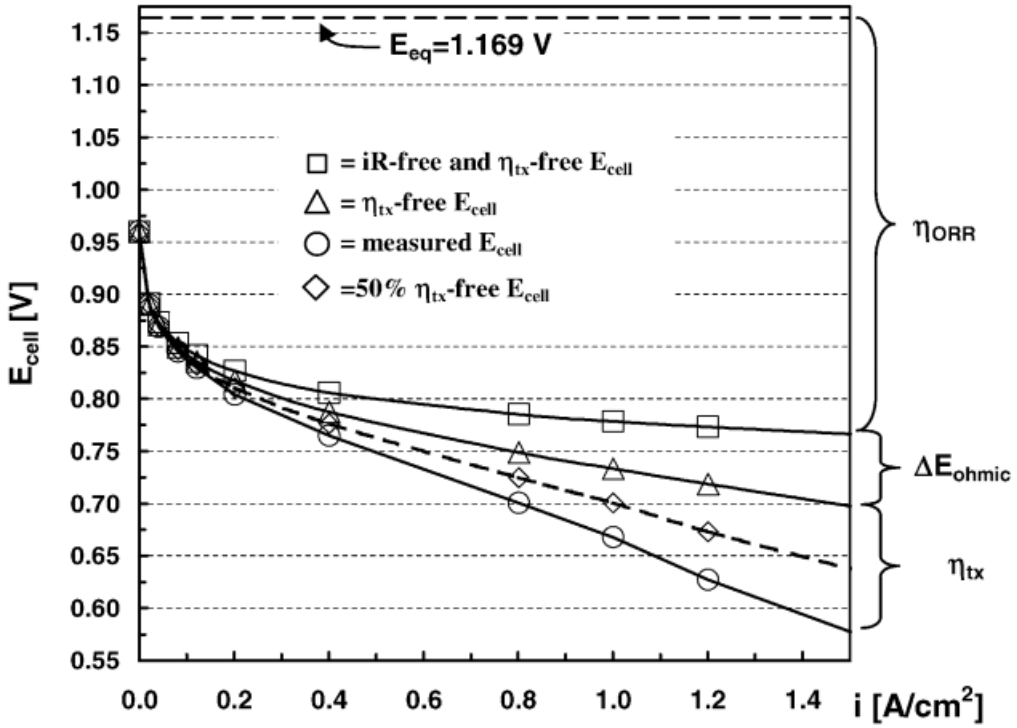

Figure 1.3: Polarization curve of a single-cell PEMFC. Circular markers(◯): measured polarization curve of a 50 cm^2 single-cell (feed: H_2/air) at 80°C and 1.5 bar (a), square markers (□): the polarization curve of (a) after corrections for the mass-transport (η_{tx}) and ohmic (iR) losses. Triangle (△) and diamond (◇) markers represents the polarization of (a) after 100% and 50% mass-transport-free correction, respectively (Gasteiger *et al.*, 2005).

1.3 The oxygen reduction reaction

Due to its inefficiencies and its importance in fuel cells and air batteries, the ORR has become one of the most important and studied reactions in electrochemistry (Gewirth & Thorum, 2010). In state-of-the-art PEMFCs this reaction occurs over a platinum surface supported over a carbon substrate at moderate conditions, i.e. 65 - 85 °C and 1 - 2 bar (Gasteiger *et al.*, 2010). The overall desired reaction process at the cathode electrode is a so-called four-electron transfer process (equation 1.4), where oxygen is reduced directly to water. An alternative and undesired reaction is the two-electron transfer reaction which results in the formation of transient superoxo/peroxo species and possibly the formation of hydrogen peroxide. The formation of hydrogen peroxide is undesired due to its detrimental effect on the integrity of the polymer electrolyte membrane (Yuan & Wang, 2008). At low overpotentials, i.e. 0.1-0.4 V, the ORR on platinum is observed to proceed via the four-electron transfer process with less than 1% hydrogen peroxide formation (Gewirth & Thorum, 2010).

To design better electrocatalysts for the ORR a much deeper understanding of the working mechanism of the catalytic process is required. A number of reaction mechanisms have been put forward in the literature to investigate the activity of different model catalysts (Schmidt *et al.*, 2001; Nørskov *et al.*, 2004; Qi & Li, 2012; Duan & Wang, 2013; Hansen *et al.*, 2014). Table 1.1 presents the elementary reaction steps of three proposed mechanisms. The proposed mechanisms differ from each other by the mode of the O-O bond cleavage and possible consecutive hydrogenation of peroxyl to hydrogen peroxide. The dissociative mechanism involves direct dissociation of O_2 before any hydrogenation, whilst for both the peroxyl and peroxide mechanisms, O_2 bond dissociation is preceded by the first and second hydrogenation steps, respectively. In many instances all these steps occur, with some being more dominant (kinetically favourable) than others depending on the type of catalyst surface; the dominance determines the controlling mechanism (Nørskov *et al.*, 2004; Duan & Wang, 2013).

1.3.1 Dependence of the ORR activity on Pt particle size

The ORR surface-area-specific activity (i.e. current density in A/cm^2) has been experimentally shown to decrease with decreasing platinum nanoparticle size (Kinoshita, 1990; Tritsaris *et al.*, 2011; Nesselberger *et al.*, 2011; Perez-Alonso *et al.*, 2012; Tripković *et al.*, 2014). Whilst the surface-area-specific activity decreases with decreasing platinum nanoparticle size, and as a consequence the mass-specific activity (i.e. current per mg of platinum in A/mg_{Pt}) is reported to have a maximum in the size range of 2-4 nm (Kinoshita, 1990; Tritsaris *et al.*, 2011; Perez-Alonso *et al.*, 2012). The maximum in mass-specific activity is observed as a result of the increase in metal dispersion and decrease in surface-area-specific activity with decreasing platinum nanoparticle size. Figure 1.4 shows the dependence of the surface-area-specific- (a) and mass-specific (b) activity on platinum nanoparticle size. Based on Figure 1.4a, Perez-Alonso *et al.* (2012) argued that there is a correlation between the observed decrease in surface-area-specific activity, with decreasing platinum nanorpaticle size, and the

Table 1.1: Classifications of oxygen reduction reaction mechanisms proposed in the literature (Duan & Wang, 2013; Li *et al.*, 2015a).

No.	Dissociative	Peroxyl mechanism	Peroxide mechanism
a	$O_2 + [\star] \rightleftarrows O_2^\star$	$O_2 + [\star] \rightleftarrows O_2^\star$	$O_2 + [\star] \rightleftarrows O_2^\star$
b	$\mathbf{O_2^\star + [\star] \rightleftarrows O^\star + O^\star}$	$\mathbf{O_2^\star + H^+ + e^- \rightleftarrows OOH^\star}$	$\mathbf{O_2^\star + H^+ + e^- \rightleftarrows OOH^\star}$
c		$OOH^\star + [\star] \rightleftarrows O^\star + OH^\star$	$\mathbf{OOH^\star + H^+ + e^- \rightleftarrows HOOH^\star}$
d	$O^\star + H^+ + e^- \rightleftarrows OH^\star$	$O^\star + H^+ + e^- \rightleftarrows OH^\star$	$HOOH^\star + [\star] \rightleftarrows OH^\star + OH^\star$
e	$OH^\star + H^+ + e^- \rightleftarrows H_2O^\star$	$OH^\star + H^+ + e^- \rightleftarrows H_2O^\star$	$OH^\star + H^+ + e^- \rightleftarrows H_2O^\star$
f[1]	$OH^\star + OH^\star \rightleftarrows H_2O^\star + O^\star$	$OH^\star + OH^\star \rightleftarrows H_2O^\star + O^\star$	$OH^\star + OH^\star \rightleftarrows H_2O^\star + O^\star$

$[\star]$ represents a vacant active site on a catalyst surface whilst $X^\star$ represents a species X adsorbed on an active site.
[1] the $OH^\star$ disproportionation reaction (f[1]) was reported by Ford *et al.* (2010)

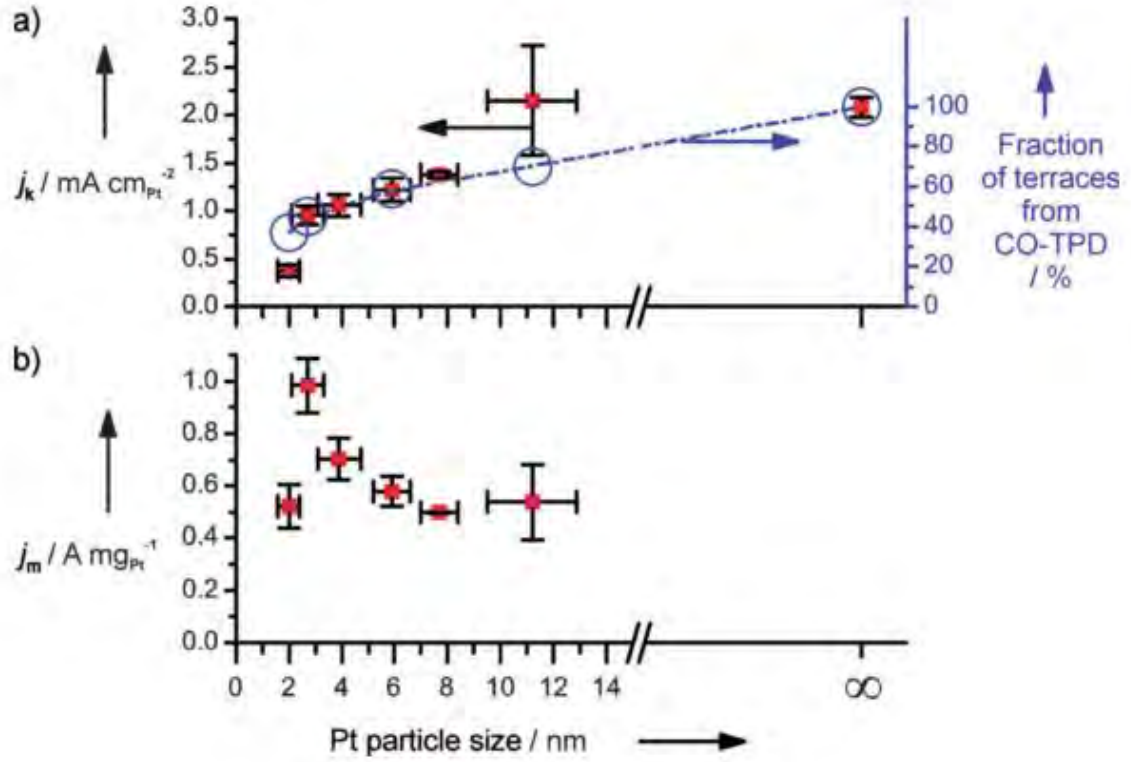

Figure 1.4: Dependence of the measured ORR activity on platinum nanoparticle size: a) surface-area-specific (j_k) and b) mass-specific (j_m) activity at 0.9 V versus the reverse hydrogen electrode (vs. RHE). The fraction of terraces measured using CO-TPD is shown in a) on the secondary axis (Perez-Alonso *et al.*, 2012).

fraction of terrace sites on polycrystalline nanoparticles, probed with carbon monoxide temperature programmed desorption (CO-TPD). This supports the notion that the terrace sites on nanoparticles are more active for ORR whilst the edges and corners are less active (Kinoshita, 1990; Greeley *et al.*, 2007). As a result of the observed dependence of the ORR activity on nanoparticle size it is crucial to understand nanoparticle-structural changes associated with decreasing particle size and how each change affects the ORR activity.

1.3.2 The ORR activity on platinum terrace sites

A number of experimental and theoretical studies have shown that the ORR is structure-sensitive (Markovic *et al.*, 1997; Schmidt *et al.*, 2001; Duan & Wang, 2013; Su *et al.*, 2014). Low-index platinum surfaces have received the most attention in both experimental and theoretical investigations. Using rotating ring-disk electrode (RRDE) experiments, Markovic *et al.* (1997) showed that under different electrolytic environments there is a variation in the ORR activity of low-index platinum surfaces. They observed that in H_2SO_4 solution the ORR activity on low-index platinum surfaces increases in the order (111) << (100) < (110); (110) was observed to be ca. 100 times more active than (111). The same authors found that over $HClO_4$ and KOH, the activity increases in a semi-reverse order to the above, i.e. (100) < (110) < (111), although in $HClO_4$ the differences were relatively small. This led to the suggestion that the change in the observed ORR activity may be due to structure-sensitive adsorption of anions in the electrolyte solution. The variation in the ORR activity in $HClO_4$ and KOH was argued to arise from an inhibiting effect of adsorbed OH anions—stronger on (100) and weaker on (110) and (111) (Markovic *et al.*, 1997). In H_2SO_4 the structure specific adsorption sulfate/bisulfate anions were argued to strongly inhibit the ORR activity on Pt(111) surfaces (Markovic *et al.*, 1997). Since adsorbed OH species are presented on the catalyst surface as ORR intermediates, it is antici-

pated that the observed structure sensitive behaviour in $HClO_4$ and KOH will be present under fuel cell operating conditions.

It has been argued that over nanosized platinum particles in H_2SO_4, the decrease in the surface-area-specific activity for the ORR can be related to the reduction in the surface-averaged distribution of terrace surfaces (Kinoshita, 1990; Markovic *et al.*, 1997; Perez-Alonso *et al.*, 2012). This link was proposed by Kinoshita (1990) after noting that within the size range where the maximum mass-specific activity is observed, the mass-averaged distribution of terrace sites has a maximum for cuboctahedral model nanoparticles. Perez-Alonso *et al.* (2012) observed from CO-TPD experiments that the surface-averaged distribution of terrace sites decreases with particle size in the same manner that the surface-area-specific activity does. This argument links the change in the distribution of the different surface sites to the observed change in the ORR activity as a function of nanoparticle size.

Density functional theory (DFT) studies have been conducted in attempt to further understand the structure-sensitive behaviour of the ORR activity of platinum catalysts, and to improve the insight at the atomic level. These studies have evaluated the reaction mechanisms presented in Table 1.1, in which the adsorption energies of the ORR intermediates have been used to predict the ORR activity (Schmidt *et al.*, 2001; Nørskov *et al.*, 2004; Qi & Li, 2012; Duan & Wang, 2013; Madala, 2013; Hansen *et al.*, 2014). Presently it is still unclear as to which ORR mechanism is dominant on platinum surfaces. A set of elementary reactions presented by Duan & Wang (2013) is shown in Table 1.1. Similar ORR mechanisms have been proposed by other researchers (Panchenko *et al.*, 2004; Nørskov *et al.*, 2004; Ford *et al.*, 2010; Madala, 2013; Hansen *et al.*, 2014; Li *et al.*, 2015a). Ford *et al.* (2010) proposed an additional possible elementary reaction, i.e. step-f in Table 1.1, which, based on DFT calculations, is feasible without an activation barrier over the Pt(111) surface. Since the Pt(111) and Pt(100) surface terminations are more thermodynamically favourable terminations, equilibrium shaped Pt nanorpaticles are anticipated to expose predominantly these surface terminations (Vitos *et al.*, 1998; Xia *et al.*, 2009). Therefore, only the Pt(111) and PT(100) surface terminations will be predominantly exposed to the reaction medium.

The first step in investigating the ORR mechanism involves understanding the stability of different ORR intermediates on a catalyst surface. In Table 1.2 adsorption energies of different ORR intermediates on Pt(111) and Pt(100) slab surfaces are presented. With the knowledge of the stability of different ORR intermediates, the reaction and activation energies for each elementary reaction can be evaluated. These energies are given in Tables 1.3 and 1.4 for each of the elementary reactions presented in Table 1.1. With the knowledge of the above energies, kinetic and energetic analyses can be conducted.

Based on energetic analyses, it is argued that the ORR mechanism varies over different platinum catalyst surfaces (Nørskov *et al.*, 2004; Ford *et al.*, 2010; Duan & Wang, 2013). This is also demonstrated in Tables 1.3 and 1.4. Based on their energetic analysis, Duan & Wang (2013) concluded that the ORR follows a peroxyl mechanism on Pt(111) and a dissociative mechanism on the Pt(100); this is consistent with findings by other researchers (Ford *et al.*, 2010; Sha *et al.*, 2011; Li *et al.*, 2015a). Although on the Pt(100) surface the dissociation of $OOH^\star$ has the lowest activation energy, the process was concluded to not follow this path (Duan & Wang, 2013), the formation of $OOH^\star$ on the Pt(100) surface has a higher activation energy than the activation energy for direct dissociation of $O_2^\star$ (see Table 1.4). Duan & Wang (2013) also reported that on the Pt(100) surface, $OOH^\star$ has no stable adsorption geometry. This is consistent with calculations by Li *et al.* (2015a). Using the data presented in Tables 1.3 and 1.4, it can be seen that the rate determining steps—from an energetic analysis perspective—on Pt(111) and Pt(100) for the ORR are $O^\star$ and $OH^\star$ hydrogenation, respectively. This is in agreement with independent literature studies (Nørskov *et al.*, 2004; Keith & Jacob, 2010; Sha *et al.*, 2011; Holewinski & Linic, 2012; Hansen *et al.*, 2014; Li *et al.*, 2015a).

An improved understanding of the ORR activity can be gained through the use of energetic data

Table 1.2: Calculated adsorption energies of ORR intermediates on Pt(111) and Pt(100) at 0.25 ML coverage. All energies are reported with respect to corresponding adsorbates in the gas phase.

Adsorbate	Pt(100) facet [eV]			Pt(111) facet [eV]			
	Atop	Bridge	Hollow	Atop	Bridge	fcc	hcp
$O_2^\star$		-1.10[a]	-0.29[a]		-0.69[a]	-0.65[b]	-0.45[b]
		-1.02[d]			-0.63[b]	-0.52[d]	-0.46[a]
					-0.46[c]		
					-0.63[d]		
					-0.72[g]	-0.68[g]	-0.58[g]
$O^\star$	-2.92[a]	-4.03[a]	-3.60[a]			-3.96[a]	-3.78[d]
			-3.70[d]			-4.08[d]	
						-3.59[c]	
$OH^\star$	-2.34[a]	-2.87[a]	-2.31[a]	-2.22[a]	-2.23[a]	-1.80[a]	
	-2.38[d]	-2.74[d]	-2.02[d]	-2.23[d]	-2.14[d]	-1.82[c]	
$OOH^\star$			-1.41[a]		-1.15[a]		
					-0.96[c]		
		-1.30[f]			-0.94[e]		
$HOOH^\star$			-0.39[a]		-0.25[a]		
			-0.31[f]		-0.29[c]		
					-0.27[e]		
$H_2O^\star$	-0.27[a]		-0.13[a]	-0.25[a]			
	-0.25[e]			-0.18[c]			
				-0.20[e]			

a: Duan & Wang (2011, 2013), VASP code, USPP−PW91, ZPE-corrected

b: Yang *et al.* (2010), VASP code, PAW−PBE, ZPE-corrected

c: Ford *et al.* (2010), DACAPO code, USPP−PW91, ZPE-corrected

d: Panchenko *et al.* (2004), VASP code, PAW−PW91

e: Li *et al.* (2015a), VASP code, PAW−PBE, ZPE-corrected

f: Li *et al.* (2015a), VASP code, USPP−PBE

g: Eichler & Hafner (1997), VASP code, USPP−PW91

Table 1.3: DFT-calculated reaction (ΔE) and activation (E_a) energies for the dissociation of the O-O bond of adsorbed ORR intermediates.

Reaction step	Pt(111) facet		Pt(100) facet	
	$\Delta E[eV]$	$E_a[eV]$	$\Delta E[eV]$	$E_a[eV]$
$O_2^\star \longrightarrow 2O^\star$	-1.02[a], -0.72[b]	0.63[a], 0.71[b]	-1.20[a], -1.28[c]	0.15[a], 0.13[c]
	-1.31[c], -1.23[d]	0.53[c], 0.51[d]		
$OOH^\star + [\star] \longrightarrow O^\star + OH^\star$	-1.51[a], -1.37[b]	0.05[a], 0.16[b]	-2.15[a], -2.13[e]	0.00[a], 0.00[e]
	-1.63[c], -1.30[d]	0.06[c], 0.12[d]		
$HOOH^\star + [\star] \longrightarrow 2OH^\star$	-1.75[a], -1.68[b]	0.26[a], 0.25[b]	-2.74[a], -2.69[e]	0.11[a], 0.08[e]
	-1.76[c], -1.62[d]	0.21[c], 0.14[d]		

a: Duan & Wang (2011, 2013), VASP code, USPP−PW91, ZPE-corrected

b: Ford *et al.* (2010), DACAPO code, USPP−PW91, ZPE-corrected, co-adsorbed products and reactants

c: Li *et al.* (2015a), VASP code, PAW−PBE, ZPE-corrected

d: Sha *et al.* (2011), SeqQuest code, norm-conserving pseudopotentials and PBE

e: Li *et al.* (2015a), VASP code, USPP−PBE

Table 1.4: DFT-calculated reaction (ΔE) and activation (E_a) energies for the hydrogenation of ORR intermediates.

Reaction step	Pt(111) facet		Pt(100) facet	
	$\Delta E[eV]$	$E_a[eV]$	$\Delta E[eV]$	$E_a[eV]$
$O_2^\star + H^+ + e^- \longrightarrow OOH^\star$	-0.15[a], -0.13[b] -0.03[c]	0.25[a], 0.29[b] 0.36[c]	-0.26[a], 0.28[e]	0.48[a], 0.53[e]
$OOH^\star + H^+ + e^- \longrightarrow HOOH^\star$	-0.28[a], -0.32[b] -0.06[c]	0.19[a], 0.21[b] 0.31[c]	0.19[e]	0.37[e]
$O^\star + H^+ + e^- \longrightarrow OH^\star$	-0.14[a], -0.16[b] 0.03[c]	0.79[a], 0.72[b] 0.86[c]	-0.43[a], -0.29[c]	0.36[a], 0.42[c]
$OH^\star + H^+ + e^- \longrightarrow H_2O^\star$	-0.70[a], -0.79[b] -0.52[c]	0.09[a], 0.08[b] 0.16[c]	0.06[a], 0.16[c]	0.80[a], 0.79[c]

a: Duan & Wang (2011, 2013), VASP code, USPP−PW91, ZPE-corrected

b: Ford *et al.* (2010), DACAPO code, USPP−PW91, ZPE-corrected, co-adsorbed products and reactants

c: Li *et al.* (2015a), VASP code, PAW−PBE, ZPE-corrected

d: Sha *et al.* (2011), SeqQuest code, norm-conserving pseudopotentials and PBE

e: Li *et al.* (2015a), VASP code, USPP−PBE

to generate a microkinetic model. The latter is crucial since it considers the effect of coverage on the rates of elementary reaction steps. Based on a microkinetic simulation Hansen *et al.* (2014) reported that between an electrode potential range of 0.75-0.95 V versus RHE, the Pt(111) surface is predominantly covered with OH species. Above this potential range adsorbed atomic O was observed to be the dominant adsorbate (Hansen *et al.*, 2014). As a result purely energetic analyses give an incomplete picture as they do not account for surface coverage. Whilst the hydrogenation of $OH^\star$ has thermodynamic rate control, a kinetic model developed by Hansen *et al.* (2014) demonstrates that the latter step kinetically is not rate limiting. Using a theoretical kinetic model, Nørskov *et al.* (2004) calculated the ORR activity as a function of adsorption energies of O and OH on M(111) facets (where M = W, Mo, Fe, Co, Ru, Ni, Rh, Cu, Ir, Pd, Pt, Ag, Au). They observed a Sabatier-type behaviour with Pt(111) being the most ORR reactive pure metal (111)-surface, as shown in Figure 1.5. Recently Viswanathan *et al.* (2012) plotted the experimental ORR activity of different surfaces against the adsorption free energy of OH (Figure 1.6) and noted the presence of an optimum OH-surface interaction. Other studies have also indicated this relationship between adsorption energies of O, OH and the ORR activity (Karlberg *et al.*, 2007; Friebel *et al.*, 2012; Stephens *et al.*, 2012; Hansen *et al.*, 2014).

1.3.3 The ORR activity on platinum edge sites

The ORR activity on edge and corner sites is thought to be poor, unlike on platinum terrace sites (Greeley *et al.*, 2007). As discussed in section 1.3.1, Perez-Alonso *et al.* (2012) argued in favour of this point based on results of a series of RRDE and CO-TPD experiments (as shown in Figure 1.4a). To model this behaviour, theoretical studies have investigated the ORR activity at different surface features of truncated octahedral nanoparticles, i.e. Pt(111) and Pt(100) facets and, edge and corner sites (Tritsaris *et al.*, 2011; Tripković *et al.*, 2014). The activity data for the Pt(111) and Pt(100) facets is obtained theoretically as presented in subsection 1.3.2 (Tables 1.3, 1.4 and 1.2), whilst edge sites have been modelled as stepped-surfaces, most commonly as Pt(211), or as nanoparticle clusters (Greeley *et al.*, 2007; Tritsaris *et al.*, 2011; Wei & Liu, 2013; Tripković *et al.*, 2014; Peng & Mavrikakis, 2015).

Since the relative contribution of edge and corner sites to total sites exposed on a nanoparticle increases with decreasing particle size, it is crucial to understand their contribution to the overall ORR activity. This can be achieved by understanding the interaction of the ORR intermediates with edge and corner sites. The adsorption and dissociation of O_2 on Pt step-surfaces has been investigated both experimentally (Yamanaka *et al.*, 1996; Wang *et al.*, 1997; Sano *et al.*, 1998; Badan *et al.*, 2015;

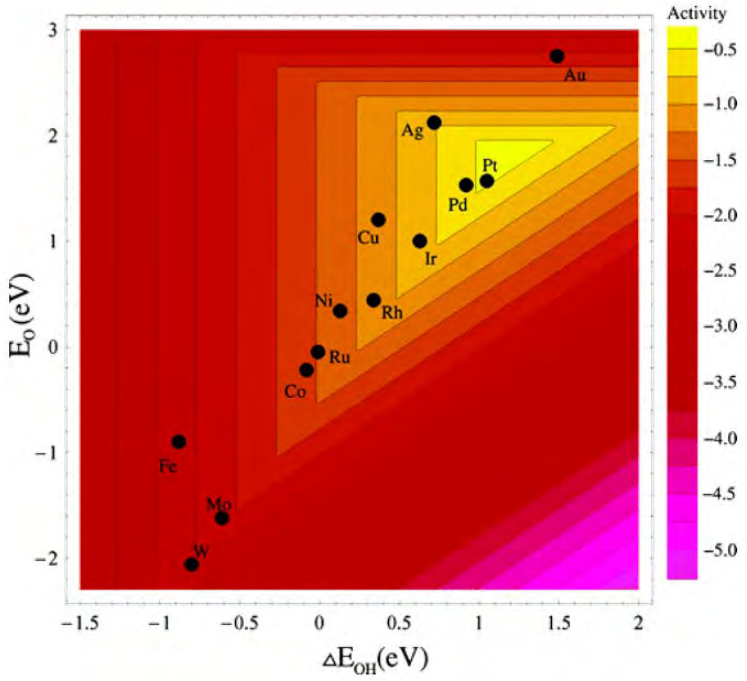

Figure 1.5: Theoretical ORR activity trends as a function of O and OH binding energy on M(111), where M represents d-band metals (Nørskov *et al.*, 2004).

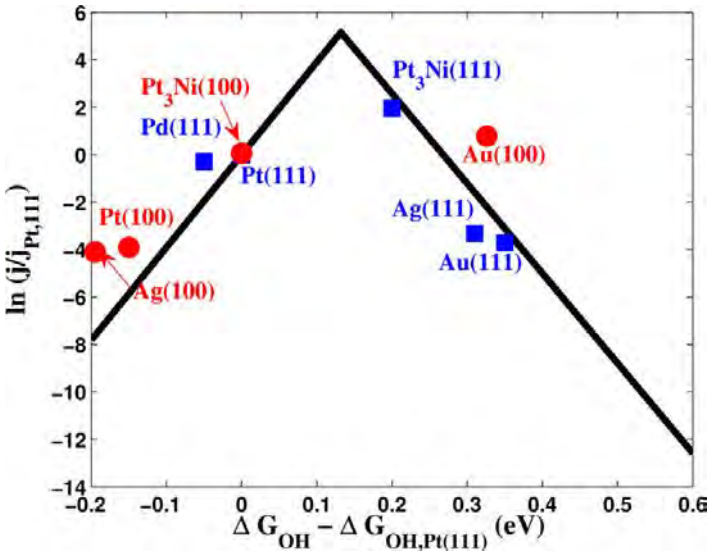

Figure 1.6: Universal activity volcano plot for ORR showing experimental current density as a function of DFT-calculated adsorption free energy of OH (Viswanathan *et al.*, 2012).

Jacobse *et al.*, 2015) and theoretically (Feibelman *et al.*, 1996; Šljivančanin & Hammer, 2002; Ogawa *et al.*, 2014; Kolb *et al.*, 2014). Experimental studies generally report an increased adsorption strength of atomic O and O_2 at edge sites compared to the adsorption on terrace sites. This is evident from a thermal desorption spectroscopy study of Wang *et al.* (1997), where for atomic O desorption from a Pt(335) step-surface, two peaks were observed at 427 °C and 577 °C. The low temperature peak was assigned to desorption from Pt(111) terrace sites whilst the higher temperature peak was assigned to desorption from step-edge sites. Recently, an independent study by van der Niet *et al.* (2010), reported desorption peaks at 390 °C and 501 °C for atomic O desorption from a Pt(533) step-surface. For desorption of atomic O from a Pt(553) step-surface desorption peaks were observed at 390 °C and 465 °C (van der Niet *et al.*, 2010). The differences in desorption peaks were argued to be as a result of different steps. Whilst Pt(533) has four atom wide (111) terraces with Pt(100) steps, the Pt(553) surface has four atom wide (111) terraces truncated by (110) steps.

These observations were also true for O_2 desorption where two desorption peaks (at -173 °C to -123 °C and -73 °C to -23 °C) were identified and assigned to desorption from terrace sites (low temperature peak) and desorption from step-edge sites (high temperature peak) (Yamanaka *et al.*, 1996; Wang *et al.*, 1997; Sano *et al.*, 1998; Badan *et al.*, 2015; Jacobse *et al.*, 2015). Theoretical studies have confirmed the above observation by predicting stronger atomic O and O_2 adsorption at step-edge sites compared to terrace sites of step-surfaces (Feibelman *et al.*, 1996; Šljivančanin & Hammer, 2002; Ogawa *et al.*, 2014; Kolb *et al.*, 2014). The adsorption energies of atomic O on edge-bridge (EB) sites of Pt(553) and Pt(533) were predicted to be -4.23 eV/O and -4.37 eV/O relative to atomic O in the gas phase, respectively (Jacobse *et al.*, 2015). Šljivančanin & Hammer (2002) calculated the adsorption energy of atomic O on Pt(211) edge-bridge site to be -4.34 eV/O. For stepped-surfaces it has been argued that the step-type plays a significant role in the reactivity of the step-edge sites (van der Niet *et al.*, 2010; Jacobse *et al.*, 2015). The latter is based on the observed differences in adsorption energies of atomic O on step-edge sites for different step-surface. From a recent theoretical study it was reported on step-edge sites of step-surface with a Pt(100) step the adsorption energies of OH, O, O_2, H_2O and H are increased compared to adsorption on terrace sites (Kolb *et al.*, 2014). The interaction of H_2O with Pt(211), Pt(553) and Pt(533) step-surfaces has also been investigated using thermal desorption spectroscopy and found to be stronger at step-edge sites than on terrace sites (van der Niet *et al.*, 2010; Badan *et al.*, 2015).

The dissociation of O_2 on Pt(211) and model nanoparticle edge sites has been investigated using theoretical methods. On Pt(211), Šljivančanin & Hammer (2002) calculated (using a PW91 function and PAW potentials) a dissociation barrier of 1.0 eV for dissociation of O_2 from an edge-bridge site to two co-adsorbed O atoms on adjacent edge-bridge sites. Using a different functional (RPBE), they also calculated an activation energy of 0.9 eV for the same dissociation process. On a model truncated octahedral Pt nanoparticle with 116 atoms, Jennings *et al.* (2014) calculated an energy barrier of 0.41 eV for O_2 dissociation to two co-adsorbed O atoms on adjacent edge-bridge sites. The difference observed between O_2 dissociation on a Pt(211) edge and on a nanoparticle edge may possibly be due to the influence of the corner atoms which are absent on Pt(211). Table 1.5 presents the DFT-calculated adsorption energies and dissociation energy barriers of O and O_2 on edge sites found on step-surfaces and model nanoparticle clusters.

Table 1.5: Calculate adsorption energies (ΔE_{ads}) of O and O_2 on edge-bridge sites. Also presented are the dissociation energy barriers (E_{diss}) for O_2 on edge sites. All adsorption energies are reported with respect to corresponding adsobates in the gas phase.

Adsorbate	Surface	$\Delta E_{ads}[eV]$	$E_{diss}[eV]$	Ref:
O_2	Pt(211)[a]	-1.5	1.0	Šljivančanin & Hammer (2002)
	[b]	-0.9	0.9	Šljivančanin & Hammer (2002)
	116-atom NP[c]	-1.68	0.41	Jennings *et al.* (2014)
O	Pt(211)[d]	-4.85		Ogawa *et al.* (2013)
	SD-Pt(211)[e]	-4.92		Ogawa *et al.* (2014)
	116-atom NP[c]	-5.02		Jennings *et al.* (2014)
	CO-NP[f]	-4.2		Li *et al.* (2013)
	147-atom NP[g]	-4.66		Peng & Mavrikakis (2015)

a: ultrasoft pseudopotentials and a PW91 functional

b: ultrasoft pseudopotentials and a RPBE functional

c: 116-atom truncated octahedral Pt nanoparticle, using VASP code, PAW potentials and PW91 functional

d: using VASP code, PAW potentials and a PBE functional

e: step-doubled Pt(211) step-surface, i.e. Pt(S)-[5(111)×2(100)], using VASP, PAW potentials and PBE functional

f: 147-atom cuboctahedral Pt nanoparticle, using VASP, PAW potentials and an RPBE functional

g: 147-atom cuboctahedral Pt nanoparticle, using VASP, PAW potentials and a PW91 functional

With the experimental and theoretical tools available, the interaction of ORR intermediates with step-edge sites of step-surfaces can be determined. Knowledge of these interactions can be further

used to generate kinetic models for the ORR activity on step-edge sites of step-surfaces (Greeley *et al.*, 2007). Using the potential energy surface (PES) calculated at 0.9 V electrode potential for a peroxyl ORR mechanism on different surfaces, Gómez-Marín *et al.* (2013) argued that the ORR specific activity decreases in the order Pt(111) > Pt(100) > Pt(110) > Pt(211). This is in agreement with experimental observations by Markovic *et al.* (1997) for low Miller index surfaces (see subsection 1.3.2). The agreement between the predicted ORR activity order of low Miller index surface with experimentally measured activities is an indication of the predictive power of DFT methods.

1.3.4 Theoretical models of overall ORR activity

The overall ORR activity over polycrystalline platinum nanoparticles has been modelled as a weigthed average of activities of different polycrystalline surface features (Greeley *et al.*, 2007; Tritsaris *et al.*, 2011; Nesselberger *et al.*, 2011; Wei & Liu, 2013; Tripković *et al.*, 2014). This is mathematically equivalent to equation 1.6,

$$J_{overall} = \sum_i \chi_i \cdot j_i \tag{1.6}$$

where $J_{overall}$, χ_i and j_i are the overall ORR activity, relative fraction of $i-type$-surface sites per nanoparticle size and the activity on a $i-type$ single crystalline surface, respectively. The relative fraction of different crystallite surface sites is dependent on the particle shape and size. Generally cuboctahedral and truncated octehedral nanoparticle models are used, the choice is mainly based on thermodynamic stability consideration of the former shapes relative to other possible crystallite shapes (Vitos *et al.*, 1998; Xia *et al.*, 2009; Long *et al.*, 2010; Wei & Liu, 2013; Tripković *et al.*, 2014). For perfect ideal cuboctahedral and truncated octahedral nanoparticles only the contributions of the Pt(111), Pt(100), edge and corner type-surface sites are considered. The relative fractional distribution of these surface sites changes with nanoparticle size. A strong fundamental assumption necessary for the relationship described by equation 1.6, is that different polycrystalline surface features behave independently (Greeley *et al.*, 2007). This further requires that diffusion of reaction intermediates across different surface-type sites, i.e. mixing of coverage across two independent surface-types, is limited.

The ORR activity on single crystalline surfaces can be experimentally determined using electrochemical techniques such as the rotating ring disk electrode (RRDE)- linear sweep voltammetry (LSV) and cyclic voltammetry (CV). Theoretically, the ORR activity for each polycrystalline surface site can be determined from DFT calculations of the energetics of elementary reactions and finding the minimum free energy pathway for oxygen reduction to water (Nørskov *et al.*, 2004; Karlberg *et al.*, 2007; Greeley *et al.*, 2007). Nørskov *et al.* (2004) proposed a simple activity model given by equation 1.7,

$$j_i(U) = \tilde{j_{k,i}} \cdot exp\left\{\frac{-\Delta G(U)_i}{k_B T}\right\} \tag{1.7}$$

where $\tilde{j_{k,i}}$, $\Delta G(U)_i$ and k_B are activity pre-factor (for activity on $i-type$-surface) which includes details of proton transfer to the surface and site density, the largest activation free energy for the ORR process at a given electrode potential U relative to the standard hydrogen electrode (vs. SHE) and Boltzmann constant, respectively. Many studies have adopted this model for describing the activity of single crystalline surfaces (Karlberg *et al.*, 2007; Greeley *et al.*, 2007; Tritsaris *et al.*, 2011; Wei & Liu, 2013; Tripković *et al.*, 2014). Using this model and equation 1.6, the latter studies have investigated the overall ORR activity over cuboctahedral (Tritsaris *et al.*, 2011) and truncated octahedral nanoparticles (Wei & Liu, 2013; Tripković *et al.*, 2014). In a theoretical study by Wei & Liu (2013) it was argued, based on calculated atomic O coverage at ca. 0.65 V electrode potential versus SHE, that the edge platinum atoms of truncated octahedral platinum nanoparticles with 288, 405 and 490 atoms do not participate in the ORR, as they become saturated with atomic oxygen, i.e. each edge Pt atom is involved in four oxygen bonds. Based on this, Wei & Liu (2013) modelled the ORR mass-specific activity as a function of only the distribution of the Pt{111} facets. At an electrode potential of 0.65

V versus SHE, Wei & Liu (2013) reported that the Pt{100} facets will also be saturated with atomic oxygen.

Tritsaris *et al.* (2011) and Tripković *et al.* (2014) make use of calculated activation free energies for the ORR over Pt(111), Pt(100) and Pt(211) which were calculated by Greeley *et al.* (2007) to be 0.1, 0.12 and 0.72 eV at an electrode potential of 0.9 V versus SHE, respectively. Using the latter activation free energies together with equations 1.6 and 1.7 and a set of cuboctahedral nanoparticles with varying diameters, Tritsaris *et al.* (2011) modelled the overall ORR activity as a function of nanoparticle size. Their model predicted a decrease in the ORR surface-area-specific activity with decreasing particle size, consistent with experimental observations (Markovic *et al.*, 1997; Perez-Alonso *et al.*, 2012). Nesselberger *et al.* (2011) performed single crystallite surface experiments to determine their activity and then modelled the overall ORR activity as a function of nanoparticle size using the measured activities, equation 1.6 and ideal cuboctahedral nanoparticle shapes. Using the location of the mass-specific ORR activity maximum, one can compare the theoretical models to experimental measurements. Experimental studies have reported a maximum mass-specific activity for nanoparticle diameters of 3-4 nm (Kinoshita, 1990; Gasteiger *et al.*, 2005; Perez-Alonso *et al.*, 2012) and 2.2 nm (Shao *et al.*, 2011), which is in reasonable agreement with theoretical studies (2-4 nm (Tritsaris *et al.*, 2011), $\sim$ 2 nm (Wei & Liu, 2013) and $\sim$ 3 nm (Tripković *et al.*, 2014)). The subtle differences maybe due to the inherent assumptions and choice of nanoparticle shapes.

Though there seem to be an apparent agreement between experiments and theoretical models, there has not been a strong justification for why is it that the different polycrystalline surface features behave independently and why the step-surface models are representative of finite nanoparticle structures. In a recent study by Badan *et al.* (2015) it was argued based on thermal desorption spectroscopic experiments that the Pt(211) step-surface can not be considered representative of Pt(111) terraces terminated by Pt(100) steps since the behaviour of oxygen and water was observed to be particularly unique for the Pt(211) compared to surfaces with a larger number of atomic rows along the Pt(111) terrace. Studies based on electrochemical experiments, using a rotating ring disc electrode (RRDE) apparatus, have also reported an increase in the ORR activity with decreasing Pt(111) terrace length (Hoshi *et al.*, 2013; Bandarenka *et al.*, 2014). Therefore, it might be argued that the choice for which step-surface to use for modelling the ORR activity at edge sites, is not trivial.

1.4 Proposed work

1.4.1 Problem statement

The decrease in the surface-area-specific activity of the ORR with decreasing platinum particle size has resulted in a number of interesting observations, in particular the observed structure-sensitivity of the ORR activity over platinum nanoparticles. The terrace sites, particularly Pt(111), are thought to be most active for the ORR process whilst the edges are thought to be less active (Greeley *et al.*, 2007; Perez-Alonso *et al.*, 2012) or not active at all as they may be fully covered by atomic oxygen (Wei & Liu, 2013). Intuitively the fractional density or relative concentration of edge and corner atoms is expected to increase with decreasing particle size. A better understanding of the activity of edge sites may result in improved platinum utilization.

To date theoretical studies have mainly focussed on the ORR process over Pt(111) and Pt(100) terraces, whilst less effort has been invested in understanding the edge region. Step-surfaces such as Pt(211) have been used to model the edge region, but these models do not allow for the investigation of the interaction/connection between edges and the terrace regions that they separate. It has been shown that the ORR activity varies with terrace length, and the Pt(211) step-surface has been found to behave particularly different from other step-surfaces with Pt(100) steps (Hoshi *et al.*, 2013; Bandarenka *et al.*, 2014; Badan *et al.*, 2015). Although an intuitive approach will be to model the edge region of nanoparticles using model clusters, the computational cost of such large systems is very high compared

to simple models such as Pt(211) slabs (a 2.7 nm cuboctahedral platinum nanoparticle consists of ca. 561 atoms). Since the use of clusters may result in large and computationally expensive systems, the use of nanorod models is proposed (Swart *et al.*, 2007; van Helden *et al.*, 2009). These will enable the investigation of the edge site activity and how the edges interact with both the Pt(111) and Pt(100) terraces. Since the thermodynamically favourable Pt nanoparticle shapes are cuboctahedra and truncated octahedra consisting of {111} and {100} terraces (Xia *et al.*, 2009; Tripković *et al.*, 2014), this study will only investigate an edge system that consists of an edge separating Pt{111} and Pt{100} terraces.

1.4.2 Key questions

On account of the reviewed literature the key questions for the present study are:

1. What is the extent of the edge effect along the Pt(111) and Pt(100) nanorod facets?
2. Can the two surface sites, i.e. Pt(111) and Pt(100) terraces, be considered to be kinetically isolated?
3. If the surface sites are connected, how are they connected?

1.4.3 Hypothesis

Due to their low coordination numbers, the nanorod edge sites will result in strong and localized adsorption of atomic O and O_2. As a consequence, edge sites will be fully saturated with oxygen and will form a separation barrier that isolates the Pt(111) and Pt(100) terraces. Therefore, diffusion of atomic O from one facet to another across the edge atomic row will be limited.

1.4.4 Project objectives

In light of the above the objectives of this study are therefore to:

1. Develop and optimize a nanorod model which can be used to model an edge region formed by the intersection of a Pt(111) and a Pt(100) terrace.
2. Use the optimized nanorod model to calculate the adsorption energies of atomic O and O_2, on various sites near and further from the nanorod edge.
3. Investigate the extent of the influence of the edge on terrace sites
4. Investigate co-adsorption of atomic O on nanorod edge sites
5. Investigate the diffusion of edge bound atomic O towards both the Pt(111) and Pt(100) terraces

Chapter 2

Method and Model Validation

2.1 Introduction

Heterogeneous catalytic processes are governed by the interaction of reactants, intermediates and products with the catalytically active surface. For many years empirical methods have been applied to gain insight into different catalytic processes. These methods are based on experimentally measured parameters and as a result, may lack predictive power and have limitations; this is more apparent for catalytic systems with complex reaction mechanisms. In recent decades theoretical methods, in particular computational chemistry, have gained traction as they allow for deeper insight into the different catalytic processes to be obtained. These methods have been applied to many reactions including the ORR. This chapter presents a brief overview of the available computational approaches and puts a greater focus on the density functional theory (DFT), as this approach has been applied extensively in theoretical studies of the ORR.

2.2 Computational Modelling Methods

Ab initio methods are based on the solution of the time-independent Schrödinger equation (TISE) given below,

$$H\Psi = E\Psi \tag{2.1}$$

where H is the Hamiltonian operator (total energy operator), and E and Ψ are the total energy and wavefunction of the system, respectively. The solution to the TISE gives fundamental information of the system (Dirac, 1929; Greeley *et al.*, 2002). The Born-Oppenheimer Approximation is applied to simplify the TISE. This approximation allows for the separation of the TISE into nuclear and electronic structure calculations by exploiting the fact that the atomic nuclei move much slower than the electrons and their position can be considered to be constant (from the perspective of the electrons) (Greeley *et al.*, 2002). Computational chemistry methods evaluate the solutions of the electronic TISE for a given atomic configuration; as a result the ground-state potential energy surface (PES) can be evaluated and is used for chemical analyses relevant to surface science and heterogeneous catalytic processes.

Since an analytical solution of the electronic TISE for a system with multiple interacting electrons does not exist, iterative methods are applied to solve the system. There are a number of methods that have been developed to iteratively solve the electronic TISE. The Hartree-Fock (HF) method is one of the earliest forms used in computational chemistry. This method is based on the assumption that the electrons can be treated as independent particles and uses a one-electron system where each electron experiences an effective potential, v_{eff}, due to the nuclei and the averaged potential of other electrons in the system. The HF method approximates the total wavefunction of an n-electron system, Ψ, as an antisymmetric product of one-electron wavefunctions, ψ(i.e. orbitals). To enforce the Pauli Exclusion Principle, which forbids any two electrons in a system to have the exact same quantum state, Slater determinantal wavefunctions are considered. This results in antisymmetric wavefunctions which

account for different electron spin states (Lewars, 2011). This is then solved by reducing the system into a one-electron electronic Schrödinger equation (SE),

$$\left(-\frac{h^2}{8\pi^2 m}\nabla^2 - v_{eff}\right)\psi = \varepsilon\psi \tag{2.2}$$

where h and m are Planck's constant and rest mass of an electron, respectively. The total HF energy of the system is therefore given as the sum of the eigenstates, ε, of all one-electron electronic SE solutions. Since v_{eff} depends on the knowledge of the one-electron wavefunctions an iterative procedure is used. This procedure is known as the self consistent-field (SCF) procedure. The SCF procedure first requires an initial guess of the one-electron wavefunctions which are used to evaluate the effective potential, v_{eff}. Once the effective potential is known, equation 2.2 is then solved for the one-electron wavefunctions and corresponding eigenstates. This is repeated using the new one-electron wavefunctions until wavefunction self-consistency is achieved.

The shortcomings of the HF method includes a lack of explicit consideration of electron correlation effects which results in poor molecular energies (Greeley *et al.*, 2002). The only correlation effects considered are the ones imposed by the antisymmetric wavefunctions (Lewars, 2011). Due to the high number of degrees of freedom in the HF method ($3n$ where n is the number of electrons in the system) and hence a high computational cost as well as a lack of explicit consideration of correlation effects, other methods are preferred. Density functional theory is one such method that has resulted in improved computational efficiency for reasonably large systems of practical interest. Furthermore, unlike the HF method where computational cost scale as $O(M^4)$, in DFT the computational cost only scales as $O(M^3)$ where M in the number of *basis-functions*(Shimojo *et al.*, 2001; Greeley *et al.*, 2002; Chen & Zhou, 2008).

2.3 Density Functional Theory

Density functional theory[1] is based on two theorems published in 1964 and 1965 by Hohenberg and Kohn, and Kohn and Sham, respectively. Hohenberg and Kohn (1964) proposed that all the ground state properties of a system of electrons and nuclei are uniquely determined by the ground state electronic density function. In particular, the total ground state energy of the system is uniquely determined by the ground state electron density function, $\rho_0(\mathbf{r})$. This is presented by equation 2.3,

$$E_0 = F[\rho_0(\mathbf{r})] = E[\rho_0(\mathbf{r})] \tag{2.3}$$

where E is an energy functional that transforms the ground state electron density function into the total ground state electronic energy of a system, E_0. The one major problem is that the exact form of the energy functional is unknown. The second theorem (Kohn & Sham, 1965) states that any trial electron density function will give an energy higher than or equal to the true ground state energy and that the minimum energy is uniquely achieved for the ground state density function. This is the DFT analogue of the variational theorem that is used in connection with wavefunction-based ab initio methods (Lewars, 2011). Mathematically this variational theorem can be expressed as,

$$E_v[\rho_t(\mathbf{r})] \geq E_0[\rho_0(\mathbf{r})] \tag{2.4}$$

where E_v is the electronic energy under an external nuclear potential $v(\mathbf{r})$, $\rho_t(\mathbf{r})$ is the trial electron density and $E_0[\rho_0(\mathbf{r})]$ is the true ground state energy. The trial electron density must satisfy the following conditions,

$$\int \rho_t(\mathbf{r})d\mathbf{r} = N \tag{2.5}$$

$$\rho(\mathbf{r}) \geq 0 \tag{2.6}$$

[1] The density functional theory description presented in this chapter is adapted from LeSar (2013), Lewars (2011), Springborg (1997) and Parr & Yang (1989) whilst the nomenclature is based on that used by Lewars (2011).

for a system with N electrons. From a variational approach, similar to that used to generate the HF equations, the Kohn-Sham equations, which are the current basis of modern DFT calculations, can be generated (Lewars, 2011). The Kohn-Sham approach (KS) allows for the mitigation of the two main problems in DFT, namely the absence of an a priori accurate electron density and the lack of knowledge of the correct energy functional. This approach expresses the ground state system energy as a sum of the kinetic energy $\langle T[\rho_0(\mathbf{r})]\rangle$, nucleus-electron attraction potential energy $\langle V_{Ne}[\rho_0(\mathbf{r})]\rangle$ and electron-electron repulsion potential energy $\langle T_{ee}[\rho_0(\mathbf{r})]\rangle$, respectively, this is mathematically described in equation 2.7.

$$E_0 = \langle T[\rho_0(\mathbf{r})]\rangle + \langle V_{Ne}[\rho_0(\mathbf{r})]\rangle + \langle V_{ee}[\rho_0(\mathbf{r})]\rangle \tag{2.7}$$

The terms in equation 2.7 represent quantum-mechanical average values. Invoking the concept of expectation value on $\langle V_{Ne}[\rho_0(\mathbf{r})]\rangle$ results in the following simplification,

$$\langle V_{Ne}[\rho_0(\mathbf{r})]\rangle = \int \rho_0(\mathbf{r}) v(\mathbf{r}) d\mathbf{r} \tag{2.8}$$

describing the Coulombic interaction of electron clouds with point charges. Kohn and Sham considered a fictitious reference system of noninteracting electrons which gives the same electron density as the real system. This allows for the recasting of the electronic kinetic energy as,

$$\Delta\langle T[\rho_0(\mathbf{r})]\rangle \equiv \langle T[\rho_0(\mathbf{r})]\rangle - \langle T[\rho_0(\mathbf{r})]\rangle_{ref} \tag{2.9}$$

where $\Delta\langle T[\rho_0(\mathbf{r})]\rangle$ and $\langle T[\rho_0(\mathbf{r})]\rangle_{ref}$ represent the deviation of the real electronic kinetic energy from that of the reference system, and the electronic kinetic energy of the reference system, respectively. The electron-electron repulsion potential energy is also simplified in a similar manner by considering $\Delta\langle V_{ee}[\rho_0(\mathbf{r})]\rangle$, the deviation of real electron-electron repulsion energy from a classical Coulombic repulsion energy, which is described mathematically below,

$$\Delta\langle V_{ee}[\rho_0(\mathbf{r})]\rangle = \langle V_{ee}[\rho_0(\mathbf{r})]\rangle - \frac{1}{2}\int\int \frac{\rho_0(\mathbf{r}_1)\rho_0(\mathbf{r}_2)}{\mathbf{r}_{12}} d\mathbf{r}_1 d\mathbf{r}_2 \tag{2.10}$$

where $\rho_0(\mathbf{r}_1)$ and $\rho_0(\mathbf{r}_2)$ represents a pair of infinitesimal volume elements separated by distance $\mathbf{r}_{12}$. The half coefficient in the second term of equation 2.10 corrects for double accounting of electron-electron interactions. Using the above equations, the total electronic energy equation can therefore be simplified to the following form,

$$E_0 = \int \rho_0(\mathbf{r}) v(\mathbf{r}) d\mathbf{r} + \langle T[\rho_0]\rangle_{ref} + \frac{1}{2}\int\int \frac{\rho_0(\mathbf{r}_1)\rho_0(\mathbf{r}_2)}{\mathbf{r}_{12}} d\mathbf{r}_1 d\mathbf{r}_2 + \Delta\langle T[\rho_0]\rangle + \Delta\langle V_{ee}[\rho_0]\rangle \tag{2.11}$$

In equation 2.11 all is known except for the last two deviation terms. In the KS approach the sum of these two energy terms is called the exchange-correlation energy, equation 2.12, which is still a functional of the electron density function.

$$E_{XC}[\rho_0(\mathbf{r})] \equiv \Delta\langle T[\rho_0(\mathbf{r})]\rangle + \Delta\langle V_{ee}[\rho_0(\mathbf{r})]\rangle \tag{2.12}$$

In this final form, equation 2.11, the first and third terms can be determined if the ground state electron density is known. The third term represents the classical electron-electron repulsion energy. The second term can be represented as an expectation value of the sum of one-electron kinetic operators over the ground state total wavefunction of the reference system (Parr & Yang, 1989). Mathematically this means,

$$\langle T[\rho_0(\mathbf{r})]\rangle_{ref} = \langle \Psi_r | \sum_{i=1}^{2n} -\frac{1}{2}\nabla_i^2 | \Psi_r \rangle \tag{2.13}$$

Since this is for a system with N noninteracting electrons, the total wavefunction, Ψ_r, can be determined exactly as a Slater determinant of occupied spin molecular orbitals (Lewars, 2011). The

elements in the Slater determinant are the products of Kohn-Sham spatial orbitals, ψ_i^{KS}, of the reference system and a spin function, α or β. Applying the Slater-Condon rules to simplify equation 2.13 results in the following expression for the electronic kinetic energy of noninteracting electrons.

$$\langle T[\rho_0(\mathbf{r})]\rangle_{ref} = -\frac{1}{2}\sum_{i=1}^{N}\langle\psi_i^{KS}|\nabla_i^2|\psi_i^{KS}\rangle \tag{2.14}$$

Now one only has to calculate the Kohn-Sham spatial orbitals to evaluate the second term in equation 2.11. To solve the Kohn-Sham equations the Kohn-Sham spatial orbitals are expressed in terms of basis functions ϕ,

$$\psi_i^{KS} = \sum_{s=1}^{m} c_{si}\phi_s \tag{2.15}$$

where m is the number of basis functions in a set. The remaining terms in equation 2.11 are the exchange-correlation energy, $E_{XC}[\rho_0(\mathbf{r})]$. Development of accurate exchange-correlation functionals in DFT is still one of the major problems. In developing the Kohn-Sham equations the exchange-correlation potential is defined as,

$$v_{XC}(\mathbf{r}) = \frac{\delta E_{XC}[\rho(\mathbf{r})]}{\delta\rho(\mathbf{r})} \tag{2.16}$$

Different approaches to approximating the exchange-correlation functionals are discussed in subsection 2.3.1. It is worth noting that there are a number of functionals in existence today and these can be categorized into different groups based on the level of theory and how each addresses the exchange and correlation contribution to $v_{XC}(\mathbf{r})$.

2.3.1 Exchange correlation functionals

In the Kohn and Sham DFT approach, all theoretical difficulties have been grouped in the exchange-correlation functional term. This not only accounts for exchange and correlation errors, but also for the self-repulsion and kinetic energy errors (Lewars, 2011). There are a number of exchange-correlation functionals that exist today and they can be classified based on their sophistication and predictive excellence. Perdew *et al.* (2005) presented this classification in what is now commonly referred to as the Jacob's ladder. Figure 2.1 presents this classification.

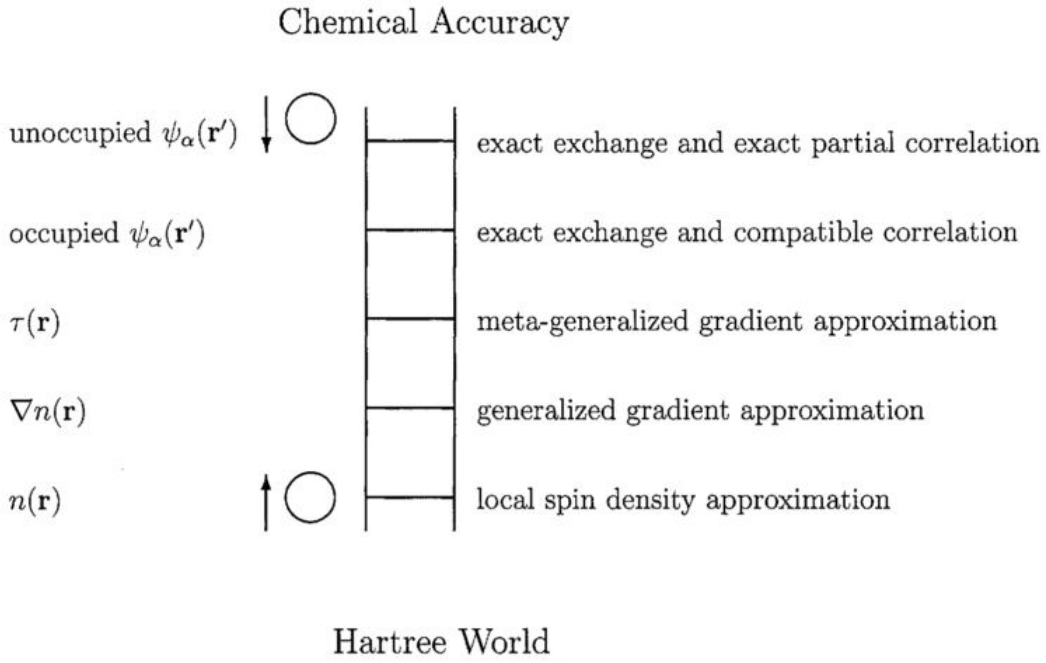

Figure 2.1: Jacob's ladder used to classify/rank the exchange-correlation functionals based on their sophistication and predictive accuracy (Perdew *et al.*, 2005).

The local density approximation (LDA) is one of the earliest and simplest approximations to the exchange-correlation functional. This approximation has been largely replaced by the local spin density approximation (LSDA). This forms the first rung of functionals in the Jacob's ladder. The mathematical formulation of this is given by,

$$E_{XC}^{LSD}[\rho(\mathbf{r})] = \int d\mathbf{r}\rho(\mathbf{r})\varepsilon_{XC}^{unif}(\rho(\mathbf{r})) \tag{2.17}$$

where $\varepsilon_{XC}^{unif}(\rho(\mathbf{r}))$ is the exchange-correlation energy per particle of an electron gas with uniform electron density $\rho(\mathbf{r})$ which is a function of position $\mathbf{r}$ (Perdew *et al.*, 2005). The LSDA, also referred to as just LSD, gives a reasonably accurate description of solids and their surfaces (Perdew *et al.*, 2005). This method however results in a poor description of chemical bonds, overestimates the ground-state energy, the atomisation energy and lattice parameters. This has been argued to be due to the overestimation of the correlation energy (Taylor *et al.*, 2003).

Application of approximation methods on the second rung, the generalized gradient approximation (GGA), has been reported to result in improved atomization energies of molecules, lattice parameters and bulk moduli of solids when compared with the LSD, which strongly overestimates these properties (Taylor *et al.*, 2003). The GGA functionals can be summarized by the general mathematical expression in equation 2.18,

$$E_{XC}^{GGA}[\rho(\mathbf{r})] = \int d\mathbf{r}\rho(\mathbf{r})\varepsilon_{XC}^{GGA}(\rho(\mathbf{r}), \nabla\rho(\mathbf{r})) \tag{2.18}$$

where $\varepsilon_{XC}^{GGA}(\rho(\mathbf{r}), \nabla\rho(\mathbf{r}))$ is the exchange-correlation energy per particle of an electron gas with electron density $\rho(\mathbf{r})$ and electron density gradient $\nabla\rho(\mathbf{r})$. The inclusion of the density gradients in the GGA method allows for the consideration of non-local effects which are not present in all LSD methods. Common GGA exchange-correlation functionals used in surface science (heterogeneous catalysis) include the Perdew-Wang functional from 1991 (PW91) (Perdew & Wang, 1992), the Perdew, Burke and Ernzerhof functional (PBE) (Perdew *et al.*, 1996) and the Revised Perdew, Burke and Ernzerhof functional (RPBE) (Hammer *et al.*, 1999). The PBE functional was designed based on the PW91 functional, however with fewer parameters (Mattsson *et al.*, 2005). As a result, the predictions made using these two functionals are found to be quite similar (Mattsson *et al.*, 2005).

The third and fourth rung of functionals are known as meta-generalized gradient approximation (mGGA) and hyper-generalized gradient approximation (hGGA) functionals respectively. Their mathematical formulation includes, in addition to local density and density gradient, the Laplacian of the spin-densities, $\nabla^2 n_\uparrow$ and $\nabla^2 n_\downarrow$, and the Kohn-Sham orbital energy densities, $\tau(\mathbf{r})$, for mGGA functionals whilst the hGGA functionals use the exact exchange functional and a compatible (non-exact) correlation functional. Equations 2.19 and 2.20 present general mathematical forms of both the mGGA and hGGA functionals respectively.

$$E_X^{mGGA}C[\rho(\mathbf{r})] = \int d\mathbf{r}\rho(\mathbf{r})\varepsilon_{XC}^{mGGA}(\rho(\mathbf{r}), \nabla\rho(\mathbf{r}), \nabla^2\rho(\mathbf{r}), \tau_\uparrow, \tau_\downarrow) \tag{2.19}$$

$$E_X^{hGGA}C[\rho(\mathbf{r})] = \int d\mathbf{r}\rho(\mathbf{r})\varepsilon_{XC}^{hGGA}(\rho(\mathbf{r}), \nabla\rho(\mathbf{r}), \nabla^2\rho(\mathbf{r}), \tau_\uparrow, \tau_\downarrow, \varepsilon_{x\uparrow}, \varepsilon_{x\downarrow}) \tag{2.20}$$

The Kohn-Sham orbital energy density is given by,

$$\tau(\mathbf{r}) = \frac{1}{2}\sum_{i=1}^{occupied} |\nabla\psi_i^{KS}(\mathbf{r})|^2 \tag{2.21}$$

where $\varepsilon_{x\uparrow}$ and $\varepsilon_{x\downarrow}$ are up-spin and down-spin exact exchange energies, respectively. The PKZB functional (Perdew *et al.*, 1999) and the TPSS functional (Tao *et al.*, 2003) are two of a number of

mGGA functionals used today. The hGGA functionals include the most common PBE0 (Adamo & Barone, 1999) and B3LYP (Becke, 1993) functionals, with the latter being semi-empirical in nature. Though the mGGA and hGGA functionals are expected to be more accurate, the improvements in the energies calculated for surface reaction systems has not been seen to be any better than what is achieved by the GGA functionals to justify the associated increase in computational cost (Adamo & Barone, 1999; Perdew *et al.*, 2005; Stroppa & Kresse, 2008; Mattsson *et al.*, 2008). The high computational cost associated with mGGA and hGGA has therefore been one major reason why almost all surface reaction studies are done using the GGA approach.

2.3.2 Solving Kohn-Sham equations

An iterative method is applied to solve the Kohn-Sham equations and predict the electronic properties of systems of electrons and nuclei. The complete form of the Kohn-Sham equation is given by (Parr & Yang, 1989; Lewars, 2011),

$$[-\frac{1}{2}\nabla_i^2 - \sum_{nucleiA}\frac{Z_A}{\mathbf{r}_{1A}} + \int\frac{\rho(\mathbf{r}_2)}{\mathbf{r}_{12}}d\mathbf{r}_2 + v_{XC}]\psi_i^{KS} = \varepsilon_i^{KS}\psi_i^{KS} \tag{2.22}$$

This is a Kohn-Sham equivalent of a wave-equation where the Kohn-Sham operator, $\hat{h}^{KS}$, is given by,

$$\hat{h}^{KS} = [-\frac{1}{2}\nabla_i^2 - \sum_{nucleiA}\frac{Z_A}{\mathbf{r}_{1A}} + \int\frac{\rho(\mathbf{r}_2)}{\mathbf{r}_{12}}d\mathbf{r}_2 + v_{XC}] \tag{2.23}$$

The procedure used in DFT calculations is similar to the HF self-consistency field procedure. This procedure follows the steps adapted from Lewars (2011):

1. Specify a geometry including charge and multiplicity
2. Specify a basis set
3. Calculate the initial guess for the ground state electron density, $\rho_0(1)$, for a system of N electrons using the specified basis set and equation 2.24 below,

$$\rho_0 = \rho_r = \sum_{i=1}^{N}|\psi_i^{KS}|^2 \tag{2.24}$$

4. Use ρ_0 to calculate the exchange-correlation potential, $v_{XC}(\mathbf{r})$ which is based on equation 2.16, the derivative of E_{XC} with respect to electron density function; E_{XC} is based on the chosen level of exchange-correlation functional theory presented in section 2.3.1
5. Use both ρ_0 and $v_{XC}(\mathbf{r})$ to calculate $\hat{h}^{KS}$ and solve equation 2.22
6. Use $\hat{h}^{KS}$ and the basis functions to calculate the elements, h_rs of the Kohn-Sham matrix

$$h_{rs} = \langle\phi_r|\hat{h}^{KS}|\phi_s\rangle \tag{2.25}$$

7. Orthogonalize the Kohn-Sham matrix to obtain an energy levels matrix and a Kohn-Sham orbital matrix
8. Using the Kohn-Sham orbital matrix and equation 2.24 calculate a new electron density function, ρ_0
9. Using the new electron density and equation 2.11 calculate a new total system energy
10. Check if the difference between the energy of successive iteration steps, ΔE, is less than the energy convergence criterion, $\Delta\epsilon$

11. If $\Delta E > \Delta\epsilon$, restart the process from step 4 using the new electron density function calculated in step 8 until $\Delta E \leq \Delta\epsilon$

After step 11 the self-consistent field loop will exit producing a ground state electronic energy for a given ion geometry. When geometry optimization is considered a secondary loop is added to the above scheme; this secondary loop changes the geometry specified in step 1 after each SCF cycle until either or both the total energy of successive geometries is converged and the Hellman-Feynman forces acting on any relaxed atoms are minimized based on a given convergence criterion. In DFT studies of heterogeneous catalytic system the Hellman-Feynman force convergence criterion are typically chosen to be between 0.01 and 0.03 eVÅ^{-1}.

2.4 Practical application of DFT to periodic systems

There are a number of computational codes available to solve Kohn-Sham equations. in this study a plane-wave code, the Vienna *Ab Initio* Simulation Package (VASP) (Kresse & Hafner, 1993, 1994a; Kresse & Furthmüller, 1996a,b), is used. To improve computational performance of the DFT method, pseudopotentials or projector-augmented-wave methods are used to describe the electron-ion interactions. This allows for the core electrons, which are effectively non-interacting in chemical processes, to be lumped together with the nuclei, while the valence electrons, which are important in chemical reactions, are treated explicitly (Mattsson *et al.*, 2005). The Vanderbilt's non-norm-conserving ultrasoft pseudopotentials (USPPs)(Vanderbilt, 1990; Kresse & Hafner, 1994b) and Blöchl's all electron projector augmented-wave (PAW) method (Blöchl, 1994; Kresse & Joubert, 1999) are used in this study.

The GGA exchange-correlation functionals were chosen for investigation in this study since the LDA functionals have been argued to be poor at describing surface reactions, while the meta-GGAs result in high compuational cost (Hammer *et al.*, 1999; Jacob *et al.*, 2003; Mattsson *et al.*, 2005). In addition, the GGA method gives better molecular bond energies for smaller molecules including O_2 than the LDA method (Perdew *et al.*, 1996; Hammer *et al.*, 1999; Kurth *et al.*, 1999). Within the GGA method the adsorption energies of small molecules such as O_2 on metal surfaces have been found to be greatly overestimated compared to experimental measurements (Hammer *et al.*, 1999; Duan & Wang, 2011; Yang *et al.*, 2010). As a results Hammer *et al.* (1999) proposed a modification of the PBE functional called the RPBE functional which result in improved adsorption energies of smaller molecules on metal surfaces. In the present study the three GGA functionals, PBE, PW91 and RPBE, are investigated to find a suitable functional for the study of the ORR process. Therefore the following combinations have been investigated:

1. PBE functional with PAW potentials (PAW−PBE)
2. RPBE functional with PAW potentials (PAW−RPBE)
3. PW91 functional with PAW potentials (PAW−PW91)
4. PW91 functional with ultrasoft pseudopotentials (USPP−PW91)

A suitable combination is selected based on the prediction of platinum bulk properties and the O_2 adsorption energy on Pt(111) surfaces compared to experimental measurements. Therefore it is desired to optimize both bulk platinum and the Pt(111) slab model for this investigation.
Implementation of DFT in computational codes including VASP requires a few other parameters to be optimized. The two most crucial of these parameters are the k-point sampling of the Brillouin zone and the plane wave basis set cut-off energy. These two parameters are normally measured by the number of k-points in the irreducible part of the Brillouin zone and the magnitude of the kinetic energy cut-off, respectively.

2.4.1 k-points

Application of Bloch's theorem enables the mapping of an infinite periodic system onto a finite system through symmetry. This then allows for the computation of electronic properties of a given system, which involves integration over all occupied electronic states, to be approximated using a finite number of wave-vectors (k-points) instead of infinite k-points which are required for the original infinite system (Mattsson *et al.*, 2005). Application of the Chadi and Cohen (Chadi & Cohen, 1973) or the Monkhorst and Pack (Monkhorst & Pack, 1977) schemes minimizes the number of k-points needed to give a reasonably accurate approximation to the full integration over k-space within the Brillouin zone (Mattsson *et al.*, 2005). Since the computational cost increases linearly with the number of k-points in the irreducible part of the Brillouin zone, it is necessary to find the minimum number of irreducible k-points that give a reasonable approximation of the system energy. This is normally termed the k-point optimization process.

2.4.2 Basis set cut-off energy

Bloch's theorem states that the electronic wave functions at each k-point can be expanded in terms of a discrete plane-wave basis set. In principle, this requires an infinite basis set. However, the plane waves with lower kinetic energies are more important especially in chemical processes with only valence electrons interacting (Mattsson *et al.*, 2005; Payne *et al.*, 1992). Therefore it is possible to truncate the basis set to include only plane waves with kinetic energies less than a chosen cut-off energy (Payne *et al.*, 1992). Since the errors in energy, Kohn-Sham eigenfunctions and forces are significantly influenced by the adequacy of the basis set, it is important to optimize this by finding a minimum kinetic energy cut-off that gives a reasonable approximation to a calculation with an infinite plane wave basis set (Mattsson *et al.*, 2005; Payne *et al.*, 1992).

2.4.3 Computational procedures

In the present study geometry optimization, vibrational analysis, oxygen diffusion and dissociation barriers will be investigated. These investigations will be conducted using DFT implemented in VASP as a computational tool. The different sets of calculations to be performed in this study are geometry optimization (to find the ground-state energy of a system), vibrational analysis (for vibrational frequencies of adsorbates) and transition state search (to find activation energies for dissociation of O_2 and diffusion of O).

Geometry optimization

For this set of calculations the conjugate-gradient algorithm is used for relaxing ions to their immediate ground-state. The force and energy convergence criteria are 0.02 eV/Å and 10^{-5} eV respectively. These stopping conditions are consistent with averages used in literature (Yang *et al.*, 2010; Duan & Wang, 2013; Ogawa *et al.*, 2013; Jennings *et al.*, 2014). Other VASP default setting were used for consistency with the present literature. For metals the description of the electronic structure optimization was based on the Methfessel-Paxton scheme with a smearing width of 0.1 eV whilst for gas phase molecules Gaussian smearing with a smearing width of 0.01 eV was used. In both cases, metals and gases, the total energies were extrapolated to zero smearing.

Vibrational analysis

For vibrational analyses, the Hessian matrix (second derivatives of energy with respect to atomic positions) is determined using finite differences. In this procedure, each relaxed atom/ion is displace in all three Cartesian directions. A displacement step of 0.02 Å was used in all vibrational analysis calculations, a smaller value, 0.015 Å, was also tested and showed no difference in vibrational frequencies (see Appendix A.1). Since platinum atoms are much more massive, i.e. have greater mass than O, their vibrations were omitted. This is done by fixing at their geometry optimized positions and only the adsorbates, i.e. O or O_2, are included in the Hessian calculation. Therefore the partial Hessian matrix consists of second derivatives of energy with respect to only the O atomic positions.

Transition state search and optimization

In this study, the minimum energy path for the two dimensional diffusion of atomic O on different platinum metal surfaces was found by interpolating and optimizing a set of images between two stable atomic O adsorbed states. Sets of images per transition state search are optimized using the nudge elastic band (NEB) method (Jonsson *et al.*, 1998) where for each image the energy is only minimized along the hyper-plane perpendicular to the current tangent. The constraint to keep images equidistant is imposed by adding spring forces (spring constant = -5 eV/Å^2—negative sign turns on nudging) along the band. The fast inertial relaxation engine (FIRE) optimizer is used for all diffusion transition state search calculations (Bitzek *et al.*, 2006; Sheppard *et al.*, 2008). The transition state search calculations are conducted with relaxed force and energy convergence criteria of 0.04 eV/Å and 10^{-4} eV, respectively. Once the transition state is located it is further optimized to achieve tighter force and energy convergence criteria of 0.02 eV/Å and 10^{-5} eV, respectively. The latter is achieved by further relaxing the ions using the quasi-Newton algorithm, a VASP-recommended method (Kresse *et al.*, 2014). The transition state is then confirmed by demonstrating that the only imaginary vibrational mode is along the direction of the diffusion band.

2.5 Bulk platinum

2.5.1 k-point optimization

The k-point sampling was optimized using the conventional unit cell of bulk platinum with an experimentally determined lattice parameter of 3.92 Å (Kittel, 2005). The cut-off energy is set to 600 eV for all studied potential−functional combinations. This cut-off energy is well converged as the VASP-recommended cut-off energy for PAW−PBE, PAW−RPBE and PAW−PW91 is 230 eV whilst 191 eV is recommended for the USPP−PW91 combination (Kresse *et al.*, 2014). Gamma-centered k-point grids based on the Monkhorst-Pack (Monkhorst & Pack, 1977) scheme were used for all calculations. The single point energy calculations using the first order Methfessel-Paxton (MP) method and a smearing width of 0.1 eV are conducted and the results are presented in Figure 2.2.

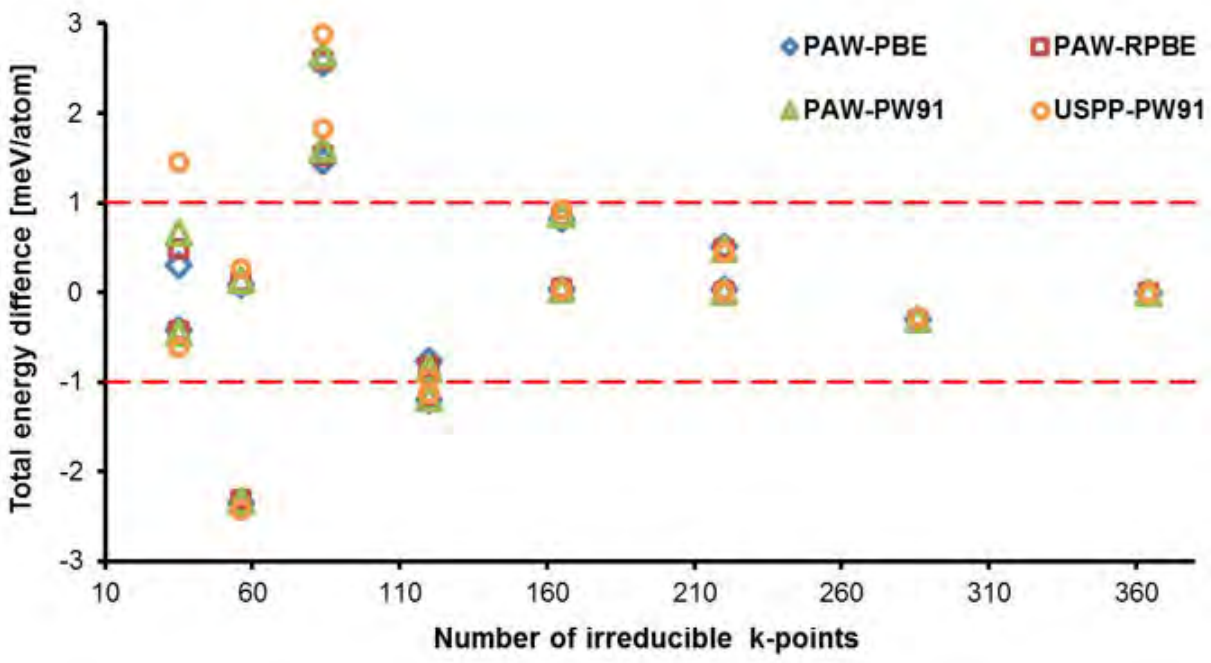

Figure 2.2: Convergence of the total energy of bulk platinum as a function of the number of irreducible k-points in the Brillouin zone. Note: the total energy is referenced to the energy of a 22x22x22 k-point grid (364 irreducible k-points). The red broken lines indicated the upper and lower limits of the convergence criterion, 1 meV/atom.

The results in Figure 2.2 show that the total energy of a platinum conventional unit cell is converged to within 1 meV for 120 irreducible k-points with respect to a system with 364 irreducible k-points, taken as an approximation of infinite k-point set, independent of potential−functional combination. This is given by a 14x14x14 k-point grid sampled with the Monkhorst-Pack k-point sampling scheme (Monkhorst & Pack, 1977). This is the case for all investigated potential−functional combinations. Therefore the converged k-spacing is 0.018 $Å^{-1}$.

2.5.2 Basis set cut-off energy optimization

The cut-off energy was optimized using a conventional unit cell of bulk platinum with a lattice parameter of 3.92 Å (Kittel, 2005), same as for k-point optimization. An optimized k-point grid of 14x14x14 was used for all potential-functional combinations. Single point energy calculations were conducted using the first order Methfessel-Paxton (MP) method and a smearing width of 0.1 eV. The results are presented in Figure 2.3. From these results it can be seen that for both the PAW−PW91 and USPP−PW91 potential−functional combinations the total energy of a platinum conventional unit cell is converged to within 1 meV at cut-off energies beyond 280 eV, whilst the PAW−PBE and PAW−RPBE potential-functional combinations require cut-off energies of 370 eV and 380 eV, respectively. The optimized cut-off energies are seen to be much larger than the VASP-recommended cut-off energies for the investigated potential−functional combinations. The latter may be due to a tight convergence criterion used in the present study—VASP-recommended cut-off energies are based on a convergence criterion of 10 meV (Kresse *et al.*, 2014).

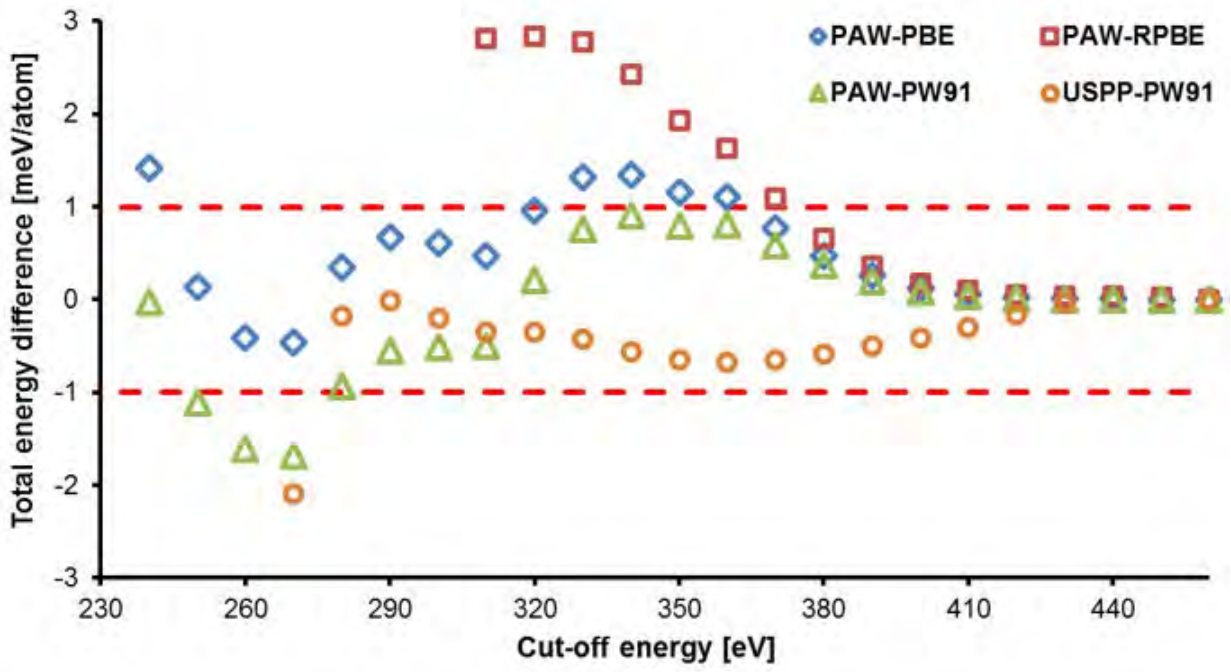

Figure 2.3: Convergence of the total energy of bulk platinum as a function of the plane wave basis set cut-off energy. Note: the total energy difference is referenced to total energy at a cut-off energy of 460 eV. The red broken lines indicated the upper and lower limits of the convergence criterion, 1 meV/atom.

2.5.3 Equilibrium lattice constant and bulk modulus

Bulk platinum has a face-centered cubic (fcc) crystallographic structure. Figure 2.4 presents both the conventional and primitive unit cell of fcc bulk platinum. These unit cells are repeated periodically in three dimensional space. There are four platinum atoms per conventional unit cell whilst a primitive cell only contains one atom. The relationship between the shortest lattice vector of a primitive cell,

x, and the lattice parameter of a conventional unit cell, a, is given by equation 2.26.

$$a = \frac{2x}{\sqrt{2}} = \sqrt{2}x \tag{2.26}$$

The volume (V) of the conventional cell is related to the lattice parameter according to equation 2.27.

$$V = a^3 \tag{2.27}$$

The key bulk properties that need to be optimized are the equilibrium lattice constant and bulk

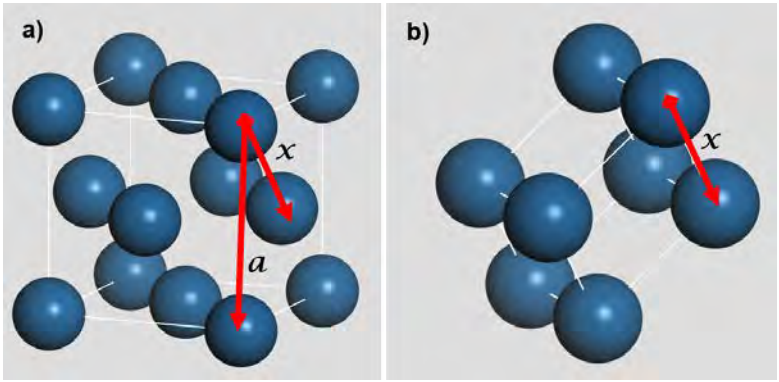

Figure 2.4: a) Conventional and b) primitive unit cells of bulk platinum: x is the shortest lattice vector of the primitive unit cell whilst a is the lattice parameter of the conventional unit cell.

modulus of platinum. The properties are crucial since they influence both the electronic and geometric structure of bulk platinum. The equilibrium lattice constant is by definition the lattice constant of a lattice structure which corresponds to the minimum structural energy, whilst the equilibrium bulk modulus is given by the second derivative of the structural energy with respect to lattice constant at the equilibrium lattice constant. To evaluate these two parameters non-spin polarized single point energy periodic DFT calculations were conducted using VASP. A set of platinum conventional unit cell with varying lattice parameters was used. The lattice parameter was varied from 3.94 to 4.07 Å for all potential-functional combinations. This range was chosen because it contains the most of the lattice parameter of bulk platinum calculated using DFT-GGA reported in literature (Eichler & Hafner, 1997; Mattsson *et al.*, 2008; Yang *et al.*, 2010; Duan & Wang, 2013; Ogawa *et al.*, 2014). This data was then fitted with the Birch-Murnaghan equation of state (B-M EOS) (Birch, 1947). A mathematical form of this equation of state is presented by equation 2.28,

$$E = E_0 + \frac{9V_0B_0}{16}\left\{\left[\left(\frac{V_0}{V}\right)^{\frac{2}{3}} - 1\right]^3 B_0' + \left[\left(\frac{V_0}{V}\right)^{\frac{2}{3}} - 1\right]^2 \left[6 - 4\left(\frac{V_0}{V}\right)^{\frac{2}{3}}\right]\right\} \tag{2.28}$$

where E is the internal energy with units of electron volts, and E_0[eV], V_0[Å^3] and B_0[eV.Å^{-3}] are the equilibrium internal energy, unit cell equilibrium volume and bulk modulus of the primitive unit cell, respectively. B_0' is the partial derivative of the bulk modulus with respect to the system pressure. Figure 2.5 presents the data and the fitted B-M EOS for all four potential-functional combinations. In Table 2.1 the parameters of the fitted B-M EOS are presented. The equation of state was found to be a very good fit to the data, as is evident from the R^2 of 0.99998. The experimental equilibrium lattice constant of bulk platinum is reported to be 3.924 Å (Arblaster, 1997). The calculated lattice constants in Table 2.1 are overestimated by ca. 1.7 % relative to experiments which is consistent with earlier calculations (Eichler & Hafner, 1997; Mattsson *et al.*, 2008; Yang *et al.*, 2010). Previous studies have, however, shown that the LSDA and AM05 functionals give equilibrium bulk properties of the transition metals that are in better agreement with experiments (Mattsson *et al.*, 2008). However the former is notoriously known to overestimate adsorption energies (Jacob *et al.*, 2003; Mattsson *et al.*, 2005) whilst the latter was found (see Appendix A.2) to be much more difficult to work with due to the requirement to optimize additional parameters and the lack of literature studies related to the

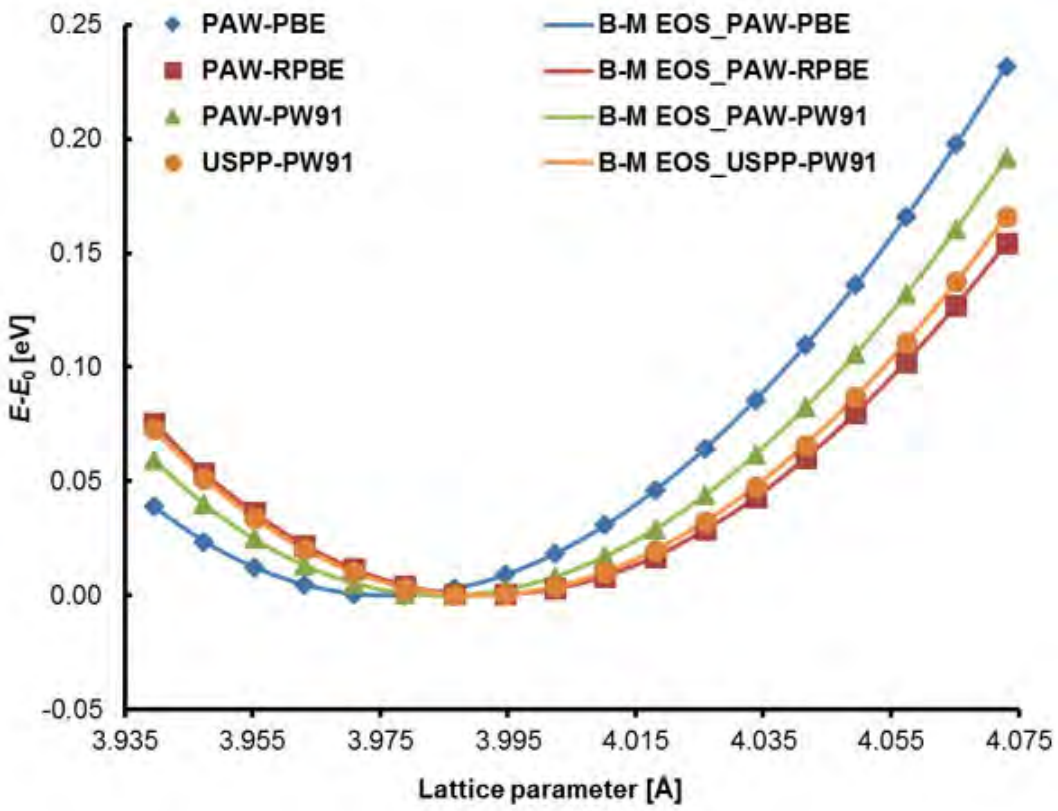

Figure 2.5: Bulk platinum lattice parameter optimization. $E - E_0$ is the difference between the total energy of a platinum conventional unit cell with a given lattice parameter and the equilibrium internal energy—energy of a platinum conventional unit cell with an equilibrium lattice parameter.

ORR on platinum surfaces, compared to standard GGA functionals.

All studied potential-functional combinations underestimate the equilibrium bulk modulus of platinum bulk metal. This is evident when the predicted results are compared to experimental measurements. At 300 K the equilibrium bulk modulus of platinum is 278 GPa (Kittel, 2005). This is already at best 10% larger than any prediction from this study. Even though the calculations are at 0 K, performing a temperature correction will only increase the difference between experimental data and theoretical predictions, as the bulk modulus has been shown to increase linearly with decreasing temperature (Kumar, 2000). The deviation of the calculated equilibrium lattice constant and bulk modulus from experimental measurements, is consistent deviations reported by Stampfl *et al.* (2001). Therefore, of the considered potential-functional combinations, the one that is closest to the experimental data is the PAW−PBE. However, the final choice of which functional will be used will be based on the performance in predicting the adsorption energies of O_2, as the focus of this study is on the oxygen reduction reaction. Further calculations will be based on the optimized equilibrium lattice parameter for each respective potential-functional combination, as given in Table 2.1.

2.6 Calculated properties of gas phase molecules

In heterogeneous catalysis the interaction of fluid phase molecules with the solid interface is of interest. Theoretical treatments used to model a system should therefore be able to predict the fluid phase properties with reasonable accuracy. In the case of ORR, molecular hydrogen, oxygen and water are the gas phase species of interest. Water is generally assumed to form in a gaseous state and appropriate corrections are applied to account for condensation to the liquid phase. This section presents energetic properties of these three gas phase species as predicted by the four considered potential-functional combinations. For all gas phase calculations the respective molecules were placed at the centre of a

Table 2.1: Summary of optimized equilibrium bulk properties of fcc platinum based on a regressed fit with the Birch-Murnaghan equation of state.

Combination	Cohesive energy [eV/atom]	V_0[Å^3]	Lattice constant [Å]	B_0 [GPa]
PAW−PBE	5.46	62.87	3.976 (3.977[e], 3.99[j])	248 (251[e])
PAW−RPBE	4.21	63.61	3.992	231
PAW−PW91	5.47	63.27	3.985	245
USPP−PW91	5.44	63.54	3.990 (3.99[f])	238
USPP−PBE		(62.65[g])		(247[g])
USPP−RPBE		(63.72[h])		(229[h])
Experimental	5.84[a]	60.42[b,d]	3.924[b,c]	273[a,c]
		60.05[i]	3.924[i]	283[i]

a from Kittel (2005), cohesive energy at 0 K and 1 atm

b from Arblaster (1997)

c measured at room temperature (293.15 K)

d calculated using equation 2.27

e DFT calculation, PAW−PBE combination, VASP code, (Mattsson *et al.*, 2008)

f DFT calculation, USPP−PW91 combination, VASP code, (Eichler & Hafner, 1997)

g DFT calculation, pseudopotentials method with PBE, (Kurth *et al.*, 1999)

h DFT calculation, pseudopotentials method with RPBE, (Kurth *et al.*, 1999)

i Experimental data from Khein *et al.* (1995)

j DFT calculation, PAW−PBE combination, VASP code, (Yang *et al.*, 2010)

rectangular box, with dimensions $a = 12$Å, $b = 13$Å and $c = 14$Å, and all atoms were fully relaxed in space. Figure 2.6 presents a water molecule in a rectangular box described above. The Gaussian smearing method was used with a smearing width of 0.01 eV which was sufficient to give an entropic value less than 1 meV/atom. The energy and force convergence criteria were 10^{-5} eV and 0.02 eV.Å^{-1}, respectively. Furthermore, a cut-off energy of 400 eV (the VASP recommendation is 400 eV for O and 250 eV for H) and k-point grid of 1x1x1, i.e. the gamma point, was used. All calculations were spin-polarized. For all vibrational analysis calculations a step size 0.02 Å was used. The total energy of oxygen and hydrogen atoms was also calculated using the system described above with the respective atom in the centre of a rectangular box. The atomization energy is defined as the required energy to separate a molecule into its constituent elements.

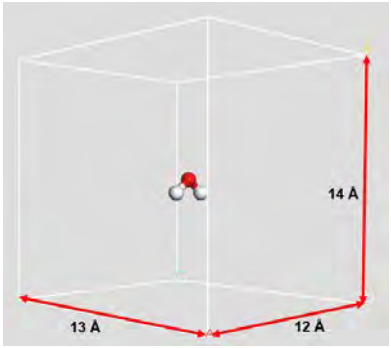

Figure 2.6: Water molecule centered in a rectangular box. Red sphere: oxygen atom, white spheres: hydrogen atoms.

2.6.1 Hydrogen

The calculated equilibrium bond length of molecular hydrogen is 0.751 Å, 0.747 Å, 0.749 Å and 0.749 Å for for the PAW−PBE, PAW−RPBE, PAW−PW91 and USPP−PW91 potential−functional combinations, respectively. The combinations overestimate the experimentally determined bond length of 0.741 Å (Haynes, 2013) by ca. 1.4 % (0.006-0.01 Å). The stretching frequency calculated using

PAW−PBE, PAW−RPBE, PAW−PW91 and USPP−PW91 is 4315 cm^{-1}, 4361 cm^{-1}, 4336 cm^{-1} and 4478 cm^{-1} respectively. Since the experimentally determined stretching frequency of H_2 is 4401 cm^{-1}, the PAW−PBE combination underestimates this frequency by 86 cm^{-1} whilst the PAW−RPBE and PAW−PW91 only underestimate it by 40 and 65 cm^{-1}, respectively. The USPP−PW91 combination is found to overestimate the stretching frequency mode by 77 cm^{-1}. The H_2 atomization energies (with zero point energy correction and finite temperature correction to 25 °C) were calculated to be 4.26 eV, 4.30 eV, 4.28 eV and 4.30 eV for the PAW−PBE, PAW−RPBE, PAW−PW91 and USPP−PW91 potential−functional combination, respectively. These values underestimate the experimentally measured H_2 atomization energy of 4.52 eV (Haynes, 2013). In their comparison of DFT-calculated atomization energies Perdew *et al.* (1996) and Kurth *et al.* (1999) found similar deviations from experimental atomization energies. In conclusion, it should be noted that all predicted atomization energies underestimate the experimentally measured value by ca. 0.25 eV.

2.6.2 Water

The water molecule has at least three important parameters, these are O-H bond lengths, stretching frequencies and the H-O-H bond angle. Experimentally the O-H equilibrium bond length has been determined to be 0.958 Å, (Haynes, 2013). The considered potential-functional combinations therefore overestimate the O-H bond length in a water molecule as they give bond lengths of 0.972 Å (PAW−PBE, PAW−PW91 and USPP−PW91) and 0.973 Å (PAW−RPBE), i.e. an overestimation by ca. 0.015 Å. The H-O-H bond angle predicted by the PAW−PBE, PAW−RPBE, PAW−PW91 and USPP−PW91 combinations is 104.52°, 104.23°, 104.67°and 105.20°, respectively, this corresponds to deviations of ca. +0.01% (PAW−PBE) +0.3% (PAW−RPBE), -0.2% (PAW−PW91) and +0.7% (USPP−PW91) from experimentally determined water bond angle of 104.51°(Haynes, 2013). The calculated vibrational frequencies corresponding to symmetric, anti-symmetric stretching and bending modes are given in Table 2.2. The largest deviation observed is for the anti-symmetric stretching frequency, of ca. 3%. The H_2O atomization energies (with zero point energy correction and finite temperature correction to 25 °C) were calculated to be 9.60 eV, 9.30 eV, 9.81 eV and 9.63 eV for the PAW−PBE, PAW−RPBE, PAW−PW91 and USPP−PW91 potential-functional combination, respectively. The PAW−PBE and USPP−PW91 combinations give the closest prediction to the experimentally measured H_2O atomization energy of 9.61 eV (Haynes, 2013). On the other hand the PAW−RPBE combination underestimate the experimental value 0.31 eV whilst the PAW−PW91 combination overestimate the experimental value by 0.20 eV. Kurth *et al.* (1999) observed similar deviations between theoretical and experimental atomization energies.

Table 2.2: The calculated vibrational frequencies of a water molecule in the gas phase. All vibrational frequencies are in cm^{-1}

	symmetric stretch	anti-symmetric stretch	bending
PAW−PBE	3723	3843	1584
PAW−RPBE	3713	3834	1601
PAW−PW91	3726	3846	1587
USPP−PW91	3732	3852	1575
Experimental[a]	3657	3742	1593

a: from (Haynes, 2013)

2.6.3 Molecular oxygen

The PAW−PBE-predicted equilibrium bond length of molecular oxygen is 1.234 Å whilst the PAW−RPBE, PAW−PW91 and USPP−PW91 predicted bond lengths of 1.239 Å, 1.235 Å and 1.236 Å, respectively. All the considered potential-functional combinations overestimate the equilibrium bond length of molecular oxygen by ca. 0.03 Å when compared to experimental value of 1.207 Å (Haynes, 2013). The stretching frequency is predicted by the PAW−PBE, PAW−RPBE, PAW−PW91 and USPP−PW91

potential-functional combinations to be 1566 cm^{-1}, 1545 cm^{-1}, 1560 cm^{-1} and 1558 cm^{-1}, respectively. Therefore these potential-functional combinations underestimate the experimental stretching frequency of 1581 cm^{-1} by ca. 22 cm^{-1} (PAW−PBE, PAW−PW91 and USPP−PW91) and 36 cm^{-1} (PAW−RPBE) (Haynes, 2013). The O_2 atomization energies (with zero point energy correction and finite temperature correction to 25 °C) were calculated to be 5.99 eV, 5.60 eV, 6.27 eV and 5.84 eV for the PAW−PBE, PAW−RPBE, PAW−PW91 and USPP−PW91 potential-functional combination, respectively. Therefore, all considered combinations overestimate the experimentally measured O_2 atomization energy of 5.17 eV (Haynes, 2013) by 0.82 eV, 0.43 eV, 1.10eV and 0.68 eV (PAW−PBE, PAW−RPBE, PAW−PW91 and USPP−PW91). Hence the error between the DFT-calculated O_2 atomization energy and experimentally determined atomization energy is much larger than the corresponding errors observed for H_2 and H_2O. The latter is not true for the PAW−RPBE combination where the differences between calculated atomization energies of O_2, H_2 and H_2O relative to corresponding experimental atomization energies are comparable.

2.6.4 Correction of the oxygen electronic energy

In the literature it has been argued that the DFT prediction of the electronic structure and energy of O_2 is very poor, even at the GGA level of theory (Kurth *et al.*, 1999; Nørskov *et al.*, 2004). This has been attributed to over-binding effects at the exchange-only level for molecules with multiple bonds (Kurth *et al.*, 1999). As a result, a number of researchers have used experimental reaction energies to back-calculate the electronic energy of O_2 (Nørskov *et al.*, 2004; Karlberg *et al.*, 2007; Martínez *et al.*, 2009). This is done, for example by using the water formation reaction from H_2 and O_2. Subtracting the DFT energy of H_2 and H_2O from the experimental formation energy of H_2O, -242 kJ/mol (-2.51 eV) at 298 K, one can obtain a corrected energy of O_2 which can then be used in the calculation of the adsorption energy of O_2 on metal surfaces. This approach assumes that both H_2O and H_2 are reasonably predicted by the GGA theory. As has been shown above, this is not entirely true for the atomization enthalpies. Table 2.3 presents the deviation between experimental and calculated atomization energies of O_2, H_2 and H_2O. Other literature studies have reported similar deviation between experimental atomization energies and those calculated with GGA functionals (Perdew *et al.*, 1996; Kurth *et al.*, 1999). Since the deviations between experimental and calculated atomization enthalpies of O_2 and H_2 have been shown to be significant in comparison to those observed for H_2O, the above method for correcting O_2 energies must be considered with caution.

The correction of the electronic energy of O_2 is calculated using the relationship between the formation energy ($\Delta_f H_{H_2O}(T)$) and the enthalpies of H_2O ($H_{H_2O}(T)$), H_2 ($H_{H_2}(T)$) and O_2 ($H_{O_2}(T)$) at a given temperature, T, given by,

$$\Delta_f H_{H_2O}(T) = H_{H_2O}(T) - H_{H_2}(T) - \frac{1}{2}H_{O_2}(T) \tag{2.29}$$

where the formation energy is given on a basis of 1 mole of H_2O. The temperature corrected enthalpies of gas molecules is calculated using thermodynamic relationships given in Appendix C. The corrected O_2 electronic energy is therefore calculated using equation 2.30. The latter equation has been arrived at by rearranging equation 2.29.

$$H_{O_2}(T) = 2 \cdot [-\Delta_f H_{H_2O}(T) + H_{H_2O}(T) - H_{H_2}(T)] \tag{2.30}$$

Since the experimentally-determined formation energy of water (-2.51 eV) is measured at 298.15 K, the corrected ground state electronic energy of O_2 (with zero point energy correction) at 0 K is given by,

$$E_{O_2}^{corr}(T = 0K) = 2 \cdot [2.51 + H_{H_2O}(298.15) - H_{H_2}(298.15)] - H_{O_2}(0K \rightarrow 298.15K) + ZPE \tag{2.31}$$

where ZPE is the zero point energy given by,

$$ZPE = \frac{1}{2}\sum_i h\nu_i \tag{2.32}$$

and $E^{corr}_{0,O_2}(T = 0K)$ is the corrected ground state electronic energy of O_2 gas with zero point energy included at absolute zero. Table 2.4 presents this energy as predicted by different potential-functional combinations. From Table 2.4 it can be seen that the correction results in an energy change of 0.30 eV, 0.59 eV, 0.22 eV and 0.20 eV for the PAW−PBE, PAW−RPBE, PAW−PW91 and USPP−PW91 potential-functional combination, respectively. These are relatively significant changes compared to the calculated adsorption energies of the ORR intermediates on platinum surfaces. In the next chapter the platinum surface models are optimized and will then be used to calculated the adsorption energy of O_2 and a comparison will be made against experimentally measured adsorption energies.

Table 2.3: DFT-calculated atomization enthalpies of gas phase molecules (O_2, H_2 and H_2O). In all the energies the zero point and finite temperature (to 25 °C) correction has been added. All energies are reported in $[eV]$ units. In round brakets, ( ), are the differences between experimental and calculated atomization enthalpies.

	O_2	H_2	H_2O
PAW−PBE	5.99 (0.82)	4.26 (-0.26)	9.60 (0)
PAW−RPBE	5.60 (0.43)	4.30 (-0.22)	9.30 (-0.31)
PAW−PW91	6.27 (1.10)	4.28 (-0.24)	9.81 (0.20)
USPP−PW91	5.84 (0.68)	4.30 (-0.22)	9.63 (0.02)
Experimental[a]	5.17	4.52	9.61

a: from (Haynes, 2013)

Table 2.4: Corrected and uncorrected ground state electronic energies of molecular oxygen in the gas phase. $E^{corr}_{O_2}(T = 0K)$ is the corrected ground state electronic energy of O_2 (including zero point energy correction) whilst the uncorrected ground state electronic energies of O_2 are given by $E^{DFT}_{0,O_2}(T = 0K)$ (excluding zero point energy correction) and $E^{ZPE}_{O_2}(T = 0K)$ (including zero point energy correction).

	$E^{DFT}_{0,O_2}(T = 0K)[eV]$	$E^{ZPE}_{O_2}(T = 0K)[eV]$	$E^{corr}_{O_2}(T = 0K)[eV]$
PAW−PBE	-9.85	-9.76	-9.46
PAW−RPBE	-10.54	-10.44	-9.85
PAW−PW91	-9.82	-9.72	-9.51
USPP−PW91	-9.88	-9.79	-9.58

2.6.5 Atomic oxygen

The gas phase electronic energy of atomic O was calculated by considering an O atom in a rectangular box, as described in Section 2.6. Two electronic energies were obtained depending on the initial system set-up. Using the Gaussian smearing method (with $\sigma = 0.01$ eV) the lowest electronic energy state with integer orbital occupancy was calculated to be -1.903 eV. The latter method is also recommended in the VASP manual for calculating the total energy of gas phase molecules (Kresse *et al.*, 2014). When the electronic energy of atomic O was calculated using a similar computational method as for adsorbed states (subsection 2.4.3) a much higher (less negative) electronic energy, -1.539 eV, was obtained. The converged electronic structure resulting from the latter energy consisted of non-integer orbital occupancies. In this study, the electronic energy of atomic O of -1.903 eV was used as it corresponds to the lowest and correct electronic state (ground state energy).

2.7 Application of the d-band theory

The change in adsorption energy of O_2 along different nanorod and slab sites was rationalized using the d-band theory. According to the d-band theory, the adsorption of O_2 on Pt-surface (the theory extends for many other adsorbates on transition metal surfaces) is influenced by two phenomena − (i) interaction of valence sp-states of O_2 with s-electrons of Pt, which results in a single resonance

with all bonding states below the Fermi-level (Hammer & Nørskov, 2000; Hammer *et al.*, 1997), and (ii) coupling/hybridization with the d-states of Pt, this results in the splitting of the renomalized adsorbate states into bonding and anti-bonding states (Hammer & Nørskov, 2000; Hammer *et al.*, 1997). The splitting of these states is possible since the d-band is narrow and shifted up closer to the Fermi-level (Hammer & Nørskov, 2000).

For CO adsorption on Pt(111), Hammer & Nørskov (2000) argued that only 5σ and doubly degenerate (empty) $2\pi^*$ electronic states (these are HOMO and LUMO molecular orbitals, respectively) are responsible for the adsorption with metal surfaces. This is equivalent to $2\pi^*$ and $6\sigma^*$ electronic states of O_2. For CO it was further argued that the interaction of the 5σ and $2\pi^*$ electronic states with s-electrons of the Pt(111) surface results in the broadening and down shift (relative to the fermi-level) of these states (Hammer & Nørskov, 2000). Further coupling of hybridised 5σ and $2\pi^*$ electronic states with the d-band states results in the formation of bonding (5σ-d and $2\pi^*$-d) and anti-bonding (5σ-d and $2\pi^*$-d) electronic states. An up-shift of the d-band center towards the Fermi-level therefore results in depopulation of the anti-bonding orbitals (as they move further above the Fermi-level) and hence a stronger bonding (less adsorbate-metal surface bond destabilization) (Hammer *et al.*, 1997; Hammer & Nørskov, 2000; Greeley *et al.*, 2002). A similar argumentation can be applied to the case of O_2. In this study the adsorption of O_2 is correlated to the d-band center in a similar manner Hammer & Nørskov (2000) correlates the adsorption energy of CO on different Pt surfaces to corresponding d-band center energies.

The d-band center energy is calculated by integrating the area under the projected density of d-electronic states (pDOS) using equation 2.33,

$$(\varepsilon_{dc} - \varepsilon_f) = \frac{\int E \cdot N_d(E) dE}{\int N_d(E) dE} \tag{2.33}$$

where ε_f and $N_d(E)$ are the Fermi level of the system and the projected density of states of an atom, respectively. Since different systems, in size or composition, may result in varying ε_f, when comparing across different systems it is best to calculate the d-band center with respect to the vacuum energy level (E^{vac}). This is achieved by subtracting the work function ($\Phi = E^{vac} - \varepsilon_f$) from the d-band center energy ($\varepsilon_{dc} - \varepsilon_f$) (equation 2.34).

$$(\varepsilon_{dc} - \varepsilon_f) - \Phi = \frac{\int E \cdot N_d(E) dE}{\int N_d(E) dE} - \Phi \tag{2.34}$$

Therefore, the d-band center energy relative to the vacuum energy level is given by equation 2.35,

$$(\varepsilon_{dc} - E^{vac}) = \frac{\int E \cdot N_d(E) dE}{\int N_d(E) dE} - \Phi \tag{2.35}$$

where E^{vac} is the vacuum energy level of a given system. The latter energy level should correspond to a zero electrostatic potential for a system with a well converged vacuum spacing between periodic surfaces.

Chapter 3

Surface models of Pt

3.1 Introduction

It has been argued that the ORR activity on platinum surfaces can be modelled as a weighted average of activities at different platinum nanoparticle sites (Greeley *et al.*, 2007; Tritsaris *et al.*, 2011). The averaged distribution of these sites can be quantified for a chosen nanoparticle morphology. Once the distribution is known, the overall activity can be calculated as a weighted average of the different site contributions. In this chapter it is argued based on the literature findings that truncated octahedral and cuboctahedral platinum nanoparticles are thermodynamically favourable. These particles expose predominantly {111} and {100} terraces. Knowledge of the ORR activity on these respective terrace sites should be of great importance. This chapter presents the development and optimization of terrace surface models used to investigate the ORR activity at terrace sites exposed on platinum nanoparticles.

The equilibrium shape of crystallites of fixed volume will expose surface terminations that minimize the total surface free energy (Miracle-Sole, 2013). Using DFT Vitos *et al.* (1998) calculated surface energies of the low Miller index surface terminations of platinum, i.e. Pt(111), Pt(100) and Pt(110), to be 2.30 J/m^2, 2.73 J/m^2 and 2.82 J/m^2, respectively. Depending on the constraints imposed by the crystallographic structure, platinum nanoparticles may therefore be expected to predominantly expose Pt{111} surface terminations, followed by Pt{100}. For synthesis reactions carried out under thermodynamic control, the obtained crystallite shapes will obey Wulff's theorem (Xia *et al.*, 2009). Song *et al.* (2005) synthesised platinum nanoparticles with a cuboctahedral, octahedral and cubic morphology, consistent with Xia *et al.* (2009) who argued that for crystallites with an fcc lattice structure synthesised under thermodynamic control, the predominant crystallite shape will be octahedral. Xia *et al.* (2009) further argued that since a cube of the same volume as the octahedron has a smaller total surface area, the resulting single-crystal shape will be a truncated octahedron exposing a mixture of {111} and {100} facets.

It may therefore be concluded that truncated octahedral platinum nanoparticles will be the predominant particle shape thermodynamically. The degree of truncation will depend predominantly on the particle size with much larger particles forming cubic shapes (Xia *et al.*, 2009; Long *et al.*, 2010). These nanoparticles expose {111} and {100} terraces which are separated by edge and corner regions where low coordinated atoms reside. It is however important to understand the morphology of these nanoparticles under the operating conditions of the cathode electrode in a fuel cell. Based on a theoretical study, considering adsorbate-induced particle shape changes as a function of electrode potential, Tripković *et al.* (2014) argued that the equilibrium particle shape between 0 and 0.7 V is a truncated octahedron, whilst at 0.9 V the edges of the truncated octahedron are dissolved owing to a rapid decrease in the surface free energy of {110} facets with increasing potential. Figure 3.1 presents the equilibrium particle shapes as a function of electrode potential as presented in Tripković *et al.* (2014)'s work. Since the electrode potentials of interest in practical fuel cells spans from 0.6 to 0.9 V, the individual ORR activity of different nanoparticle sites, i.e. {111}, {100}, {110} facets, edges and corners, is important to understand the overall ORR activity of the nanoparticles. Tripković *et al.*

(2014) further calculated that a ca. 3 nm equilibrium nanoparticle at an electrode potential of 0.9 V will expose the Pt{111} and Pt{100} terraces in the proportions illustrated in Figure 3.2.

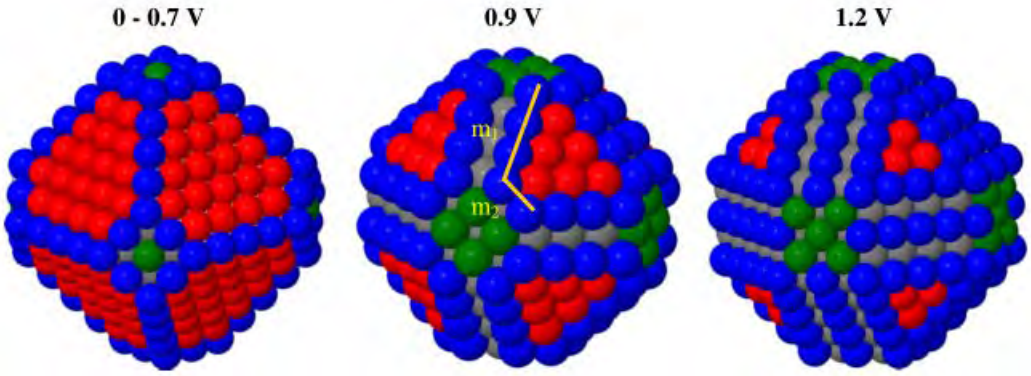

Figure 3.1: Equilibrium platinum nanoparticle shapes predicted at three different electrode potentials; $\{111\} - red$, $\{100\} - green$, edges+corner$-blue$ and subsurface atoms$-grey$ (Tripković *et al.*, 2014).

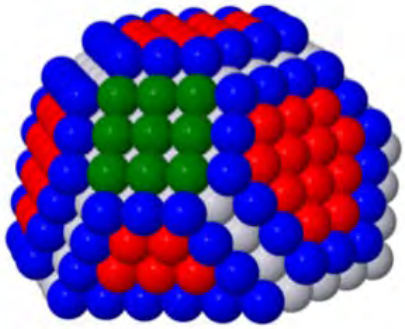

Figure 3.2: Equilibrium platinum nanoparticle with a particle diameter of ca. 3 nm predicted at an electrode potential of 0.9 V; $\{111\} - red$, $\{100\} - green$ and, edges+corner$-blue$ and subsurface atoms$-grey$ (Tripković *et al.*, 2014).

3.2 Pt(111) surface model optimization

Pt{111} and Pt{100} are the predominant surface terminations in cuboctahedral platinum nanoparticles. When the edges are not corroded or dissolved to form Pt{110} steps, only the former surface terminations are exposed on model cuboctahedral nanoparticles. Therefore, these two surface terminations are of importance. As a result a large number of theoretical and experimental studies have investigated the ORR activity over these surface terminations modelled as Pt(111) and Pt(100) slabs (a detailed discussion for Pt(100) is presented in section 3.4). The key features of the Pt(111) slab model are illustrated in Figure 3.3. The Pt(111) slab models for each potential-functional combination were constructed using optimized bulk lattice parameters (presented in Table 2.1). The models were then optimized to minimize computational cost with minimal compromise to the model accuracy. The key parameters that need to be optimized are the k-point density, cut-off energy, slab thickness, vacuum gap between periodic slabs and the number of relaxed atomic layers. The k-point and cut-off energy are computational parameters and were optimized first. The slab thickness, vacuum gap between periodic slabs and number of relaxed atomic layers were optimized in the given order.

3.2.1 k-points and cut-off energy optimization

The k-points and cut-off energy were both optimized using a 5-layered Pt(111)-p(1x1) unit cell with a 12 Å vacuum gap between periodic slabs. For both cases spin-polarized single point DFT energy

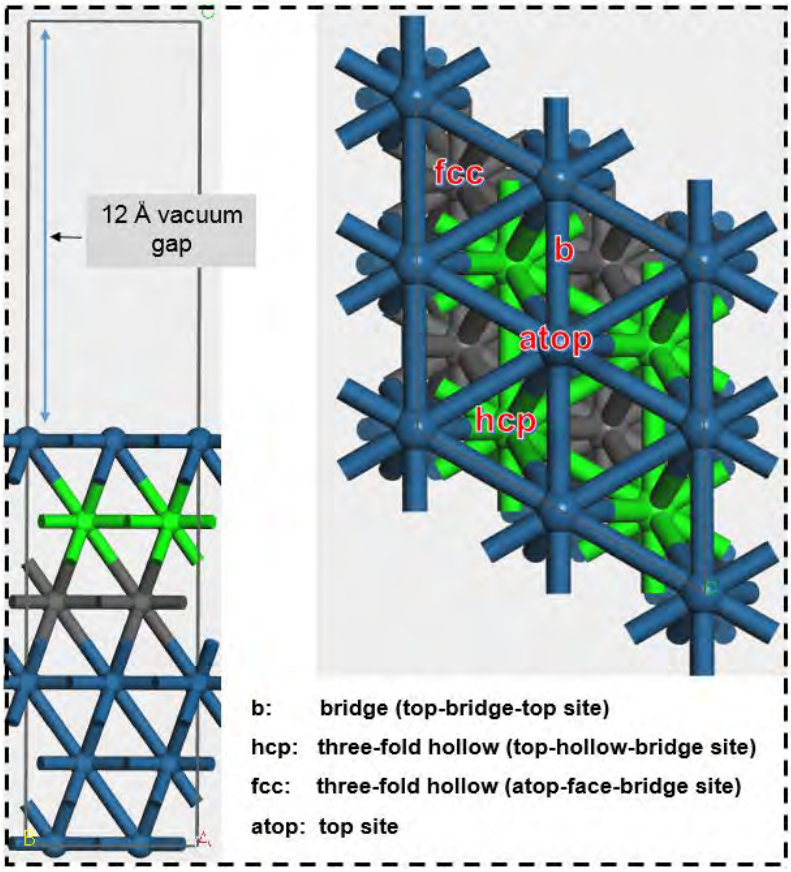

Figure 3.3: Pt(111)-p(2x2) slab model with 6 atomic layers and vacuum spacing. Left: side view, Right: surface normal view showing high symmetry adsorption sites on a Pt(111) slab. All spheres in the two diagrams represent Pt atoms. Blue: top layer (and bottom 3), Green: second atomic layer, Grey: third atomic layer.

calculations were conducted with the first order Methfessel-Paxton (MP) method and a smearing width of 0.1 eV, which is common for this type of calculation. The most crucial requirement for choosing the smearing width is that the entropy term is less than 1 meV/atom. The total energies were extrapolated to zero smearing. In optimizing the k-point sampling, different single point energy calculations with varying k-point grids from 5x5x1 to 22x22x1 were performed with a selected cut-off energy of 600 eV, which is above the converged cut-off energy for bulk Pt as reported in subsection 2.5.2. Since the lattice vector parallel to the surface normal is much longer than the other two lattice vectors, the corresponding reciprocal lattice vector is much shorter and hence only one k-point along the longer lattice vector (z-direction) is needed. By comparing the calculated system energy for each grid against that calculated for the largest grid and using a convergence criterion of 5 meV/atom, 14 irreducible k-points were found to be sufficient to give energies converged to within 5 meV relative to the solution where 52 k-points are used. Figure 3.4 presents the calculated data. The 14 irreducible k-points correspond to a 10x10x1 grid and a 0.041 $Å^{-1}$ k-point density respectively; this is within the same range as reported in other literature studies (Madala, 2013; Duan & Wang, 2013).

Since the interest of this study is to investigate the interaction of O and O_2 with platinum substrates, the cut-off energy optimization was conducted for a system consisting of both platinum and oxygen atoms. The simplest model system used in this case consists of a 6-layered Pt(111)-p(2x2) slab and an oxygen atom adsorbed on an fcc site. A vacuum spacing of 12 Å and a converged k-point sampling density of 0.041 Å (5x5x1 k-point grid) were used. Spin-polarized periodic DFT single point energy calculations were performed to determine the total energies which were used to evaluate the adsorption energies (using equation 3.1). The oxygen atom was only introduced on one side of the slab and the position of oxygen was kept the same for calculations at different cut-off energies. In all energy calculations a dipole correction was applied along the surface normal vector. The adsorption

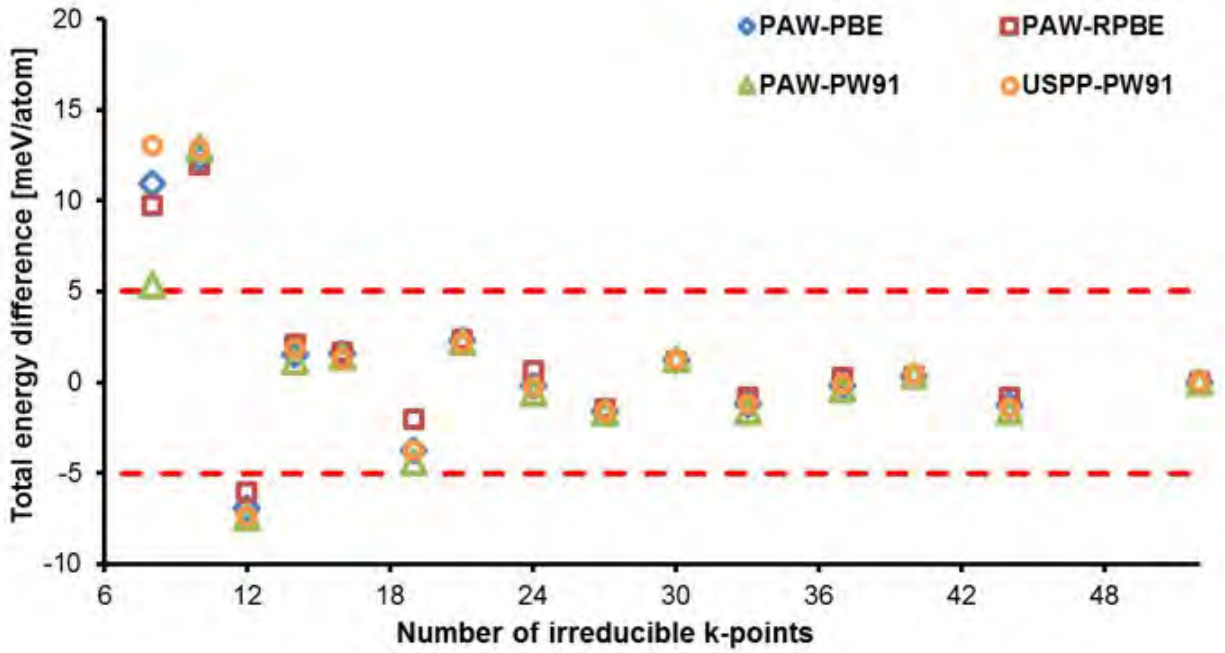

Figure 3.4: Total energy, of a 5-layered Pt(111)-p(1x1) slab as a function of the number of irreducible k-points in the Brillouin zone. Note: the total energy is reference to the energy of a 22x22x1 k-point grid (52 irreducible k-points). The red broken lines indicated the upper and lower limits of the convergence criterion, 5 meV/atom.

of atomic oxygen on an fcc site was investigated at 4 different cut-off energies (400 eV, 430 eV, 450 eV and 500 eV) for all 4 potential-functional combinations. This range was conveniently chosen to start from the upper bound of the VASP-recommended cut-off energy of 400 eV for oxygen for all potential-functional combinations. The adsorption energies are presented in Table 3.1 for all combinations at different cut-off energies. For all studied potential-functional combinations, a cut-off energy of 400 eV was found to be sufficient to achieve convergence of the adsorption energy to within 10 meV/O atom. Therefore, for all potential combinations considered, the converged k-point density and cut-off energy are 0.041 Å and 400 eV respectively. These parameters were used in the optimization of structural properties of the Pt(111) slab model such as slab thickness, number of relaxed atomic layers and vacuum gap between periodic slabs.

Table 3.1: Adsorption energies of atomic O, at different cut-off energies, on an fcc site of a 6-layered Pt(111)-p(2x2) slab—excluding zero point energy and surface relaxation contributions. All energies are reported with respect to $\frac{1}{2}O_2$ in the gas phase.

Cut-off energy	400 eV	430 eV	450 eV	500 eV
PAW−PBE	-0.76	-0.76	-0.75	-0.75
PAW−RPBE	-0.60	-0.59	-0.59	-0.59
PAW−PW91	-0.62	-0.61	-0.61	-0.61
USPP−PW91	-0.88	-0.88	-0.88	-0.88

3.2.2 Slab thickness optimization

Due to increases in computational cost with increasing size of the model system, a minimum sized model that gives reasonable accuracy is required. For slab models, the slab thickness and vacuum spacing are normally optimized to give reasonable adsorption energies of the adsorbing species. Since the main focus of this study is to investigate the reactivity behaviour of different platinum surfaces, energy differences (adsorption, activation and reaction energies) are particularly important. Therefore, the convergence of these energy differences needs to be established with respect to model structural

parameters. This convergence was investigated by using Pt(111)-p(2x2) slab models of different sizes with one atomic oxygen per unit cell adsorbed on an fcc site on one side of the slab. The two top layers closest to the oxygen atom were allowed to relax whilst the bottom layers were fixed in their bulk optimized positions. A vacuum spacing between periodic slabs of 12 Å was maintained. The converged cut-off energy and k-point sampling density of 400 eV and 0.041 $Å^{-1}$, were used. Periodic DFT calculations were performed using VASP to obtain the total energies of clean slabs, slabs with atomic oxygen on an fcc site and atomic oxygen in a rectangular box (see Section 2.6). The adsorption energy is defined by equation 3.1,

$$E_{O,\ ads} = E_{slab+O} - E_{slab} - E_{O,\ gas} \tag{3.1}$$

where E_{slab+O}, E_{slab} and $E_{O,\ gas}$ are total energies of the slab with atomic oxygen adsorbed on an fcc site, the clean slab and atomic oxygen in the gas phase, respectively. The adsorption energy as a function of slab thickness in the size range of 3 to 13 atomic layers is shown in Figure 3.5. There is an apparent fluctuation in the oxygen adsorption energy with increasing number of slab layers. Slab models with 8 atomic layers or more, up to 13 layers, exhibit an oscillatory behaviour in the adsorption energy of atomic oxygen; this is true for all potential-functional combinations investigated. The maximum difference in adsorption energy of atomic oxygen on slabs with 6 or more atomic layers is ca. 47 meV/O atom. Qi *et al.* (2008) and Panchenko *et al.* (2004) showed that for a 4-layered Pt(111) slab model, introducing an O_2 and other adsorbates resulted in Friedel type oscillations of the charge density which perturbed through the slab. Furthermore, a number of studies have shown that properties such as surface energy, work function and interlayer spacing do not converge easily with slab thickness (Kiejna *et al.*, 1999; Wei & Chou, 2002; Da Silva *et al.*, 2006; Sun *et al.*, 2007; Liu, 2010). This non-convergence behaviour has therefore been attributed to quantum-size effects which may be the cause of the observed oscillatory behaviour in the current study.

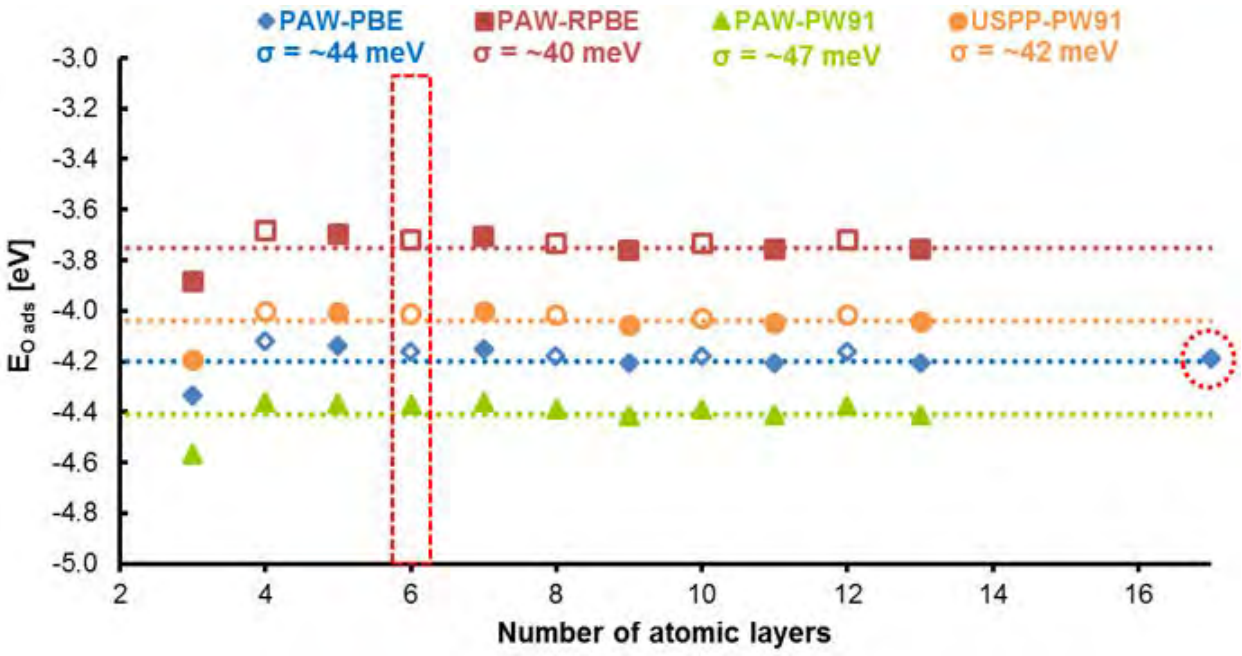

Figure 3.5: Adsorption energy of atomic O as a function of the number of atomic layers in a Pt(111)-p(2x2) slab model; σ is the variation in oxygen adsorption energy between 6 and 13-layered slabs (the data point for a 7-layered slab is excluded for σ calculations). Even- (odd-) layered slabs are indicated by open (filled) markers. The dotted line for each plot corresponds to adsorption energy of O on a 13-layered slab.

Further tests were also conducted to ascertain the dependence on adsorbate, k-point sampling density and adsorption site-type, of these oscillations in the adsorption energy. From these tests no significant improvements in convergence behaviour were observed (Figure 3.6 summarizes the results). The latter

tests were conducted using single point energy calculations with an adsorbate on one side of the slab. Other parameters used in the tests were a cut-off energy of 400 eV and a vacuum gap between periodic slab of 12 Å. The PAW−PW91 potential−functional combination was used and all calculations were spin-polarized with dipole correction along the surface normal vector.

The first test investigated the effect of adsorbate, on the adsorption energy convergence behaviour, by comparing the observed oscillations in the adsorption energy of atomic O and O_2 as a function of slab thickness (Figure 3.6a). This test was intended to investigate if the observed energy oscillations were adsorbate-specific. Figure 3.6a shows that both the adsorption energy of atomic O and O_2 exhibit this oscillation behaviour. Therefore, the oscillations were observed to be adsorbate independent, at least for the case of atomic O and O_2. The second test investigated the effect of k-point sampling density along the surface normal vector. The aim of this was to test if the oscillations were influenced by the k-point sampling density along the slab thickness. Since it had been shown in the first test that the oscillation behaviour was not adsorbate-specific, O_2 was used as a probe molecule. Figure 3.6b shows that the calculated adsorption energy of O_2 is not influenced by increasing the k-point sampling density along the surface normal vector.

The final test considered, investigated whether the oscillations in the adsorption energy of O_2 were site-dependent (Figure 3.6c). From the results it was observed that regardless of the adsorption site of O_2, the oscillations in the adsorption energy were present. There was a small variation in the oscillation amplitudes for adsorption on different sites, with adsorption on bridge sites seen to exhibit the smallest oscillation amplitude. It should be noted that in all cases investigated the oscillation frequency was the same. Figure 3.6d presents the combined results from the above test. Also tested was the effect of using thicker slab models (Figure 3.6d). It was observed from Figure 3.6d that the adsorption energy of O_2 on fcc sites was relatively converged for slab models with 16 or more atomic layers.

The data in Figure 3.6 has been referenced to the adsorption energy of an adsorbate on the respective site for a 13 layered slab, i.e. for each slab thickness i the energy is reported as $\Delta E_{X,ads,i} = E_{X,ads,i-layered\,slab} - E_{X,ads,13-layered\,slab}$. From the data presented in Figure 3.6 it is observed that the oscillatory behaviour persists in all cases investigated and as such cannot be linked to the k-point sampling parallel to the surface normal vector, the type of oxygen adsorbate species (O or O_2), and the site investigated. The reduced fluctuation observed for much thicker slabs shows that a tighter convergence criterion will result in a much larger system.

Limited by the computational efficiency, the convergence test results demonstrate that the achievable adsorption energy convergence is ca. 0.05 eV/O atom (0.06 eV/O atom when the 7-layered slab model is included). A similar convergence error (0.03 - 0.05 eV/O atom) in adsorption energies of atomic oxygen as a function of slab thickness, was reported for Pt(100) slab models (with varying surface unit cell sizes and thickness ranging from 5 to 15 atomic layers) by Liu & Evans (2010). The 6-layered Pt(111)-p(2x2) slab model corresponds to the smallest model system that gives adsorption energies within the above convergence criterion, 0.05 eV/O atom (broken red rectangle in Figure 3.5). Furthermore, it is clear that when considering only the slab models with even numbered layers, adsorption energies for a 6-layered slab are converged within ca. 0.02 eV/O atom for all studied potential-functional combinations.

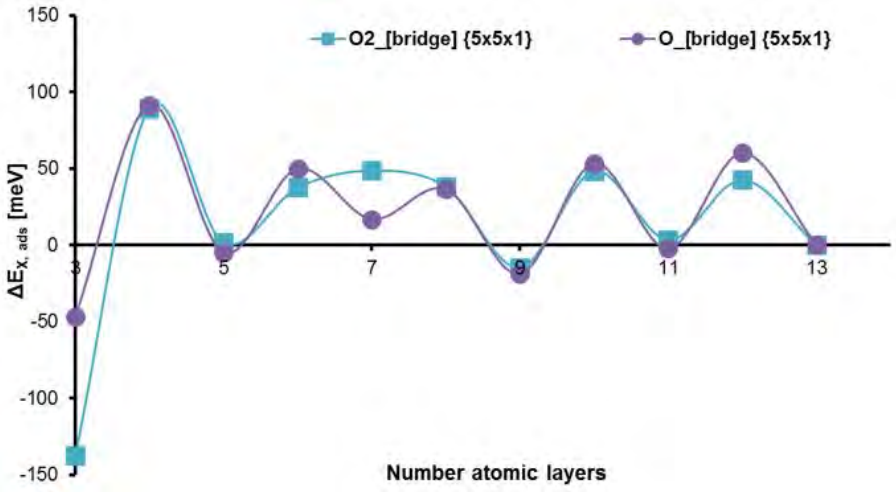

(a) Effect of adsorbate type on the oscillation behaviour in the adsorption energy.

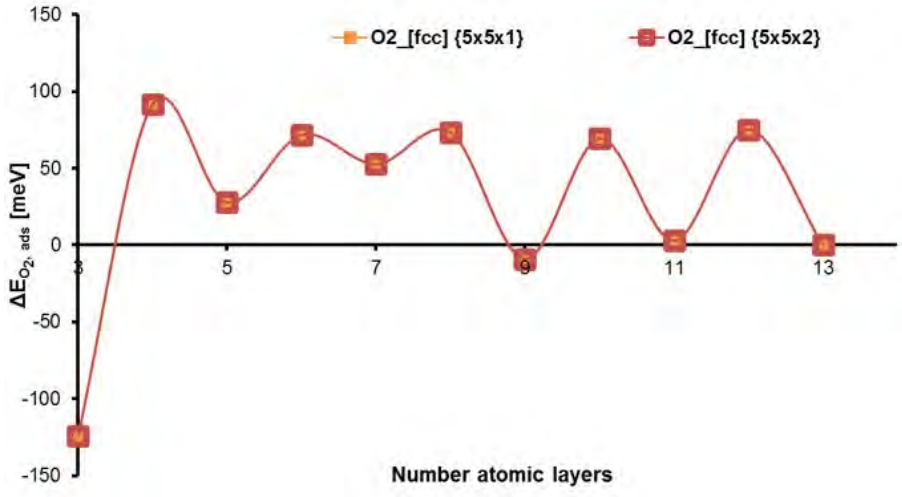

(b) Effect of k-point sampling density on the oscillation behaviour in the adsorption energy.

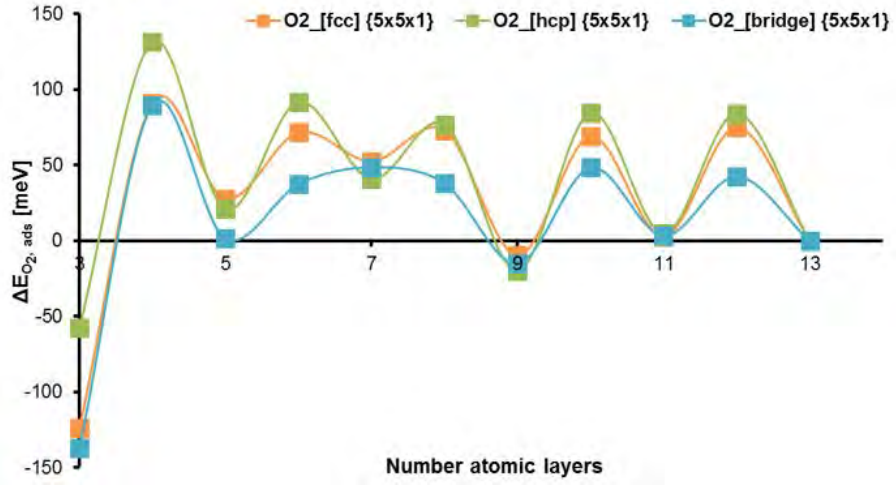

(c) Effect of adsorption site on the oscillation behaviour in the adsorption energy.

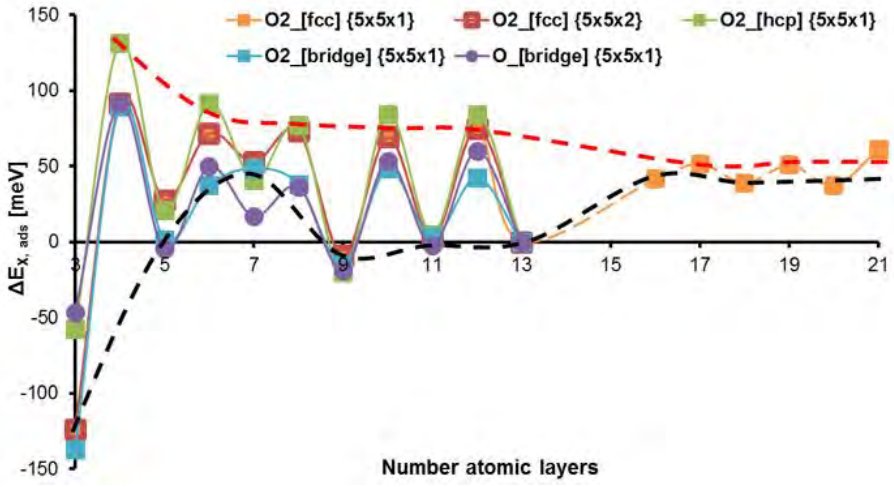

(d) Oscillation behaviour as a function of Pt(111)-p(2x2) slab thickness.

Figure 3.6: Adsorption energy difference ($\Delta E_{X,ads,i} = E_{X,ads,i-layered\ slab} - E_{X,ads,13-layered\ slab}$) of atomic O and O_2. All energies are referenced to the adsorption energy on a 13-layered slab. The red and black dotted fitting (in Figure 3.6d) only serves to guide the eye for the convergence behaviour of even- and odd-layered slab models, respectively.

3.2.3 Layer relaxation and vacuum spacing optimization

Optimization of the vacuum spacing and the number of relaxed atomic layers was conducted on a Pt(111)-p(2x2) slab with 6 atomic layers. For optimization of the vacuum spacing molecular oxygen was used as a probe molecule and adsorbed at an fcc site with one oxygen atom oriented away from the surface. A single point energy calculation was then conducted for this system with different vacuum spacings. The results in Table 3.2 show that the energy is converged to within 1 meV for vacuum spacings above 12 Å. In literature the vacuum spacings normally used range from 10 to 12 Å (Gu & Balbuena, 2007; Yang *et al.*, 2010; Duan & Wang, 2013; Ogawa *et al.*, 2013), therefore in this study a minimum vacuum gap of 12 Å was maintained for all calculations. The vacuum gap is minimized since computational cost increases with increasing vacuum gap. For optimization of the number of atomic layers relaxed in a slab, geometry optimization calculations were conducted. These calculations used atomic oxygen instead of molecular oxygen as a probe species. The choice was motivated by the fact that atomic oxygen interacts more strongly with platinum surfaces than does molecular oxygen (Eichler & Hafner, 1997; Ford *et al.*, 2010; Duan & Wang, 2011). In this optimization process a 6-layered Pt(111)-p(2x2) slab was used and the number of fully relaxed layers was systematically increased from just 1 top layer up to 3 top layers whilst the bottom layers were fixed in the bulk-optimized positions. Atomic oxygen was introduced on one side of the slab model and on an fcc site. For all energy calculations a dipole correction was applied along the surface normal vector. The data presented in Table 3.3 shows that for all four combinations, relaxing the top 2 atomic layers is sufficient. The adsorption energies are converged to within 0.001 eV for a model system with the top 2 atomic layers relaxed and the bottom layers fixed in their bulk position. Table 3.4 presents a summary of the Pt(111) optimization results.

Table 3.2: Adsorption energy of O_2 ($E_{O_2,ads}$) as a function of the vacuum gap between periodic slab (see equation 3.2).

Vacuum spacing [Å]	$E_{O_2,ads}$ $[eV/O_2]$			
	PAW−PBE	PAW−RPBE	PAW−PW91	USPP−PW91
8	-0.242	-0.401	-0.314	-0.228
10	-0.244	-0.403	-0.316	-0.231
12	-0.245	-0.404	-0.318	-0.231
14	-0.244	-0.404	-0.318	-0.231
16	-0.245	-0.405	-0.318	-0.231

Table 3.3: Adsorption energy of atomic oxygen ($E_{ads,O}$) on the fcc site at 0.25 ML. All energies are reported with respect to $\frac{1}{2}O_2$ in the gas phase.

	$E_{ads,O}$ $[eV/\frac{1}{2}O_2]$		
Atomic layers relaxed	1	2	3
PAW−PBE	-1.09	-1.13	-1.13
PAW−RPBE	-0.84	-0.88	-0.88
PAW−PW91	-1.16	-1.20	-1.20
USPP−PW91	-1.16	-1.20	-1.20

Since it is not practical to conduct a full investigation into the activity of the ORR using all four potential-functional combinations, it is necessary to choose one. One method of doing this is to compare predicted bulk properties to experimentally-determined bulk properties. However, this approach is not sufficient for this study since the focus is on surface reactivity and adsorption of oxygen-containing species. Therefore, the choice of a potential−functional combination will also be based on how well each combination predicts the adsorption energy of molecular oxygen on a Pt(111) surface.

Table 3.4: Summary of optimized Pt(111) slab model parameters, used for all potential-functional combinations.

k-point mesh grid for a (1x1) cell	10x10x1
k-point spacing	0.041 $Å^{-1}$
plane wave basis set cut-off energy	400 eV
slab thickness	6 atomic layers
vacuum spacing	12 Å
number of atomic layers relaxed	2 layers

3.3 Choice of exchange-correlation energy functional

The interaction of molecular oxygen with platinum surfaces is an important step in the ORR. Ultrahigh vacuum (UHV) experiments have been used to measure adsorption energies and vibrational modes of adsorbed molecular oxygen. In their UHV experiments using thermal desorption spectroscopy, Gland *et al.* (1980) reported a binding energy for molecular oxygen on a clean Pt(111) surface of 0.34 eV at temperatures below 120 K and a coverage of 0.25 ML. The saturation coverage of O_2 was reported to be 0.4 ML O_2. The molecular adsorption of oxygen was interpreted as resulting in the formation of a peroxo-type (O_2^{-2}) species at these conditions (Gland *et al.*, 1980). The identification of the peroxo species was based on the observation of two vibrational modes corresponding to the stretching of an oxygen-oxygen bond. The vibrational frequencies measured by Gland *et al.* (1980) using electron energy loss spectroscopy (EELS) were 870 cm^{-1} and 710 cm^{-1}. These vibrational frequencies are consistent with those calculated by Eichler & Hafner (1997). The latter researchers calculated vibrational frequencies of 850 cm^{-1} (bridge adsorption site), 710 cm^{-1} (hcp adsorption site) and 690 cm^{-1} (fcc adsorption site). Under different thermal conditions, Gland *et al.* (1980) observed vibrational modes characteristic of atomic oxygen. Recently, Miller *et al.* (2010) derived an adsorption energy of O_2 on a Pt(111) surface, from temperature programmed X-ray photoelectron spectroscopy (TP-XPS) experiments, of 0.38 eV which is consistent with that reported by Gland *et al.* (1980).

Theoretical studies based on DFT have shown that PBE and PW91 functionals overestimate the binding energy of O_2 on Pt(111) (Duan & Wang, 2011; Yang *et al.*, 2010). The RPBE functional of Hammer *et al.* (1999) has been reported to improve the prediction of adsorption energies of gaseous species on metal surfaces compared to the PBE and PW91 functionals. However, in some instances this functional has also been observed to underestimate adsorption energies (Ford *et al.*, 2010). It has been shown that molecular oxygen preferentially adsorbs on either fcc or bridge sites on Pt(111) (Yang *et al.*, 2010; Duan & Wang, 2011). The energy difference between these two adsorption states has been reported to be very small: 0.01 eV (Bocquet *et al.*, 1999; Duan & Wang, 2011), 0.02 eV (Yang *et al.*, 2010; McEwen *et al.*, 2012) or 0.04 eV (Eichler & Hafner, 1997), which is within the observed variation in slab thickness optimization (see section 3.2). Therefore, an fcc site has been used to compare the calculated adsorption energies of O_2 with the adsorption energy measured by Gland *et al.* (1980). For all four potential-functional combinations, spin-polarized DFT calculations were conducted using a Pt(111)-p(2x2) surface model with six atomic layers. Only the top two layers were allowed to relaxed while the bottom four were fixed in their bulk optimized positions. A converged k-point grid of 5x5x1 was used with a cut-off energy of 400 eV. In all total energy calculations a dipole correction was applied along the surface normal vector. Only the top side of the slab model is covered in O_2. The adsorption energy was defined as follows,

$$E_{ads,\ O_2} = E_{slab+O_2} - E_{slab} - E_{O_2,\ gas} \tag{3.2}$$

where $E_{O_2,\ gas}$ is the energy of O_2 in the gas phase. The calculated adsorption energies for all four combinations are presented in Table 3.5. Both the corrected and uncorrected adsorption energies of O_2 are presented in Table 3.5. The calculated adsorption energies were then compared to the experimental adsorption energy of O_2 on Pt(111)—reported by Gland *et al.* (1980).

Table 3.5: Calculated differential adsorption enthalpies of O_2 on Pt(111) at 120 K[a]. In round brakets, (), are the adsorption enthalpies reference to the corrected O_2 energy in the gas phase (Table 2.4).

Coverage		PAW−PBE	PAW−RPBE	PAW−PW91	USPP−PW91
0.25 ML	E_{ads,O_2} [eV/O_2]	-0.52 (-0.82)	-0.10 (-0.68)	-0.63 (-0.85)	-0.53(-0.74)
0.50 ML	E_{ads,O_2} [eV/O_2]	-0.04 (-0.34)	0.41 (-0.18)	-0.14 (-0.36)	-0.06 (-0.27)

a finite temperature corrections are based on the formulas presented in Appendix C

Based on the results in Table 3.5, none of the investigated potential−functional combinations were observed to give a particularly good prediction of the adsorption of O_2 on the Pt(111) surface. The experimentally derived adsorption energy of O_2 on Pt(111) was reported to be -0.34 eV/O_2 at ca. 0.25 ML O_2 coverage (Gland *et al.*, 1980). The PAW−PBE, PAW−PW91 and USPP−PW91 potential−functional combinations were observed to overestimate the latter adsorption energy by 0.18 eV, 0.29 eV and 0.19 eV at 0.25 ML coverage, respectively. On the other hand, the PAW−RPBE potential−functional combination was observed to underestimate the experimental adsorption energy of O_2 by 0.24 eV. Therefore, it can be concluded that in terms of prediction of the adsorption energy of O_2 at 0.25 ML coverage, none of the investigated combinations was particularly better. Consideration of the O_2 correction resulted in an even poorer agreement with experimentally measured adsorption energy of O_2 on the Pt(111) surface (see Table 3.5). Therefore, only the uncorrected O_2 energy was considered for further calculations in this study.

The PAW−PBE and USPP−PW91 were seen to be better at predicting the adsorption enthalpy of O_2 than the PAW−PW91 and PAW−RPBE combinations. Furthermore, the PAW−PBE was observed to give better prediction of the equilibrium bulk properties of platinum (Chapter 2). Therefore, for further calculations in this study, the PAW−PBE potential−functional combination will be used. The other advantage in using this combination is the availability of recent data which can be used to compare with (Gu & Balbuena, 2007; Qi *et al.*, 2008; Yang *et al.*, 2010; Madala, 2013; Ogawa *et al.*, 2014). It has been shown that even though the absolute values across different combinations are different, the relative energy trends are very similar (Gu & Balbuena, 2007; Ogawa *et al.*, 2013; Duan & Wang, 2013; Ogawa *et al.*, 2014). Therefore one needs to choose a functional and compare against data generated for that functional and relative differences across different functionals. Results generated from this study using the PAW−PBE potential−functional combination will thus be compared with a number of other literature studies which have used this combination.

3.4 Pt(100) surface model optimization

The optimization of the Pt(100) slab was only conducted using the PAW−PBE potential−functional combination. Since this study only considers systems with oxygen and platinum, the converged cut-off energy should be the same as for the Pt(111) slab, 400 eV. By converging the total energy of a 6-layered Pt(100)-p(1x1) slab with respect to the k-point sampling density, a k-point grid of 10x10x1 corresponding to 21 irreducible k-points and a k-point sampling density of 0.035 $Å^{-1}$, was found to yield a total energy that was converged to within ca. 5 meV/atom (7 meV for an odd k-point grid corresponding to 21 irreducible k-points). Figure 3.7 presents the results of the k-point optimization calculations. A converged vacuum spacing of 12 Å was used since its convergence is not as strongly influenced by the change in configuration of surface atoms as it is by adsorbed species. The slab thickness and degree of layer relaxation incorporated was explicitly optimized. For the optimization of the Pt(100) slab, adsorption of atomic oxygen on a bridge site was considered. Figure 3.8 shows the high symmetry adsorption sites found on a Pt(100)-p(2x2) slab model.

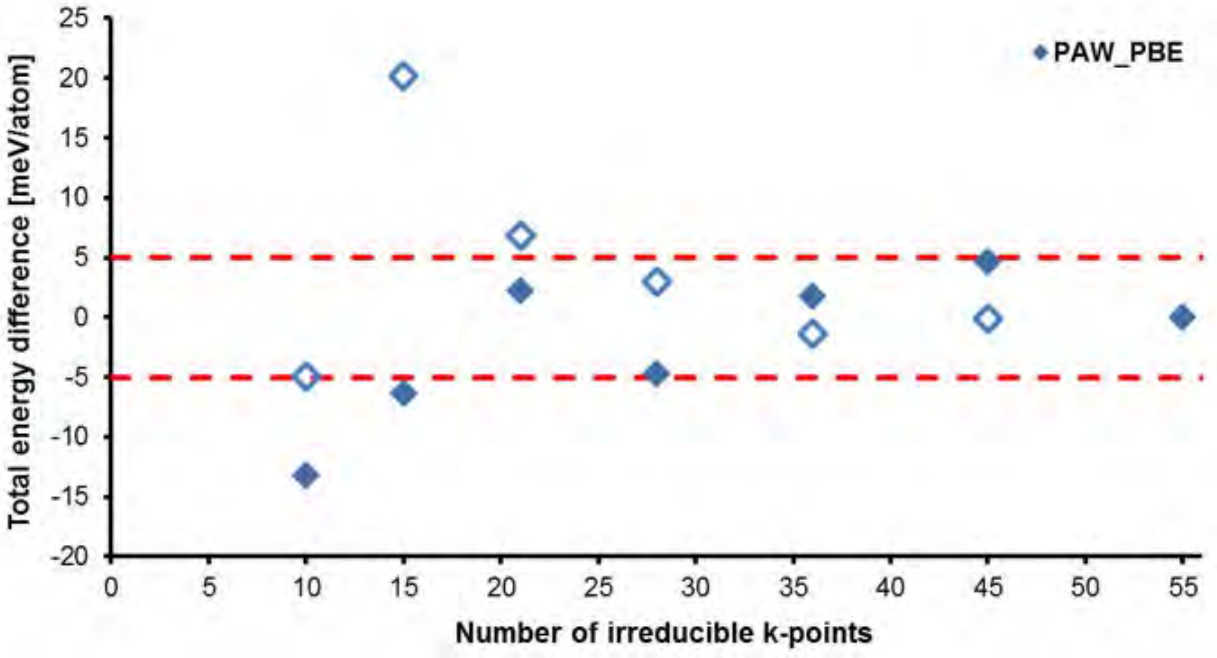

Figure 3.7: Pt(100)-p(1x1) total energy convergence as a function of the number of irreducible k-points in the Brillouin zone. Note: the total energy is referenced to the energy obtained using an 18x18x1 k-point grid (corresponding to 55 irreducible k-points). The red broken lines indicated the upper and lower limits of the convergence criterion, 5 meV/atom. The open markers represent a k-point grid NxNx1 where N is even, on the other hand, the solid markers represents cases where N is odd.

3.4.1 Slab thickness optimization

Using the converged k-point sampling density of 0.035 $Å^{-1}$, a cut-off energy of 400 eV and a 12 Å vacuum spacing, geometry optimization calculations were performed for Pt(100)-p(2x2) slab models of different thickness ranging from 3 to 16 atomic layers. For each slab the top two layers were allowed to relax during geometry optimization whilst the bottom layers were fixed in their bulk optimized positions. Three sets of calculations were performed for each slab: i) clean slab without any adsorbate (slab), ii) slab with atomic oxygen on a bridge site (slab+O) and iii) slab with two O atoms on neighbouring bridge sites (slab+2O) (see Figure 3.9). The calculated total energies from the three sets were then used to calculate the adsorption energy of atomic oxygen as a function of slab thickness. The adsorption energy was defined with respect to the total energy of atomic oxygen in the gas phase (see equation 3.1) whilst the total energy of atomic oxygen was calculated as described in section 2.6. In all total energy calculations a dipole correction was applied along the surface normal.

The adsorption energy of atomic O at 0.25 ML coverage is described by equation 3.1 whilst the adsorption energy of atomic O at 0.50 ML coverage is given by equation 3.3,

$$E_{ads,O\ @\ 0.5\ ML} = E_{slab+2O} - E_{slab+O} - E_{O,\ gas} \tag{3.3}$$

where $E_{slab+O\ @\ 0.5\ ML}$ and $E_{slab+2O}$ are the adsorption energy of atomic O on a Pt(100)-p(2x2) slab that has been pre-covered with 0.25 ML of atomic oxygen (differential O adsorption energy at 0.5 ML) and the total energy of a Pt(100)-p(2x2) slab with two oxygen atoms on bridge sites (slab+2O), respectively. Figure 3.10 presents the calculated adsorption energy of atomic O, at a 0.25 ML and 0.50 ML coverage, as a function of slab thickness. From the latter figure it was observed that reasonable convergence, within 10 meV, in the adsorption energy of atomic O on Pt(100)-p(2x2) slab models (at both 0.25 ML and 0.50 ML coverage) only occurs on slab models with 13 or more atomic layers. A potential outlier, corresponding to a 9-layered slab (broken red circles in Figure 3.10), was observed at both the 0.25 ML and 0.50 ML coverages.

To investigate this further, the geometric structure of the 9-layered slab was compared to that of the 8- and 10-layered slabs. The first interlayer spacing (between the first and second slab atomic

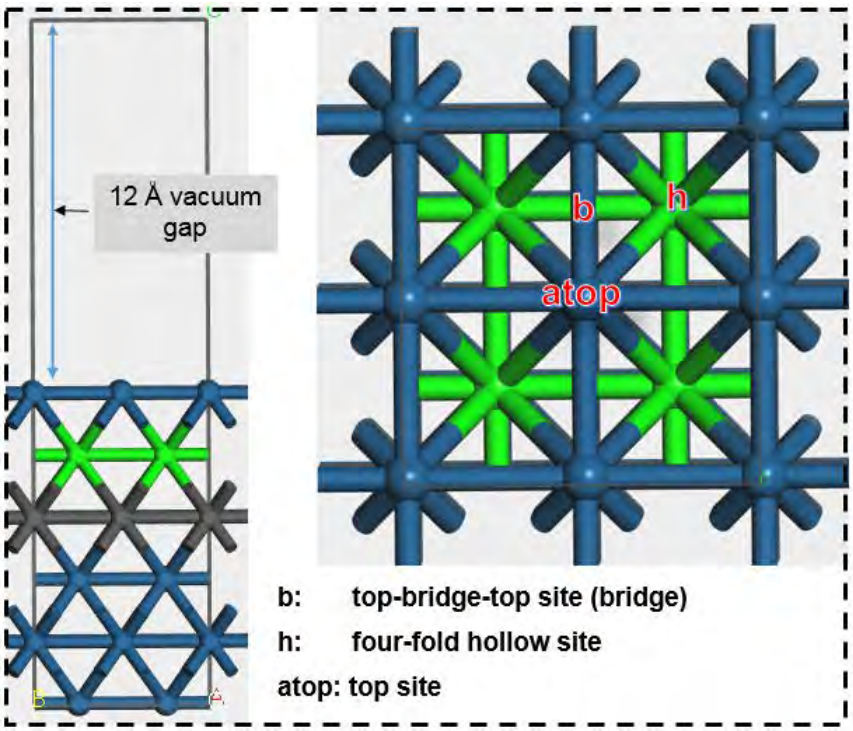

Figure 3.8: Pt(100)-p(2x2) slab model with 6 atomic layers. Left: side view, Right: surface normal view showing high-symmetry adsorption sites on a Pt(100) slab. All spheres in the two diagrams represent Pt atoms. Blue: top layer (and bottom 3), Green: second atmic layer, Grey: third atomic layer.

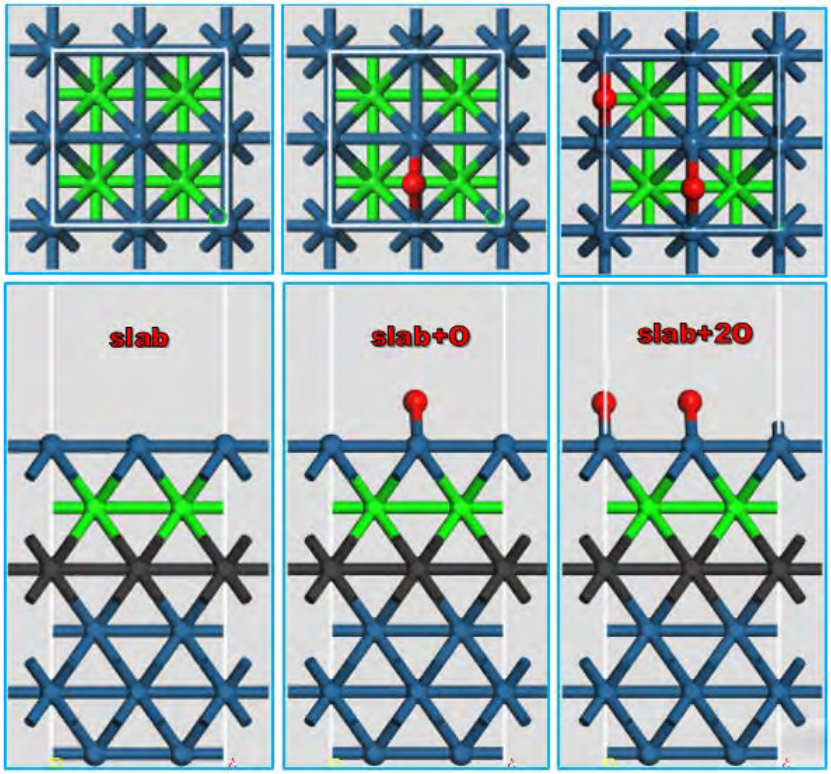

Figure 3.9: 6-layered Pt(111)-p(2x2) slab models for investigating atomic O adsorption at a 0.25 ML and 0.50 ML coverage. Surface normal view (top) and side view (bottom).

layers) of a relaxed clean Pt(100)-p(2x2) slab with 8, 9 and 10 atomic layers was calculated to be 1.942, 1.943 and 1.943 Å, respectively. The second interlayer spacing of the above slab models was also calculated to be 1.984, 1.982 and 1.980 Å for the 8-, 9- and 10-layered slab models, respectively.

Therefore, no significant geometric differences were observed in the clean slab models to explain the observed outlier behaviour of the 9-layered slab in Figure 3.10. The converged geometric structures of Pt(100)-p(2x2) slab models with 8, 9 and 10 atomic layers and each with one atomic O on a bridge site were compared. The first average interlayer spacing was calculated to be 1.990, 1.993 and 1.990 Å for the 8-, 9- and 10-layered slab models, respectively. The differences in the interlayer spacing were also seen to be relatively small and could not be directly linked to the observed anomalous behaviour of the 9-layered slab. The Pt-O bond lengths on bridge sites of the geometry optimized 8-, 9- and 10-layered Pt(100)-p(2x2) slab models were calculated to be 1.950, 1.951 and 1.949 Å, respectively. In summary, the observed geometric differences were considered to be insignificant to explain the observed anomalous behaviour of the 9-layered slab.

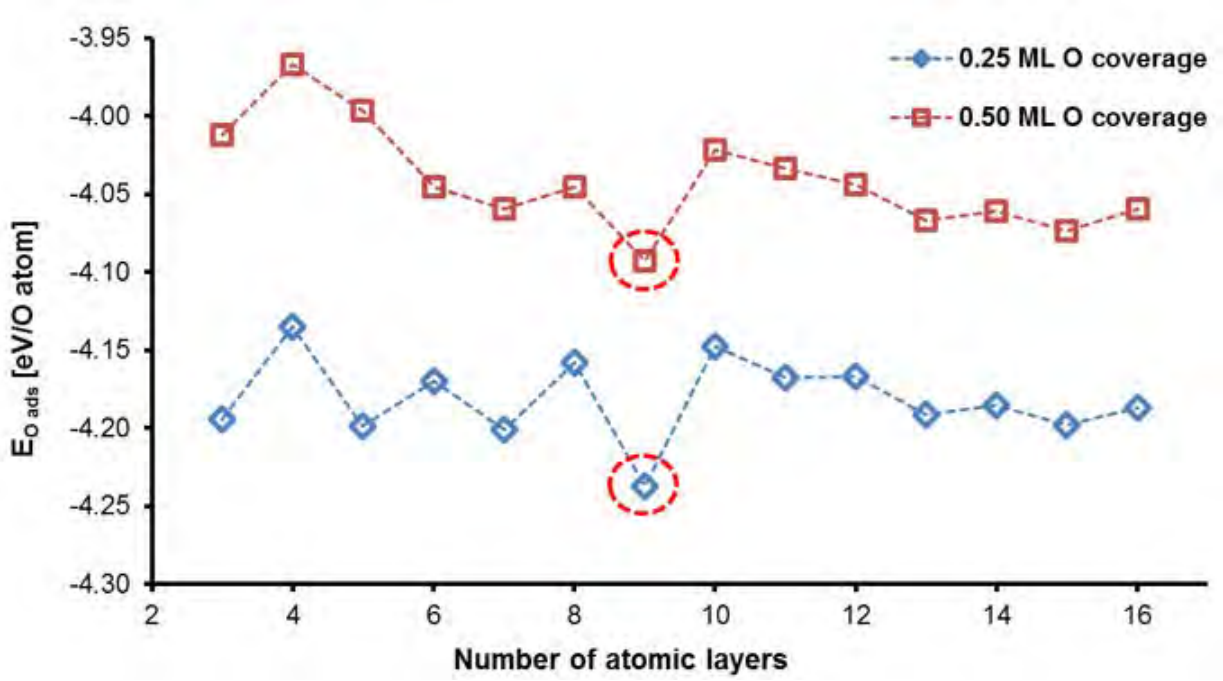

Figure 3.10: Adsorption energy of atomic oxygen as a function of the Pt(100)-p(2x2) slab thickness. Adsorption energies were calculated with respect to atomic oxygen in the gas phase (equation 3.1 and 3.3). The red broken circles indicate the anomalous data points corresponding to a 9-layered slab.

It is anticipated that beyond a converged slab thickness, increasing the slab thickness will result in a constant increase in total energy of the slab, corresponding to the number of layers added. This is due to the fact that beyond some slab thickness an increase in the number of atomic layers by one layer is equivalent to adding a bulk layer with platinum atoms fixed in their bulk optimized positions. Therefore, the change in the total energy of a clean slab, slab with one O atom (slab+O) and slab with two O atoms (slab+2O), with the number of atomic layers was calculated as $E_{i,total} - E_{i+1,total}$ (where $E_{i,total}$ is the total energy of a slab with an i-number of atomic layers) and plotted in Figure 3.11. From the latter figure, it was observed that all points involving the total energy of the 9-layered slab exhibited an anomalous behaviour. Therefore, based on the latter it was concluded that the main contributor to this anomalous behaviour was the total energy of the clean slab with 9 atomic layers. Limited by computational efficiency, though better convergence was only achieved for slab models consisting of at least 13 atomic layers, a 6 layered slab model is considered in this study. This slab model size gives adsorption energy of atomic O converged to within 40 meV when compared to the converged 13- to 16-layered slab models. The latter convergence criterion is comparable to the convergence observed for the Pt(111) slab models. Furthermore, Liu & Evans (2010) also reported a standard deviation of 50 meV in the adsorption energy of atomic O on different Pt(100) slab models with varying slab thickness from 5 to 9 atomic layers. Therefore, it was concluded that a 6-layered slab model would be sufficient for the purpose of this study.

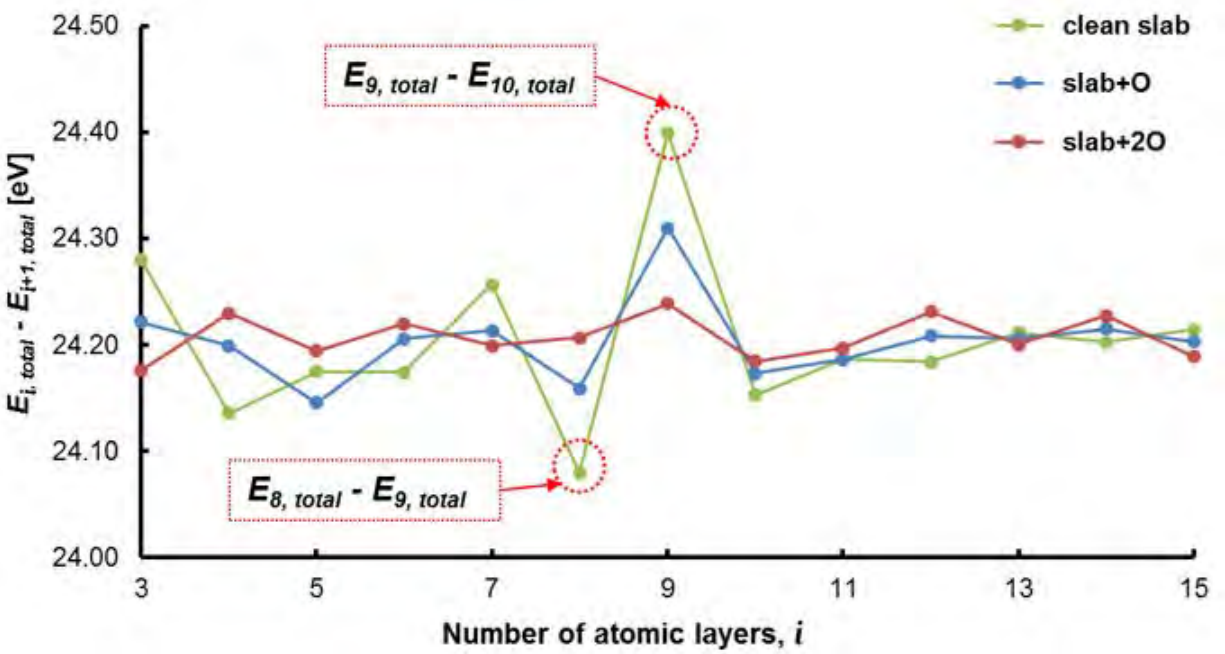

Figure 3.11: The change in total energy of Pt(100)-p(2x2) slab models (clean slab, slab with one O atom (slab+O) and slab with two O atoms (slab+2O) as shown in Figure 3.9) as a function slab thickness, i. The energies are given in eV per atomic layer which consist of four platinum atoms. The red broken circles indicate the points involving the total energy of a 9-layered slab model.

3.4.2 Layer relaxation

Optimization of the number of relaxed atomic layers was conducted using a Pt(100)-p(2x2) slab model with 6 atomic layers. Geometry optimization calculations were conducted using the converged k-point sampling density, cut-off energy and vacuum spacing of 0.035 $Å^{-1}$, 400 eV and 12 Å, respectively. Atomic oxygen, the probe adsorbate, was adsorbed on one side of a 6-layered Pt(100)-p(2x2) slab on a four-fold hollow site. The number of relaxed layers was then systematically increased from one top layer to four top layers whilst each time the bottom layers were fixed in their bulk optimized positions calculated using the PAW−PBE potential−functional combination. For each studied case an adsorption energy of atomic oxygen was calculated using equation 3.1. Table 3.6 shows that relaxing only the top three layers results in adsorption energy that is converged to within 10 meV/O atom.

Table 3.6: Adsorption energy of atomic oxygen on the 4-fold hollow site at a 0.25 ML coverage (equation 3.1). Adsorption energies are given in eV/O atom.

Atomic layers relaxed	2	3	4	5
PAW−PBE	-3.784	-3.798	-3.802	-3.804

Chapter 4

Development of a nanorod model

4.1 Introduction

Presently nanoparticle clusters and step-surfaces are used to model the ORR activity on edge sites (Greeley *et al.*, 2007; Tritsaris *et al.*, 2011; Wei & Liu, 2013; Tripković *et al.*, 2014). The number of platinum atoms increases rapidly with increasing particle size. Therefore it becomes computationally demanding to model these systems using DFT methods as the computational cost scales as N^3, where N is the number of valence electrons (Shimojo *et al.*, 2001; Greeley *et al.*, 2002; Chen & Zhou, 2008). Figure 4.1 presents one example of the change in total number of atoms in cuboctahedral model nanoparticles. In both experimental and theoretical activity/kinetic studies, it has been shown that the optimal particle size range, in terms of maximum mass-specific ORR activity, is 2-4 nm (Kinoshita, 1990; Tritsaris *et al.*, 2011; Perez-Alonso *et al.*, 2012). A 2.7 nm platinum model cuboctahedral nanoparticle will consists of ca. 561 atoms and each edge will consist of 6 atoms. Due to the computational cost of modelling these large systems, a smaller sized model system is required to model the behaviour of different regions found on model nanoparticles.

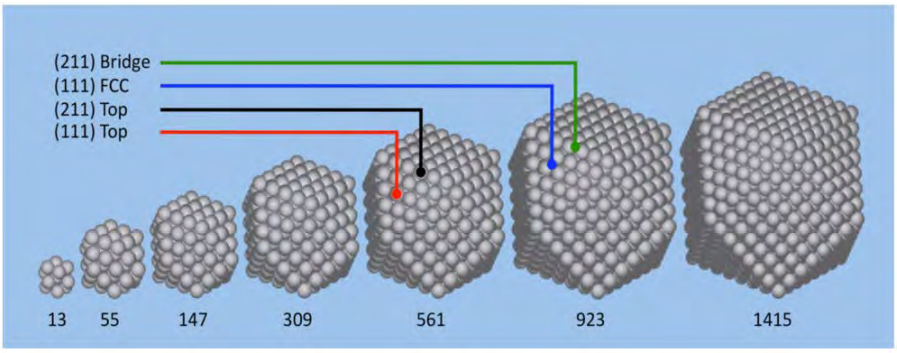

Figure 4.1: Illustration of cuboctahedral platinum nanoparticles consisting of 13 to 1415 atoms. Different sites are identified on a 561 atom nanoparticle (Li *et al.*, 2013). The Pt(211) Bridge and Pt(211) Top represents a bridge and a top site along the edge atomic row, respectively.

Generally Pt(211) step-surface models (Greeley *et al.*, 2007; Ogawa *et al.*, 2014) and small platinum clusters (38−201 atoms) (Calle-Vallejo *et al.*, 2014; Jennings *et al.*, 2014; Peng & Mavrikakis, 2015) have been used to model the edge region of nanoparticles. Whilst smaller clusters are more realistic if fully relaxed, for nanoparticle sizes of interest in fuel cell systems, the required cluster sizes are computationally too demanding. Pt(211) and other step-surface models are limited by the length of Pt{111} and Pt{100} terraces. Though it is possible to modify these surface models, the total number of atoms generally increases with an increase in terrace length. Figure 4.2 presents a comparison between the Pt(211) double stepped surface used by Ogawa *et al.* (2014) and a small platinum cluster (116 atoms) used by (Peng & Mavrikakis, 2015). These two systems are limited by size in terms of both the total number of atoms and terrace area. In literature both the cuboctahedral and truncated octahedral geometries are generally considered as the expected equilibrium platinum nanoparticle particle shape (Kinoshita, 1990; Tritsaris *et al.*, 2011; Li *et al.*, 2013; Calle-Vallejo *et al.*, 2014; Jennings

et al., 2014). Since both cuboctahedral and truncated octahedral model nanoparticle shapes expose an edge region formed as an intersection of {111} and {100} terraces, this study focuses, for modelling edge sites, on this particular edge type. For consistency, in this work the cuboctahedal nanoparticle shape is considered. This morphology also forms a midpoint between cubic and octahedral geometries (Long *et al.*, 2010).

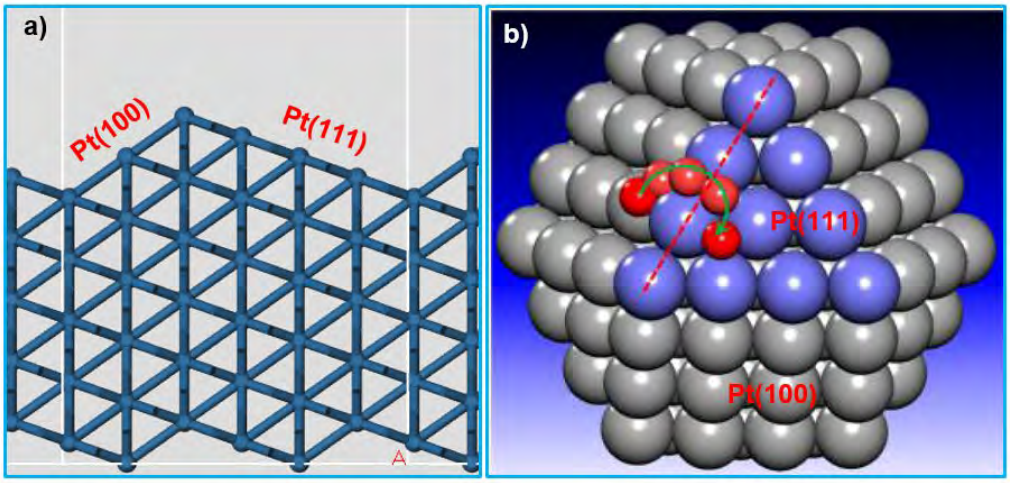

Figure 4.2: Illustration of models used to study edge reactivity behaviour: (a) step-double Pt(211) surface, i.e. Pt(S)-[5(111)×2(100)], with 68 atoms and (b) 147-atom cuboctahedral platinum nanoparticle with an atomic O diffusion path indicated by a set of red spheres (Peng & Mavrikakis, 2015).

4.2 Nanorod construction

This study investigates the interaction of atomic O and O_2 with nanorod edge sites which are formed at the intersection of a Pt(111) and a Pt(100) facet. The total number of atoms in a nanorod model system, with a fixed terrace area A, is minimized by minimizing the number of exposed terraces or edges. Figure 4.3a presents cross-sectional representations of different possible nanorod models with varying number of terraces. Intuitively triangular and square nanorod models will result in the smallest system size, respectively. However due to the intersection angle and the atom arrangements in the bulk fcc platinum structure, these models will not yield the desired Pt(111)-Pt(100) intersection edge. Therefore, this leaves two possible models, the hexagonal and rhombic nanorod models (Figure 4.3).

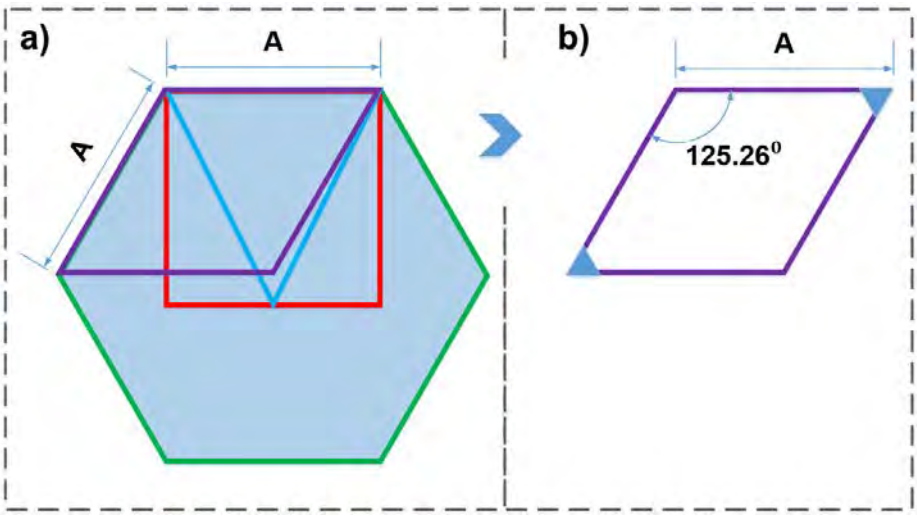

Figure 4.3: Cross-sectional model shapes of potential nanorod models (a), and the cross-sectional model of a rhombic, parallelogram, nanorod model (b).

Since both the hexagonal and rhombic nanorod model exposes Pt{111} and Pt{100} terraces, the optimized k-point sampling density of the Pt(111) and Pt(100) slab models was used. Furthermore, a minimum vacuum spacing between periodic nanorod surfaces of 12 Å was maintained. The latter vacuum spacing was obtained from the optimization of slab models in Chapter 3. The flattening of the planar-averaged electrostatic potential in the vacuum, shown in Figure 4.4, is a direct indication that a 12 Å spacing is sufficient. The smallest rhombic nanorod model consists of 6 atomic rows along each nanorod terrace (Figure 4.5b). This is based on the smallest slab models that give adsorption energies of atomic O converged to within ca. 50 meV (Chapter 3). This initial rhombic nanorod model corresponds to a Pt(NR)-[6(111)×6(100)] nanorod when represented using a modified Somorjai step-terrace notation (Lang *et al.*, 1972). Therefore, in this study the general notation for nanorods is defined as Pt(NR)-[m(111)×n(100)], where m and n represent the number of atomic rows along the Pt(111) and Pt(100) nanorod terraces, respectively. Since two of the plane intersection angles on rhombic nanorod models are less than 90 °(Figure 4.3b and 4.5b), atoms that reside at these edges are anticipated to be unstable, i.e. a large extent of relaxation at these intersections is anticipated to occur and potentially influence the calculated energies. To avoid the latter, all low coordinated edge atoms that reside at these edges were removed from the rhombic nanorod models considered. This modified nanorod system is denoted by Pt(mNR)-[5(111)×5(100)], where mNR refers to a modified nanorod shown in Figure 4.5a. This modified nanorod model has 5 atomic rows along each of its terraces. In all nanorod calculation two unit cell were considered along the infinite nanorod dimension (see Figure 4.3a: bottom). Therefore, for the considered modified rhombic nanorod model a k-point grid of 1x5x1, a cut-off energy of 400 eV and a vacuum gap of 12 Å was used.

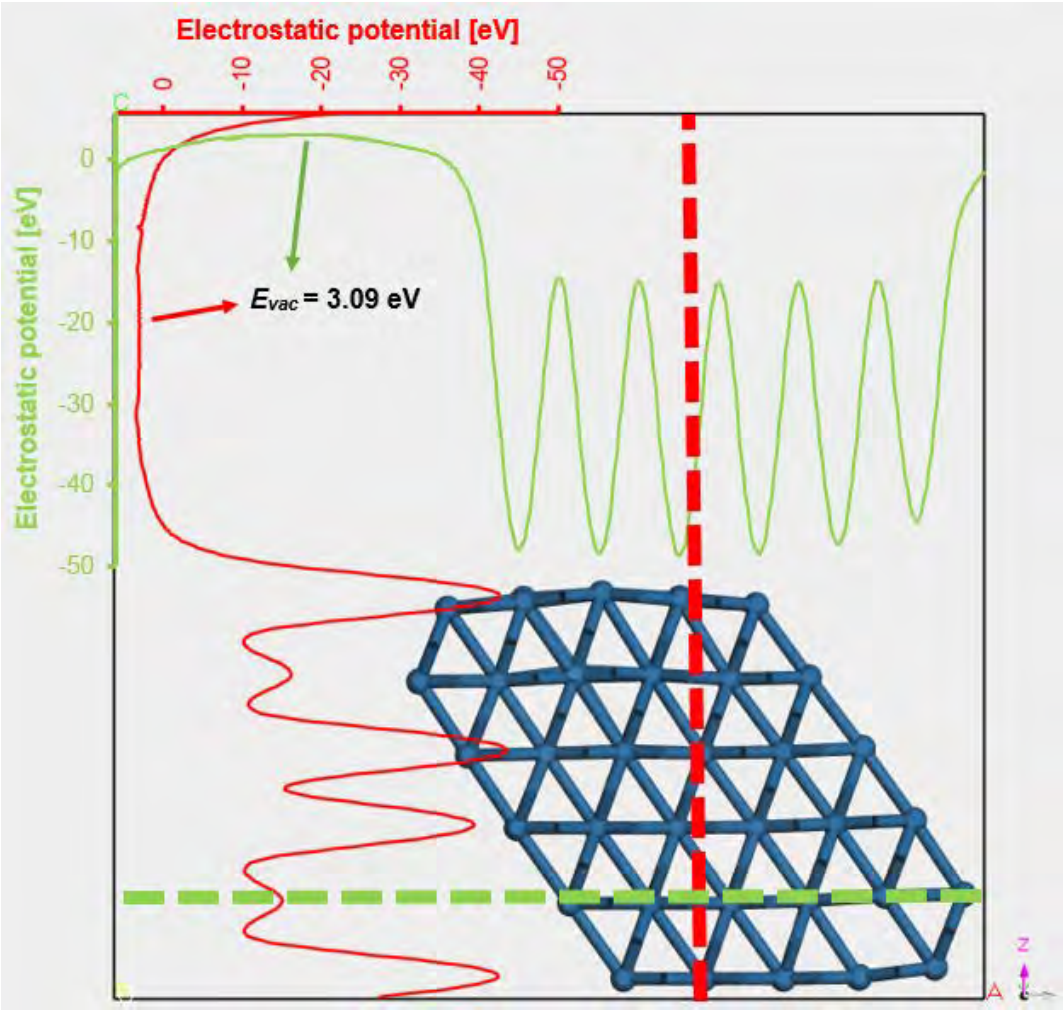

Figure 4.4: Change in electrostatic potential along the finite dimensions of the Pt(mNR)-[5(111)×5(100)] nanorod model. Each electrostatic potential plot is extracted along the dashed line and E_{vac} is the vacuum-level electrostatic potential.

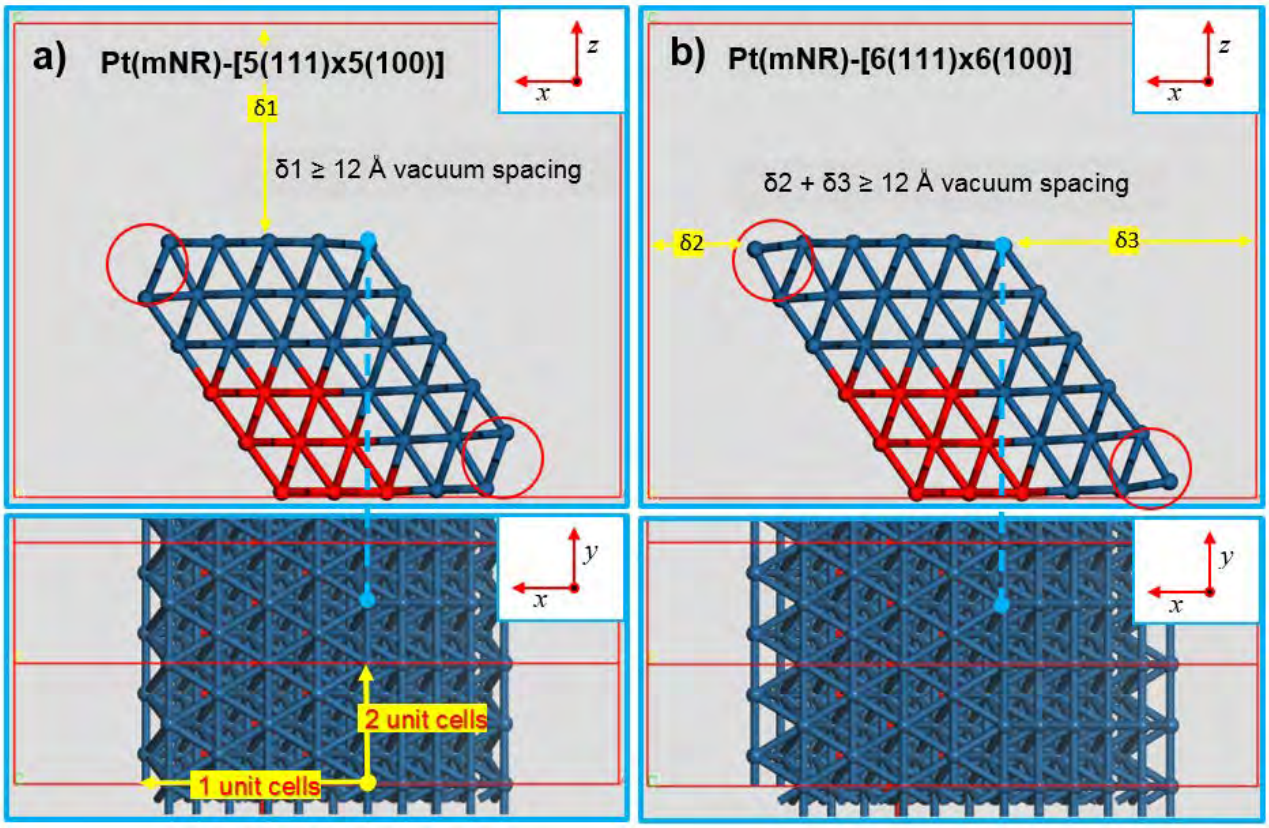

Figure 4.5: Illustration of rhombic nanorod models. (a) Projection onto the infinite dimension (top) and Pt(111) terrace-surface normal view (bottom) of a Pt(mNR)-[5(111)×5(100)] nanorod model. (b) Projection onto the infinite dimension (top) and Pt(111) terrace-surface normal view (bottom) of a Pt(NR)-[6(111)×6(100)] nanorod model. Red and blue spheres represents fixed and relaxed Pt atoms during all geometry optimization calculations, respectively.

The construction of the rhombic nanorod model follows from modifications of a hexagonal nanorod model. The relationship between the two models is demonstrated in Figure 4.6. Since the aim of this study is to investigate the activity of nanorod edges for the purpose of gaining insight into the activity of edge sites found on cuboctahedral nanoparticles, edge E-A in Figure 4.6b is an ideal edge model. Furthermore, the Pt(111)-Pt(100) terrace intersection angle at this edge is equal to that found in cuboctahedral model shape of fcc platinum nanoparticles (125.26 °). For the same number of atomic rows along each nanorod terrace, a rhombic nanorod model will have a much smaller number of atoms than a hexagonal nanorod model. To illustrate the latter, a hexagonal nanorod with 6 atomic rows along each terrace has a total of 183 atoms compared to the Pt(mNR)-[5(111)×5(100)] nanorod model (rhombic) which has 68 atoms. Therefore, in the present study only rhombic nanorod models were considered.

To determine a suitable number of layers to be relaxed in rhombic nanorod models, full geometry relaxation (with all atoms relaxed) of a hexagonal nanorod, shown in Figure 4.6a, was performed. The change in interlayer spacing relative to bulk interlayer spacing, Δd_{ij} where i and j are neighbouring atomic layers, is reported in Table 4.1. A 3.0% and 0.8% expansion of the first and second Pt(111) facet interlayer spacings, along line−A in Figure 4.6a, is observed. This is ca. 1% more than the observed expansion of a Pt(111) slab model with 3 atomic layers relaxed. Between the first and second Pt(100) interlayer spacing, along line−B in Figure 4.6a, a 2.6% and 2.0% contraction and expansion was observed, respectively. While the contraction of the first interlayer spacing was relatively similar to that observed on Pt(100) slab models with 3 atomic layers relaxed, the expansion of the second interlayer spacing was observed to be much larger in magnitude than that calculated for a Pt(100) slab model. The third, fourth and fifth Pt(111) and Pt(100) interlayer spacings were observed to have relatively smaller changes compared to the bulk interlayer spacing for the hexagonal nanorod model.

Considering these interlayer relaxations, it was concluded that relaxing only the top three layers (or shells) on a hexagonal nanorod model will result in a relatively well converged geometry (and energy). This is consistent with the layer relaxation optimization results for individual slab models (Chapter 3). Therefore, since the rhombic nanorod model, Figure 4.6b, is equivalent to a slice of a hexagonal nanorod as illustrated in Figure 4.6a, only the atoms marked in red will be fixed in their optimized bulk geometry (corresponding to an extended crystal). The interlayer spacings between the Pt(111) and Pt(100) layers of a Pt(mNR)-[5(111)× 5(100)] nanorod model are also presented in Table 4.1. A 4.3% (first interlayer spacing) and 1.4% (second interlayer spacing) expansion was observed between the relaxed Pt(111) layers of a Pt(mNR)-[5(111)× 5(100)] nanorod model. The third interlayer spacing of the Pt(111) and Pt(100) rhombic nanorod layers was observed to be relatively similar to the spacing on slab models. The expansion of the first and second interlayer spacings of the Pt(111) layers of a Pt(mNR)-[5(111)× 5(100)] nanorod model are a direct indication of the observed curvature along the Pt(111) nanorod terrace. This curvature was attributed to the presence of the edge atoms and their contraction. Along the Pt(100) nanorod terrace a relatively small curvature was observed, consistent with the data presented in Table 4.1. Noting that the E-A edge (Figure 4.6b) is the edge of interest in the present study, the objective of the optimization process was to generate a minimum sized system with well separated edges, i.e. reasonably small interaction between the E-A edge and the other two edges, E-A1 and E-A0.

4.3 Nanorod optimization

The nanorod edge model formed by the intersection of a Pt(111) and Pt(100) facet exposes unique high-symmetry adsorption sites, as illustrated in Figure 4.7. The adsorption on the edge-bridge (EB) site is expected to be the most interesting and strongly interacting due to its unique nature, i.e. composed of only low-coordinated platinum atoms present at Pt(111)-Pt(100) edge, compared to other high-symmetry sites on terrace regions. Therefore the first optimization approach was to systematically lengthen the initial nanorod model (Pt(mNR)-[5(111)×5(100)]) along the Pt(111) and Pt(100) facets, whilst observing the change in the adsorption energy of oxygen adsorbed on EB sites. This will enable the quantification of the influence of the E-A1 and E-A0 edge on the adsorption energy of atomic O and O_2 adsorbed on an EB site found at the E-A edge.

The interaction of edge E-A with edge E-A1 was investigated by looking at the change in the adsorption energy of atomic O and O_2, adsorbed on EB sites, with increasing Pt(111) terrace length. This was done by probing the EB sites of Pt(mNR)-[m(111)×5(100)] nanorod models, where m = [3, 4, 5, 6, 7], with atomic O and O_2. The calculated adsorption energies were then plotted against m (length of the Pt(111) nanorod terrace) as shown in Figure 4.8. Based on the data presented in Figure 4.8, it was observed that the variation in the adsorption energy of atomic O and O_2 is within 20 meV and 30 meV on nanorod models with $m \geq 5$, respectively. Considering the change in the number of atoms with increasing m (increasing m by one increases the total number of model atoms by 12) it was concluded that m = 5 will give a reasonable separation of the E-A and E-A1 edge. Applying a similar method as above, the interaction of the E-A and E-A0 edge was investigated. Atomic O and O_2 adsorbates were used to probe the EB sites of Pt(mNR)-[5(111)×n(100)] nanorod models with n = [3, 4, 5, 6, 7]. This resulted in a set of adsorption energies of atomic O and O_2 on EB sites as a function of the Pt(100) nanorod terrace length (Figure 4.9). Based on the data presented in Figure 4.9, the adsorption energy of atomic O is relatively constant for n = 4 and 5. A step change in the adsorption energy of atomic O was observed from n = 5 to n = 6. A similar behaviour was observed for the adsorption energy of O_2. Considering a nanorod model with n = 5 will results in the overestimation of the adsorption energy of both atomic O and O_2 of 70 meV and 40 meV compared to choosing nanorod models with n = [6 7] or more, respectively. Therefore, limited by computational efficiency, it was concluded that a nanorod model with n = 5 will give a reasonable separation of the E-A and E-A0 edges. In summary, the Pt(mNR)-[5(111)×5(100)] nanorod model was considered to be a reasonably sized model, in both computational efficiency and edge-edge interaction respects.

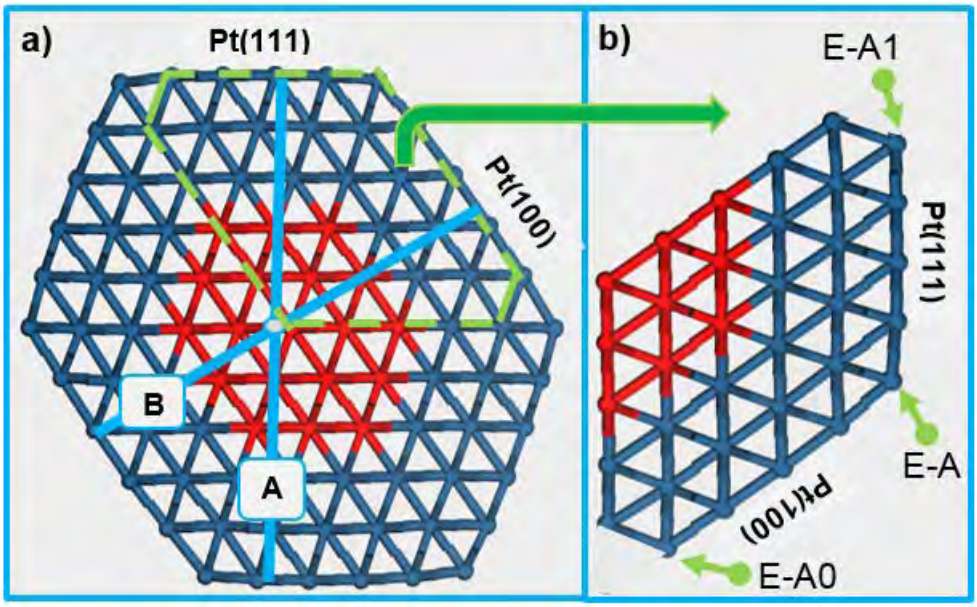

Figure 4.6: (a) Hexagonal nanorod model illustrating axis perpendicular to the terrace, Pt(111): line−A and Pt(100): line−B, and a segment corresponding to a rhombic nanorod model (dashed green line). (b) Pt(mNR)-[5(111)× 5(100)] rhombic nanorod model illustrating different edges. The edge of interest is illustrated by E-A while the adjacent edges to E-A are E-A1 and E-A0, along the Pt(111) and Pt(100) terraces, respectively. In (b) red and blue spheres represent Pt atoms which were fixed and relaxed in all geometry optimization calculations, respectively. All atoms in (a) were relaxed during geometry optimization calculations.

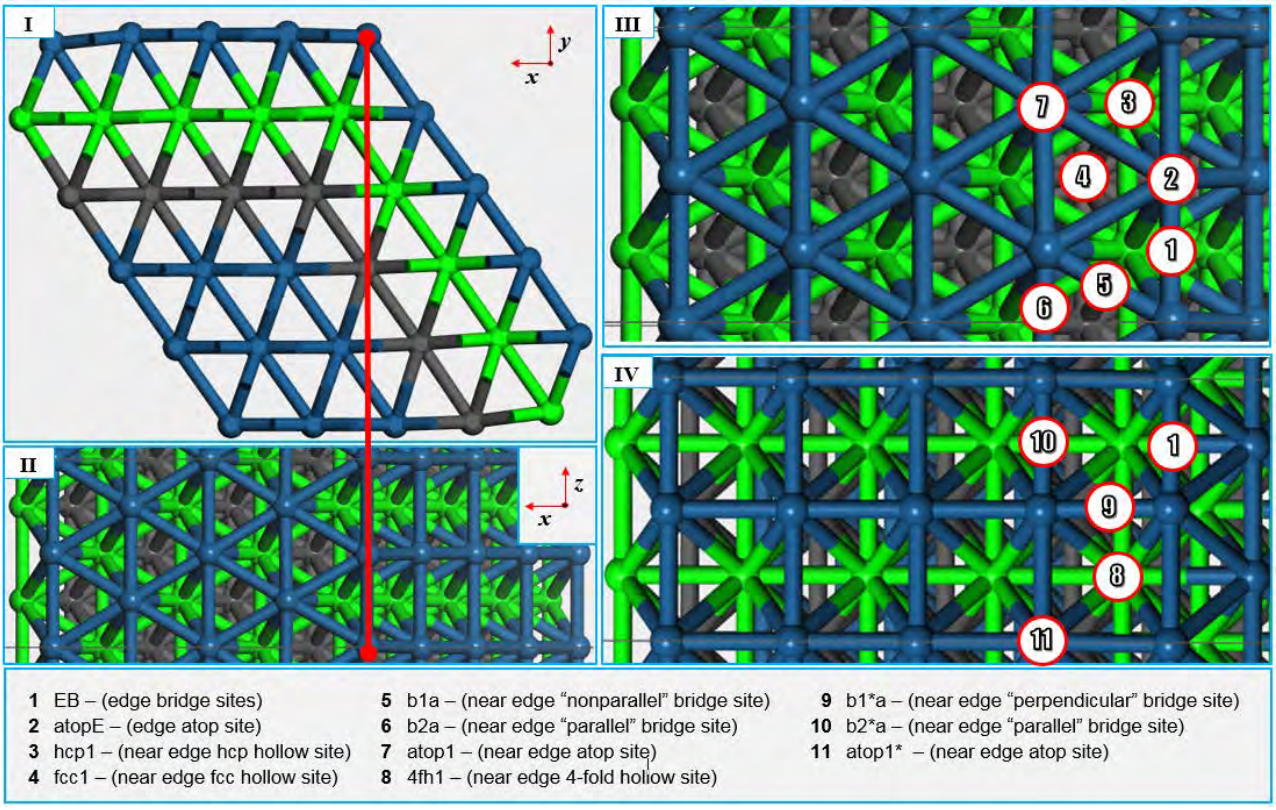

Figure 4.7: Illustration of high-symmetry adsorption sites on the model nanorod system. Side (I) and Pt(111) facet normal view (II) of a Pt(mNR)-[5(111)× 5(100)] nanorod model. (III) Pt(111) facet and (IV) Pt(100) facet sites near the E-A edge. The * on site labels is used for Pt(100) facet sites only (bridge and atop).

Table 4.1: Change in the interlayere spacings of relaxed slab models, Pt(111) and Pt(100), and nanorod models, rhombic and hexagonal. For nanorod models both the Pt(111)- and Pt(100)-layeres are presented.

Interlayer spacing between neighbouring layers, i and j, $[d_{ij}]$.						
Model system	slab models		Pt(mNR)-[5(111)× 5(100)]		hexagonal nanorod	
	Pt(111)	Pt(100)	Pt(111)	Pt(100)	Pt(111)	Pt(100)
d_{12} [Å]	2.33	1.94	2.39	1.97	2.36	1.93
d_{23} [Å]	2.29	1.98	2.32	2.03	2.31	2.03
d_{34} [Å]	2.28	1.99	2.28	1.99	2.29	2.00
d_{45} [Å]	2.29	1.99	2.30	1.99	2.29	1.98
d_{56} [Å]	2.29	1.99	2.29	1.99	2.29	1.98
% change in interlayer spacing relative to the bulk interlayer spacing $[\Delta d_{ij}]^a$.						
Δd_{12}	1.7%	-2.3%	4.3%	-0.9%	3.0%	-2.6%
Δd_{23}	-0.1%	-0.2%	1.4%	2.1%	0.8%	2.0%
Δd_{34}	-0.7%	-0.1%	-0.6%	0.3%	0.0%	0.4%
Δd_{45}	-[b]	-	-	-	-0.2%	-0.4%
Δd_{56}	-	-	-	-	0.1%	-0.2%

a $\Delta d_{ij} = d_{ij}|_{relaxed} - d_{ij}|_{bulk}$

b'-' corresponds to interlayer spacings between atomic layers fixed in their bulk optimized positions.

From the calculated convergence behaviour of the adsorption energies of atomic O and O_2 it was observed that using the Pt(mNR)-[5(111)×5(100)] nanorod model will result in uncertainties in adsorption energies of atomic O and O_2 of up to 70 meV and 40 meV, respectively. Use of larger nanorod models was not considered in this study since this results in increased computational cost, i.e. extending one facet by one atomic row increases the model size by 12 atoms (120 valence electrons). Considering both computational and model accuracy limitations, in this study the Pt(mNR)-[5(111)× 5(100)] nanorod model will be used to further investigate the interaction of atomic O and O_2 with edge and near edge sites. The considered nanorod model consists thus of 68 platinum atoms. The top three layers along each facet connected to the E-A edge (in Figure 4.6b) were allowed to relax during geometry optimization calculations. Therefore, this nanorod model consists of 50 relaxed atoms and 18 atoms fixed in their bulk optimized positions (corresponding to an extended crystal). This nanorod model was tested further as described below.

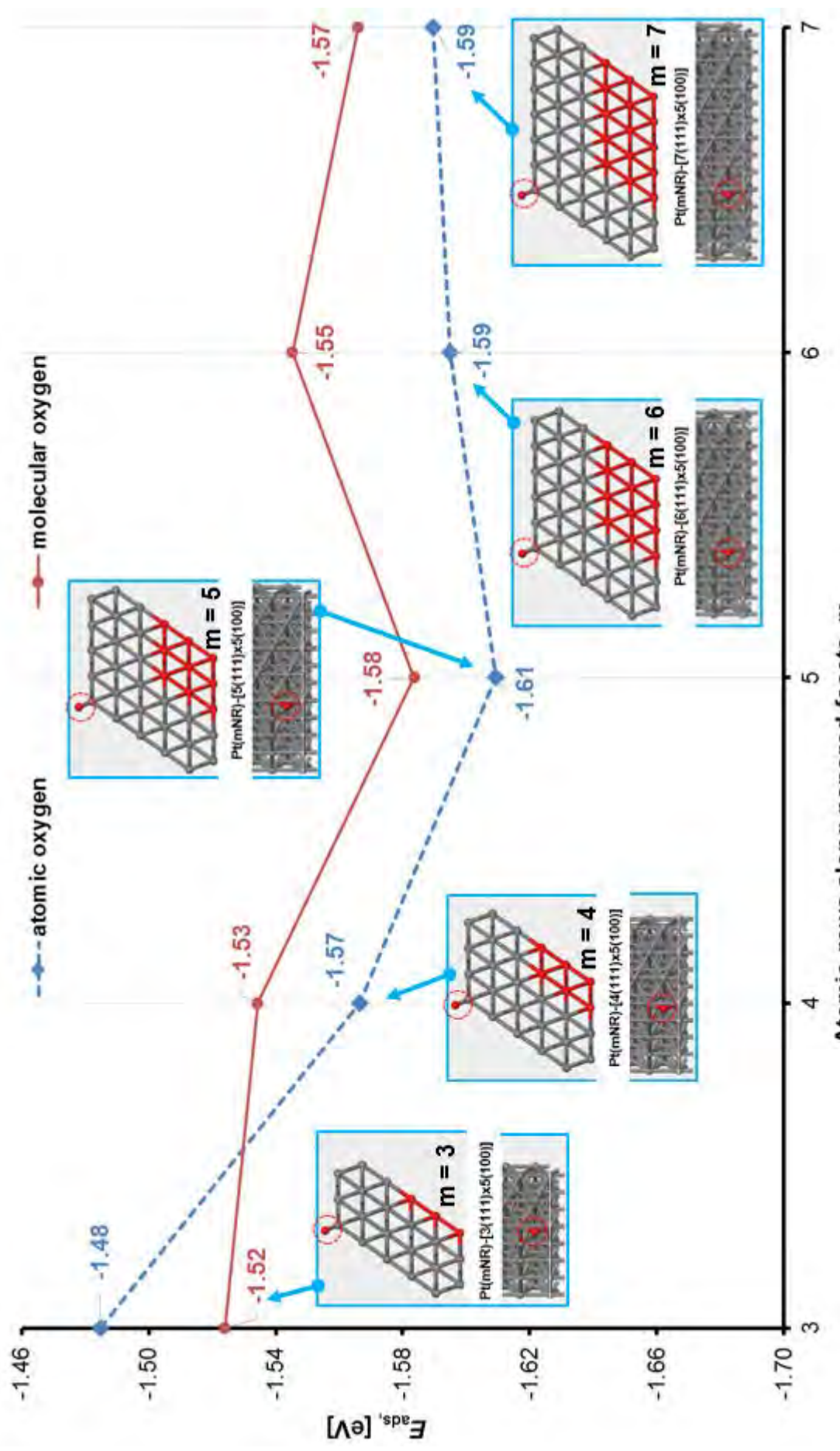

Figure 4.8: Adsorption energy of atomic O and O_2, on EB sites of Pt(mNR)-[m(111)×5(100)] nanorod models, as a function of m (number of atomic rows along the Pt(111) terrace). The adsorption energies were calculated with respect to $\frac{1}{2}O_2$ (equation 5.1) and O_2 (equation 3.2) in the gas phase for atomic O and O_2, respectively. For inserts on the plot area: side view (top), surface normal view (bottom). The grey and red spheres represents relaxed and fixed Pt atoms during geometry optimization calculations. Inside a red circle is an O atom on an EB site.

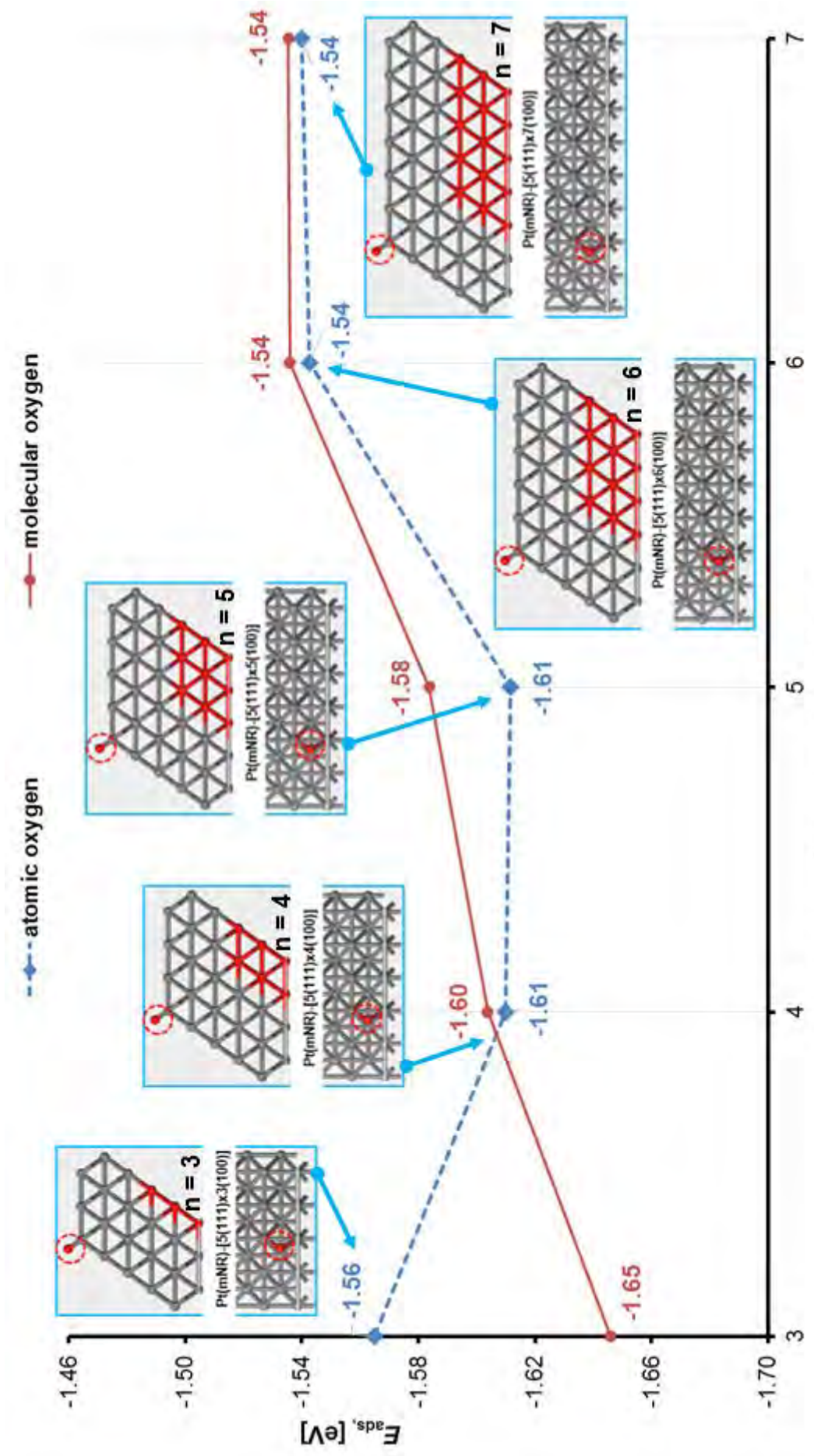

Figure 4.9: Adsorption energy of atomic O and O_2, on EB sites of Pt(mNR)-[5(111)×n(100)] nanorod models, as a function of n (number of atomic rows along the Pt(100) terrace). The adsorption energies were calculated with respect to $\frac{1}{2}O_2$ (equation 5.1) and O_2 (equation 3.2) in the gas phase for atomic O and O_2, respectively. For inserts on the plot area: side view (top), surface normal view (bottom). The grey and red spheres represents relaxed and fixed Pt atoms during geometry optimization calculations. Inside a red circle is an O atom on an EB site.

4.4 Nanorod model testing

To further estimate the error in the optimized nanorod model further tests were conducted; these included: (1) investigating the adsorption of atomic O on nanorod terrace sites vs. equivalent adsorption on slab models, and (2) investigating the effect of pre-adsorbed atomic oxygen on E-A1 edge on the adsorption energy of atomic oxygen adsorbed on the E-A edge (Figure 4.6b).

4.4.1 Adsorption on nanorod terrace sites compared to slab terrace sites

For a very large nanorod model with very wide terraces, it is expected that the atomic O interaction with central terrace sites will be similar to the equivalent interaction with extended slab models. The key problem with the nanorod model system is the possible interaction between the edges along a terrace, i.e. E-A and E-A1 or E-A0 illustrated in Figure 4.6b. The adsorption energy of atomic O on a central fcc (of the Pt(111) facet) and bridge (of the Pt(100) facet) site were calculated. These adsorption energies were compared to equivalent adsorption energies calculated using slab models (see Table 4.2). As shown in Figure 4.10, the terraces in a Pt(mNR)-[5(111)×5(100)] nanorod model are expected to have a p(2x4) surface unit cell size. However, due to the presence of the two edges and their relaxation during geometry optimization, it is anticipated that the region closest to the edges may behave differently to the surface of a p(2x4) extended slab model. Therefore an equivalent cell size for the Pt(mNR)-[5(111)×5(100)] nanorod model is anticipated to be within the p(2x2) and p(2x4) size range. The adsorption energies presented in Table 4.2 shows that for the Pt(111) nanorod facet the calculated adsorption energy of atomic O is lower than equivalent adsorption on Pt(111) slabs even at low coverage limit (0.25 ML corresponding to a p(2x2) unit cell size). The Pt(100) nanorod facet central bridge site (b2*b) gives a calculated adsorption energy of atomic O similar to that calculated on corresponding bridge sites of extended Pt(100)-p(2x4) slab model.

Table 4.2: Comparison of the adsorption energy of atomic O on central terrace sites of a Pt(mNR)-[5(111)× 5(100)] (mNR5) nanorod model with adsorpiton on extended slab models. All energies are reported relative to $\frac{1}{2}O_2$.

Site	$E_{ads,mNR5}$	$E_{ads,Pt(111)-p(2x2)}$	$E_{ads,Pt(111)-p(2x4)}$	$E_{ads,Pt(100)-p(2x2)}$	$E_{ads,Pt(100)-p(2x4)}$
Pt(111)					
fcc	-1.00	-1.14	-1.22	-	-
hcp	-0.66	-0.71	-0.81	-	-
Pt(100)					
bridge	-1.20	-	-	-1.14	-1.24

Comparing the adsorption energy of atomic O on a central fcc site (fcc2) of a Pt(mNR)-[5(111)× 5(100)] nanorod to adsorption on extended Pt(111) slabs shows that adsorption on the nanorod is weaker by 0.14 eV/O atom (Pt(111)-p(2x2)) and 0.22 eV/O atom (Pt(111)-p(2x4)). This is consistent with results reported by Ogawa *et al.* (2014) which showed an adsorption energy difference of 0.17 eV/O between adsorption on a central Pt(111) terrace fcc site of a modified Pt(211)[1] step-surface and extended Pt(111)-p(4x4) slab model (adsorption on the step surface terrace was weaker than on an extended slab). These observations indicate that the edges, on the nanorod, and steps, on Pt(211), influence the stability of adsorbates on the Pt(111)-terraces. Further remarks on this phenomena are presented in Chapter 6.

4.4.2 Effects of co-adsorption along the Pt(111) nanorod facet

Further tests was performed to quantify the extent of interaction of the E-A and E-A1 edge (Figure 4.6b). This was achieved by comparing the adsorption energy of atomic oxygen on an fcc1 site observed under two cases: (1) adsorption on a clean nanorod model and (2) adsorption on a nanorod

[1]The modified Pt(211) surface consists of a double step and 6 atomic rows along the Pt(111) terrace and is denoted by Pt(S)-[5(111)×2(100)] (Figure 4.2a)

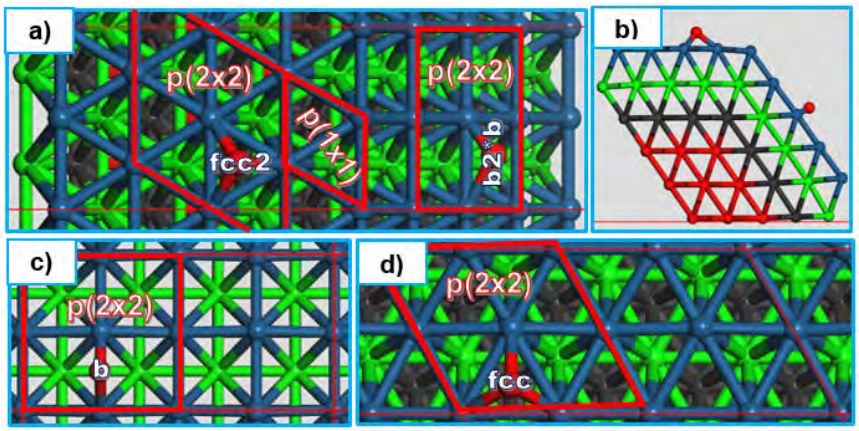

Figure 4.10: Comparison of the Pt(mNR)-[5(111)×5(100)] nanorod model terrace size with p(2x2) and p(2x4) surface sizes. (a) Pt(111) facet normal view and (b) side view of the Pt(mNR)-[5(111)×5(100)] nanorod model, respectively. Surface normal view of (c) Pt(100)-p(2x4) and (d) Pt(111)-p(2x4) slab models. In each model a p(2x2) unit cell is illustrated. The central Pt(111) and Pt(100) nanorod terrace sites are defined as fcc2 and b2*b, respectively.

model with atomic O already pre-adsorbed on the E-A1 EB site (see Figure 4.11). This was aimed at investigating the perturbation of electronic structure change from E-A1 to E-A. When these two edges are well separated it is anticipated that the effect or difference in the adsorption energies calculated in the presence and absence of co-adsorbed atomic O will be within model error. From the calculations it was found that the difference was ca. 50 meV, stronger when atomic oxygen is pre-adsorbed on the E-A1 EB site. This difference is within the average variation observed during optimization of multiple model parameters, i.e. slab thickness, terrace lengths. Therefore, the Pt(mNR)-[5(111)×5(100)] nanorod model was concluded to be a reasonably converged model with reasonable separation of edges.

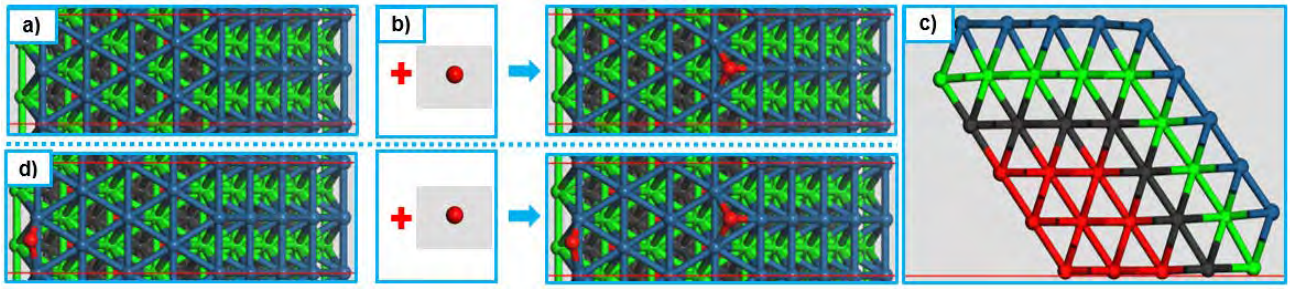

Figure 4.11: Illustration of atomic O adsorption on a clean Pt(mNR)-[5(111)×5(100)] nanorod fcc1 site (a+b). Illustration of atomic O adsorption on an fcc1 site of a Pt(mNR)-[5(111)×5(100)] nanorod with atomic O pre-adsorbed on the EB site near the E-A1 edge (d). Side view of a Pt(mNR)-[5(111)×5(100)] nanorod (c).

Chapter 5

Interaction of oxygen with platinum surfaces

5.1 Introduction

The adsorption of molecular and atomic oxygen is one of the key reaction steps in the ORR mechanism. At a steady state operation of a fuel cell a constant rate of O_2 adsorption and dissociation has to be maintained. Depending on the type of metal surface, O_2 either adsorbs dissociatively or as a molecular precursor to a dissociated state (Gee & Hayden, 2000; van der Niet *et al.*, 2010; Duan & Wang, 2013; Badan *et al.*, 2015; Jacobse *et al.*, 2015). The latter is a key motivation for investigating the interaction of both atomic O and O_2 with platinum surfaces. Furthermore, the adsorption energy of atomic O on metal surfaces has been used as a key ORR activity descriptor in a number of studies (Nørskov *et al.*, 2004; Greeley *et al.*, 2007; Karlberg *et al.*, 2007; Friebel *et al.*, 2012; Stephens *et al.*, 2012; Viswanathan *et al.*, 2012; Hansen *et al.*, 2014). Nørskov *et al.* (2004) derived a simple ORR activity expression for {111} surface models of different metals (equation 1.7). Using this expression they showed that the ORR activity scales with both the adsorption energy of O and OH. Moreover, their model predicted platinum to be the most active pure metal for the ORR process. Due to this scaling behaviour it is of some importance to investigate the interaction of atomic O with different surface features relevant to stable platinum nanoparticles. This chapter therefore investigates the adsorption of atomic O and O_2 on Pt(111) and Pt(100) slab models and on nanorod edge sites.

5.2 Computational methods

5.2.1 Computational parameters

First-principles periodic density functional theory (DFT) calculations were performed using the Vienna *Ab-Initio* Simulation Package (VASP)(Kresse & Hafner, 1993, 1994a; Kresse & Furthmüller, 1996a,b) with the projector augmented wave (PAW) potential method (Blöchl, 1994; Kresse & Joubert, 1999) and the Perdew-Burke-Ernzerhof (PBE) (Perdew *et al.*, 1996) exchange-correlation functional. To calculate the adsorption energy of atomic and molecular oxygen on platinum surfaces, geometry optimization calculations were performed using the Methfessel-Paxton (MP) method to the first order with a smearing width of 0.1 eV. The total energies were extrapolated to $k_BT = 0$ eV, corresponding to zero smearing. For all calculations the cut-off energy used was 400 eV whilst the k-point grid varied for each model system: for slab models, Pt(111)-p(2x2) and Pt(100)-p(2x2), a 5x5x1 k-point grid was used whilst for the nanorod model, Pt(mNR)-[5(111)× 5(100)] with two primitive surface unit cells along the infinite y-dimension (Figure 4.5), a 1x5x1 grid was used. Further details of the latter surface models are given in Chapter 3 (Pt(111) and Pt(100) slab models) and Chapter 4 (Pt(mNR)-[5(111)× 5(100)] nanorod model).

5.2.2 Adsorption energy definitions

The adsorption energy of atomic oxygen relative to atomic O in the gas phase ($E_{O,\ ads}$) was defined in equation 3.1. While the adsorption energy of atomic O relative to $\frac{1}{2}O_2$ in the gas phase ($E_{O,\ ads/\frac{1}{2}O_2}$) is given by equation 5.1,

$$E_{O,\ ads/\frac{1}{2}O_2} = E_{slab+O} - E_{slab} - \frac{1}{2}E_{O_2,gas} \tag{5.1}$$

where E_{slab+O}, E_{slab} and $E_{O_2,gas}$ are total energies of the slab with atomic oxygen adsorbed on a model substrate (slab or nanorod), clean model substrate (slab or nanorod) and molecular oxygen in the gas phase, respectively. This calculation results in adsorption energies which are referenced to the energy of half O_2 in the gas phase. Zero-point energy corrected adsorption energies are calculated using equation 5.2,

$$E^{ZPE}_{O,\ ads/\frac{1}{2}O_2} = \left(E_{slab+O} + \frac{1}{2}h\Sigma\upsilon_i\right) - E_{slab} - \frac{1}{2}\left(E_{O_{2,gas}} + \frac{1}{2}h\Sigma\upsilon_{O_2}\right) \tag{5.2}$$

where h and υ_i are Planck's constant and vibrational frequencies of mode i, respectively; υ_{O_2} is the stretching frequency of a gas phase O_2 molecule. Vibrational frequencies were calculated as described in Subsection 2.4.3.

5.2.3 Reference state energy

The gas phase electronic energy of atomic O and O_2 was calculated as described in Section 2.6. For atomic O two electronic energies were obtained depending on the computational method used. Using a method recommended in the VASP manual (Kresse *et al.*, 2014), the ground state energy of atomic O was calculated to be -1.903 eV. When using a computational set-up similar to the one used to calculate the energy of adsorbed states (subsection 2.4.3) the total energy of atomic O was calculated to be -1.539 eV (see Section 2.6 for further details). In this study, the electronic energy of atomic O of -1.903 eV was used as it corresponds to the lowest and correct electronic state (ground state energy). The electronic energy of O_2 is given in Table 2.4, column 2 (excludes zero point energy contribution) and column 3 (includes zero point energy contribution). DFT correction total energy of O_2 (column 4 of Table 2.4) is not used in further sections of this study.

5.2.4 Definitions of geometric properties

The adsorption properties, including geometric structures, of atomic O and O_2 on different platinum surface sites are considered in this chapter. For atomic O adsorption, the important properties include, Pt-O bond lengths (d_{Pt-O}) given in Angstrom (Å) and the perpendicular height above the surface (Δd_{h1}). For adsorption on slab surface and on nanorod terrace sites, Δd_{h1} is defined as the vertical (parallel to the surface normal vector) distance of the O atom above the surface plane. The latter is illustrated for all geometric structure presented in the following sections. The surface plane is defined as a plane containing the coordinates of the Pt atom(s) which are involved in the adsorption and also has the same surface normal vector as the surface or nanorod facet. For nanorod edge-bridge (EB) adsorption states, Δd_{h1} refers to the perpendicular (shortest) distance from the edge atomic row to the O atom.

For O_2 adsorption in addition to d_{Pt-O}, the O-O bond length (d_{O-O}) is important in describing different adsorption states. Furthermore, each O atom in O_2 may have a different perpendicular height (distance) above a surface plane or from an edge atomic row. Therefore, the shorter of the two perpendicular heights is defined as Δd_{h1} whilst the other is defined as Δd_{h2}. For O_2 adsorption the angle formed between surface plane and the axis of the O-O bond is defined as α_{O-O}. Two other angles are important in describing adsorption on nanorods, especially on the EB sites. These are θ and β which are the tilt of the adsorbate from the normal of a Pt(111) and a Pt(100) nanorod facet (see Figure 5.7). The relationship between the angles is given by $\theta - \beta = 55°$.

5.3 Atomic O adsorption on platinum surfaces

The interaction of atomic O with different platinum surfaces was investigated by considering adsorption on different high-symmetry sites. On Pt(111) surfaces the high-symmetry sites considered were fcc, hcp, bridge and atop (Figure 3.3), whilst on Pt(100) surfaces the bridge, 4-fold hollow and atop sites (Figure 3.8) were considered. The high-symmetry adsorption sites on the nanorod (near-edge) were described in Figure 4.7. In the following subsections the equilibrium geometries and adsorption energies of atomic O on the above high-symmetry sites are presented.

5.3.1 Atomic O on Pt(111)

Considering a number of initial starting positions of atomic O, in the vicinity of the high-symmetry sites, geometry optimization calculations were performed to obtain equilibrium properties of atomic O on high-symmetry sites. It was observed that whilst the fcc, hcp and atop high-symmetry sites had an equilibrium state where the net force acting on relaxed atoms was below 0.02 eV/Å, attempts to obtain a similar equilibrium state for atomic O on a bridge site converged to either an fcc or hcp high-symmetry site. The latter is consistent with a number of previous studies (Ford *et al.*, 2010; Madala, 2013). Furthermore, it has been shown that the transition state for atomic O diffusion from an fcc to an hcp site is a bridge state (Ogawa *et al.*, 2013). The equilibrium fcc, hcp and atop states were confirmed to be stable adsorption states as confirmed with a vibrational analysis for each converged geometry which showed that all vibrational modes were real, indicative of a local minimum on the potential energy surface (PES).

fcc site

The geometric properties of atomic O adsorption on fcc sites are presented in Figure 5.1 and Table 5.1. This adsorption state was observed to be highly symmetrical as all the Pt-O bond lengths were calculated to be 2.041 Å. The symmetry was broken on a Pt(111)-p(2x4) slab where two of the Pt-O bonds remain unchanged whilst one increases by ca. 0.02 Å (see Table 5.1). It was further observed that at low coverage atomic O adsorbs much closer to the surface. This was observed from a ca. 0.03 Å shift closer to the surface plane on a Pt(111)-p(2x4) relative to a Pt(111)-p(2x2) slab model (see Table 5.1). The calculated equilibrium geometry of atomic O on fcc sites is consistent with that reported in literature (Gu & Balbuena, 2007; Ogawa *et al.*, 2013).

The adsorption energy of atomic O on fcc sites was calculated to be -1.14 eV/$\frac{1}{2}O_2$ and -1.21 eV/$\frac{1}{2}O_2$ on the Pt(111)-p(2x2) and Pt(111)-p(2x4) slab model, respectively (see Table 5.4). The higher adsorption energy at a 0.125 ML coverage is consistent with the observed decrease in the height of atomic O above the surface (Δd_{h1}). Good agreement between the calculated adsorption energy of atomic O on fcc sites and that reported in the literature was observed (Qi & Li, 2012; Madala, 2013). Although Gu & Balbuena (2007) and Ogawa *et al.* (2013) used the same potential−functional combination as the present study, they reported stronger adsorption of atomic O on an fcc site than observed in the present study. The adsorption energy of atomic O, on an fcc site, calculated in the present study was 0.45 eV weaker than that reported by Gu & Balbuena (2007) and Ogawa *et al.* (2013) for the same adsorption state. The studies by Gu & Balbuena (2007) and Ogawa *et al.* (2014) considers atomic O in the gas phase as a reference state. The latter difference was suspected to be due to the use of different reference state energies (subsection 2.6.5).

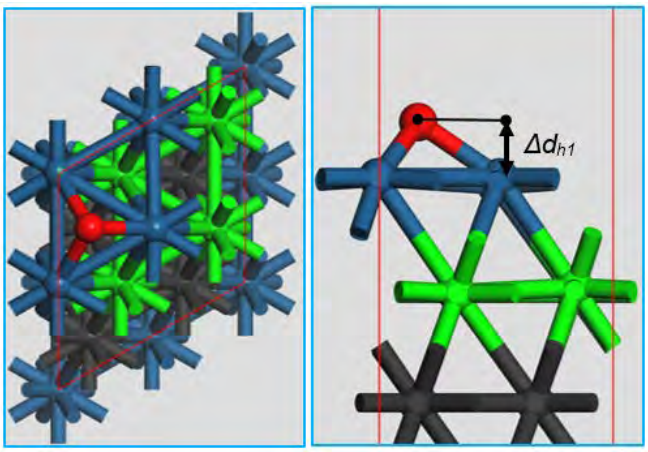

Figure 5.1: Equilibrium geometry of atomic O on an fcc site of a Pt(111)-p(2x2) slab model. Surface normal view (left) and side view (right). Δd_{h1} is the hight of atomic O above the surface plane.

Table 5.1: Equilibrium geometric properties of atomic O on fcc sites of Pt(111) slab models.

site: fcc	Pt(111)-p(2x2)	Pt(111)-p(2x4)
Δd_{h1} [Å]		
This study	1.149	1.116
d_{Pt-O} [Å]		
This study	2.041	2.042, 2.043 2.059
Literature	2.04[a]	2.05[b]

a Pt(111)-p(2x2), PAW−PBE, VASP code (Gu & Balbuena, 2007)

b Pt(111)-p(4x4), PAW−PBE, VASP code (Ogawa *et al.*, 2013)

hcp site

The geometric properties of atomic O adsorption on hcp sites are presented in Figure 5.2 and Table 5.2. As was observed on fcc sites, atomic O adsorption on hcp site results in a three fold coordinated state with equal Pt-O bond lengths of 2.053 Å. The adsorption height of atomic O above the Pt(111)-p(2x2) surface (Δd_{h1}) was calculated to be 1.197 Å. At low coverage, Pt(111)-p(2x4), Δd_{h1} decreased to 1.152 Å. The calculated Pt-O bond lengths remained relatively unchanged even at low coverage, i.e. adsorption on a Pt(111)-p(2x4) hcp site (Table 5.2). The adsorption energy of atomic O was calculated to be -0.71 eV/$\frac{1}{2}O_2$ and -0.81 eV/$\frac{1}{2}O_2$ for adsorption on an hcp site of a Pt(111)-p(2x2) and Pt(111)-p(2x4) slab model, respectively (see Table 5.4). The calculated adsorption energies compared well with previous calculations by Madala (2013). The adsorption energy of atomic O, on an hcp site, calculated in the present study was 0.48 eV weaker than that reported by Gu & Balbuena (2007) and Ogawa *et al.* (2013) for the same adsorption state. The latter difference was suspected to be due to the use of different reference state energies (subsection 2.6.5).

Table 5.2: Equilibrium geometric properties of atomic O on hcp sites of Pt(111) slab models.

site: hcp	Pt(111)-p(2x2)	Pt(111)-p(2x4)
Δd_{h1} [Å]		
This study	1.197	1.152
d_{Pt-O} [Å]		
This study	2.053	2.052, 2.053, 2.050
Literature	2.05[a]	2.05[b]

a Pt(111)-p(2x2), PAW−PBE, VASP code (Gu & Balbuena, 2007)

b Pt(111)-p(4x4), PAW−PBE, VASP code (Ogawa *et al.*, 2013)

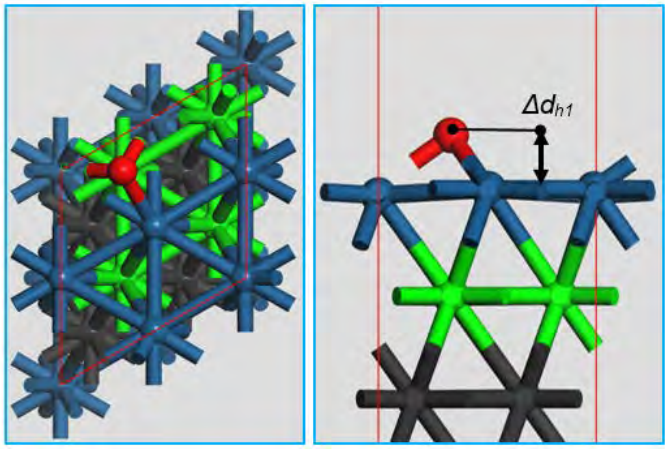

Figure 5.2: Equilibrium geometry of atomic O on an hcp site of a Pt(111)-p(2x2) slab model. Surface normal view (left) and side view (right). Δd_{h1} is the hight of atomic O above the surface plane.

atop site

The equilibrium geometric structure of atomic O on a Pt(111)-p(2x2) atop site is presented in Figure 5.3. The equilibrium Pt-O bond axis was observed to be parallel to the surface normal vector. Therefore, the hight of atomic O above the Pt(111) surface plane is equivalent to the Pt-O bond length which was calculated to be 1.833 Å, in good agreement with 1.83 Å and 1.84 Å reported by Gu & Balbuena (2007) and Ogawa *et al.* (2013), respectively. Even at a low coverage of 0.125 ML, i.e. on a Pt(111)-p(2x4) atop site, the Pt-O bond length remained relatively constant (decreased by a mere 0.004 Å). The adsorption of atomic O on an atop site was observed to be an endothermic process relative to $\frac{1}{2}O_2$ in the gas phase. This adsorption precess had an adsorption energy of 0.23 eV/$\frac{1}{2}O_2$ and 0.11 eV/$\frac{1}{2}O_2$ at 0.25 ML and 0.125 ML coverage, respectively (see Table 5.4).

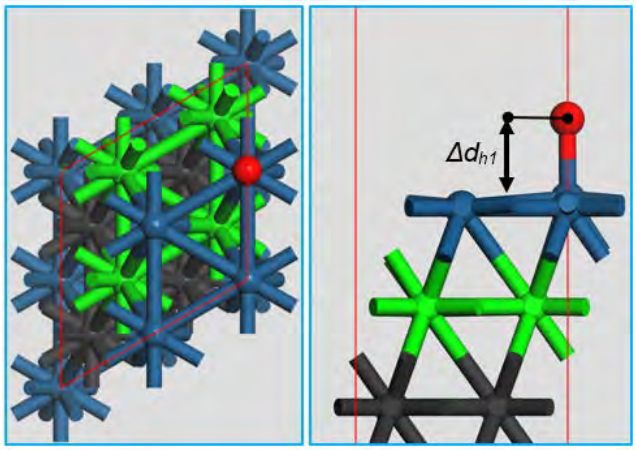

Figure 5.3: Equilibrium geometry of atomic O on an atop site of a Pt(111)-p(2x2) slab model. Surface normal view (left) and side view (right). Δd_{h1} is the hight of atomic O above the surface plane.

unstable adsorption states

For atomic O adsorption on Pt(111) surfaces it was observed that only one of the high-symmetry adsorption sites, bridge, was unstable. It was observed that depending on the starting position the geometry converged to either an fcc or hcp state. This is illustrated in Figure B.1 (Appendix B.1.1), where atomic O converges to an fcc site. This adsorption state (atomic O on a Pt(111) bridge site) has been reported to be a transition state for atomic O diffusion from an fcc state to an hcp state (and vice versa) (Ogawa *et al.*, 2013).

Discussion

On a Pt(111)-p(2x2) surface atomic O preferentially adsorbs on an fcc site with an adsorption energy of -1.14 eV/$\frac{1}{2}O_2$. The latter adsorption state was 0.43 eV more stable than the hcp adsorption state, where atomic O adsorbs with the second strongest adsorption strength, -0.71 eV/$\frac{1}{2}O_2$. The calculated relative difference between the stability of atomic O on fcc and hcp site, 0.43 eV, was found to be consistent with 0.40 eV (literature) calculated using the PAW−PBE potential−functional combination (Gu & Balbuena, 2007; Ogawa *et al.*, 2014). Both Gu & Balbuena (2007) and Ogawa *et al.* (2013) reported adsorption energies which are consistently larger (more stable adsorption), by ca. 0.45 eV than the adsorption energies of atomic O calculated in this study. Although Ogawa *et al.* (2014) considered a much lower coverage (0.0625 ML), the coverage considered by Gu & Balbuena (2007) was the same as the one used in this study, 0.25 ML. Furthermore, both Gu & Balbuena (2007) and Ogawa *et al.* (2013) reported equilibrium geometric properties of atomic O similar to those calculated in this study. Therefore, the only potential cause of the former difference in adsorption energies of atomic O, was suspected to be in the total energy of atomic O in the gas phase (which was used as a reference state in this study and also in the studies by Gu & Balbuena (2007) and Ogawa *et al.* (2013)). It was observed in this study, that depending on the predicted orbital occupancy of the converged electronic structure of atomic O, the total energy of atomic O can vary from -1.54 eV (with non-integer orbital occupancy) to -1.90 eV (with integer orbital occupancy, used in this study). Since both Gu & Balbuena (2007) and Ogawa *et al.* (2014) do not report the electronic structure of their reference state, the differences between the present study and their calculations were expected to be as high as 0.36 eV depending on the electronic structure of atomic O which the total energy of the reference state was based.

The calculated adsorption energies, -4.16 eV/O (fcc), -3.74 eV/O (hcp) and -2.79 eV/O (atop), were observed to be ca. 0.3 eV more stable than the adsorption energies reported by Ford *et al.* (2005) who used the PAW−PW91 potential−functional combination and the DACAPO code (see Table 5.4). The latter difference was suspected to be due to the use of different computational setup. Vibrational analysis for each optimized geometry confirmed all three states, fcc, hcp and atop, to be stable states at a minimum of the potential energy surface (see Table 5.3). The calculated vibrational mode (perpendicular to the surface) of oxygen on an fcc site, 451 cm^{-1}, is in reasonable agreement with that reported by Ford *et al.* (2005), 442 cm^{-1}, and that measured by Gland *et al.* (1980), 490 cm^{-1}. In summary, the calculated equilibrium geometric and energetic properties of atomic O on Pt(111)-p(2x2) were found to be in good agreement with previous studies. Furthermore, decreasing atomic O coverage resulted in an increase in adsorption energy of atomic O of ca. 0.1 eV across all studied adsorption states.

Table 5.3: Calulated vibrational frequencies of atomic O on Pt(111) high-symmetry sites

Adsorption site:	fcc	hcp	atop
υ_i [cm^{-1}]	451, 387, 385	436, 321, 320	686, 38, 22
Lit.:	442[a]		
Exp.:	490[b]		

a Pt(111)-p(2x2), PAW−PW91, DACAPO code (Ford *et al.*, 2005)

b EELS measurements of Gland *et al.* (1980)

5.3.2 Atomic O on Pt(100)

The high-symmetry adsorption sites on Pt(100) surfaces were probed with atomic O to obtain equilibrium adsorption properties. Geometry optimization calculations with initial states in the vicinity of the high-symmetry sites, converged to stable adsorption states. The equilibrium adsorption states, 4-fold hollow, bridge and atop, were confirmed to be stable states at a local minimum of the potential energy surface (PES).

Table 5.4: Adsorption energy of atomic O on high-symmetry sites of the Pt(111)-p(2x2) slab model.

reference state	$\frac{1}{2}O_2$	$\frac{1}{2}O_2$ + ZPE	Atomic O
Units	[eV/$\frac{1}{2}O_2$]	[eV/$\frac{1}{2}O_2$]	[eV/O]
Adsorption site: fcc			
This study	-1.14	-1.11	-4.16
Literature		-1.18[a], -1.10[f]	-4.61[b], -3.96[c]
			-3.87[d], -4.62[e]
Experimental			-3.7[g]
Adsorption site: hcp			
This study	-0.71	-0.69	-3.74
Literature		-0.70[f]	-3.43[d], -4.21[b], -4.22[e]
Adsorption site: atop			
This study	0.23	0.23	-2.79
Literature			-2.46[d], -3.35[e]

a Pt(111)-p(2x2), PAW−PBE, VASP code, ZPE corrected (Qi & Li, 2012)

b Pt(111)-p(2x2), PAW−PBE, VASP code (Gu & Balbuena, 2007)

c Pt(111)-p(2x2), USPP−PBE, VASP code, ZPE corrected (Duan & Wang, 2013)

d Pt(111)-p(2x2), PAW−PW91, DACAPO code (Ford *et al.*, 2005)

e Pt(111)-p(4x4), PAW−PBE, VASP code (Ogawa *et al.*, 2013)

f Pt(111)-p(2x2), PAW−PBE, VASP code (Madala, 2013)

g thermal desorption spectroscopy measurements of Gland *et al.* (1980)

bridge site

The geometric properties of atomic O adsorption on Pt(100) bridge sites are presented in Figure 5.4 and Table 5.5. On the Pt(100)-p(2x2) and Pt(100)-p(2x4) bridge sites, the adsorption state of atomic O consists of equal Pt-O bond lengths of 1.950 Å and 1.945 Å, respectively. The observed change at these two coverages was the vertical height of atomic O from the Pt(100) surface plane. At low coverage (0.125 ML) atomic O was observed to be 0.013 Å closer to the surface plane than observed at high coverage (0.25 ML). The calculated Pt-O bond lengths were consistent with literature (Gu & Balbuena, 2007; Ogawa *et al.*, 2013). The adsorption energy of atomic O was calculated to be -1.14 eV/$\frac{1}{2}O_2$ and -1.25 eV/$\frac{1}{2}O_2$ on bridge sites of a Pt(100)-p(2x2) and Pt(100)-p(2x4) slab model, respectively (see Table 5.7). Atomic O adsorption on a Pt(100)-p(2x4) bridge site is 0.11 eV more stable than adsorption on a Pt(100)-p(2x2) bridge site. The calculated adsorption energy of atomic O at 0.25 ML coverage (-1.14 eV/$\frac{1}{2}O_2$ or -4.17 eV/O) is consistent with -1.14 eV/$\frac{1}{2}O_2$ and -4.20 eV/O reported by Qi & Li (2012) and Liu & Evans (2010) for adsorption at 0.25 ML, respectively. Comparison with the results of Gu & Balbuena (2007) and Ogawa *et al.* (2013), showed a deviation of 0.45 eV as was observed in the case of adsorption on Pt(111) sites.

Table 5.5: Equilibrium geometric properties of atomic O on bridge sites of Pt(100) slab models.

site: bridge	Pt(100)-p(2x2)	Pt(100)-p(2x4)
Δd_{h1} [Å]		
This study	1.286	1.273
d_{Pt-O} [Å]		
This study	1.950	1.945
Literature	1.95[a]	1.95[b]

a Pt(111)-p(2x2), PAW−PBE, VASP code (Gu & Balbuena, 2007)

b Pt(111)-p(4x4), PAW−PBE, VASP code (Ogawa *et al.*, 2013)

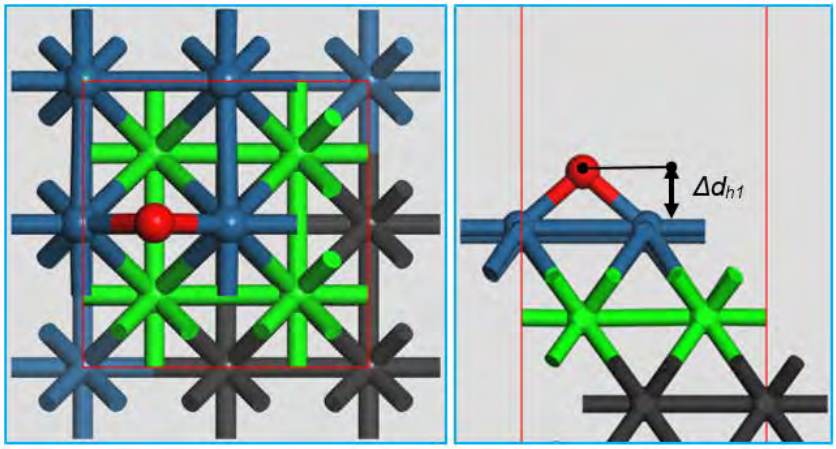

Figure 5.4: Equilibrium geometry of atomic O on an bridge site of a Pt(100)-p(2x2) slab model. Surface normal view (left) and side view (right). Δd_{h1} is the hight of atomic O above the surface plane.

4-fold hollow site

The equilibrium geometric properties of atomic O adsorption on Pt(100) 4-fold hollow sites are presented in Figure 5.5 and Table 5.6. On 4-fold hollow sites atomic O is coordinated to four surface platinum atoms. The equilibrium adsorption geometry of atomic O on 4-fold hollow sites was found to have Pt-O bond lengths ca. 2.22 Å and 2.23 Å on Pt(100)-p(2x2) and Pt(100)-p(2x4) slab surfaces, respectively. The vertical height of atomic O above the Pt(100) surface was observed to be 0.008 Å shorter on Pt(100)-p(2x4) than on Pt(100)-p(2x2) 4-fold hollow sites. The calculated Pt-O bond lengths were in good agreement with those reported by Ogawa *et al.* (2013). The adsorption energy of atomic O on a Pt(100)-p(2x2) 4-fold hollow site is presented in Table 5.7. The adsorption energy of atomic O was calculated to be -0.78 eV/$\frac{1}{2}O_2$ and -1.45 eV/$\frac{1}{2}O_2$ on 4-fold hollow sites of the Pt(100)-p(2x2) and Pt(100)-p(2x4) slab models, respectively. Based on the latter it was observed that on the Pt(100)-p(2x4) atomic O is more stable (0.20 eV) on a 4-fold hollow site than is on a bridge site (see Table 5.7). The calculated adsorption energy of atomic O on the 4-fold site at 0.25 ML coverage, -3.80 eV/O, was observed to be in good agreement with with -3.87 eV/O reported by Liu & Evans (2010) based on the same computational setup as the present study (Table 5.7).

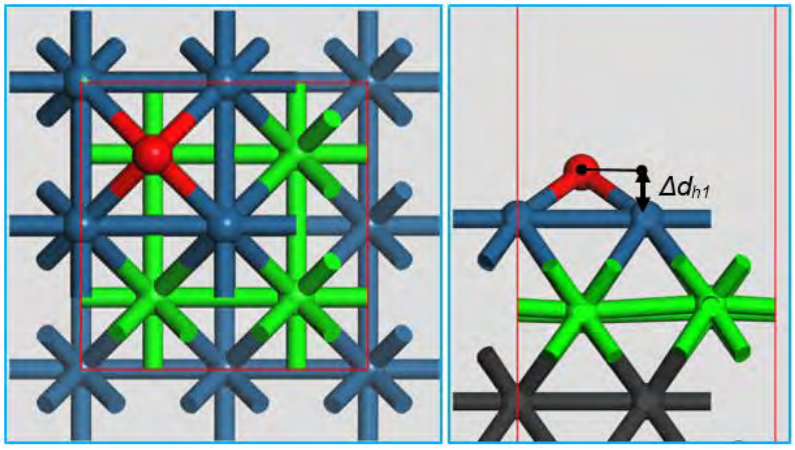

Figure 5.5: Equilibrium geometry of atomic O on a 4-fold hollow site of a Pt(100)-p(2x2) slab model. Surface normal view (left) and side view (right). Δd_{h1} is the hight of atomic O above the surface plane.

Table 5.6: Equilibrium geometric properties of atomic O on 4-fold hollow sites of Pt(100) slab models.

site: 4-fold hollow	Pt(100)-p(2x2)	Pt(100)-p(2x4)
Δd_{h1} [Å]		
This study	1.015	1.007
d_{Pt-O} [Å]		
This study	2.221	2.228
Literature	2.22[a]	

a Pt(111)-p(2x2), PAW−PBE, VASP code (Gu & Balbuena, 2007)

atop site

The equilibrium geometric structure of atomic O on an atop site of the Pt(100)-p(2x2) surface is presented in Figure 5.6. It was observed that atomic O adsorbs parallel to the Pt(100) surface normal with a Pt-O bond length of 1.818 Å and 1.815 Å on Pt(100)-p(2x2) and Pt(100)-p(2x4) atop sites, respectively. The latter adsorption geometry is in good agreement with literature (Gu & Balbuena, 2007; Ogawa *et al.*, 2013). The adsorption energy was calculated to be -0.11 eV/$\frac{1}{2}O_2$ and -0.19 eV/$\frac{1}{2}O_2$ on Pt(100)-p(2x2) and Pt(100)-p(2x4) atop sites, respectively. This was observed to be in good agreement with calculations of Liu & Evans (2010) (see Table 5.7).

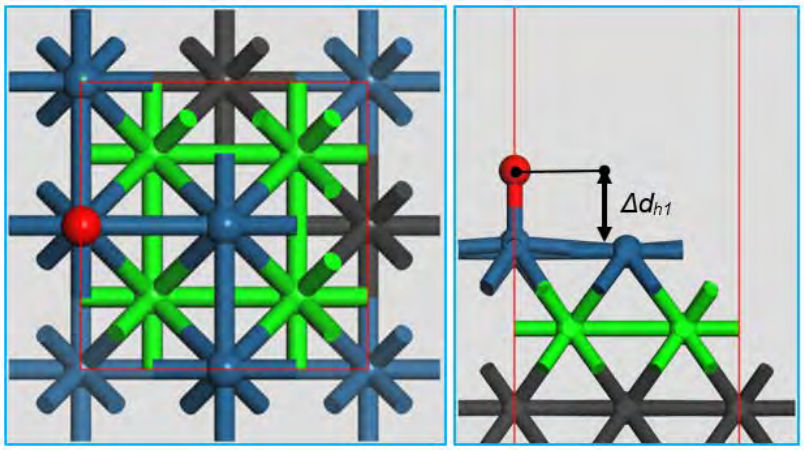

Figure 5.6: Equilibrium geometry of atomic O on an atop site of a Pt(100)-p(2x2) slab model. Surface normal view (left) and side view (right). The hight of atomic O above the surface plane, Δd_{h1}, equals to 1.818 Å.

Discussion

On the Pt(100)-p(2x2) surface, atomic O preferentially adsorbs on a bridge site with an adsorption energy of -1.14 eV/$\frac{1}{2}O_2$. The second most stable adsorption state was observed to be atomic O on a 4-fold hollow site, -0.78 eV/$\frac{1}{2}O_2$. Interestingly, at 0.125 ML coverage (on a p(2x4) surface cell) atomic O adsorbs with a relatively similar strength on the fcc site as on the Pt(100) bridge site. The atop adsorption state of atomic O on Pt(100)-p(2x2) was observed to be the least stable adsorption state with an adsorption energy of -0.11 eV/$\frac{1}{2}O_2$. When comparing to the work of Liu & Evans (2010), who used the PBE functional with PAW potentials, the adsorption energies calculated in this study were in close agreement: Liu & Evans (2010) reported the adsorption energies of atomic O to be -4.20 eV/O (bridge), -3.87 eV/O (4-fold hollow) and -3.05 eV/O (atop), consistent with -4.17 eV/O (bridge), -3.80 eV/O (4-fold hollow) and -3.13 eV/O (atop) calculated in the present study (see Table 5.7). Whilst this study used only a six layered slab with 3 top layers relaxed, Liu & Evans (2010) took an average of calculated adsorption energies on a series of slabs, from 5- to 9-layered slabs, and in all their calculations only the bottom layer was fixed. The fluctuation in adsorption energy with slab thickness, observed in both the present study and the study by Liu & Evans (2010), is therefore a potential cause of these subtle differences. Therefore considering the model error (see Section 3.4),

Table 5.7: Adsorption energy of atomic O on high-symmetry sites of the Pt(100)-p(2x2) slab model.

reference state	$\frac{1}{2}O_2$	$\frac{1}{2}O_2$ + ZPE	Atomic O
Units	[eV/$\frac{1}{2}O_2$]	[eV/$\frac{1}{2}O_2$]	[eV/O]
Adsorption site: bridge			
This study	-1.14	-1.12	-4.17
Literature		-1.14[a]	-4.62[b], -4.20[c]
			-4.03[d], -4.71[e]
Adsorption site: 4-fold hollow			
This study	-0.78	-0.79	-3.80
Literature			-4.31[b], -3.87[c], -3.60[d]
Adsorption site: atop			
This study	-0.11	-0.11	-3.13
Literature			-3.08[c], -2.92[d], -3.58[e]

a Pt(111)-p(2x2), PAW−PBE, VASP code, ZPE corrected (Qi & Li, 2012)

b Pt(111)-p(2x2), PAW−PBE, VASP code (Gu & Balbuena, 2007)

c Pt(111)-p(2x2), PAW−PBE, VASP code, ZPE corrected (Liu & Evans, 2010)

d Pt(111)-p(2x2), USPP−PBE, VASP code, ZPE corrected (Duan & Wang, 2013)

e Pt(111)-p(4x4), PAW−PBE, VASP code (Ogawa *et al.*, 2013)

it can be argued that the present study is in good agreement with the study by Liu & Evans (2010).

The adsorption energies calculated in this study, -4.17 eV/O (bridge), -3.80 eV/O (4-fold hollow) and -3.13 eV/O (atop), were observed to be ca. 0.2 eV more stable than the adsorption energy calculated using the USPP−PBE potential−functional combination (Duan & Wang, 2013) (see Table 5.7). The latter difference was also observed in the case of atomic O adsorption on the Pt(111)-p(2x2) fcc site (see Table 5.4). These differences were attributed to the use of different potential−functional combinations (this study used a PAW−PBE combination). Vibrational frequency analysis for each optimized geometry confirmed all three states, bridge, 4-fold hollow and atop on Pt(100)-p(2x2), to be stable states at a minimum on the potential energy surface (see Table 5.8). In summary, the calculated equilibrium properties of atomic O on Pt(100)-p(2x2) were found to be in good agreement with previous studies. Furthermore, decreasing atomic O coverage from 0.25 ML to 0.125 ML resulted in an increase in the adsorption energy of atomic O of ca. 0.1 eV (only for the bridge and atop adsorption states). A much larger stabilization, 0.67 eV, of atomic O on 4-fold hollow sites was observed with a decrease in coverage (from a p(2x2) surface cell size to a p(2x4) surface cell size).

Table 5.8: Calulated vibrational frequencies of atomic O on Pt(100) high-symmetry sites

Adsorption site:	bridge	4-fold hollow	atop
υ_i [cm^{-1}]	521, 459, 114	363, 105, 110	710, 20, 33

5.3.3 Atomic O on nanorod edge sites

The high-symmetry adsorption sites, near the edge of the Pt(mNR)-[5(111)×5(100)] nanorod model, were probed with atomic O to investigate stable adsorption configurations. Geometry optimization calculations with initial states in the vicinity of different high-symmetry edge sites (see Figure 4.7) were conducted. The converged equilibrium geometries, within a force convergence criterion of 0.02 eV/Å for all relaxed atoms, were EB, fcc1, atopE, b1*a and b2*a. The other high-symmetry sites, hcp1, b1a, b2a, atop1, atop1* and 4fh1, were observed to be unstable as they converged to EB, fcc1, b1*a and b2*a equilibrium geometries depending on the initial positions. The EB, fcc1, b1*a and b2*a equilibrium adsorption geometries were confirmed to be stable states at the minimum of the potential energy surface (PES). The atopE state was found to have a single imaginary vibrational mode. The adsorption energies and vibrational frequencies corresponding to stable adsorption states of atomic O on near-edge sites are presented in Table 5.13 and 5.14, respectively.

EB site

The geometric properties of atomic O adsorption on the nanorod EB site are presented in Figure 5.7 and Table 5.9. At this adsorption site the interesting properties are the Pt-O bond lengths (d_{Pt-O}), shortest distance between the O atom and the edge atomic row (Δd_{h1}), deviation angle of the oxygen bond axis from the surface normal of the Pt(111) facet (θ) and Pt(100) facet (β). On nanorod EB site atomic O adsorbs with two equal Pt-O bond lengths of 1.943 Å. The latter bond length is consistent with that reported by Ogawa *et al.* (2014) for atomic O adsorption on EB sites of a Pt(S)-[5(111)×2(100)] slab model (Table 5.9). It was further observed that the bond axis of atomic O on the nanorod EB site is not aligned with either of the surface normal vectors ($\theta = 33°$ and $\beta = 22°$ see Table 5.9 and Figure 5.7). The shortest length of atomic O from the edge atomic row, was observed to be relatively similar to the vertical distance of atomic O above a Pt(100) surface. The adsorption energy of atomic O on the nanorod EB site was calculated to be -1.61 eV/$\frac{1}{2}O_2$ (Table 5.13). It was observed that atomic O adsorbs ca. 0.24 eV and 0.17 eV more strongly on the Pt(mNR)-[5(111)×5(100)] nanorod EB site than on Pt(211) and step-double Pt(211) (Pt(S)-[5(111)×2(100)]) EB sites, respectively (Table 5.13). The difference between the adsorption energy on the Pt(mNR)-[5(111)×5(100)] nanorod EB site, -4.64 eV/O and adsorption on an EB site of a 147-atom cuboctahedral cluster, -4.20 eV/O, reported by Li *et al.* (2013) was argued to be due to the use of different functionals. Li *et al.* (2013) used the RPBE functional which is known to give weaker adsorption energies than the PBE functional used in this study (Hammer *et al.*, 1999).

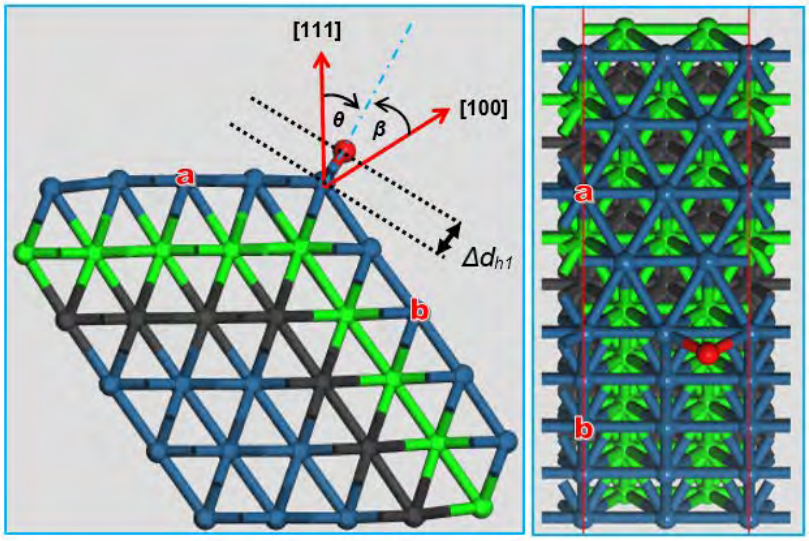

Figure 5.7: Equilibrium geometry of atomic O on the EB site of the Pt(mNR)-[5(111)×5(100)] nanorod model. Side view (left) and [111] surface normal view (right). θ, β and Δd_{h1} values are given in Table 5.9. The red lines represents the [111] and [100] surface normal vectors.

Table 5.9: Equilibrium geometric properties of atomic O on the EB site of the Pt(mNR)-[5(111)×5(100)] nanorod model.

site: EB	Pt(mNR)-[5(111)×5(100)]	Pt(S)-[5(111)×2(100)][a]
Δd_{h1} [Å]		
This study	1.283	
d_{Pt-O} [Å]		
This study	1.943	
Literature		1.94
θ	33°	
β	22°	

a step-double Pt(211) surface, PAW−PBE, VASP code (Ogawa *et al.*, 2014)

fcc1 site

The geometric properties of atomic O adsorption on the fcc1 site are presented in Figure 5.8 and Table 5.10. Atomic O adsorbs on the fcc1 site with Pt-O bond lengths of 2.096 Å (coordination with an edge Pt atom) and 2.042 Å (coordination with two Pt atoms along the first atomic row from the edge). With respect to Pt-O bond lengths, coordination of atomic O with the non-edge Pt atoms, on the nanorod, is relatively similar to coordination observed on the Pt(111)-p(2x2) slab. However, the vertical height of atomic O above the Pt(111) surface is larger, 1.185 Å, on the fcc1 site than on the Pt(111)-p(2x2) slab fcc site (1.149 Å). The adsorption energy of atomic O on the fcc1 site was calculated to be -1.01 eV/$\frac{1}{2}O_2$ (see Table 5.13). Compared to equivalent adsorption on the Pt(111)-p(2x2) slab, it was observed that on the fcc1 site atomic O adsorbs weaker by 0.13 eV.

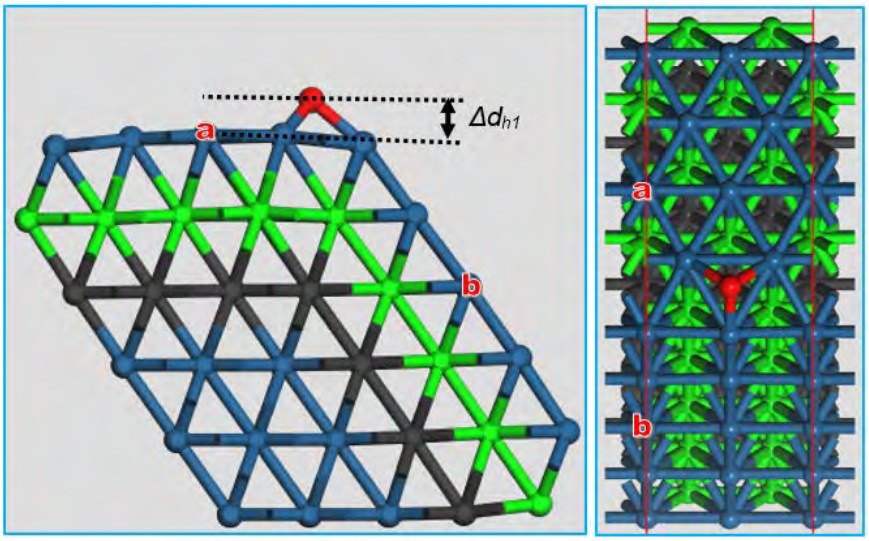

Figure 5.8: Equilibrium geometry of atomic O on the fcc1 site of the Pt(mNR)-[5(111)×5(100)] nanorod model. Side view (left) and [111] surface normal view (right).

Table 5.10: Equilibrium geometric properties of atomic O on the fcc1 site of the Pt(mNR)-[5(111)×5(100)] nanorod model.

site: fcc1	Pt(mNR)-[5(111)×5(100)]	Pt(S)-[5(111)×2(100)][a]
Δd_{h1} [Å]		
This study	1.185	
d_{Pt-O} [Å]		
This study	2.096, 2.042x2	
Literature		2.10, 2.04x2

a step-double Pt(211) surface, PAW−PBE, VASP code (Ogawa *et al.*, 2014)

b1*a site

The equilibrium geometric properties of atomic O adsorption on the b1*a site are presented in Figure 5.9 and Table 5.11. The Pt-O bond lengths of the equilibrium adsorption state of atomic O on the b1*a site were calculated to be 1.958 Å (coordination with edge row atom) and 1.953 Å. The shortest distance from the Pt(100) facet plane and atomic O (Δd_{h1}) was calculate to be 1.288 Å (cf. Δd_{h1} = 1.286 Å for adsorption on a bridge site of a Pt(100)-p(2x2) slab). The adsorption energy of atomic O on the b1*a site was calculated to be -1.13 eV/$\frac{1}{2}O_2$ (see Table 5.13). This was found to be the same as the adsorption energy of atomic O on the bridge site of a Pt(100)-p(2x2) slab.

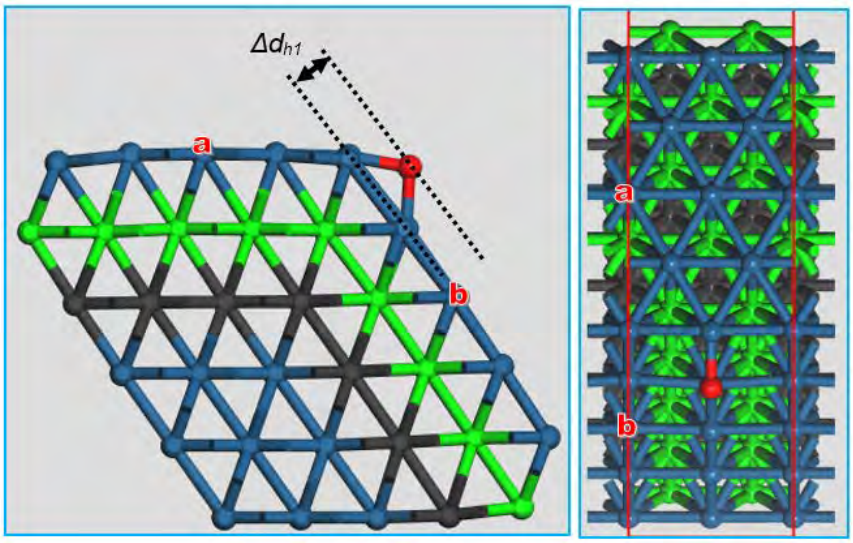

Figure 5.9: Equilibrium geometry of atomic O on the b1*a site of the Pt(mNR)-[5(111)×5(100)] nanorod model. Side view (left) and [111] surface normal view (right).

Table 5.11: Equilibrium geometric properties of atomic O on the b1*a site of the Pt(mNR)-[5(111)×5(100)] nanorod model.

site: b1*a	Pt(mNR)-[5(111)×5(100)]	Pt(S)-[5(111)×2(100)][a]
Δd_{h1} [Å] This study	1.288	
d_{Pt-O} [Å] This study Literature	1.958, 1.953	 1.95

a step-double Pt(211) surface, PAW−PBE, VASP code (Ogawa *et al.*, 2014)

b2*a site

Geometric properties of atomic O adsorption on the b2*a site are presented in Figure 5.10 and Table 5.12. On the latter site, atomic O was observed to adsorb with two equal Pt-O bond lengths of 1.954 Å. The latter was observed to be consistent with calculated Pt-O bond lengths for atomic O adsorption on a bridge site of a Pt(100)-p(2x2) slab and the Pt-O bond lengths reported by Ogawa *et al.* (2014) for atomic O adsorption on a bridge site found on a Pt(100) facet of a Pt(S)-[5(111)×2(100)] step-surface model (Table 5.12). Interestingly, the adsorption of atomic O was observed to result in a slight tilt (β = 16°), off the Pt(100) facet normal vector. The tilt was observed to point towards the edge atomic row (see Figure 5.10). The shortest distance from the Pt(100) facet plane and atomic O (Δd_{h1}) was calculate to be 1.298 Å (0.01 Å larger than that observed for atomic O adsorption on the b1*a site). The calculated adsorption energy of atomic O on the b2*a site was -1.23 eV/$\frac{1}{2}O_2$ (see Table 5.13). The latter adsorption state of atomic O was observed to be ca. 0.1 eV more stable than the bridge adsorption state on the Pt(100)-p(2x2) slab. It was further noted that on the b2*a site atomic O adsorbs with the same adsorption strength as the adsorption on the bridge site of the Pt(100)-p(2x4) slab. The latter may be an indication that the nanorod Pt(100) facet behaves as though it was a Pt(100)-p(2x4) surface.

unstable adsorption states

For atomic O adsorption on near-edge Pt(mNR)-[5(111)×5(100)] nanorod sites, it was observed that hcp1, bridge (on the Pt(111) facet), 4fh1 and atop adsorption states were unstable. Appendix B.1.2 presents a select few initial and final states that illustrate the observe instability of the hcp1, b1a, atop1, 4fh1 and atop1* adsorption states. The b1a site on the Pt(111) facet behaved in a similar manner as a Pt(111)-p(2x2) bridge sites. Initial geometries in the vicinity of the b2a and b1a converged to an

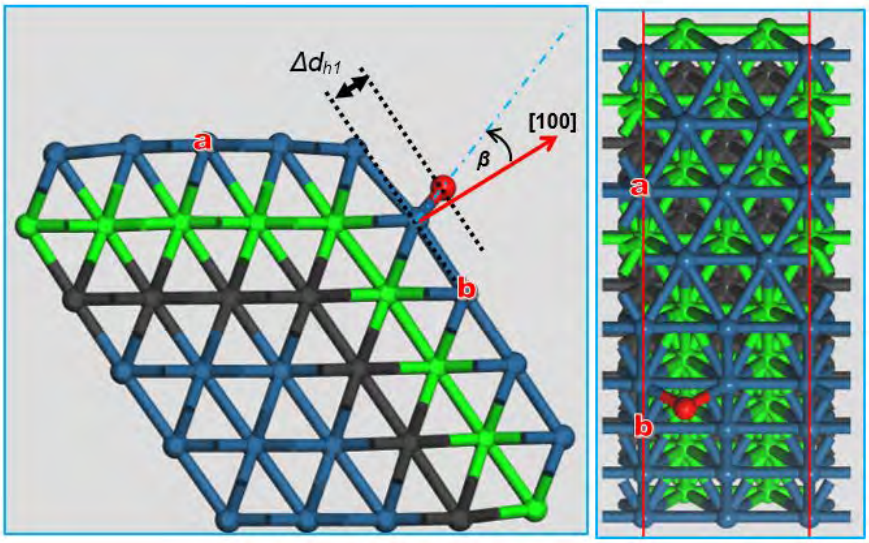

Figure 5.10: Equilibrium geometry of atomic O on the b2*a site of the Pt(mNR)-[5(111)×5(100)] nanorod model. Side view (left) and [111] surface normal view (right). Red arrow represents the Pt[100] surface normal vector.

Table 5.12: Equilibrium geometric properties of atomic O on the b2*a site of the Pt(mNR)-[5(111)×5(100)] nanorod model.

site: b2*a	Pt(mNR)-[5(111)×5(100)]	Pt(S)-[5(111)×2(100)][a]
Δd_{h1} [Å] This study	1.298	
d_{Pt-O} [Å] This study Literature	1.954	 1.95
β	16°	

a step-double Pt(211) surface, PAW−PBE, VASP code (Ogawa *et al.*, 2014)

fcc1 equilibrium adsorption state. Figure B.5 in Appendix B.1.2 illustrates the latter where atomic O on a b1a site (initial state) converges to an O atom on an fcc1 site (final state). The non-edge atop sites were also seen to be unstable−the atop1* initial geometry converged to a b1*a equilibrium state and the atop1 initial geometry converged to an EB equilibrium state. Adsorption on the atopE site (atop adsorption on an edge Pt atom) converged to an equilibrium adsorption which was later found to be unstable as it had an imaginary vibrational mode. The converged atopE geometry consisted of a Pt-O bond length of 1.81 Å and $\theta = 31°$, $\beta = 24°$. Based on vibrational frequency analysis it was concluded that this adsorption state was unstable (ν_i= [730, 73, 35i]). The hcp1 site was also observed to be unstable; initial atomic O positions near this adsorption site converged to an EB adsorption state. Figure B.6 in Appendix B.1.2 illustrates the latter where atomic O on an hcp1 site (initial state) converges to an O atom on an EB site (final state).

Discussion

The adsorption of atomic O on sites near the edge region of the Pt(mNR)-[5(111)×5(100)] nanorod model was investigated. It was observed that the atomic O adsorbs strongest on the EB site with an adsorption energy of -1.61 eV/$\frac{1}{2}O_2$. On other near-edge adsorption sites, atomic O adsorbs with an adsorption energy of -1.01 eV/$\frac{1}{2}O_2$ (fcc1), -1.13 eV/$\frac{1}{2}O_2$ (b1*a) and -1.23 eV/$\frac{1}{2}O_2$ (b2*a). The latter adsorption energies were 0.6 eV (fcc1), 0.48 eV (b1*a) and 0.38 eV (b2*a) weaker than the adsorption energy of atomic O on the EB site. Whilst the adsorption energy of atomic O fcc1, b1*a and b2*a were relatively similar to the adsorption energies on equivalent sites found on Pt(211), the adsorption energy on the nanorod EB site was found to be much stronger than that reported by Ogawa *et al.* (2014) for atomic O adsorption on the EB site of a step-double Pt(211) surface (see Table 5.13). Due to lack of

literature data for the adsorption of atomic O on EB site of platinum model clusters, a comprehensive comparison could not be made. The equilibrium geometries were confirmed to be stable adsorption states, at the minimum of the potential energy surface, through vibrational frequency analyses. The vibrational modes on the fcc1 site were observed to be relatively similar to vibrational modes on the Pt(111)-p(2x2) fcc site. All vibrational modes corresponding to b1*a and b2*a adsorption states were also observed to be in good agreement with equivalent vibrational modes on the Pt(100)-p(2x2) bridge site.

Table 5.13: Adsorption energy of atomic O on the Pt(mNR)-[5(111)×5(100)] nanorod near-edge high-symmetry sites.

reference state	$\frac{1}{2}O_2$	$\frac{1}{2}O_2$ + ZPE	Atomic O
Units	[eV/$\frac{1}{2}O_2$]	[eV/$\frac{1}{2}O_2$]	[eV/O]
Adsorption site: EB			
This study	-1.61	-1.59	-4.64
Literature			-4.92[a], -4.66[b], -4.20[c], -4.85[d]
Adsorption site: fcc1			
This study	-1.01	-0.99	-4.03
Literature			-4.52[a]
Adsorption site: b1*a			
This study	-1.13	-1.11	-4.16
Literature			-4.60[a]
Adsorption site: b2*a			
This study	-1.23	-1.21	-4.25
Literature			-4.60[a]

a step-double Pt(211) surface, PAW−PBE, VASP code (Ogawa *et al.*, 2014)

b 147-atom cuboctahedral cluster, PAW−PW91, VASP code, (Peng & Mavrikakis, 2015)

c 147-atom cuboctahedral cluster, PAW−RPBE, VASP code, (Li *et al.*, 2013)

d Pt(211) surface, PAW−PBE, VASP code (Ogawa *et al.*, 2014)

Table 5.14: Calulated vibrational frequencies of atomic O on nanorod near-edge high-symmetry sites

Adsorption site:	EB	fcc1	b1*a	b2*a
υ_i [cm^{-1}]	532, 464, 138	444, 377, 316	507, 446, 118	518, 454, 114

5.4 O_2 adsorption on platinum surfaces

The interaction of O_2 with different platinum surfaces was investigated by considering adsorption on different high-symmetry sites. The platinum surfaces considered were, Pt(111), Pt(100) and nanorod near edge sites. In the following subsections the equilibrium geometric and energetic properties of O_2 on different high-symmetry sites are presented.

5.4.1 O_2 on Pt(111)

Considering a number of starting geometries in the vicinity of the high-symmetry sites, geometry optimization calculations were performed to obtain equilibrium properties of O_2 on high-symmetry sites. Equilibrium adsorption states of O_2 were only observed on the fcc, hcp and bridge high-symmetry sites. Initial geometries with O_2 on an atop site converged to an fcc geometry (see Figure B.2 in Appendix B.1.1). The equilibrium geometries, on fcc, hcp and bridge sites, were confirmed to be stable adsorption states at a minimum of the potential energy surface. The equilibrium properties of the stable adsorption states on Pt(111) surfaces are presented below.

bridge site

The geometric properties of O_2 adsorption on a bridge site are presented in Figure 5.11 and Table 5.15. The calculated O-O bond length on the Pt(111)-p(2x2) and Pt(11)-p(2x4) bridge sites was 1.359 Å and 1.362 Å, respectively. The latter was consistent with literature (1.35 Å (Qi *et al.*, 2008) and 1.36 Å (Yang *et al.*, 2010)) and a NEXAFS derived experimental measurement of 1.37 Å (Puglia *et al.*, 1995). The Pt-O bond lengths were calculated to be 2.037 Å and 2.025 Å on Pt(111)-p(2x2) and Pt(11)-p(2x4) bridge sites, respectively. On the Pt(111)-p(2x4) bridge site O_2 was found to adsorbs 0.02 Å closer to the surface plane than on the Pt(111)-p(2x2) bridge site.

The calculated adsorption energies of O_2 on Pt(111) surface sites are presented in Table 5.18. The adsorption energy of O_2 on the Pt(111)-p(2x2) and Pt(111)-p(2x4) bridge sites was calculated to be -0.61 eV/O_2 and -0.73 eV/O_2, respectively. The calculated energies were consistent with literature values of -0.63 eV/O_2 (Yang *et al.*, 2010), -0.65 eV/O_2 (Qi *et al.*, 2008), and -0.73 eV/O_2 (Eichler & Hafner, 1997) (see Table 5.18). The 0.12 eV difference in the adsorption energy of O_2 between this study and the value reported by Eichler & Hafner (1997) was attributed to different computational setup. Eichler & Hafner (1997) used a 4-layered slab with O_2 molecules adsorbed on both sides and p($\sqrt{3}$x3) surface cell size (compared to a 6-layered slab with O_2 on one side of a p(2x2) surface unit cell used in this study).

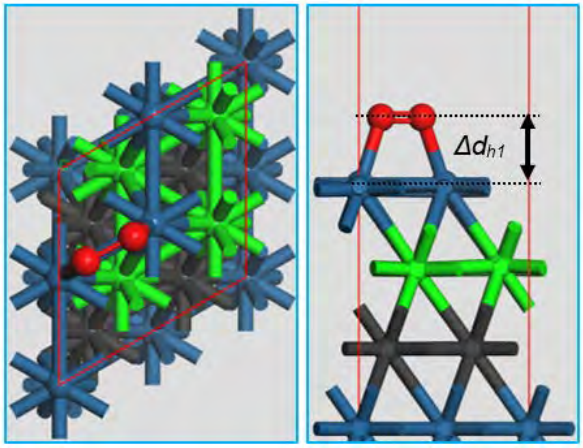

Figure 5.11: Equilibrium geometry of O_2 on a bridge site of a Pt(111)-p(2x2) slab model. Surface normal view (left) and side view (right). Δd_{h1} is the hight of O_2 above the surface plane.

Table 5.15: Equilibrium geometric properties of O_2 on bridge sites of Pt(111) slab models.

site: bridge	Pt(111)-p(2x2)	Pt(111)-p(2x4)
Δd_{h1} [Å]		
This study	1.910	1.890
d_{O-O} [Å]		
This study	1.359	1.362
Literature	1.36[a], 1.35[b], 1.37[c]	
Experimental	1.37[d]	
d_{Pt-O} [Å]		
This study	2.037	2.025
Literature	2.04[c]	

a Pt(111)-p(2x2), PAW−PBE, VASP code (Yang *et al.*, 2010)

b Pt(111)-p($\sqrt{3}$x3), PAW−PBE, VASP code (Qi *et al.*, 2008)

c Pt(111)-p(2x2), PAW−PBE, VASP code (Madala, 2013)

d Experimental estimate based on NEXAFS (Puglia *et al.*, 1995)

fcc site

The equilibrium geometric properties of O_2 on an fcc site are presented in Figure 5.12 and Table 5.16. The calculated O-O bond lengths were 1.398 Å and 1.400 Å on a Pt(111)-p(2x2) and Pt(111)-p(2x4) fcc site, respectively. The latter is consistent with 1.39 Å and 1.40 Å reported by Qi *et al.* (2008) and Yang *et al.* (2010), respectively (see Table 5.16). Compared to NEXAFS derived experimental O-O bond length on fcc sites (Puglia *et al.*, 1995), the bond lengths calculated in this study were observed to be ca. 0.03 Å shorter. The Pt-O bond lengths were calculated to be in good agreement with the equivalent Pt-O bond lengths reported by Madala (2013) (Table 5.16). A 10° angle between the Pt(111) surface plane and the O-O bond axis (α_{O-O}) was calculated for O_2 adsorption on the fcc site. It was observed that on an Pt(111)-p(2x4) fcc site, O_2 atoms are ca. 0.03 Å closer to the Pt(111) surface plane than on a Pt(111)-p(2x2) fcc site.

The calculated adsorption energy of O_2 on fcc sites is reported in Table 5.18. The adsorption of O_2 was calculated to be -0.60 eV/O_2 and -0.68 eV/O_2 on Pt(111)-p(2x2) and Pt(111)-p(2x4) bridge sites, respectively. The increase in adsorption energy at low coverage can be rationalized by increase separation of adjacent O_2 molecules, and hence the decrease in lateral interactions at low coverage. The calculated adsorption energy of O_2 on a Pt(111)-p(2x2) fcc site compared well with literature studies (see Table 5.18). Furthermore, the calculated adsorption energy of O_2 on an fcc site was observed to be more exothermic than the experimentally derived adsorption energies (see Table 5.18). The latter is a well known shortfall of the PBE exchange-correlation functional, used in this study, (Hammer *et al.*, 1999).

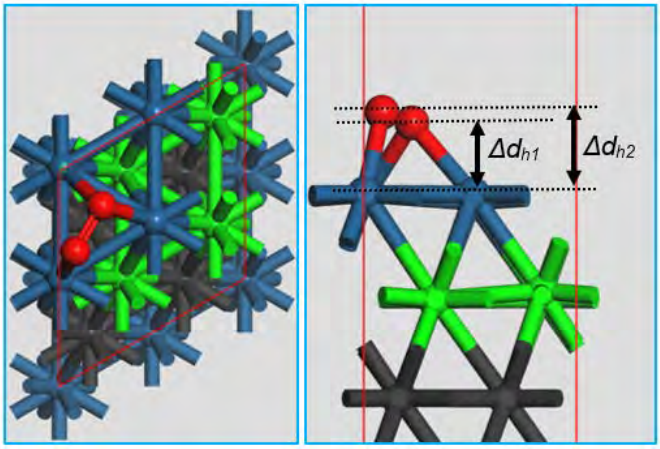

Figure 5.12: Equilibrium geometry of O_2 on an fcc site of a Pt(111)-p(2x2) slab model. Surface normal view (left) and side view (right). Δd_{h1} is the hight of O_2 above the surface plane.

hcp site

The adsorption of O_2 on an hcp site results in bridge-hollow-top structure, with one O atom across a bridge and another almost on an atop sites (see Figure 5.13). The equilibrium geometric properties of O_2 on hcp sites are presented in Table 5.17. On hcp site of the Pt(111)-p(2x2) and Pt(111)-p(2x4) surfaces, O_2 was observed to adsorbs with an O-O bond length of 1.388 Å and 1.385 Å, respectively. Moreover, the angle between the O-O bond axis and the Pt(111) surface plane (α_{O-O}) was calculated to be 8° (compared to $\alpha_{O-O} = 10°$ on an fcc site). The vertical heights above the Pt(111)-p(2x2) surface plane, Δd_{h1} and Δd_{h2}, of O atoms in O_2 were calculated to be 1.696 Å and 1.900 Å, respectively (Table 5.17). The Pt-O bond lengths were calculated to be 2.224 Å (for one O atom across a bridge site) and 2.042 Å (for the second O atom on an atop site).

The calculated adsorption energies of O_2 on Pt(111)-p(2x2) and Pt(111)-p(2x4) were -0.45 eV/O_2 and -0.51 eV/O_2, respectively (see Table 5.18). The calculated adsorption energy of O_2 on a Pt(111)-p(2x2) hcp site, -0.45 eV/O_2, was consistent with -0.45 eV/O_2 reported by Qi *et al.* (2008). As was the

Table 5.16: Equilibrium geometric properties of O_2 on fcc sites of Pt(111) slab models.

site: fcc	Pt(111)-p(2x2)	Pt(111)-p(2x4)
Δd_{h1} [Å]	1.629	1.603
Δd_{h2} [Å]	1.859	1.826
d_{O-O} [Å]		
This study	1.398	1.400
Literature	1.40[a], 1.39[b], 1.40[c]	
Experimental	1.43[d]	
d_{Pt-O} [Å]		
This study	2.178x2, 2.019	2.193, 2.154, 2.019
Literature	2.20[c]	

a Pt(111)-p(2x2), PAW−PBE, VASP code (Yang *et al.*, 2010)
b Pt(111)-p($\sqrt{3}$x3), PAW−PBE, VASP code (Qi *et al.*, 2008)
c Pt(111)-p(2x2), PAW−PBE, VASP code (Madala, 2013)
d Experimental estimate based on NEXAFS (Puglia *et al.*, 1995)

case for the adsorption energies of O_2 on Pt(111)-p(2x2) bridge and fcc sites, the adsorption energy of O_2 on hcp sites was calculated to be weaker, 0.13 eV less stable, compared to the adsorption energy reported by Eichler & Hafner (1997). This was argued to be due to different computational systems between this study and the study by Eichler & Hafner (1997).

Discussion

The interaction of O_2 with Pt(111) high-symmetry adsorption sites was investigated. It was observed that calculated adsorption energies and equilibrium geometries in this study were consistent with those reported in literature (Eichler & Hafner, 1997; Qi *et al.*, 2008; Yang *et al.*, 2010; Madala, 2013). On Pt(111)-p(2x2) the stability of O_2 decreased in the order bridge, fcc and hcp with adsorption energies of -0.61 eV/O_2, -0.60 eV/O_2 and -0.45 eV/O_2, respectively. It was observed that at 0.125 ML coverage, i.e. on Pt(111)-p(2x4) sites, O_2 adsorbed relatively more stable by 0.12 eV (bridge), 0.08 eV (fcc) and 0.06 eV (hcp), than on equivalent adsorption sites at 0.25 ML coverage. Moreover, at low coverage O_2 was observed to adsorb closer to the Pt(111)-p(2x4) surface than equivalent adsorption on Pt(111)-p(2x2) surface. The latter was attributed to decrease crowding of O_2 molecules at low coverage and hence decreased lateral interactions. This decrease in lateral interaction was observed as an increase in the adsorption energy of O_2 with decreasing coverage.

Table 5.19 presents the calculated vibrational modes for O_2 on different Pt(111)-p(2x2) high symmetry

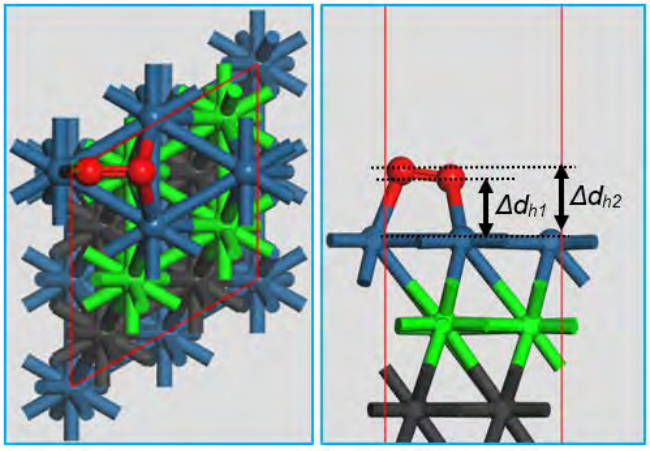

Figure 5.13: Equilibrium geometry of O_2 on an hcp site of a Pt(111)-p(2x2) slab model. Surface normal view (left) and side view (right). Δd_{h1} is the hight of O_2 above the surface plane.

Table 5.17: Equilibrium geometric properties of O_2 on hcp sites of Pt(111) slab models.

site: hcp	Pt(111)-p(2x2)	Pt(111)-p(2x4)
Δd_{h1} [Å]	1.696	1.709
Δd_{h2} [Å]	1.900	1.881
d_{O-O} [Å]		
This study	1.388	1.385
Literature	1.39[a]	
d_{Pt-O} [Å]		
This study	2.224x2, 2.042	2.187, 2.282, 2.032

a Pt(111)-p(2x2), PAW−PBE, VASP code (Yang *et al.*, 2010)

adsorption sites (only the adsorption states with equilibrium geometries). It was observed that in all equilibrium adsorption state cases, vibrational modes were all real, indicative of stable states at a minimum of the potential energy surface. The calculated vibrational frequencies (stretching of O-O bond) for each of the stable geometries were 811 cm^{-1} (fcc), 899 cm^{-1} (bridge) and 834 cm^{-1} (hcp). This was in reasonable agreement with results reported by Qi *et al.* (2008): 836 cm^{-1} (fcc) and 913 cm^{-1} (bridge). Eichler & Hafner (1997) reported frequencies of 690 cm^{-1} (fcc), 850 cm^{-1} (bridge) and 710 cm^{-1} (hcp). There is a large disagreement between results of Eichler & Hafner (1997) and Qi *et al.* (2008), which might be due to the use of different pseudopotentials, i.e. Eichler & Hafner (1997) used ultrasoft pseudopotentials whilst Qi *et al.* (2008) used PAW potentials. Furthermore, Eichler & Hafner (1997) considered adsorption of O_2 on both sides of a 4-layered Pt(111) slab whilst Qi *et al.* (2008) considered adsorption of one O_2 molecule on one side of a 4-layered Pt(111) slab. The present study is in much closer agreement with Qi *et al.* (2008) than Eichler & Hafner (1997). This could also be due to the use of a similar computational setup, i.e. both the present study and Qi *et al.* (2008) considered O_2 adsorption on one side of a slab and used the PAW−PBE potential−functional combination. The present study was also in reasonable agreement with experimentally derived vibrational modes (Gland *et al.*, 1980) (see Table 5.19).

Table 5.18: Equilibrium adsorption energy of O_2 on high-symmetry sites of the Pt(111)-p(2x2) slab model.

reference state	O_2	O_2 + ZPE
Units	[eV/O_2]	[eV/O_2]
Adsorption site:	bridge	
This study	-0.61	-0.56
Literature	-0.65[a], -0.63[b]	
	-0.72[c], -0.52[d]	-0.48[d]
Adsorption site:	fcc	
This study	-0.60	-0.55
Literature	-0.53[a], -0.65[b]	-0.52[d]
	-0.68[c], -0.57[d]	
Experimental		-0.38[e], -0.36[f]
Adsorption site:	hcp	
This study	-0.45	-0.40
Literature	-0.45[b], -0.58[c]	
	-0.46[d]	-0.42[d]

a Pt(111)-p($\sqrt{3}$x3), PAW−PBE, VASP code (Qi *et al.*, 2008)

b Pt(111)-p(2x2), PAW−PBE, VASP code (Yang *et al.*, 2010)

c Pt(111)-p($\sqrt{3}$x3), USPP−PW91, VASP code (Eichler & Hafner, 1997)

d Pt(111)-p(2x2), PAW−PBE, VASP code (Madala, 2013)

e Thermal desorption spectroscopy (Gland *et al.*, 1980)

f Temperature programmed XPS (Miller *et al.*, 2010)

5.4.2 O_2 on Pt(100)

A number of starting starting geometries in the vicinity of the Pt(100) high-symmetry sites were probed with O_2 and optimized to within 0.02 eV/Å force convergence on each relaxed atom. Initial adsorption geometries near the 4-fold hollow converged to two co-adsorbed O atoms on bridge sites (see Figure B.3 in Appendix B.1.2) whilst initial geometries near the atop site (with one O atom sticking away from the Pt(100) surface) converged into bridge adsorption state with the O-O bond parallel to the Pt(100) surface plane (see Figure B.4 in Appendix B.1.2). Therefore, only the bridge equilibrium geometry of O_2 on a Pt(100)-p(2x2) surface was obtained using the above force convergence criterion. This equilibrium adsorption geometry was then confirmed to be a minimum of the potential energy surface.

bridge site

The equilibrium adsorption properties of O_2 on a Pt(100) bridge site are presented in Figure 5.14 and Table 5.20. The calculated O-O bond length on the Pt(100)-p(2x2) and Pt(100)-p(2x4) bridge sites was ca. 1.36 Å. The latter was found to be ca. 0.01 Å and 0.02 Å shorter than the O-O bond lengths reported by Duan & Wang (2013) and Vasić *et al.* (2013), respectively. These differences in the bond lengths were attributed to the use of different potential−functional combinations (see Table 5.20). In section 2.5 it was demonstrated that different potential−functional combinations result in different bulk Pt-Pt equilibrium bond lengths. The latter can be a potential cause of the observed differences in O-O bond lengths calculated in this study and those reported in literature (Duan & Wang, 2013; Vasić *et al.*, 2013). The calculated Pt-O bond lengths were ca. 1.99 Å for O_2 adsorption on Pt(100) surfaces, i.e. both p(2x2) and p(2xx4) surface unit cells. It was observed that on Pt(100)-p(2x4) O_2 adsorbed ca. 0.01 Å closer to the Pt(100) surface plane than on Pt(100)-p(2x2) (see Table 5.20).

The adsorption energy of O_2 on Pt(100)-p(2x2) bridge site is presented in Table 5.21. On Pt(100)-p(2x2) and Pt(100)-p(2x4) bridge sites, the adsorption energy of O_2 was calculated to be -1.11 eV/O_2 and -1.22 eV/O_2, respectively. The calculated adsorption energy on Pt(100)-p(2x2) bridge site was consistent with -1.10 eV/O_2 reported by Duan & Wang (2013). The vibrational modes calculated for O_2 adsorbed on a Pt(100)-p(2x2) bridge site were all real (see Table 5.21). Therefore, the adsorption of O_2 on a Pt(100)-p(2x2) bridge site correspond to a stable adsorption state at a minimum of the potential energy surface. Compared to O_2 adsorption properties on a Pt(111)-p(2x2) bridge site, O_2 adsorption on a Pt(100)-p(2x2) bridge site was found to have an adsorption energy and a O-O stretching frequency which were 0.5 eV (more stable) and 13 cm^{-1} (smaller), respectively.

Table 5.19: Calulated vibrational frequency modes of O_2 on Pt(111) high-symmetry sites

Adsorption site:	bridge	fcc	hcp
υ_i [cm^{-1}]	899, 546, 353	811, 510, 368	834, 500, 339
	228, 133, 119	317, 234, 131	305, 200, 87
Literature	913[a], 850[b]	826[a], 690[b]	710[b]
Experimentally	870[c]	710[c]	

a Pt(111)-p($\sqrt{3}$x3), PAW−PBE, VASP code (Qi *et al.*, 2008)

b Pt(111)-p($\sqrt{3}$x3), USPP−PW91, VASP code (Eichler & Hafner, 1997)

c EELS measurements of Gland *et al.* (1980)

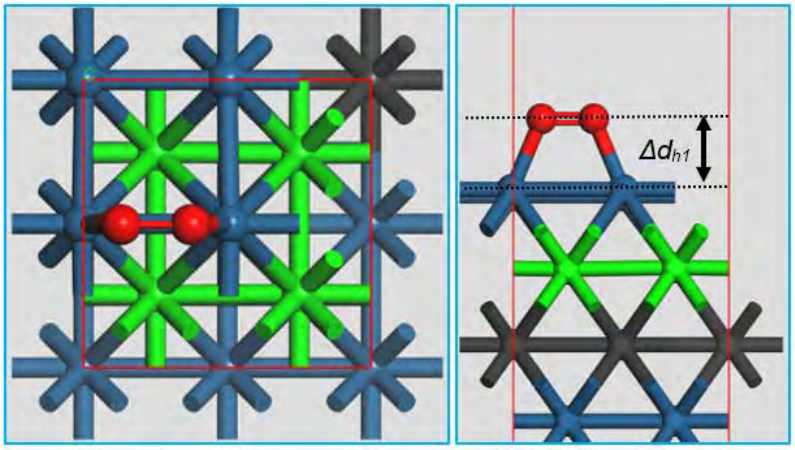

Figure 5.14: Equilibrium geometry of O_2 on a bridge site of a Pt(100)-p(2x2) slab model. Surface normal view (left) and side view (right). Δd_{h1} is the hight of O_2 above the surface plane.

Table 5.20: Equilibrium geometric properties of O_2 on bridge sites of Pt(100) slab models.

site: bridge	Pt(100)-p(2x2)	Pt(100)-p(2x4)
Δd_{h1} [Å]	1.835	1.828
d_{O-O} [Å]		
This study	1.364	1.364
Literature	1.37[a], 1.38[b]	
d_{Pt-O} [Å]		
This study	1.989	1.986

a Pt(100), PAW−PW91, VASP code (Panchenko *et al.*, 2004)

b Pt(100)-p(2x2), USPP−PBE, QUANTUM ESPRESSO (Vasić *et al.*, 2013)

Table 5.21: Equilibrium adsorption energy of O_2 on high-symmetry sites of the Pt(100)-p(2x2) slab model.

reference state	O_2	O_2 + ZPE
Units	[eV/O_2]	[eV/O_2]
Adsorption site:	bridge	
This study	-1.11	-1.07
Literature	-1.10[a], 0.96[b], -1.02[c]	
υ_i [cm^{-1}]	886, 568, 411, 269, 208, 80	

a Pt(100)-p(2x2), USPP−PW91, VASP code (Duan & Wang, 2013)

b Pt(100)-p(2x2), USPP−PBE, QUANTUM ESPRESSO (Vasić *et al.*, 2013)

c Pt(100), PAW−PW91, VASP code (Panchenko *et al.*, 2004)

5.4.3 O_2 on nanorod edge sites

The high-symmetry adsorption sites, near the edge of the Pt(mNR)-[5(111)×5(100)] nanorod model, were probed with O_2 to investigate stable adsorption configurations. Geometry optimization calculations with initial states in the vicinity of different high-symmetry edge sites (see Figure 4.7) were conducted. The converged geometries, within a force convergence criterion of 0.02 eV/Å for all relaxed atoms, were found to be EB, fcc1, hcp1, b1a, b2a, b1*a and b2a. The other high-symmetry sites, 4-fold hollow (near edge) and atop (on edge and terrace), were observed to be unstable as they converged to other equilibrium geometries. All converged equilibrium geometries were confirmed to be stable states at the minimum of the potential energy surface. The adsorption energies and vibrational modes corresponding to stable adsorption states of O_2 on near-edge sites are presented in Table 5.30 and Table 5.31, respectively.

EB site

The geometric properties of O_2 adsorption on the nanorod EB site are presented in Figure 5.15 and Table 5.22. At this adsorption site, the equilibrium O-O bond length was calculated to be 1.382 Å. This bond length was ca. 0.02 Å and 0.01 Å longer than the O-O bond lengths of O_2 adsorbed on Pt(111) and Pt(100) bridge sites, respectively. The Pt-O bond lengths were calculated to be 1.969 Å. These bond lengths were 0.01 Å and 0.005 Å shorter than the O-O bond lengths of O_2 adsorbed on Pt(111)-p(2x2) and Pt(100)-p(2x2) bridge sites, respectively. The O_2 molecule was observed to be tilted 31° (θ) and 24° (β) away from the Pt(111) and Pt(100) nanorod facet normal vector, respectively (Figure 5.15). The latter was observed to be relatively similar to atomic O adsorption on EB site (see Table 5.9). The shortest distance between the edge atomic row and the O_2 molecule (Δd_{h1}) was calculated to be 1.816 Å.

The adsorption energy of O_2 on the nanorod EB site was calculated to be -1.58 eV/O_2 (Table 5.30). The latter adsorption energy was observed to be 0.08 eV more stable and 0.10 eV less stable than adsorption on EB sites of a Pt(211) slab and a truncated octahedral platinum cluster, respectively (see Table 5.30). The difference between the adsorption energy of O_2 calculated in this study and that reported by Jennings *et al.* (2014) for adsorption on an EB site of a 116-atom truncated octahedral Pt cluster was attributed to the effect of corners which are present on the cluster and not on the nanorod model used in this study. Furthermore, the use of different potential−functional combinations may be another significant contributor to the observed differences in adsorption energy.

hcp1 site

The geometric properties of O_2 adsorption on the nanorod hcp1 site are presented in Figure 5.16 and Table 5.23. The O-O bond length was calculated to be 1.434 Å (0.046 Å longer than the O-O bond length on a Pt(111)-p(2x2) hcp site). The Pt-O bond lengths were calculated to be 2.136 Å (coordinated to two edge Pt atoms) and 2.048 Å (coordinated to one Pt atom on the Pt(111) terrace). The angle between the Pt(111) facet plane and the O-O bond axis (α_{O-O}) was calculated to be 17° . The latter was ca. 9° wider than the equivalent angle on Pt(111) hcp site. The adsorption energy of O_2 on the hcp1 site was calculated to be -0.88 eV/O_2 (see Table 5.30). The latter adsorption energy was 0.35 eV larger than the adsorption energy of O_2 on a Pt(111)-p(2x2) hcp site.

fcc1 site

The geometric properties of O_2 adsorption on the nanorod fcc1 site are presented in Figure 5.17 and Table 5.24. This equilibrium adsorption state was calculated to have a O-O bond length of 1.405 Å and Pt-O bond lengths of 2.183 Å (coordinated to two Pt atoms along the first atomic row from the edge) and 2.026 Å (coordinated to one edge Pt atom). Compared to adsorption on a Pt(111)-p(2x2)

Table 5.22: Equilibrium geometric properties of O_2 on the EB site of the Pt(mNR)-[5(111)×5(100)] nanorod model.

site: EB	Pt(mNR)-[5(111)×5(100)]
Δd_{h1} [Å]	1.816
d_{O-O} [Å]	
This study	1.382
Literature	1.38[a], 1.37[b]
d_{Pt-O} [Å]	
This study	1.969
θ	31°
β	24°

a 116-atom truncated octahedral Pt cluster, PAW−PW91, VASP code (Jennings *et al.*, 2014)

b Pt(211)-p(3x1), USPP−PW91 (Šljivančanin & Hammer, 2002)

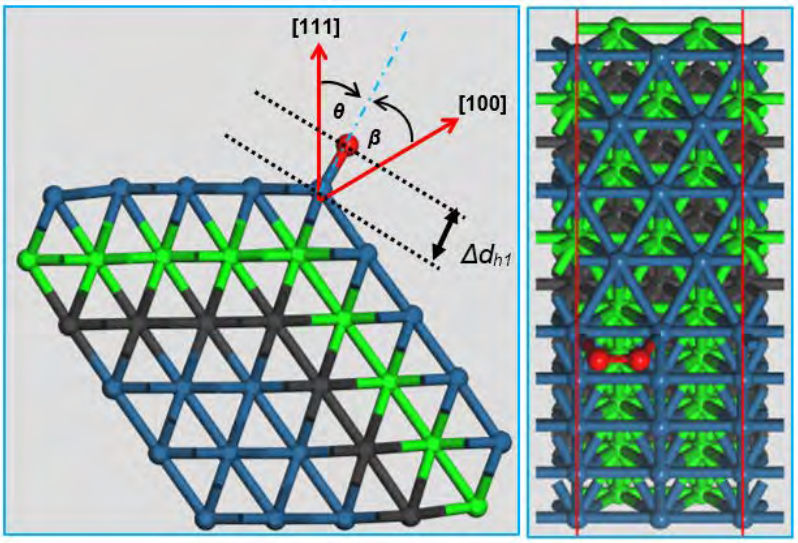

Figure 5.15: Equilibrium geometry of O_2 on the EB site of the Pt(mNR)-[5(111)×5(100)] nanorod model. Side view (left) and [111] surface normal view (right).

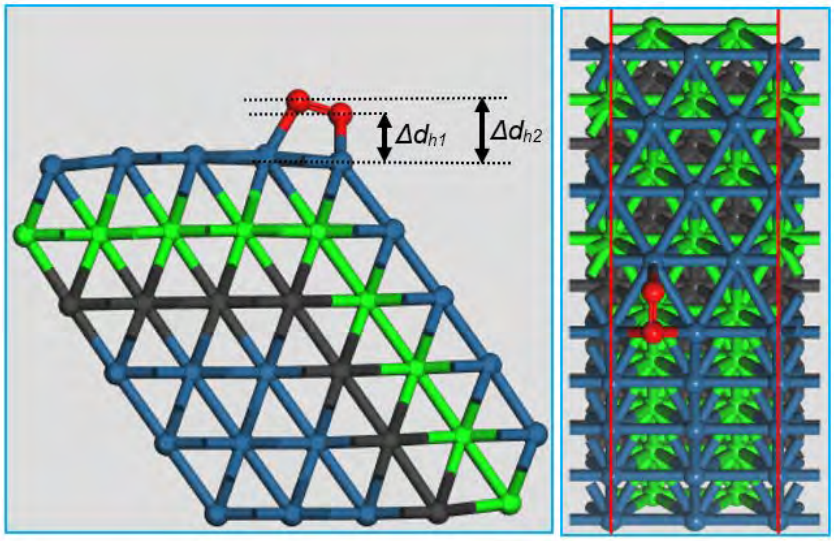

Figure 5.16: Equilibrium geometry of O_2 on the hcp1 site of the Pt(mNR)-[5(111)×5(100)] nanorod model. Side view (left) and [111] surface normal view (right).

Table 5.23: Equilibrium geometric properties of O_2 on the hcp1 site of the Pt(mNR)-[5(111)×5(100)] nanorod model.

site: hcp1	Pt(mNR)-[5(111)×5(100)]
Δd_{h1} [Å]	1.575
Δd_{h2} [Å]	1.769
d_{O-O} [Å]	
This study	1.434
Literature	1.42[a]
d_{Pt-O} [Å]	
This study	2.136x2, 2.048

a 116-atom truncated octahedral Pt cluster, PAW−PW91, VASP code (Jennings *et al.*, 2014)

fcc site, it was observed that the O-O and Pt-O bond lengths of an fcc1 adsorbed O_2 state were within 0.007 Å of each other (see Tables 5.16 and 5.24). The angle between the Pt(111) nanorod facet plane and the O-O bond axis (α_{O-O}) was calculated to be 5° (compared to a 10° angle on a Pt(111)-p(2x2) fcc site). The adsorption energy of O_2 on the fcc1 site was calculated to be -0.63 eV/O_2 (see Table 5.30). The latter adsorption energy was only 0.03 eV more stable than the equivalent adsorption energy on the Pt(111)-p(2x2) fcc site.

fcc1^t site

The geometric properties of O_2 adsorption on the nanorod fcc1^{t1} site are presented in Figure 5.18 and Table 5.25. This equilibrium adsorption state was calculated to have an O-O bond length of 1.394 Å and Pt-O bond lengths of 2.166 Å (coordination to a none edge Pt atom), 2.251 Å(coordination to one edge Pt atom) and 2.026 Å (atop coordination to a none edge Pt atom). The angle between the Pt(111) nanorod facet plane and the O-O bond axis (α_{O-O}) was calculated to be 5° (compared to a 10° angle on Pt(111)-p(2x2) fcc site). The adsorption energy of O_2 on the fcc1^t site was calculated to be -0.58 eV/O_2 (see Table 5.30). The latter adsorption energy was only 0.02 eV less stable than the equivalent adsorption energy on the Pt(111)-p(2x2) fcc site.

b1a site

The geometric properties of O_2 adsorption on the nanorod b1a site are presented in Figure 5.19 and Table 5.26. This adsorption state consists of a 1.372 Å O-O bond length and 2.038 Å (coordination to Pt(111) terrace Pt atom) and 2.014 Å (coordination to edge Pt atom) Pt-O bond lengths. The adsorption energy of O_2 on the b1a site was calculated to be -0.73 eV/O_2 (see Table 5.30). As a result, O_2 was observed to be more stable on the b1a site than on a Pt(111)-p(2x2) bridge site.

b2a site

The geometric properties of O_2 adsorption on the nanorod b2a site are presented in Figure 5.20 and Table 5.27. This adsorption state consists of a 1.360 Å O-O bond length and has all Pt-O bond lengths equal to 2.032 Å. The vertical height of O_2 from the surface was calculated to be 1.896 Å. The latter was observed to be 0.014 Å shorter than the equivalent height on a Pt(111)-p(2x2) bridge site. The adsorption energy of O_2 on the b2a site was calculated to be -0.65 eV/O_2 (Table 5.30).

b1*a site

The equilibrium geometric properties of O_2 adsorption on the nanorod b1*a site are presented in Figure 5.21 and Table 5.28. This adsorption state consists of a 1.367 Å O-O bond length and the Pt-O bond lengths were calculated to be 1.981 Å (coordination to edge Pt atom) and 1.989 Å. The height of O_2 above the Pt(100) facet plane (along the plane normal) was calculated to be 1.792 Å. On the b1*a site O_2 adsorbs with an adsorption energy of -1.18 eV/O_2 (Table 5.30).

[1] ^{t} represents an alternative adsorption mode over the first fcc site from the edge atomic row

Table 5.24: Equilibrium geometric properties of O_2 on the fcc1 site of the Pt(mNR)-[5(111)×5(100)] nanorod model.

site: fcc1	Pt(mNR)-[5(111)×5(100)]
Δd_{h1} [Å]	1.569
Δd_{h2} [Å]	1.926
d_{O-O} [Å]	
This study	1.405
d_{Pt-O} [Å]	
This study	2.183x2, 2.026

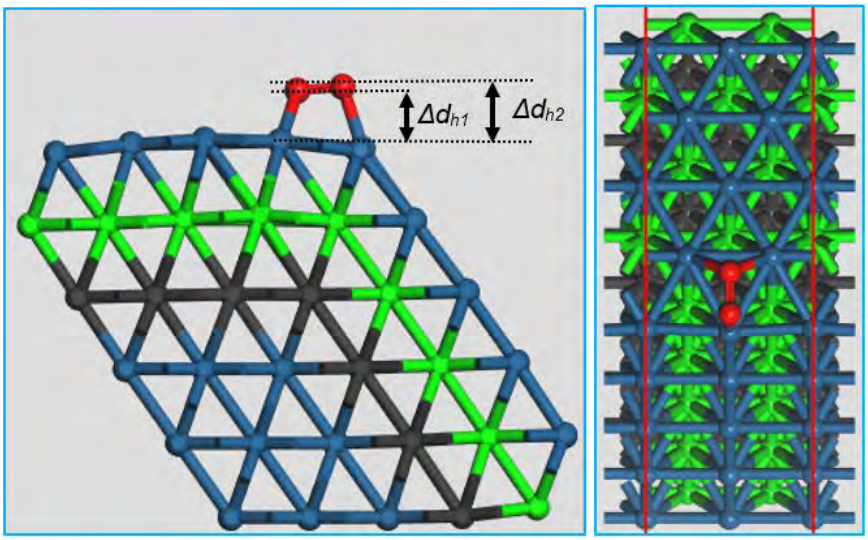

Figure 5.17: Equilibrium geometry of O_2 on the fcc1 site of the Pt(mNR)-[5(111)×5(100)] nanorod model. Side view (left) and [111] surface normal view (right).

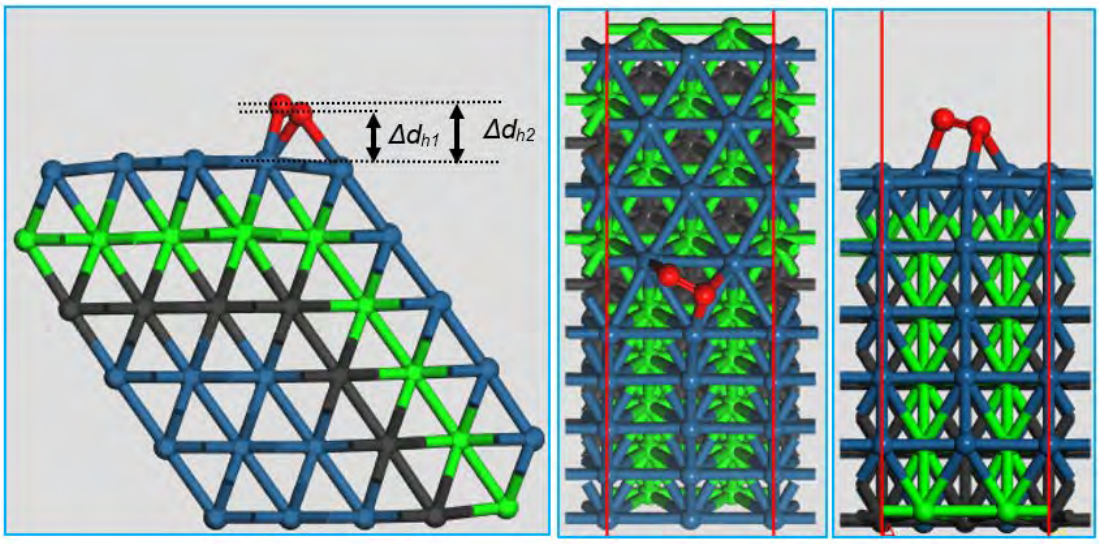

Figure 5.18: Equilibrium geometry of O_2 on the fcc1^t site of the Pt(mNR)-[5(111)×5(100)] nanorod model. Side view (left), [111] surface normal view (middle) and [100] surface view (right).

Table 5.25: Equilibrium geometric properties of O_2 on the fcc1^t site of the Pt(mNR)-[5(111)×5(100)] nanorod model.

site: fcc1^t	Pt(mNR)-[5(111)×5(100)]
Δd_{h1} [Å] Δd_{h2} [Å]	1.785 1.835
d_{O-O} [Å] This study	1.394
d_{Pt-O} [Å] This study	2.166, 2.251, 2.026

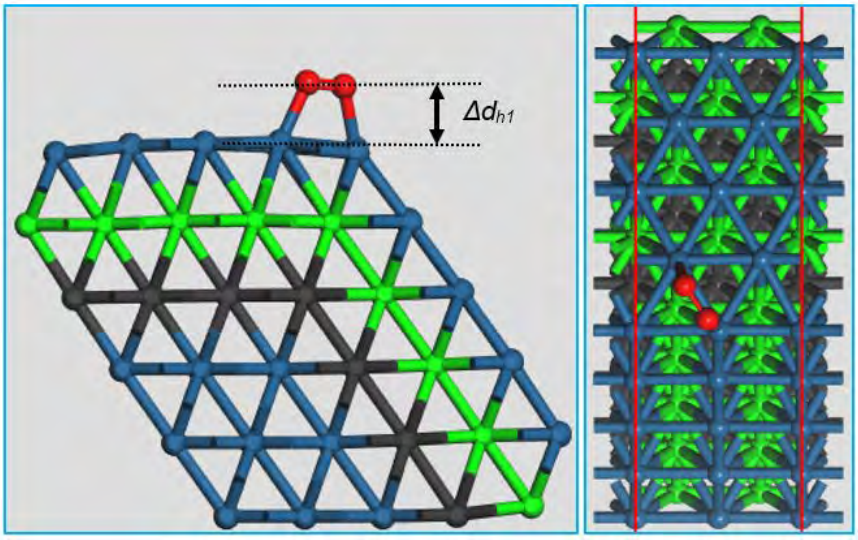

Figure 5.19: Equilibrium geometry of O_2 on the b1a site of the Pt(mNR)-[5(111)×5(100)] nanorod model. Side view (left), [111] surface normal view (middle) and [100] surface view (right).

Table 5.26: Equilibrium geometric properties of O_2 on the b1a site of the Pt(mNR)-[5(111)×5(100)] nanorod model.

site: b1a	Pt(mNR)-[5(111)×5(100)]
Δd_{h1} [Å]	1.844
d_{O-O} [Å] This study	1.372
d_{Pt-O} [Å] This study	2.038, 2.014

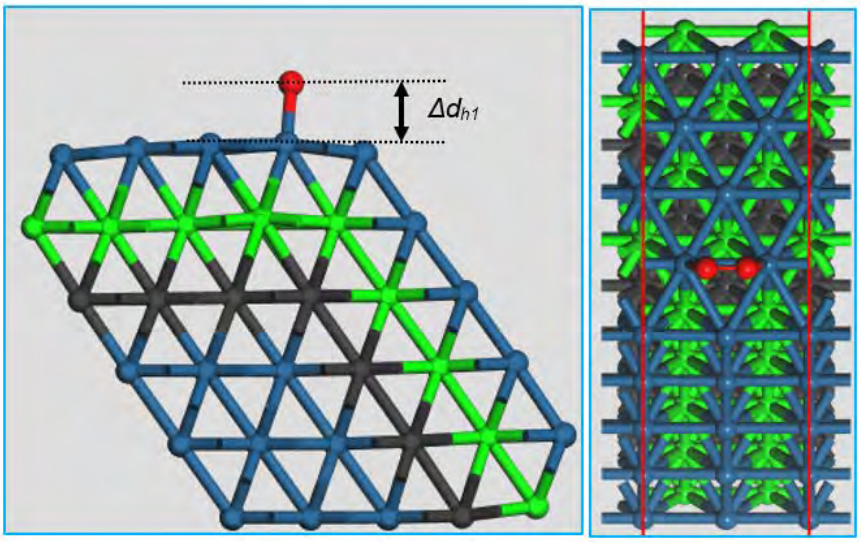

Figure 5.20: Equilibrium geometry of O_2 on the b2a site of the Pt(mNR)-[5(111)×5(100)] nanorod model. Side view (left), [111] surface normal view (middle) and [100] surface view (right).

Table 5.27: Equilibrium geometric properties of O_2 on the b2a site of the Pt(mNR)-[5(111)×5(100)] nanorod model.

site: b2a	Pt(mNR)-[5(111)×5(100)]
Δd_{h1} [Å]	1.896
d_{O-O} [Å] This study	1.360
d_{Pt-O} [Å] This study	2.032

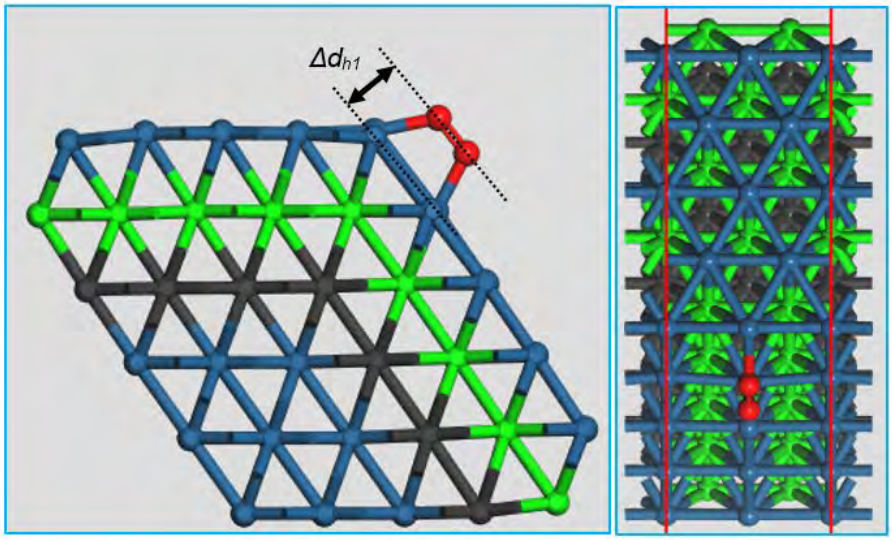

Figure 5.21: Equilibrium geometry of O_2 on the b1*a site of the Pt(mNR)-[5(111)×5(100)] nanorod model. Side view (left), [111] surface normal view (middle) and [100] surface view (right).

Table 5.28: Equilibrium geometric properties of O_2 on the b1*a site of the Pt(mNR)-[5(111)×5(100)] nanorod model.

site: b1*a	Pt(mNR)-[5(111)×5(100)]
Δd_{h1} [Å]	1.792
d_{O-O} [Å] This study	1.367
d_{Pt-O} [Å] This study	1.981, 1.989

b2*a site

The geometric properties of O_2 adsorption on the nanorod b2*a site are presented in Figure 5.22 and Table 5.29. This adsorption state consists of a 1.370 Å O-O bond length and two equal Pt-O bonds with lengths of 1.989 Å. The adsorption of O_2 on the b2*a site resulted in a 11° tilt (β) of O_2 off the Pt(100) facet normal and towards the edge (as shown in Figure 5.22). The latter angle is 6° smaller than the equivalent angle made by atomic O on the b2*a site. The adsorption energy of O_2 on the b2*a site was calculated to be -1.15 eV/O_2 (Table 5.30).

Table 5.29: Equilibrium geometric properties of O_2 on the b2*a site of the Pt(mNR)-[5(111)×5(100)] nanorod model.

site: b2*a	Pt(mNR)-[5(111)×5(100)]
Δd_{h1} [Å]	1.836
d_{O-O} [Å] This study	1.370
d_{Pt-O} [Å] This study	1.989
β	11°

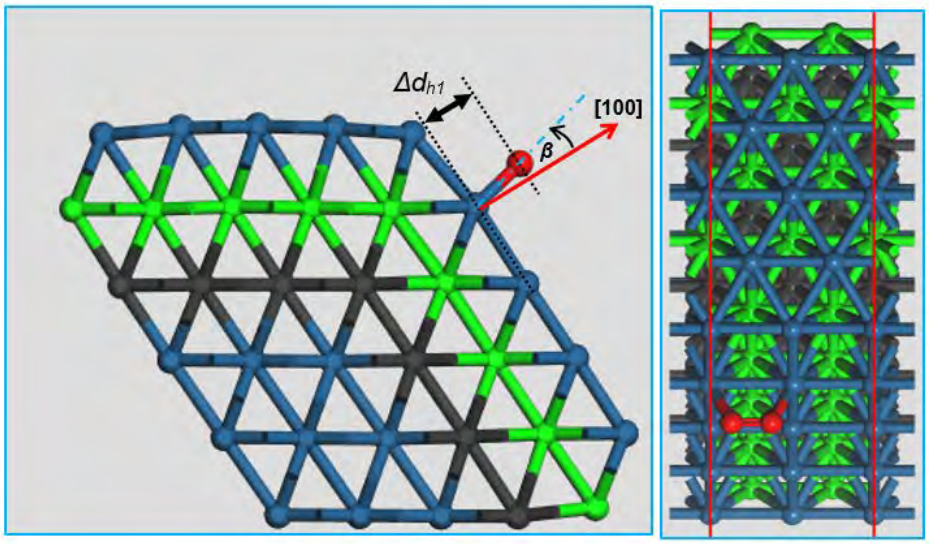

Figure 5.22: Equilibrium geometry of O_2 on the b2*a site of the Pt(mNR)-[5(111)×5(100)] nanorod model. Side view (left), [111] surface normal view (middle) and [100] surface view (right).

Discussion

The adsorption of O_2 on sites near the edge region of the Pt(mNR)-[5(111)×5(100)] nanorod model was investigated. It was observed that O_2 interacts strongest with the EB site with an adsorption energy of -1.58 eV/O_2. On other near-edge adsorption sites, O_2 adsorbs with an adsorption energy, in a decreasing order, of -1.18 eV/O_2 (b1*a), -1.15 eV/O_2 (b2*a), -0.88 eV/O_2 (hcp1), -0.73 eV/O_2 (b1a), -0.65 eV/O_2 (b2a), -0.63 eV/O_2 (fcc1) and -0.58 eV/O_2 (fcc1^t). Therefore, compared to the second most stable adsorption state near the edge, adsorption on a b1*a site, adsorption of O_2 on an EB site is 0.4 eV more stable (compared to 0.38 eV for atomic O adsorption). For atomic O adsorption on near-edge sites, the b1*a state was observed to be more stable than the b2*a state; for O_2 adsorption the latter was reversed. Moreover, the adsorption strength of O_2 was observed to be stronger for the Pt(100) facet bound states compared to the Pt(111) facet bound states. The latter was also the case for atomic O adsorption. A comprehensive comparison to literature could not be made due to the lack of detailed data on O_2 adsorption on nanorod and step-surface edge sites.

The interaction of O_2 with different bridge sites was observed to be relatively similar on the nanorod near-edge region as on extended surfaces. The geometric structure of O_2 on the b2a site (Figure 5.20) was observed to be relatively similar to the adsorption geometric structure of O_2 on a Pt(111)-p(2x2) slab bridge site. The same was also observed between the adsorption geometric structure of O_2 on the b2*a site and that on a Pt(100)-p(2x2) slab bridge site. In terms of geometric structure, it was observed that the near edge Pt(111) facet bound bridge states (b1a and b2a) were similar to Pt(111)-p(2x2) bridge adsorption state. The latter was also true for Pt(100) facet bound bridge states (b1*a and b2*a) and Pt(100)-p(2x2) bridge adsorption state. Slight geometric differences in bridge states were within 0.01 Å.

The stable O_2 adsorption state on the hcp1 site was observed to be geometrically different from the O_2 adsorption state on Pt(111)-p(2x2) hcp site. The O-O bond length was calculated to be 0.046 Å longer on the hcp1 site than on a Pt(111)-p(2x2) hcp site. The Pt-O bond lengths were calculated to be ca. 0.09 Å shorter on the hcp1 site than on the Pt(111)-p(2x2) hcp site. Moreover, on the hcp1 site Δd_{h1} and Δd_{h2} were calculated to be 1.575 Å and 1.769 Å, respectively; compared to 1.696 Å (Δd_{h1}) and 1.900 Å (Δd_{h2}) on Pt(111)-p(2x2) hcp site. Differences were also observed in the adsorption energies of O_2. On the hcp1 site O_2 was calculated adsorb 0.35 eV more stable than on a Pt(111)-p(2x2) hcp site. Only slight differences in the adsorption geometric and energetic (ca. 0.05 eV) properties were observed between O_2 adsorption on fcc1, fcc1^t and Pt(111)-p(2x2) fcc site.

Table 5.30: Adsorption energy of O_2 on the Pt(mNR)-[5(111)×5(100)] nanorod near-edge high-symmetry sites.

reference state	O_2	O_2 + ZPE
Units	[eV/O_2]	[eV/O_2]
Adsorption site:	EB	
This study	-1.58	-1.53
Literature	-1.68[a], -1.50[b]	
Adsorption site:	hcp1	
This study	-0.88	-0.84
Literature	-0.99[a]	
Adsorption site:	fcc1	
This study	-0.63	-0.59
Literature	-0.88[b]	
Adsorption site:	$fcc1^t$	
This study	-0.58	-0.53
Adsorption site:	b1a	
This study	-0.73	-0.69
Adsorption site:	b2a	
This study	-0.65	-0.60
Adsorption site:	b1*a	
This study	-1.18	-1.12
Adsorption site:	b2*a	
This study	-1.15	-1.10

a 116-atom truncated octahedral Pt cluster, PAW−PW91, VASP code (Jennings *et al.*, 2014)
b Pt(211)-p(3x1), USPP−PW91 (Šljivančanin & Hammer, 2002)

Table 5.31: Calulated vibrational frequency modes of adsorbed O_2 on the Pt(mNR)-[5(111)×5(100)] nanorod near-edge high-symmetry sites.

nanorod facet	edge	Pt(111)					Pt(100)	
Adsorption site:	EB	hcp1	fcc1	$fcc1^t$	b1a	b2a	b1*a	b2*a
υ_i [cm^{-1}]	829	713	781	814	849	897	865	862
	574	495	477	498	542	548	551	562
	459	354	353	360	367	369	425	416
	287	312	313	288	221	233	276	268
	214	206	215	226	123	155	208	202
	62	174	132	103	94	111	101	80

Chapter 6

Edge effect on terrace sites

6.1 Introduction

Studies which investigate the overall ORR activity as obtained over polycrystalline nanoparticles using DFT, generally assume that the different polycrystalline facets are isolated (Greeley *et al.*, 2007; Tritsaris *et al.*, 2011; Wei & Liu, 2013). The overall activity is then treated as a weighted average of the activities of different sites considered, i.e. Pt(111), Pt(100) and Pt(211) contributions (see detailed discussion in Subsection 1.3.4). Tritsaris *et al.* (2011) briefly investigate this assumption by looking at the extent of the edge effect on a Pt(111) terrace of a Pt(533) step-surface. They calculate the adsorption free energies of atomic O and OH at various distances from the step-edge of a Pt(533) step-surface. From this they reported that beyond the first atomic row from the edge atomic row the adsorption free energies of atomic O and OH quickly converges to the corresponding adsorption free energies on terrace sites.

This chapter investigates the extent of the nanorod edge effect on Pt(111) and Pt(100) nanorod facets. To the best of my knowledge, the edge effect on the Pt(100) facet has not been investigated elsewhere. The change in adsorption energy of O_2 as a function of distance from the edge atomic row is correlated with the corresponding change in d-band center (ε_{dc}). For transition metals a strong correlation between adsorption energy of an adsorbate and the d-band center of the adsorption site has been reported (Hammer *et al.*, 1996). It is generally observed that the adsorption energy increases with increasing d-band center (Hammer *et al.*, 1996; Mavrikakis *et al.*, 1998; Hammer *et al.*, 1997; Greeley *et al.*, 2002; Calle-Vallejo *et al.*, 2015). Since site geometric symmetry may influence the adsorption strength (e.g. O_2 adsorption on hcp site versus fcc site: see Table 5.18), all comparison herein are made for geometrically equivalent sites.

6.2 Computational method

Using two nanorod models, Pt(mNR)-[7(111)×5(100)] and Pt(mNR)-[5(111)×7(100)], the adsorption of atomic O and O_2 was investigated along the nanorod terrace sites, i.e. from EB sites towards central terrace sites. The use of nanorod models with wider terraces was motivated by the desire to capture a convergence trend from edge towards central terrace sites. Therefore, for each adsorption geometry, three adsorption states were considered. These states correspond to adsorption between edge and first atomic rows from the edge (EB+1: adsorption sites), adsorption between first and second atomic rows from the edge (EB+2: adsorption sites) and finally, adsorption between second and third atomic rows from the edge (EB+3: adsorption sites). As was the case for the optimized Pt(mNR)-[5(111)×5(100)] nanorod model, the vacuum spacing, k-point grid and cut-off energy were set to 12 Å, 1x5x1 and 400 eV, respectively. Only the top three layers were allowed to relax to a force below 0.02 eV/Å for each atom in all geometry optimization calculations, the other platinum atoms were fixed in their bulk optimized geometric positions. The computational setup and method (for geometry optimization calculations) was as described in subsection 2.4.3. Results obtained from using a Pt(mNR)-[5(111)×5(100)] nanorod model are presented in Appendix B.2.

6.3 O adsorption along the nanorod terrace sites

The adsorption properties of atomic O and O_2 on different Pt surface sites were presented in Chapter 5. For atomic O it was observed that on Pt(111) surfaces the bridge adsorption states were unstable. Furthermore, on nanorod near edge sites it was observed that the atop and hcp1 adsorption states were also unstable. On the Pt(100) facet of the Pt(mNR)-[5(111)×5(100)] nanorod model, the 4fh1 and atop1* adsorption states were observed to be unstable as they converged to bridge adsorption states (see Chapter 5). Therefore, the effect of the edge on the adsorption energy of atomic O along nanorod terrace sites was investigated for fcc and bridge adsorption geometries along the Pt(111) and Pt(100) nanorod facet, respectively. Figure 6.2 presents the calculated adsorption energies of atomic O as a function of distance from the nanorod edge atomic row (further data is given in Appendix B.2).

The adsorption energy of atomic O along the Pt(111) nanorod facet sites was investigated using the Pt(mNR)-[7(111)×5(100)] nanorod model. The Pt(mNR)-[5(111)×7(100)] nanorod model was used for investigating the adsorption of atomic O along the Pt(100) nanorod facet sites. On EB sites of Pt(mNR)-[7(111)×5(100)] and Pt(mNR)-[5(111)×7(100)] nanorod models, the adsorption energy of atomic O was calculated to be -1.59 eV/$\frac{1}{2}O_2$ and -1.54 eV/$\frac{1}{2}O_2$, respectively. A similar adsorption energy of atomic O of -1.61 eV/$\frac{1}{2}O_2$ on an EB site of a Pt(mNR)-[5(111)×5(100)] nanorod model was also calculated (Table 5.13 and Figure 5.7). The adsorption properties of atomic O along the Pt(111) and Pt(100) nanorod facet sites are presented in the following subsections.

6.3.1 Atomic O along Pt(111) facet sites

The geometric and energetic adsorption properties of atomic O on fcc sites along the Pt(111) facet of the Pt(mNR)-[7(111)×5(100)] nanorod model are presented in Figure 6.1a and Table 6.1. Atomic O was observed to adsorb ca. 0.05 Å closer to the Pt(111) facet plane at fcc1 site than at the other fcc sites, i.e. fcc2 and fcc3. The geometric structures of atomic O adsorption at the fcc2 and fcc3 sites were observed to be relatively similar to equivalent adsorption structure on a Pt(111)-p(2x2) fcc site (Table 6.1). The adsorption energy of atomic O was observed to be relatively constant from the fcc1 adsorption state to the fcc3 adsorption state − only a 0.08 eV change in energy was observed (Table 6.1). The adsorption energy of atomic O on the fcc3 site (central terrace site) was observed to be 0.14 eV weaker than the equivalent adsorption energy of atomic O on a Pt(111)-p(2x2) fcc site. Figure 6.2 presents the adsorption energy of atomic O along the Pt(111) nanorod facet sites. Compared to the change in adsorption energy of atomic O from the EB state to the fcc1 state (0.53 eV), it was observed that further changes in the adsorption energy of atomic O from the fcc1 site towards the fcc3 site were relatively small ($\leq$ 0.08 eV).

Table 6.1: Calculated equilibrium geometric and energetic adsorption properties of atomic O on the fcc1, fcc2 and fcc3 sites of the Pt(mNR)-[7(111)×5(100)] nanorod model.

site	$\Delta E_{O,\,ads}$ [eV/$\frac{1}{2}O_2$]	d_{Pt-O} [Å]	Δd_{h1} [Å]
fcc1	-1.08	2.099, 2.040, 2.041	1.101
fcc2	-1.03	2.033, 2.046, 2.046	1.152
fcc3	-1.00	2.045, 2.048, 2.047	1.161
slab-fcc[a]	-1.14	2.041, 2.041, 2.041	1.149

a Pt(111)-p(2x2) slab fcc site

6.3.2 Atomic O along Pt(100) facet sites

The geometric and energetic adsorption properties of atomic O on b2* sites[1] along the Pt(100) facet of the Pt(mNR)-[5(111)×7(100)] nanorod model are presented in Figure 6.1b and Table 6.2. Along the Pt(100) nanorod facet, only the bridge sites parallel to the edge atomic row, i.e. b2*a, b2*b and b2*c, are presented. The b2*a, b2*b and b2*c adsorption states of atomic O were observed to have

[1] b2* sites are bridge sites parallel to the edge atomic row−these sites are found on the Pt(100) nanorod facet.

Pt-O bond lengths of ca. 1.95 Å. The latter Pt-O bond lengths were also equal to the bond lengths corresponding to atomic O adsorption on a Pt(100)-p(2x2) bridge site (see Table 6.2). The height of atomic O above the Pt(100) facet plane, Δd_{h1}, was calculated to be 1.273 Å, 1.276 Å and 1.281 Å for the b2*a, b2*b and b2*c adsorption states, respectively. Compared to Δd_{h1} for atomic O on a Pt(100)-p(2x2) bridge site, Δd_{h1} for the b2*c site was ca. 0.01 Å shorter. The adsorption energies of atomic O corresponding to the above geometries are presented in Table 6.2. The adsorption energy of atomic O was observed to vary by 0.07 eV from the b2*a site to the b2*c site. Figure 6.2 presents the adsorption energy of atomic O along the Pt(100) nanorod facet sites. Compared to the change in adsorption energy of atomic O from the EB state to the b2*a state (0.31 eV), it was observed that further changes in the adsorption energy of atomic O from the b2*a site towards the b2*c site were relatively small ($\leq$ 0.07 eV). The adsorption energy of atomic O along the Pt(100) nanorod facet bridge sites was observed to be relatively similar to the equivalent adsorption energy on a Pt(100)-p(2x2) bridge site (Table 6.2). The adsorption energy trend of atomic O along b1* sites [2] was observed to similar to the adsorption trend of atomic O along b2* sites (see Figure 6.2).

Table 6.2: Calculated equilibrium geometric and energetic adsorption properties of atomic O on the b2*a, b2*b and b2*c sites of the Pt(mNR)-[5(111)×7(100)] nanorod model.

site	$\Delta E_{O,\,ads}$ [eV/$\frac{1}{2}O_2$]	d_{Pt-O} [Å]	Δd_{h1} [Å]
b2*a	-1.23	1.950, 1.949	1.273
b2*b	-1.21	1.947, 1.947	1.276
b2*c	-1.16	1.948, 1.948	1.281
slab-bridge[a]	-1.14	1.950, 1.950	1.286

a Pt(100)-p(2x2) slab bridge site

6.4 O_2 adsorption along nanorod terrace sites

The edge effect on the adsorption energy of O_2 was investigated by considering adsorption along different nanorod terrace sites. Along the Pt(111) nanorod facet, the fcc, hcp and b2[3] adsorption sites were considered. Along the Pt(100) nanorod facet, the b2* adsorption sites ware considered. The adsorption energies of O_2 along the fcc, hcp, b2 and b2* adsorption sites are presented in Figure 6.5. The following subsections present the geometric and energetic adsorption properties of O_2 along the Pt(111) and Pt(100) nanorod facets.

6.4.1 O_2 along Pt(111) facet sites

O_2 along fcc sites

The geometric and energetic adsorption properties of O_2 on fcc sites along the Pt(111) facet of the Pt(mNR)-[7(111)×5(100)] nanorod model are presented in Figure 6.3a and Table 6.3. The adsorption geometry of O_2 on fcc2 and fcc3 adsorption sites was observed to be relatively similar to the equivalent adsorption geometry on a Pt(111)-p(2x2) fcc site (Table 6.3). On the fcc1 adsorption site the O-O bond length was observed to be 1.408 Å. On other fcc sites (including a Pt(111)-p(2x2) fcc site) the O-O bond length was calculated to be ca. 1.40 Å (see Table 6.3). On fcc1 site it was observed that O_2 adsorb much closer to the Pt(111) facet plane (Δd_{h1} = 1.562 Å) than on the fcc2 and fcc3 sites. The angle between the O-O bond axis and the Pt(111) facet plane (α_{O-O}) was calculated to be similar for O_2 adsorption on fcc2, fcc3 and Pt(111)-p(2x2) slab fcc site. For O_2 adsorption on the fcc1 site, the α_{O-O} value is half that on other fcc sites listed above–this is potentially due to the direct interaction of O_2 with edge atomic row Pt atoms. The adsorption energy of O_2 was also observed to be relatively stronger on the fcc1 site (-0.69 eV/O_2) than on the fcc2 and fcc3 adsorption sites (see Table 6.3). The difference between the adsorption energy of O_2 on fcc1 and fcc3 was calculated to be 0.27 eV (with

[2] b1* sites are bridge sites perpendicular to the edge atomic row − these sites are found on the Pt(100) nanorod facet.
[3] b2 site are bridge sites parallel to the edge atomic row−these sites are found on the Pt(111) nanorod facet.

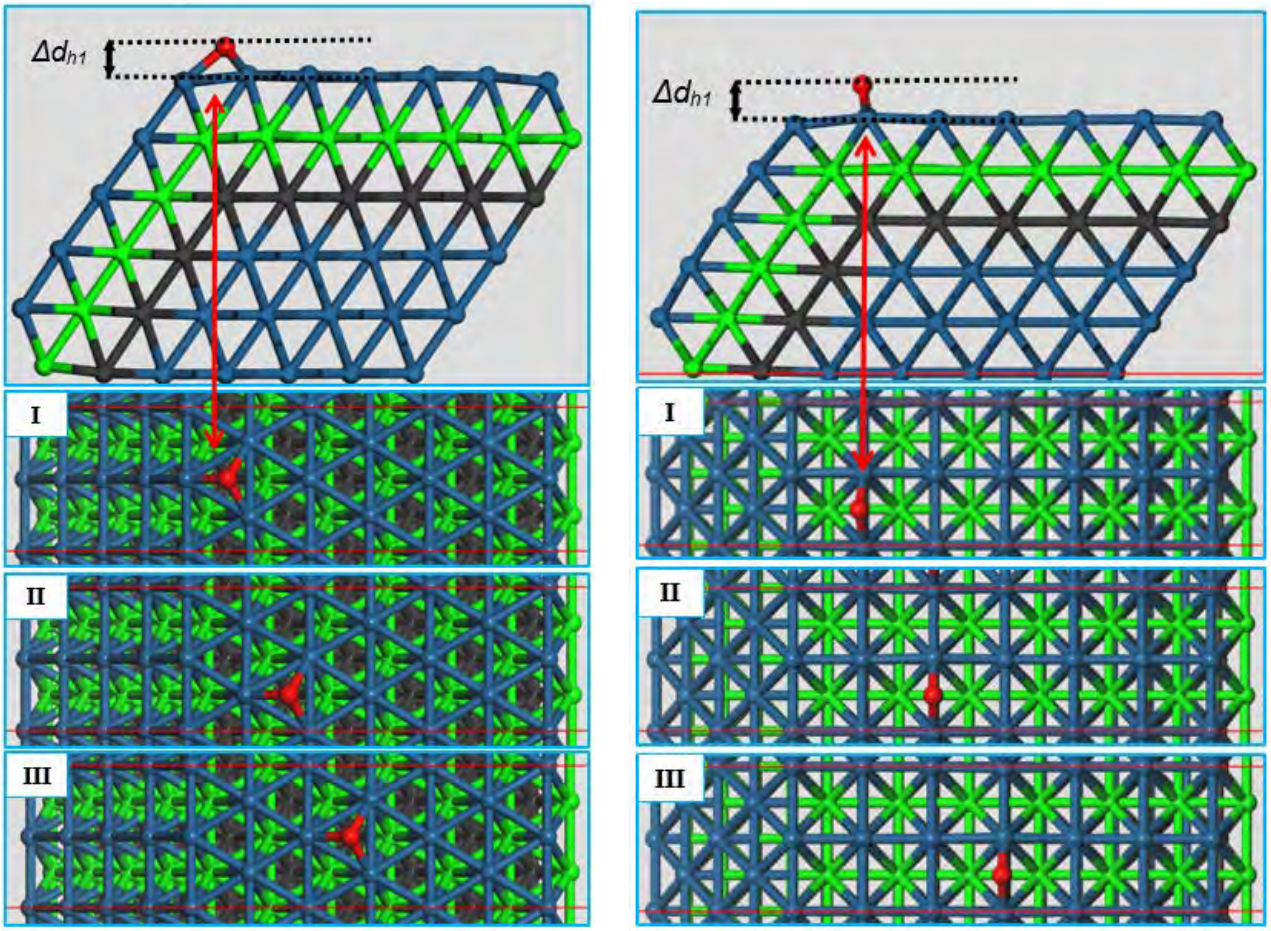

(a) Pt(111) nanorod facet—fcc adsorption states. (b) Pt(100) nanorod facet—bridge adsorption states.

Figure 6.1: Equilibrium adsorption geometries of atomic O on sites along the (a) Pt(111) and (b) Pt(100) nanorod facets. Top: side view, bottom (I, II, III): top view.

stronger adsorption on the fcc1 site). The adsorption strength of O_2 on the fcc1 site was observed to be 0.88 eV weaker than the adsorption strength on the EB site (see Figure 6.5).

Table 6.3: Calculated equilibrium geometric and energetic adsorption properties of O_2 on the fcc1, fcc2 and fcc3 sites of the Pt(mNR)-[7(111)×5(100)] nanorod model.

site	$\Delta E_{O,\,ads}$ [eV/O_2]	d_{O-O} [Å]	d_{Pt-O} [Å]	Δd_{h1} [Å]	α_{O-O}
fcc1	-0.69	1.408	2.030, 2.175, 2.174	1.562	5
fcc2	-0.45	1.397	2.031, 2.177, 2.177	1.598	9
fcc3	-0.42	1.395	2.032, 2.183, 2.183	1.605	10
slab-fcc[a]	-0.60	1.398	2.019, 2.178, 2.178	1.629	10

a Pt(111)-p(2x2) slab fcc site

O_2 along hcp sites

The geometric and energetic adsorption properties of O_2 on hcp sites along the Pt(111) facet of the Pt(mNR)-[7(111)×5(100)] nanorod model are presented in Figure 6.3b and Table 6.4. The adsorption geometry of O_2 on the hcp1 site was observed to be significantly different from those on other hcp sites. The hcp1 adsorption state of O_2 consisted of a O-O bond length of 1.431 Å, which was 0.043 Å longer than the equivalent bond length on a Pt(111)-p(2x2) hcp site. The Pt-O bond length of the hcp1 adsorption state were also significantly different from the equivalent bond lengths on the hcp2, hcp3 and Pt(111)-p(2x2) hcp sites (see Table 6.4). Overall O_2 was observed to adsorb ca. 0.34 Å closer to the Pt(111) facet on the hcp1 site than on a Pt(111)-p(2x2) hcp sites. Moreover, the angle

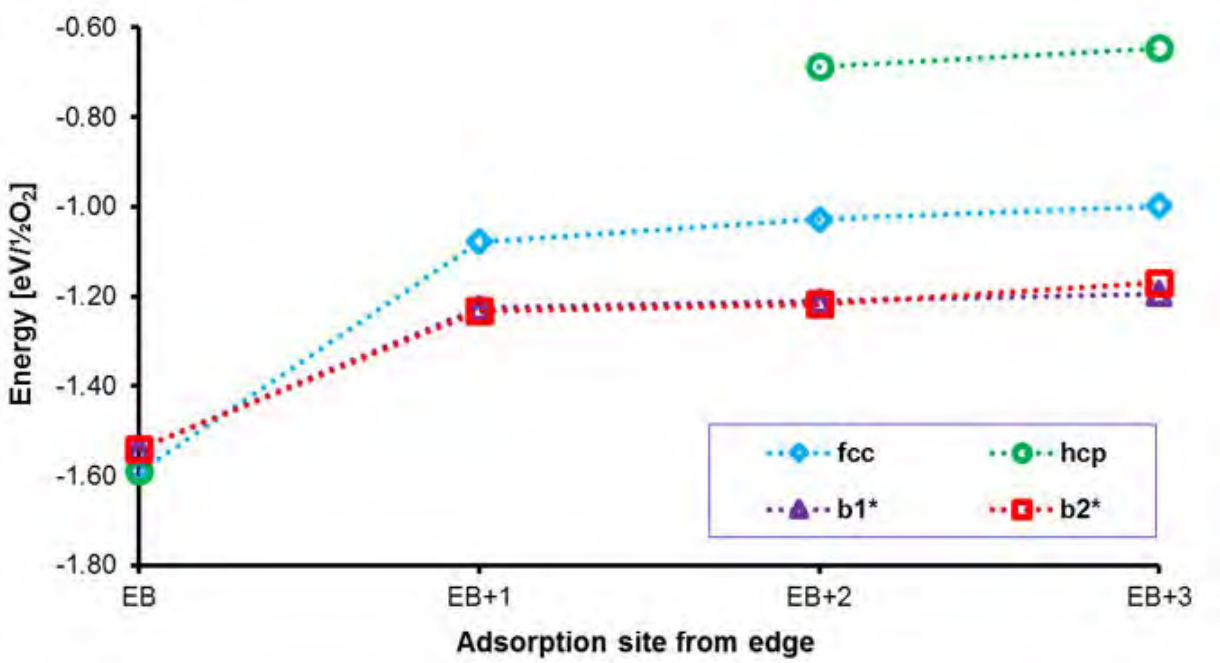

Figure 6.2: Adsorption energies of atomic O along Pt(111) and Pt(100) terrace sites of the Pt(mNR)-[7(111)×5(100)] and Pt(mNR)-[5(111)×7(100)] nanorod models, respectively. The terrace sites are: EB (edge-bridge adsorption), EB+1 (fcc1, b1*a and b2*a), EB+2 (fcc2, hcp2, b1*b and b2*b) and EB+3 (fcc3, hcp3, b1*c and b2*c).

between the O-O bond axis and the Pt(111) facet plane was calculated to be 17° (compared to 10° − hcp2, 8° − hcp3 and 8° − Pt(111)-p(2x2) hcp site). The adsorption strength of O_2 was also observed to be stronger on the hcp1 site than on the hcp2, hcp3 and Pt(111)-p(2x2) sites. On the EB site O_2 adsorbs with an adsorption energy of -1.57 eV/O_2 whilst on the hcp1 site the adsorption energy of O_2 was calculated to be -0.91 eV/O_2. Therefore, a 0.66 eV adsorption energy decrease was observed from the EB adsorption state towards the hcp1 state. Figure 6.5 presents the adsorption energy of O_2 along different hcp adsorption sites.

Table 6.4: Calculated equilibrium geometric and energetic adsorption properties of O_2 on the hcp1, hcp2 and hcp3 sites of the Pt(mNR)-[7(111)×5(100)] nanorod model.

site	$\Delta E_{O,\,ads}$ [eV/O_2]	d_{O-O} [Å]	d_{Pt-O} [Å]	Δd_{h1} [Å]	α_{O-O}
hcp1	-0.91	1.431	2.141, 2.141, 2.048	1.356	17
hcp2	-0.36	1.389	2.220, 2.220, 2.049	1.652	10
hcp3	-0.29	1.379	2.235, 2.236, 2.053	1.731	8
slab-hcp[a]	-0.45	1.388	2.224, 2.224, 2.042	1.696	8

a Pt(111)-p(2x2) slab hcp site

O_2 along b2 sites

The geometric and energetic adsorption properties of O_2 on b2 sites along the Pt(111) facet of the Pt(mNR)-[7(111)×5(100)] nanorod model are presented in Figure 6.4a and Table 6.5. The adsorption geometric properties of O_2 on b2b and b2c were the same as the adsorption properties on a Pt(111)-p(2x2) bridge site −with O-O and Pt-O bond lengths of ca. 1.36 Å and 2.04 Å, respectively. Slight geometric differences from the above were observed for the b2a adsorption state. On the b2a O_2 was observed to adsorb ca. 0.02 Å closer to the Pt(111) facet plane than on the other bridge sites, i.e. b2b and b2c. The adsorption energy of O_2 on the b2a site was calculated to be -0.70 eV/O_2 (Table 6.5). The latter energy decreases by 0.17 eV from b2a to b2b and b2c adsorption states. Compared to adsorption on a Pt(111)-p(2x2) bridge site, O_2 was observed to adsorb 0.08 eV weaker on b2b and

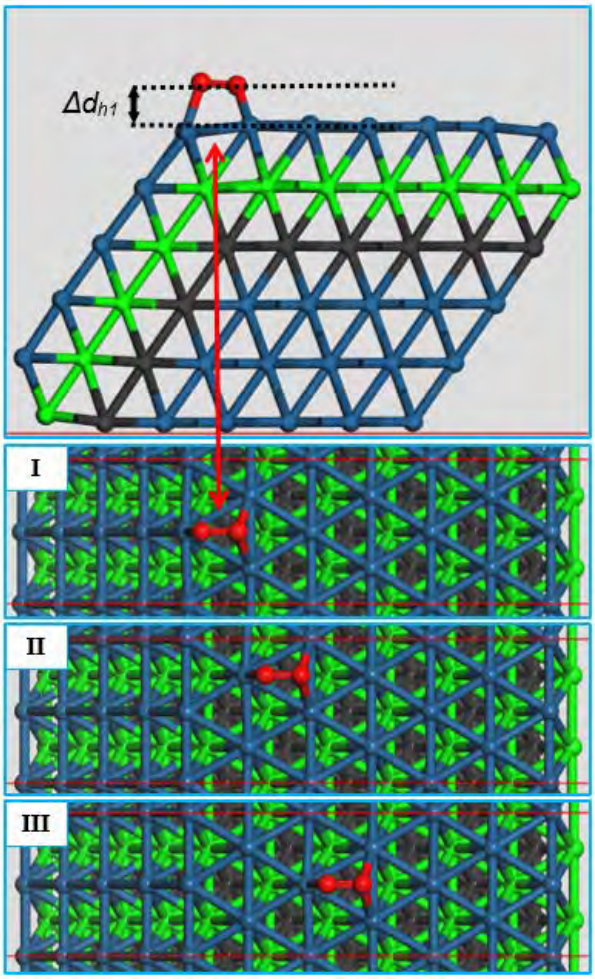

(a) Pt(111) nanorod facet—fcc adsorption states.

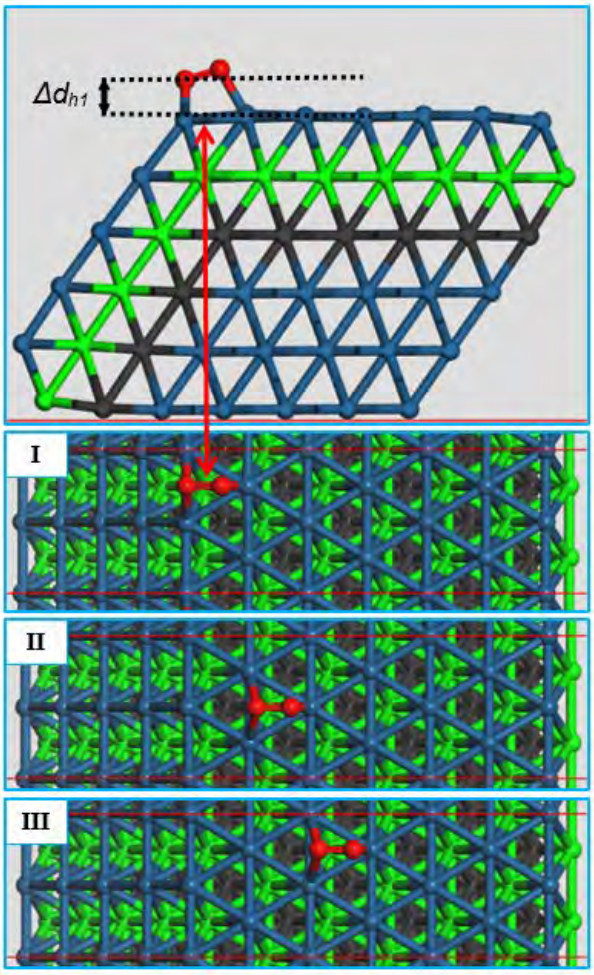

(b) Pt(111) nanorod facet—hcp adsorption states.

Figure 6.3: Equilibrium adsorption geometries of O_2 along the Pt(111) nanorod terrace sites (a) fcc and (b) hcp. Top: side view, bottom (I, II, III): top view.

b2c sites (Pt(111) central terrace bridge sites). Figure 6.5 presents the adsorption energy of O_2 along different b2 adsorption sites.

Table 6.5: Calculated equilibrium geometric and energetic adsorption properties of O_2 on the b2a, b2b and b2c sites of the Pt(mNR)-[7(111)×5(100)] nanorod model.

site	$\Delta E_{O,\,ads}$ [eV/O_2]	d_{O-O} [Å]	d_{Pt-O} [Å]	Δd_{h1} [Å]
b2a	-0.70	1.363	2.026, 2.026	1.888
b2b	-0.53	1.357	2.037, 2.037	1.906
b2c	-0.53	1.357	2.040, 2.039	1.909
slab-bridge[a]	-0.61	1.359	2.037, 2.037	1.910

a Pt(111)-p(2x2) slab bridge site

6.4.2 O_2 along Pt(100) facet sites

O_2 along b2* sites

The geometric and energetic adsorption properties of O_2 on b2* sites along the Pt(100) facet of the Pt(mNR)-[5(111)×7(100)] nanorod model are presented in Figure 6.4b and Table 6.6. The adsorption geometry of O_2 on all b2* sites was observed to be relatively similar to the adsorption geometry on Pt(100)-p(2x2) bridge site (see Table 6.6). The O-O bond length on b2* sites was observed to be within ca. 0.005 Å variation of that for O_2 adsorbed on a Pt(100)-p(2x2) bridge site. On b2*a O_2

was observed to adsorb 0.017 Å closer to the Pt(100) facet plane than on Pt(100)-p(2x2) bridge site. The adsorption energy of O_2 on the b2*a site was observed to be 0.02 eV stronger than on the b2*c site. Furthermore, it was observed that on the b2*c site O_2 adsorbs more strongly by 0.05 eV than on a Pt(100)-p(2x2) bridge site. Figure 6.5 presents the adsorption energy of O_2 along different b2* adsorption sites. The adsorption energy of O_2 along b2* sites was observed to be equivalent to the adsorption energy along b1* sites[4] (see Table 6.7 and Figure 6.5).

Table 6.6: Calculated equilibrium geometric and energetic adsorption properties of O_2 on the b2*a, b2*b and b2*c sites of the Pt(mNR)-[5(111)×7(100)] nanorod model.

site	$\Delta E_{O,\,ads}$ [eV/O_2]	d_{O-O} [Å]	d_{Pt-O} [Å]	Δd_{h1} [Å]
b2*a	-1.18	1.369	1.986, 1.986	1.818
b2*b	-1.16	1.364	1.985, 1.986	1.827
b2*c	-1.16	1.366	1.984, 1.984	1.826
slab-bridge[a]	-1.11	1.364	1.989, 1.989	1.835

a Pt(111)-p(2x2) slab bridge site

Table 6.7: Calculated equilibrium geometric and energetic adsorption properties of O_2 on the b1*a, b1*b and b1*c sites of the Pt(mNR)-[5(111)×7(100)] nanorod model.

site	$\Delta E_{O,\,ads}$ [eV/O_2]	d_{O-O} [Å]	d_{Pt-O} [Å]	Δd_{h1} [Å]
b1*a	-1.15	1.368	1.980, 1.988	1.766
b1*b	-1.13	1.366	1.991, 1.989	1.795
b1*c	-1.13	1.362	1.996, 1.998	1.827
slab-bridge[a]	-1.11	1.364	1.989, 1.989	1.835

a Pt(111)-p(2x2) slab bridge site

6.5 Correlation of adsorption energy with site properties

The adsorption energy along the b2 (i.e. b2a, b2b and b2c) and b2* (i.e. b2*a, b2*b and b2*c) sites were correlated to the d-band center energies of the platinum atoms participating in the respective adsorption states. Since different geometries may result in varying adsorption energies, in this section only the bridge geometries are considered. Two cases were considered for investigating the correlation between the adsorption energy of O_2 and the d-band center of the adsorption site and consequently the site coordination. A further empirical correlation between the adsorption energy of O_2 and the site coordination number was investigated.

Case I

The adsorption and d-band center energies were calculated using Pt(mNR)-[7(111)×5(100)] and Pt(mNR)-[5(111)×7(100)] nanorod models. In all calculations corresponding to *Case-I*, the Pt-Pt bond lengths were fixed at 2.811 Å, i.e. the nanorod models were bulk terminated. For all calculations, a rigid O_2 adsorbate was positioned perpendicular to the surface plane with Pt-O and O-O bond lengths of 2.03 Å and 1.36 Å, respectively. The latter bond lengths correspond closely to the equilibrium adsorption geometry of O_2 on a Pt(111)-p(2x2) bridge site (see subsection 5.3.1). Single point energy calculations were then conducted to obtained the adsorption energy of O_2 along b2 and b2* adsorption sites. For the adsorption energy on EB sites, two geometries were considered. On the Pt(mNR)-[7(111)×5(100)] nanorod EB site, O_2 was positioned perpendicular to the Pt(111) facet plane. On the Pt(mNR)-[5(111)×7(100)] nanorod EB site, O_2 was positioned perpendicular to the Pt(100) facet plane. The d-band center energies of the edge, the first, second and third atomic row from the edge, along the Pt(111) and Pt(100) facets, were calculated. This case corresponds closely

[4] b1* site are bridge sites perpendicular to the edge atomic row−these sites are found on the Pt(100) nanorod facet.

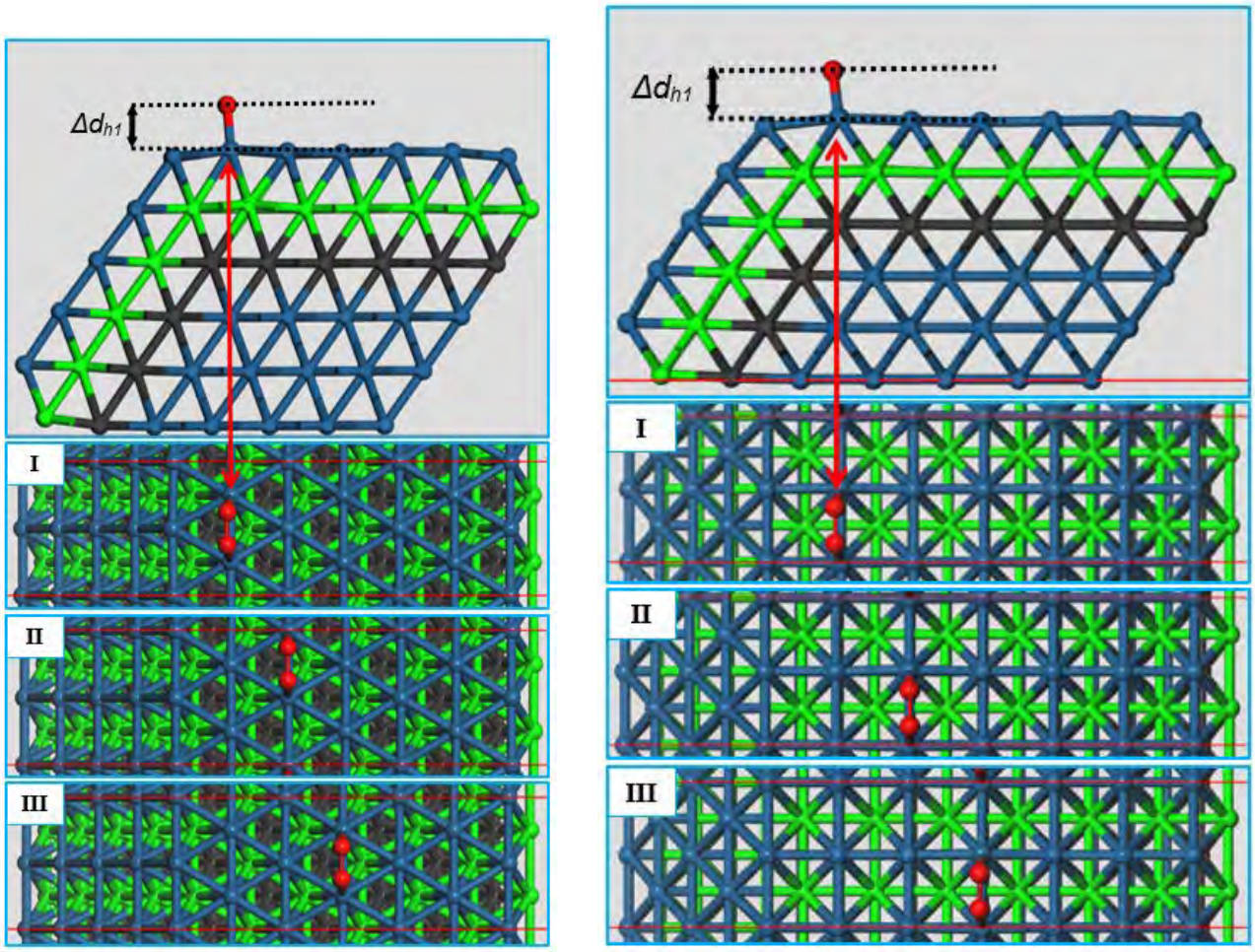

(a) Pt(111) nanorod facet—b2 adsorption states. (b) Pt(100) nanorod facet—b2* adsorption states.

Figure 6.4: Equilibrium adsorption geometries of O_2 along the (a) Pt(111) nanorod terrace b2 sites and (b) Pt(100) nanorod terrace b2* sites. Top: side view, bottom (I, II, III): top view.

with the approach applied by Hammer *et al.* (1997) who used bulk terminated Pt surfaces and a fixed CO adsorption geometry to generate a correlation between the adsorption energy of CO and the d-band center of different surface atoms.

Case II

In this case the adsorption energies reported in Tables 6.5 and 6.6 were correlated with the corresponding d-band center energies (and coordination number of the adsorption sites). The d-band center energies were calculated from the pDOS of relaxed clean Pt(mNR)-[7(111)×5(100)] and Pt(mNR)-[5(111)×7(100)] nanorod models. The geometric adsorption structures of O_2 along the b2 and b2* adsorption sites are presented in Tables 6.5 and 6.6. *Case-II* differs from *Case-I* in the fact that it considers surface relaxation on both the d-band center and adsorption energy calculations. Therefore, whilst the d-band center energy calculated in *Case-I* is based on a system with a constant Pt-Pt spacing, in *Case-II* the d-band center energy is based on a system with relaxed Pt-Pt atom spacing.

6.5.1 Correlation with the d-band center

Figure 6.6 presents the correlation of the adsorption energy of O_2 with the corresponding adsorption site d-band center. It was observed that *Case I* resulted in a better correlation than *Case II*. The R^2 corresponding to the correlation of data from *Case I* was calculated to be 0.91. The latter was observed to be closely similar to $R^2 = 0.94$ obtained from the results of Hammer *et al.* (1997). The correlation corresponding with *Case-II* resulted in an R^2 value of 0.68 (Figure 6.6). This decrease in

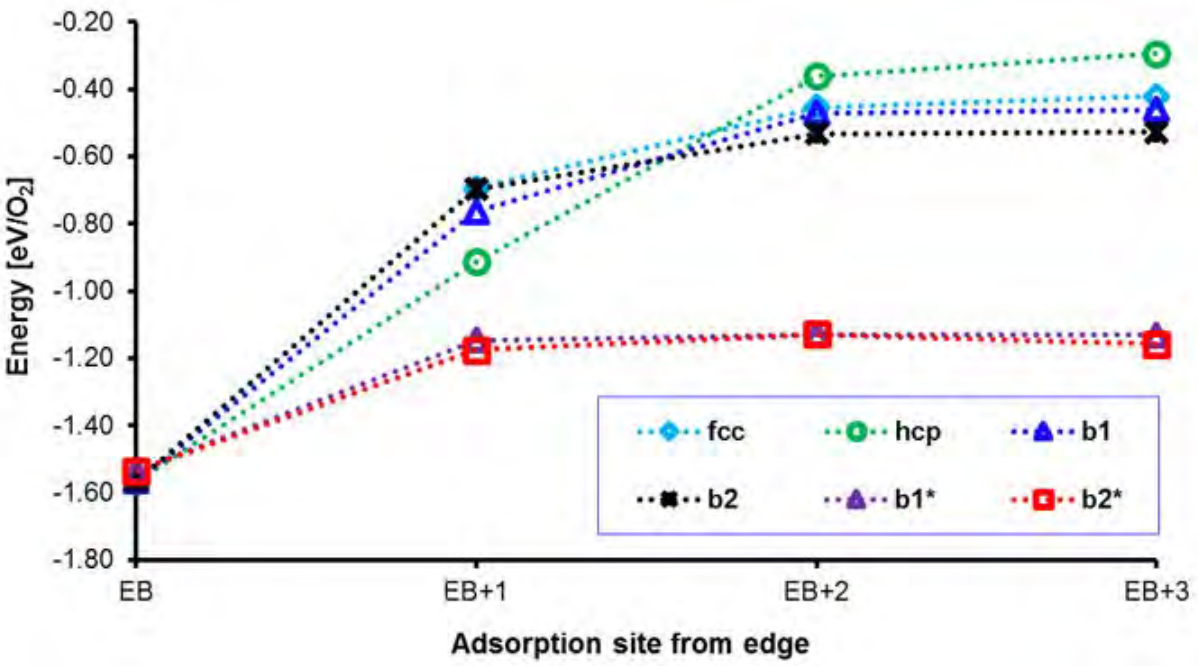

Figure 6.5: Adsorption energies of O_2 along Pt(111) and Pt(100) terrace sites of the Pt(mNR)-[7(111)×5(100)] and Pt(mNR)-[5(111)×7(100)] nanorod models, respectively. The terrace sites are: EB (edge-bridge adsorption), EB+1 (fcc1, hcp1, b1a, b2a, b1*a and b2*a), EB+2 (fcc2, hcp2, b1b, b2b, b1*b and b2*b) and EB+3 (fcc3, hcp3, b1c, b2c, b1*c and b2*c).

the R^2 value was attributed to the change in the d-band center of edge atom upon nanorod relaxation. Figure 6.7 presents a comparison of the d-band center of bulk terminated and relaxed nanorod models. It was observed that the d-band center energy of the edge atoms converges towards the d-band center energy of the Pt(100) nanorod facet atoms (Figure 6.7). Although the d-band center energies of the edge atoms and Pt(100) facet atoms were observed to be effectively the same (Figure 6.7), the adsorption energy of O_2 on the edge is significantly more stable (≥0.34 eV) than any adsorption on b2* sites along the Pt(100) facet. The latter is inconsistent with expectations from application of the d-band theory. It may be argued that the strong adsorption on EB sites versus equivalent adsorption on Pt(100) facet bridge sites is a geometric factor. Therefore, the EB sites may be geometrically different from the normal plane bridge sites.

Considering the above, it was argued that the poor correlation (in *Case II*) was due to the observed change in the d-band center energy. It was further anticipated that upon adsorption of O_2 on a given site, relaxation of the local atoms would result in a slight change in the d-band center energy. The edge atomic row relaxes by contracting towards its nearest neighbouring atomic rows. This relaxation was quantified as a local mean displacement (LMD) of nearest neighbouring atoms from the atom of interest relative the bulk optimized Pt-Pt bond length. This local mean displacement was calculated using equation 6.1,

$$LMD_j = \left(\sum_i \frac{d_{Pt_j*-Pt_i} - d_{Ptj-Pti}}{CN} \right) \tag{6.1}$$

where $d_{Pt_j-Pt_i}$ and CN are the bond length between Pt atoms i and j for a relaxed nanorod geometry, and the coordination number of a Pt atom j, $d_{Pt_j-Pt_i}*$ is the bulk optimized Pt-Pt bond length which is equal to 2.811 Å for the PAW−PBE combination. Figure 6.8 presents the observed change in the d-band center energy ($\Delta\varepsilon_{dc} = \varepsilon_{dc}|_{bulk\ terminated\ geometry} - \varepsilon_{dc}|_{relaxed\ geometry}$) as a function of the local mean displacement, occurring as a result of geometry relaxation. From this figure, it was observed that a decrease in LMD_j results in a down shift (away from the fermi-level) of the d-band center energy of the corresponding Pt atom.

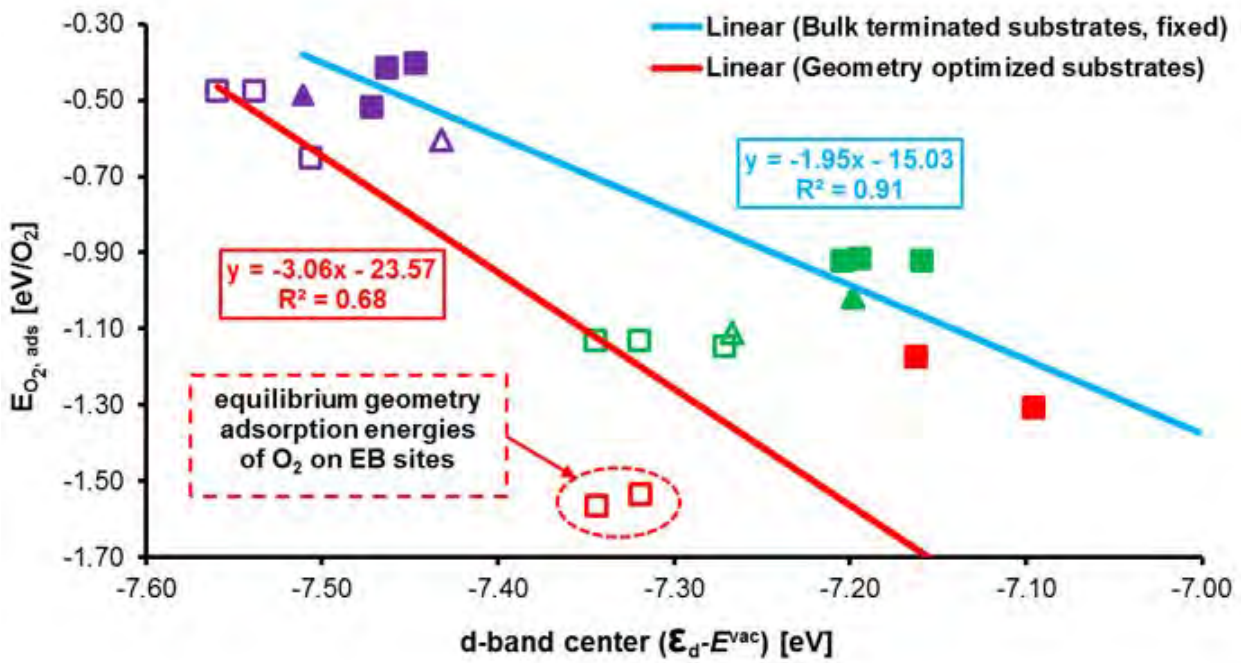

Figure 6.6: Adsorption energy of O_2 as a function of the d-band center of various nanorod bridge sites. The d-band center has been referenced to the vacuum energy using work functions ($\Phi_{Pt(111)-slab}$ = 5.65 eV, $\Phi_{Pt(100)-slab}$ = 5.56 eV, $\Phi_{nanorod\,models} = 5.58 - 5.54eV$ eV). Solid markers corresponds to single energy calculations for bulk terminated nanorod models (*Case I*). Open markers corresponds to calculations based on geometry optimized structures (*Case II*). Triangular markers (△/▲) represents adsorption on extended slab models. The red, green and purple markers correspond to edge-bridge, Pt(100) nanorod face and Pt(111) nanorod facet adsorption states, respectively.

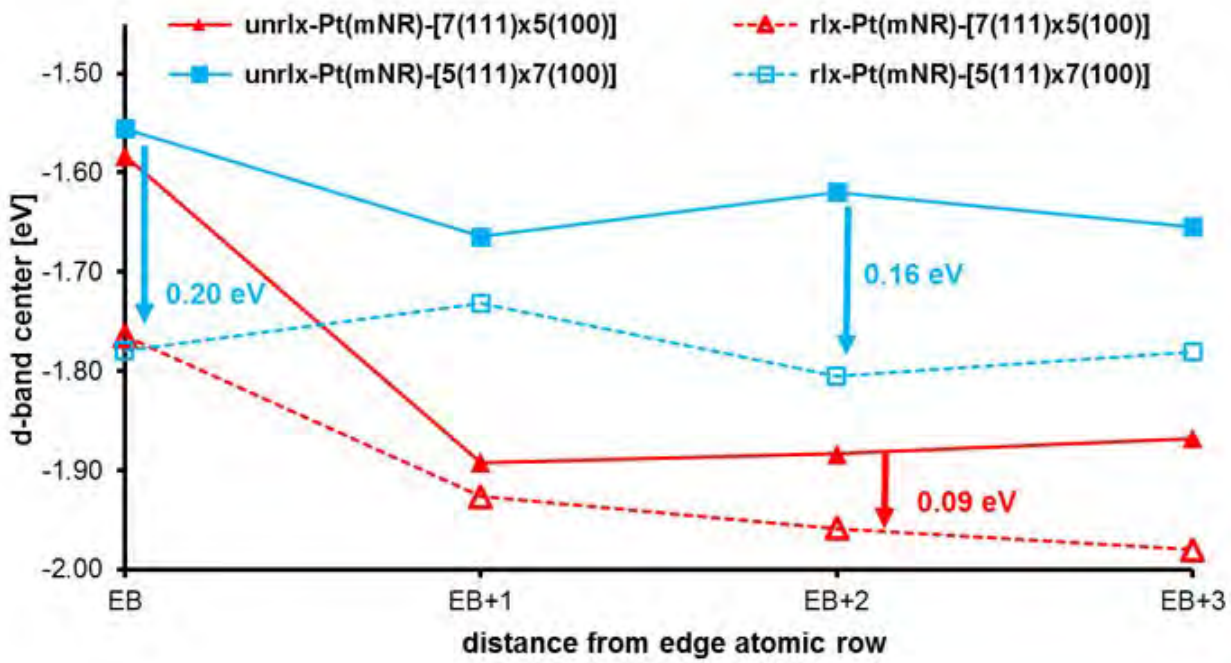

Figure 6.7: Effects of nanorod relaxation on the d-band center of surface atoms of nanorod models. EB, EB+1, EB+2 and EB+3 represents atoms in the edge atomic row, the first, second and third atomic rows from the edge, respectively. The Pt(mNR)-[5(111)×7(100)] data corresponds to the Pt(100) facet, whilst the Pt(mNR)-[7(111)×5(100)] data corresponds to the Pt(111) facet. The prefixes, unrlx- and rlx- refer to unrelaxed (*Case I*) and relaxed geometries (*Case II*), respectively.

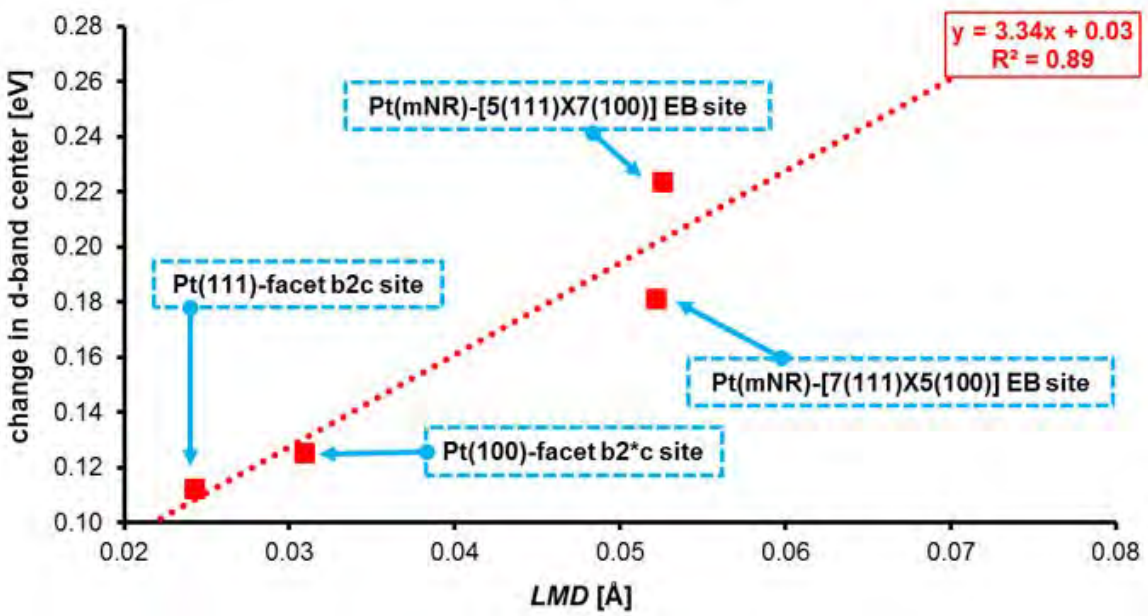

Figure 6.8: Calculated correlation between the local mean displacement (LMD) with the change in the d-band center as a result of substrate relaxation. Comparison of the displacement, from bulk spacing to equilibrium relaxed geometry spacing, of nearest neighbouring Pt atoms from a Pt atom of interest.

Considering the relationship between the change in the d-band center and LMD (Figure 6.8), it was argued that the O_2 induced geometric structure relaxation would result in a change in the d-band center energy and consequently a change in hybridization of the normalized O_2 sp-states with local d-states. Therefore, correlating the equilibrium geometry adsorption energy of O_2 with a d-band center energy which account for adsorbate induced relaxation was anticipated to give a reasonable correlation. This was investigated by first optimizing a set of nanorod models with O_2 on the b2c, EB and b2*c sites. The optimized geometries were than modified by removing the O_2 adsorbate without changing the positions of platinum atoms. Using the latter modified geometries, single point energy calculations (to obtained corresponding density of states) were conducted. The d-band center energy of the b2c, EB and b2*c sites was then calculated using equation 2.33 and the corresponding density of states. The latter d-band center energies contain information about the adsorbate induced geometric relaxation. The correlation of these d-band center energies with the equilibrium adsorption energy is presented in Figure 6.9. Contrary to expectation, a poor correlation, $R^2 = 0.52$, was observed when adsorbate induced relaxations were incorporated in the d-band center energies.

6.5.2 Correlation with coordination number

The coordination number (CN) of edge atoms is lower than atoms found on the Pt(111) and Pt(100) facet. The nanorod edge atoms are only coordinated to 7 atoms each whilst the Pt(111) and Pt(100) facet atoms have coordination numbers of 9 and 8, respectively. It has been previously argued that the adsorption strength of O, O_2 and other molecules increases with the decrease in site coordination number (Tritsaris *et al.*, 2011; Calle-Vallejo *et al.*, 2015). The empirical correlation of the adsorption energy of O_2 (calculated based on *Case I* and *Case II*) with the adsorption site coordination numbers is presented in Figure 6.10. For both *Case I* and *Case II* a good correlation was observed between the adsorption energy on b2, b2* and EB sites and the site coordination number.

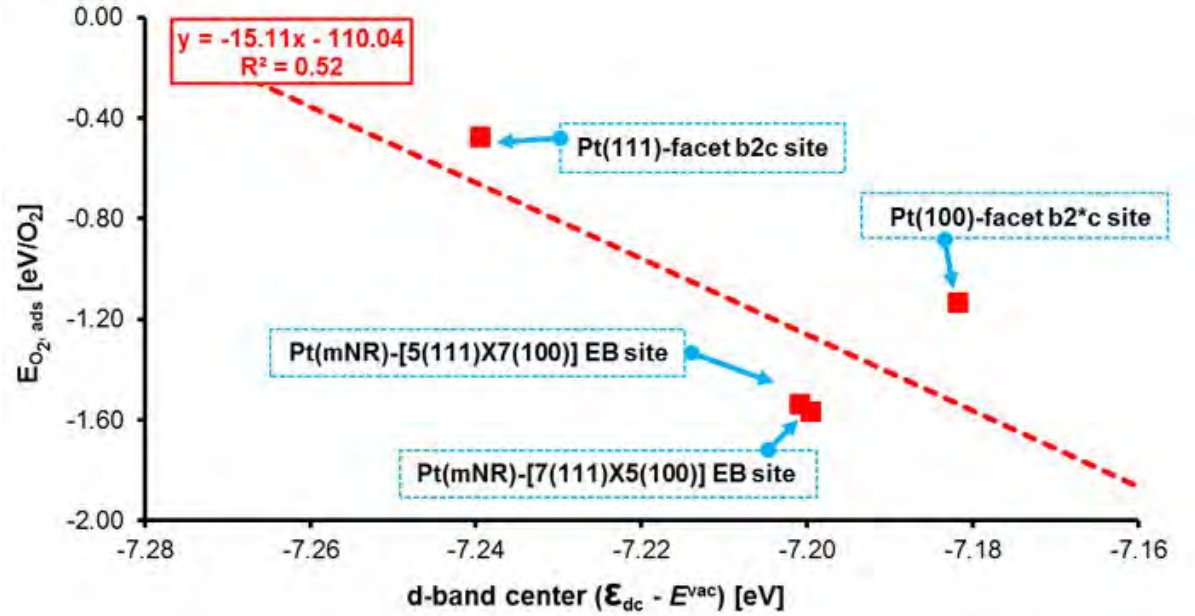

Figure 6.9: Effect of adsorbate induced relaxation on the correlation between the adsorption energy of O_2 and the d-band center of various nanorod bridge sites. The d-band center has been referenced to the vacuum energy using the work function ($\Phi_{Pt(111)-slab} = 5.65$ eV, $\Phi_{Pt(100)-slab} = 5.56$ eV, $\Phi_{Nanorodmodels} = 5.58 - 5.54eV$ eV).

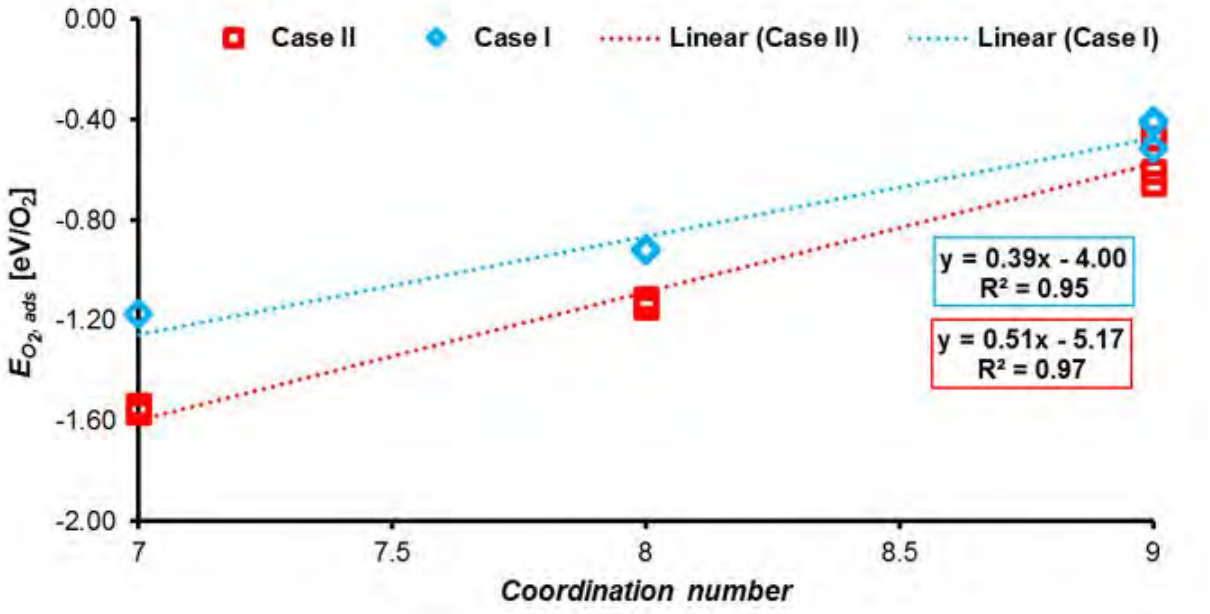

Figure 6.10: Empirical correlation between the adsorption energy of O_2 and the coordination number of various nanorod bridge sites.

6.6 Discussion

The effect of edge sites was investigated using atomic O and O_2 as probe adsorbates. The observed rapid convergence of the adsorption energy of atomic O along different sites on the Pt(111) and Pt(100) nanorod facets, is consistent with earlier calculations by Tritsaris *et al.* (2011). However, for O_2 it was observed that the adsorption energy exhibit a slow convergence behaviour, especially for adsorption along the hcp sites. This was attributed to the direct interaction of O_2 with the edge atoms. Beyond the first atomic row from the edge along the Pt(111) nanorod face, the adsorption

energy of O_2 was found to be relatively converged. On the Pt(100) nanorod facet, convergence in the adsorption energy of O_2 was observed for all bridge adsorption states (excluding the EB site). The stability of both atomic O and O_2 on all Pt(100) facet bridge sites extending from the edge towards the central terrace bridge site was found to be invariant and comparable with adsorption on extended Pt(100) slab surfaces. However, on the Pt(111) nanorod facet sites, fcc, hcp and bridge, the adsorption strength of atomic O and O_2 was observed to be weaker compared to adsorption on extended Pt(111) slab sites—for equivalent adsorption states. Recently Li *et al.* (2015b) reported that, due to surface tension effects, the adsorption strength of atomic O on terrace sites of nanoparticle clusters is weaker than the adsorption strength on extended surface sites—for equivalent adsorption states. The latter is argued to be the cause of the observed difference between the adsorption energy of atomic O and O_2 on Pt(111) nanorod terrace sites and equivalent extended Pt(111) surface sites. The geometry of atomic O and O_2 along the Pt(111) nanorod terrace sites were relatively similar for all equivalent EB+2 and EB+3 adsorption sites. Along the Pt(100) nanorod terrace sites, geometry of atomic O and O_2 was quite similar for all equivalent EB+1, EB+2 and EB+3 adsorption states. Therefore, in summary, the edge effect on the Pt(100) facet can be considered to be localized at the edge atomic row. On the Pt(111) facet, the edge has a destabilizing effect on the adsorption of both atomic O and O_2. For atomic O, although the adsorption strength decreased on the Pt(111) nanorod terrace, the adsorption energy along the terrace from the edge was relatively constant. This is not quite true for O_2 where the adsorption only becomes constant beyond the first atomic row from the edge.

A poor correlation between the equilibrium adsorption energy of O_2 and the d-band center energies, corresponding to adsorption sites on relaxed geometries, was observed. Correlating the adsorption energies with a set of d-band center energies which incorporate the adsorbate induced relaxation of the nanorod, resulted in an even poorer correlation. Since the d-band center theory is anticipated to hold, it was suggested that the excess adsorption energy of O_2 at the EB site could be due to edge relaxation and the unique position of the EB site compared to terrace bridge sites. A good empirical correlation between the adsorption energy of O_2 and the site coordination number was observed. The latter was true for both single point energy calculations (*Case I*) and equilibrium energy calculations (*Case II*). It was suggested that since low coordination corresponds to high surface energy, higher reactivity would be anticipated for edges (compared to terraces).

Chapter 7

Interactions between the nanorod facets

7.1 Introduction

In modelling the catalytic activity of polycrystalline platinum nanoparticles towards the ORR, generally it is assumed that different crystalline regions of the nanoparticles behave independently (Greeley *et al.*, 2002; Tritsaris *et al.*, 2011; Nesselberger *et al.*, 2011; Wei & Liu, 2013; Tripković *et al.*, 2014). At least two conditions need to be satisfied for the latter assumption to be valid. These are: (i) invariant adsorption energy of ORR intermediates as a function of distance from the edge atomic row and (ii) the cross diffusion of ORR intermediates between adjacent facets must be limited (negligible). In Chapter 6, the first condition was demonstrated and found to be true at least for atomic O, a result consistent with Tritsaris *et al.* (2011). The second condition was explicitly stated by Greeley *et al.* (2007) without any further verification. Understanding the level of this connection is key especially since the Pt(111) and Pt(100) facets have varying interactions with ORR intermediates (different reaction mechanisms on these two facets are presented in Chapter 1).

Using DFT calculations, the interaction and coverage of atomic O at edge sites has been reported to be higher than on terrace sites (Greeley *et al.*, 2002; Tritsaris *et al.*, 2011; Wei & Liu, 2013). Wei & Liu (2013) argued, based on calculated full atomic O coverage of the edge sites at electrode potentials greater than 0.65 V (versus SHE), that these sites do not participate in the ORR. So far literature presents a view that the edge sites are highly reactive towards O and O_2 adsorption and they provide a separation barrier between different nanoparticle facets. In this chapter the degree of connection between the Pt(111) and Pt(100) facets through the edge region is investigated. This is done using the diffusion of atomic O from a Pt(111) facet towards a Pt(100) facet of a Pt(mNR)-[5(111)×5(100)] nanorod model (or vice versa). The involved calculation details include, (i) geometry optimization, (ii) vibrational analysis, (iii) transition state search for diffusion (i, ii, iii - have been discussed in subsection 2.4.3), and (iv) calculation of thermodynamic properties (Gibbs free energy of adsorption at fuel cell operating temperature and pressure).

7.2 Connection of nanorod facets through the edge

The adsorption of atomic O on Pt(111) and Pt(100) surfaces is known from experimental measurements to be an exothermic process (Gland *et al.*, 1980; Barteau *et al.*, 1981; Norton *et al.*, 1984). Theoretical studies have confirmed this and furthermore predicted an even stronger interaction at low coordinated sites (Tritsaris *et al.*, 2011; Duan & Wang, 2013; Calle-Vallejo *et al.*, 2015). The predicted strong adsorption of atomic O and O_2 on step edge sites of step-surfaces has also been observed in a number of experimental studies (Wang *et al.*, 1997; Badan *et al.*, 2015; Jacobse *et al.*, 2015). In Chapter 5 it was demonstrated that both atomic O and O_2 adsorbs much stronger on EB site than on any other site along the nanorod facets. Furthermore, on nanorod sites and extended surface sites atomic O was found to be more stable than O_2 per mole of O_2 in the gas phase. In this section the thermodynamic

stability of atomic O on various sites along the nanorod, i.e. sites on the diffusion pathway of atomic O along the nanorod, is investigated. Since high coverage of the edge sites has been reported (Wei & Liu, 2013), in this section low and high coverage limits will be investigated.

7.2.1 Thermodynamic stability of atomic O at a low coverage limit

Using the optimized nanorod model, i.e. Pt(mNR)-[5(111)×5(100)]−with two primitive unit cells (two surface atoms) along the infinite dimension, the lowest model coverage possible is one atomic oxygen per nanorod. Therefore, in this subsection the adsorption stability of atomic O on various sites along the atomic O diffusion path (shown in Figure 7.1) on a nanorod will be investigated. The illustrated sites were probed with atomic O to determine the adsorption free energy relative to O_2 in the gas phase and a clean Pt(mNR)-[5(111)×5(100)] nanorod. Using equation 7.1 and 7.2 the respective adsorption enthalpies and free energies were calculated.

$$\Delta H_{O,\ ads}(T) = 2 \cdot H_{NR6+O}(T) - 2 \cdot H_{NR6}(T) - H_{O_{2,gas}}(T) \tag{7.1}$$

$$\Delta G_{O,\ ads}(T) = 2 \cdot G_{NR6+O}(T) - 2 \cdot G_{NR6}(T) - G_{O_{2,gas}}(T) \tag{7.2}$$

Here $\Delta H_{O,\ ads}(T)$, $H_{NR6+O}(T)$, $H_{NR6}(T)$ and $H_{O_{2,gas}}(T)$ are adsorption enthalpy of atomic O on a Pt(mNR)-[5(111)×5(100)] nanorod model site, total enthalpy of a nanorod with one adsorbed O atom, total enthalpy of a clean nanorod and total enthalpy of O_2 in the gas phase, at temperature T, respectively. The above definition also holds for the free energies (where H is substituted with G). All calculated energies are corrected for temperature, i.e. energies are reported at 85 °C and 1 bar − typical conditions of in a PEMFC (Yuan & Wang, 2008). Details for the temperature corrections are presented in Appendix C. Using the calculated adsorption energies and vibrational frequencies, thermal corrections were conducted to determine the thermodynamic stability of different adsorption states at typical PEMFC conditions. Figure 7.3 presents the thermodynamic stability of atomic O on different nanorod sites along an O atom diffusion path. From this data it can be seen that the edge bridge (EB) adsorption geometry is the most stable geometry at the investigated coverage (i.e. one O atom per nanorod system) and thermal conditions. The latter is consistent with both experimental observations and theoretical studies (see Chapters 1 and 5). All adsorbed states of atomic O on the nanorod sites are calculated to be exergonic (i.e. $\Delta G_{O,ads} < 0$) with respect to O_2 in the gas phase at 85 °C and 1 bar. At this coverage, thermodynamically atomic O will preferentially adsorb on an EB site at equilibrium. On EB sites the change of the free energy of adsorption of atomic O is -1.22 eV/$\frac{1}{2}O_2$. This is more stable than adsorption on the fcc1 and b1*a sites by 0.60 eV/$\frac{1}{2}O_2$ and 0.48 eV/$\frac{1}{2}O_2$, respectively. Given the relative stability of atomic O on EB site to terrace sites, it is anticipated that the diffusion free energy barrier of one O atom from an EB site towards the fcc1 or b1* site will be atleast 0.6 eV/O or 0.48 eV/O, respectively—corresponding to the reaction free energies (Gibbs free energy difference between two stable state along a diffusion pathway). The next interesting question is therefore related to the diffusion of the adsorbed O atom from an EB site towards the Pt(111) and Pt(100) central terrace sites (see Figure 7.1).

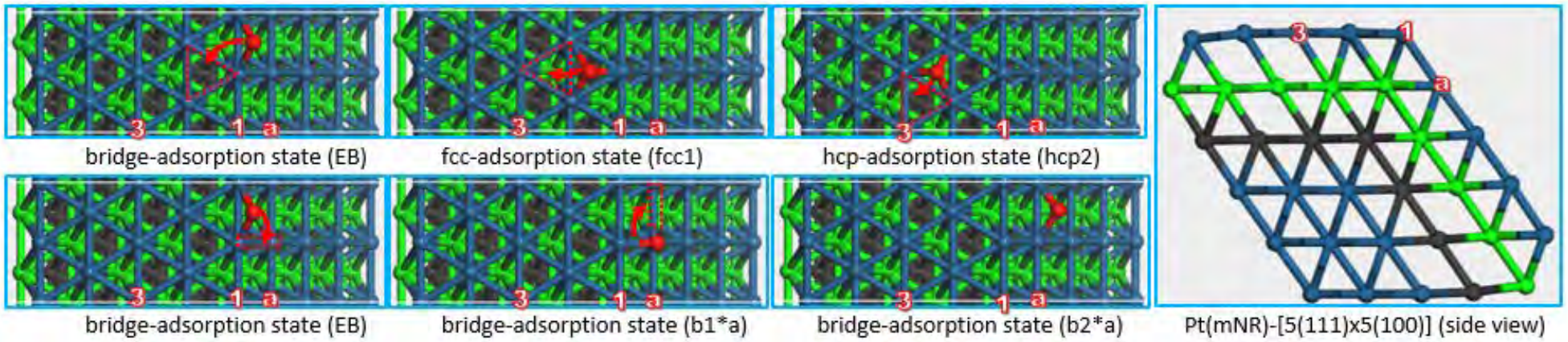

Figure 7.1: Diffusion pathway for atomic O diffusion from an EB site towards the Pt(111)-central-fcc site (fcc2) and the Pt(100)-near-central-bridge site (b2*a), at a lower coverage limit.

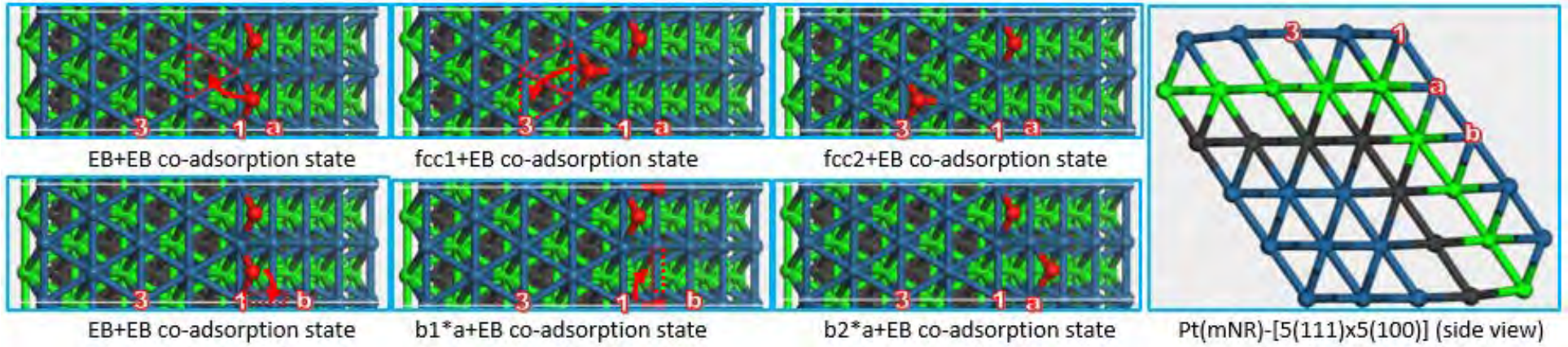

Figure 7.2: Diffusion pathway for atomic O diffusion from an EB site towards the Pt(111)-central-fcc site (fcc2) and the Pt(100)-near-central-bridge site (b2*a), at a high coverage limit.

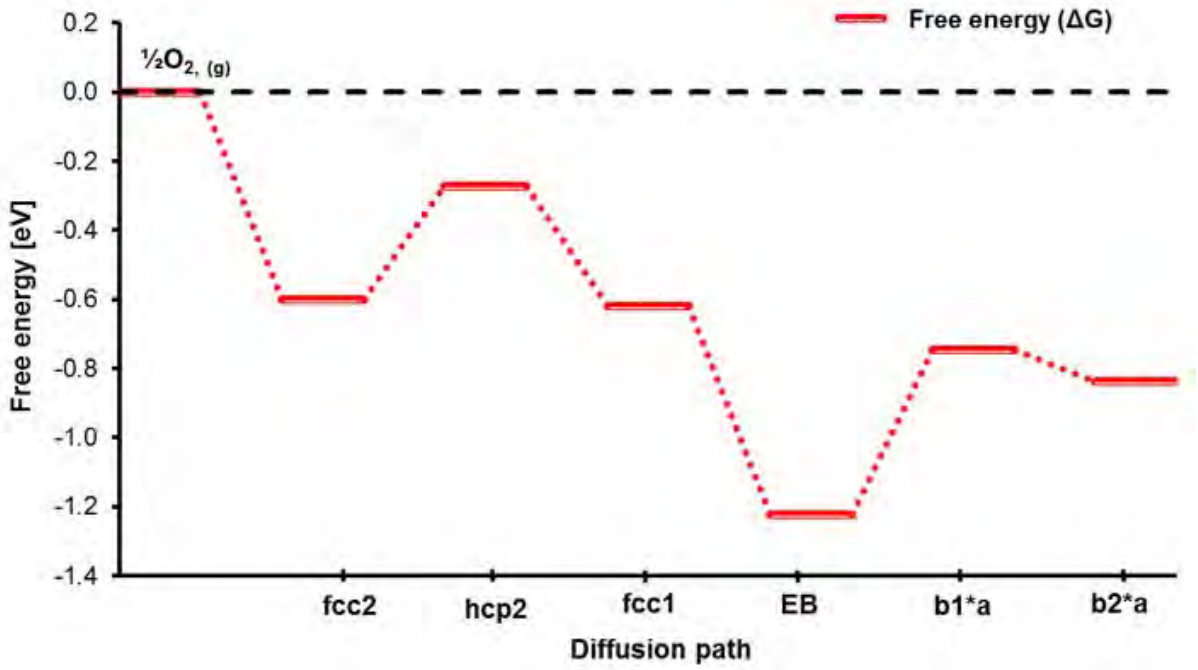

Figure 7.3: Adsorption free energies of atomic O on different sites along a diffusion pathway from the Pt(111)-central-fcc site (fcc2) towards the Pt(100)-near-central-bridge site (b2*a) (Figure 7.1). A temperature and pressure correction to 85 °C and 1 bar, has been considered. All energies are referenced to $\frac{1}{2}O_2$ in the gas phase and a clean Pt(mNR)-[5(111)×5(100)] nanorod.

7.2.2 Diffusion of O at a low coverage limit

The diffusion of atomic O along the given path was investigated using DFT calculations and finding a saddle point between two stable states presented in Figures 7.1 and 7.3. Once a saddle point was found using transition state search calculations, it was optimized and verified through demonstrating that the only imaginary vibrational mode was along the diffusion path. Using the calculated adsorption free energies of the initial, transition and final states, the activation ($\Delta G^{\ddagger}_{ACT}$) and reaction ($\Delta G_{rxn}$) free energies were calculated as follows,

$$\Delta G^{\ddagger}_{ACT}(T) = G_{TS}(T) - G_{IS}(T) \tag{7.3}$$

$$\Delta G_{rxn}(T) = G_{FS}(T) - G_{IS}(T) \tag{7.4}$$

where G is the Gibbs free energy and the subscripts IS, TS and FS represents initial, transition and final states, respectively. The kinetic rate constant (diffusion hopping frequency) for atomic O diffusion from one adsorption state to another through a transition state was therefore defined as follows,

$$k(T) = \frac{k_B T}{h} exp\left(\frac{-\Delta G^{\ddagger}_{ACT}(T)}{k_B T}\right) \tag{7.5}$$

where $k(T)$ and $\Delta G^{\ddagger}_{ACT}(T)$ are the diffusion frequency (rate constant) [s^{-1}] and diffusion free energy barrier (equation 7.3) with entropic corrections at temperature T, respectively; k_B and h are the Boltzmann and Planck constants, respectively. The diffusion of atomic O from an EB adsorption state towards the Pt(111) central terrace sites and the Pt(100) central terrace sites was considered. Two diffusion steps were considered for each direction. Along the Pt(111) nanorod facet atomic O was considered to diffuse from the EB to the fcc1 adsorption state (EB→fcc1) and then from the fcc1 to the hcp2 adsorption state (fcc1→hcp2). Along the Pt(100) nanorod facet atomic O was considered to diffuse from the EB to the b1*a adsorption state (EB→b1*a) and then from the b1*a to the b2*a adsorption state (b1*a→b2*a). The adsorption stability of the above states are presented in Figure 7.3.

EB→fcc1 diffusion step

The transition state for atomic O diffusion from the EB to the fcc1 adsorption state was observed to be equivalent to the bridge adsorption geometry with Pt-O bond lengths of 1.98 Å (coordination with an edge Pt atom) and 2.00 Å (coordination with a non-edge Pt atom). Figure 7.4 presents the optimized diffusion path of atomic O from the EB to the fcc1 adsorption state. The adsorption properties of the initial, transition and final states are presented in Table 7.1. Also presented in Table 7.1 are the vibrational frequencies of the transition state. Only one imaginary vibrational mode was observed—in the direction diffusion pathway. The activation free energy for this diffusion step was calculated to be 1.04 eV. The corresponding hopping frequency of atomic O from the EB to the fcc1 adsorption state was calculated to be 1.88×10^{-2} s^{-1} at 358 K and 1 bar−typical PEMFC operating conditions.

Table 7.1: Thermodynamic properties of atomic O along the EB→fcc1 diffusion path.

diffusion step	IS	TS	FS
geometry	EB	bridge	fcc1
d_{Pt-O} [Å]	1.94	1.98, 2.00	2.10, 2.04×2
E_{tot} [eV]	-385.42	-384.37	-384.82
$G(358.15K)$ [eV]	-385.32	-384.28	-384.72
E_a [eV]		1.05	
$\Delta G^{\ddagger}_{ACT}(358.15K)$ [eV]		1.04	
ν_i [cm^{-1}]	532, 464, 138	503, 373, 167/i	444, 377, 316

/i indicates that a vibrational mode is imaginary

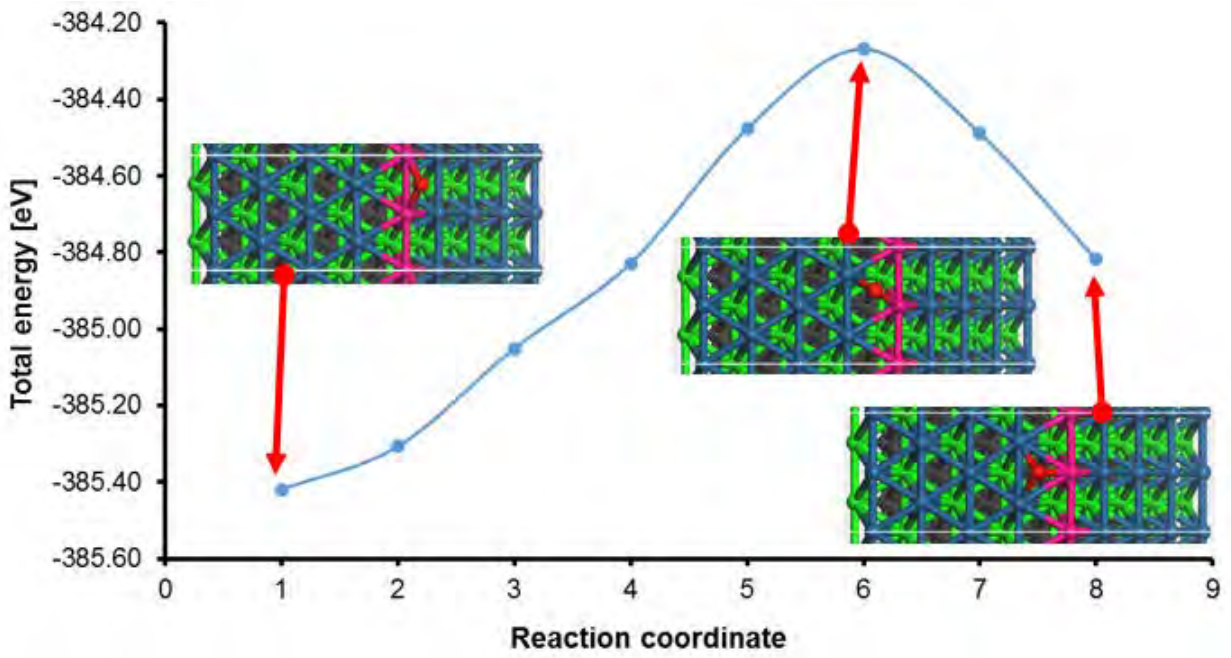

Figure 7.4: Diffusion of atomic O from the EB to the fcc1 adsorption state at a low coverage limit.

fcc1→hcp2 diffusion step

The transition state for atomic O diffusion from the fcc1 to the hcp2 adsorption state was observed to be equivalent to the bridge adsorption geometry with Pt-O bond lengths of 1.99 Å (coordination with two non-edge Pt atoms). Figure 7.5 presents the optimized diffusion path of atomic O from the fcc1 to the hcp2 adsorption state. The adsorption properties of the initial, transition and final states are presented in Table 7.2. Also presented in Table 7.2 are the vibrational frequencies of the transition state. Only one imaginary vibrational mode was observed—in the direction of the diffusion pathway. The activation free energy for this diffusion step was calculated to be 0.54 eV. The corresponding hopping frequency of atomic O from the fcc1 to the hcp2 adsorption state was calculated to be 2.06×10^5 s^{-1} at 358 K and 1 bar−typical PEMFC operating conditions.

Table 7.2: Thermodynamic properties of atomic O along the fcc1→hcp2 diffusion path.

diffusion step	IS	TS	FS
geometry	fcc1	bridge	hcp2
d_{Pt-O} [Å]	2.10, 2.04×2	1.99	2.03, 2.04×2
E_{tot} [eV]	-384.82	-384.27	-384.47
$G(358.15K)$ [eV]	-384.72	-384.18	-384.37
E_a [eV]		0.55	
$\Delta G^{\ddagger}_{ACT}(358.15K)$ [eV]		0.54	
ν_i [cm^{-1}]	444, 377, 316	500, 394, 141/i	445, 376, 317

/i indicates that a vibrational mode is imaginary

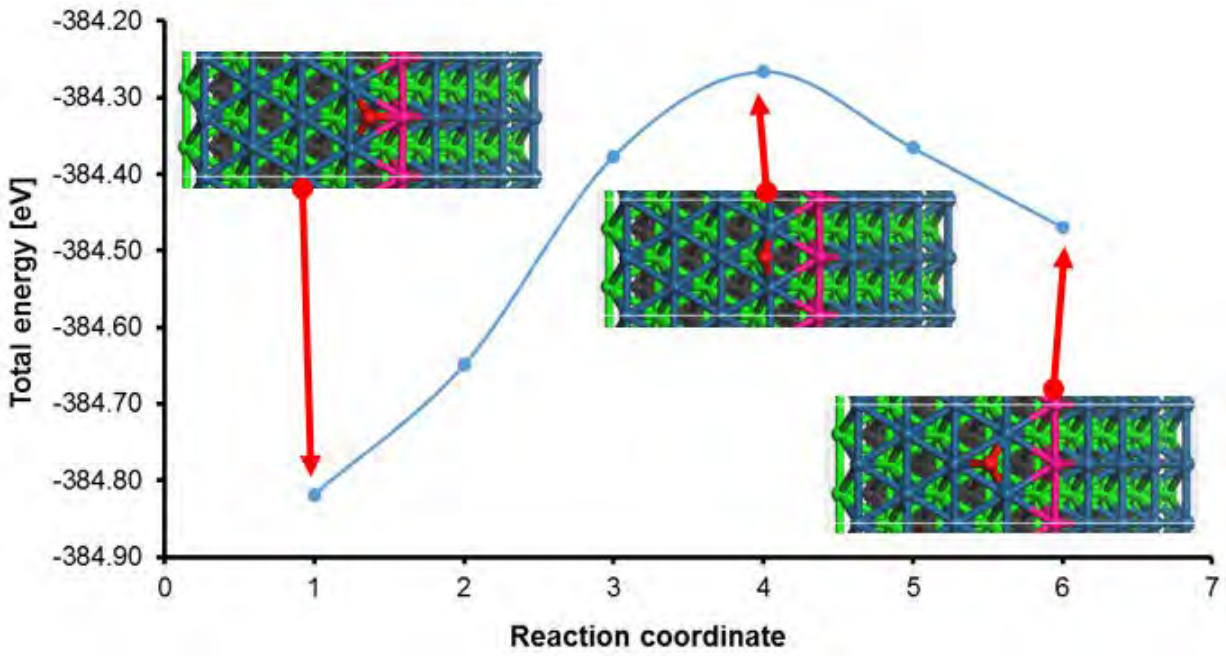

Figure 7.5: Diffusion of atomic O from the fcc1 to the hcp2 adsorption state at a low coverage limit.

fcc→hcp diffusion on a Pt(111)-p(2x2) slab

The transition state for atomic O diffusion from the fcc to the hcp adsorption state on a Pt(111)-p(2x2) slab was observed to be equivalent to the bridge adsorption geometry with Pt-O bond lengths of 1.99 Å. Figure 7.6 presents the optimized diffusion path of atomic O from an fcc to an hcp adsorption state. The adsorption properties of the initial, transition and final states are presented in Table 7.3. Also presented in Table 7.3 are the vibrational frequencies of the transition state. Only one imaginary vibrational mode was observed—in the direction of the diffusion pathway. The activation free energy for this diffusion step was calculated to be 0.64 eV. The corresponding hopping frequency of atomic O diffusion from an fcc to an hcp adsorption state was calculated to be 7.36×10^{3} s^{-1} at 358 K and 1 bar−typical PEMFC operating conditions.

Table 7.3: Thermodynamic properties of atomic O along the fcc→hcp diffusion path.

diffusion step	IS	TS	FS
geometry	fcc	bridge	hcp
d_{Pt-O} [Å]	2.04×3	1.99	2.05×3
E_{tot} [eV]	-146.25	-145.59	-145.82
$G(358.15K)$ [eV]	-146.10	-145.50	-145.72
E_a [eV]		0.65	
$\Delta G^{\ddagger}_{ACT}(358.15K)$ [eV]		0.64	
ν_i [cm^{-1}]	451, 387, 385	507, 394, 130/i	436, 321, 320

/i indicates that a vibrational mode is imaginary

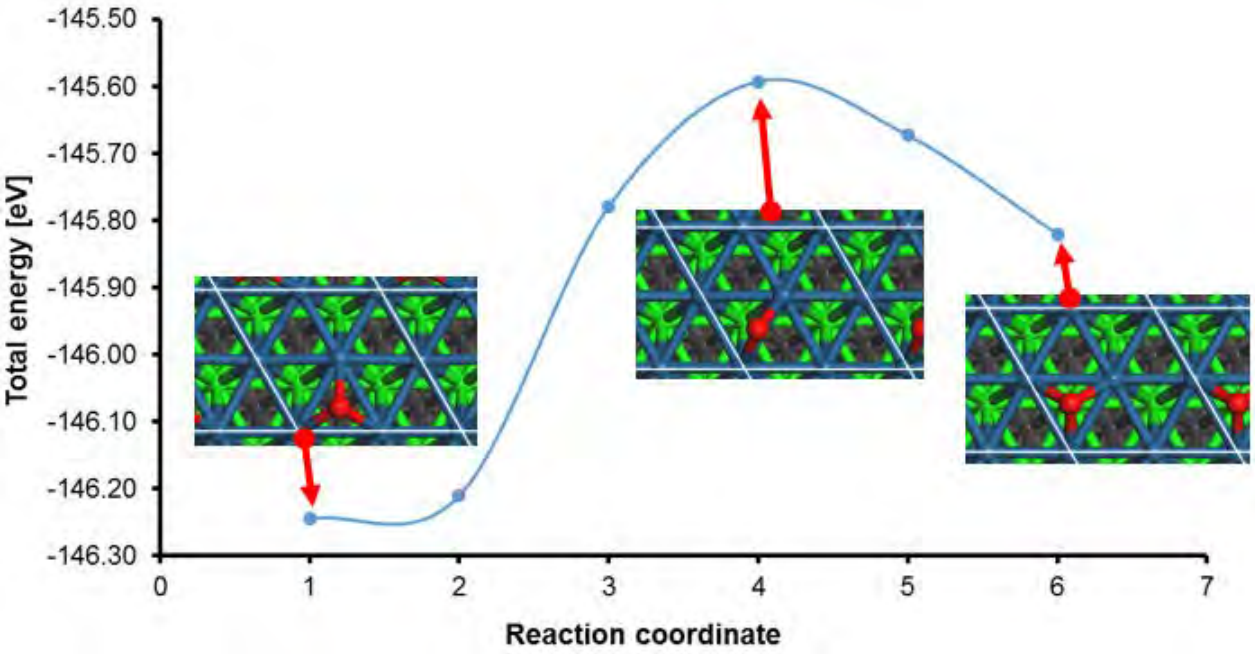

Figure 7.6: Diffusion of atomic O from the fcc to the hcp adsorption state on a Pt(111)-p(2x2) slab surface.

EB→b1*a diffusion step

The transition state for atomic O diffusion from the EB to the b1*a adsorption state was observed to be equivalent to the bridge-hollow adsorption geometry with Pt-O bond lengths of 1.99 Å (coordination with an edge Pt atom) and 2.01 Å (coordination with a non-edge Pt atom). Figure 7.7 presents the optimized diffusion path of atomic O from the EB to the b1*a adsorption state. The adsorption properties of the initial, transition and final states are presented in Table 7.4. Also presented in Table 7.4 are the vibrational frequencies of the transition state. Only one imaginary vibrational mode was observed—in the direction of the diffusion pathway. The activation free energy for this diffusion step was calculated to be 0.58 eV. The corresponding hopping frequency of atomic O diffusion from the EB to the b1*a adsorption state was calculated to be 5.27×10^4 s^{-1} at 358 K and 1 bar−typical PEMFC operating conditions.

Table 7.4: Thermodynamic properties of atomic O along the EB→b1*a diffusion path.

diffusion step	IS	TS	FS
geometry	EB	bridge-hollow	b1*a
d_{Pt-O} [Å]	1.94	1.99, 2.01	1.96, 1.95
E_{tot} [eV]	-385.42	-384.82	-384.94
$G(358.15K)$ [eV]	-385.32	-384.74	-384.84
E_a [eV]		0.60	
$\Delta G^{\ddagger}_{ACT}(358.15K)$ [eV]		0.58	
ν_i [cm^{-1}]	532, 464, 138	481, 372, 57/i	507, 446, 118

/i indicates that a vibrational mode is imaginary

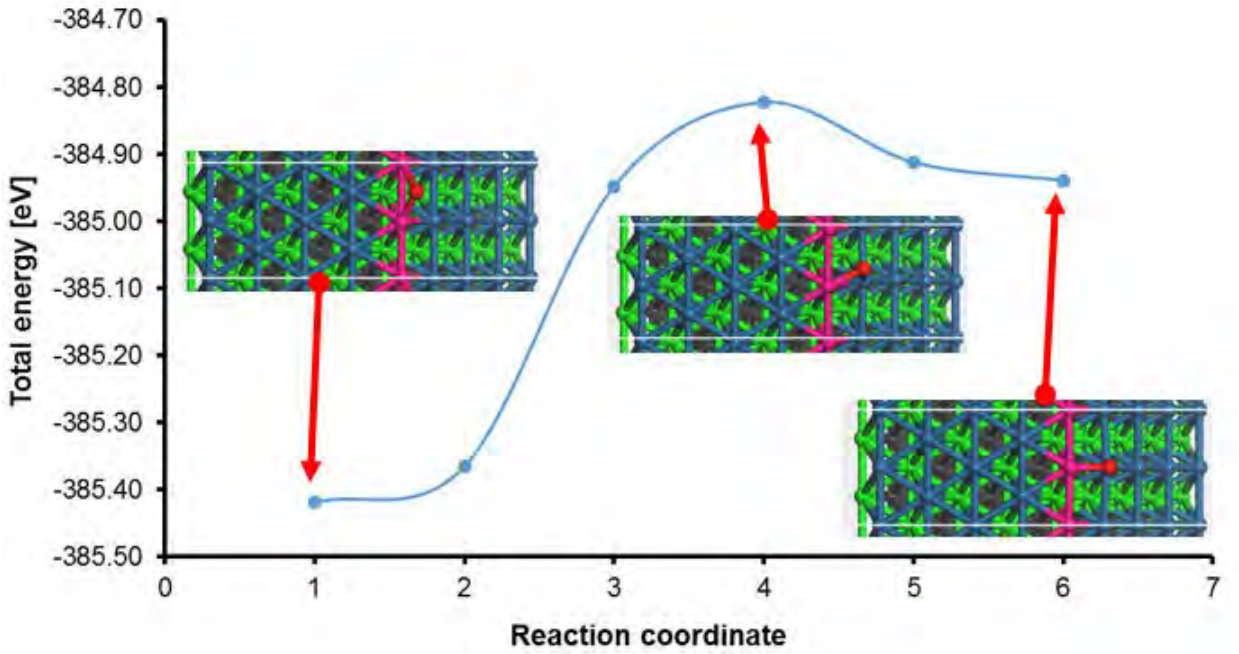

Figure 7.7: Diffusion of atomic O from the EB to the b1*a adsorption state at a low coverage limit.

b1*a→b2*a diffusion step

The transition state for atomic O diffusion from the b1*a to the b2*a adsorption state was observed to be equivalent to the bridge-hollow adsorption geometry with Pt-O bond lengths of 2.02 Å (coordination with an edge Pt atom) and 1.97 Å (coordination with a non-edge Pt atom). Figure 7.8 presents the optimized diffusion path of atomic O from the b1*a to the b2*a adsorption state. The adsorption properties of the initial, transition and final states are presented in Table 7.5. Also presented in Table 7.5 are the vibrational frequencies of the transition state. Only one imaginary vibrational mode was observed—in the direction of the diffusion pathway. The activation free energy for this diffusion step was calculated to be 0.10 eV. The corresponding hopping frequency of atomic O diffusion from the b1*a to the b2*a adsorption state was calculated to be 2.84×10^{11} s^{-1} at 358 K and 1 bar−typical PEMFC operating conditions.

Table 7.5: Thermodynamic properties of atomic O along the b1*a→b2*a diffusion path.

diffusion step	IS	TS	FS
geometry	b1*a	bridge-hollow	b2*a
d_{Pt-O} [Å]	1.95, 1.96	1.97, 2.02	1.95
E_{tot} [eV]	-384.94	-384.82	-385.03
$G(358.15K)$ [eV]	-384.84	-384.74	-384.94
E_a [eV]		0.11	
$\Delta G^{\ddagger}_{ACT}(358.15K)$ [eV]		0.10	
ν_i [cm^{-1}]	507, 446, 118	494, 371, $80/i$	518, 454, 114

$/i$ indicates that a vibrational mode is imaginary

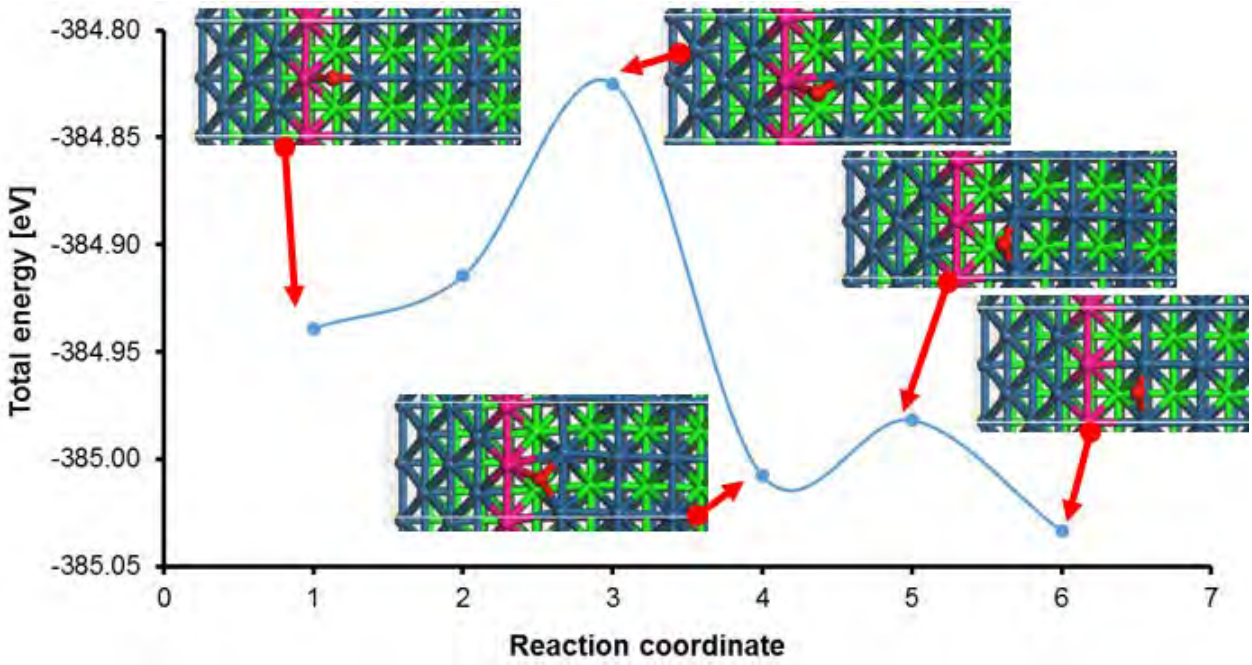

Figure 7.8: Diffusion of atomic O from the b1*a to the b2*a adsorption state at a low coverage limit.

bridge→bridge diffusion on a Pt(100)-p(2x2) slab

The transition state for atomic O diffusion from a bridge to an adjacent bridge adsorption state on a Pt(100)-p(2x2) slab was observed to be equivalent to the bridge-hollow adsorption geometry with Pt-O bond lengths of 1.97 Å and 2.00 Å. Figure 7.9 presents the optimized diffusion path of atomic O from a bridge to an adjacent bridge adsorption state. The observed two peaks in Figure 7.9 are an indication of the surface symmetry. The state at the potential energy surface well corresponds to a three fold coordinated O atoms (at this state there were large forces acting on the O atom, see Table D.6 in Appendix D). The adsorption properties of the initial, transition and final states are presented in Table 7.6. Also presented in Table 7.6 are the vibrational frequencies of the transition state. Only one imaginary vibrational mode was observed—in the direction of the diffusion pathway. The activation free energy for this diffusion step was calculated to be 0.18 eV. The corresponding hopping frequency of atomic O diffusion from an bridge to an adjacent bridge adsorption state was calculated to be 2.19×10^{10} s^{-1} at 358 K and 1 bar−typical PEMFC operating conditions.

Table 7.6: Thermodynamic properties of atomic O along the bridge→bridge diffusion path on a Pt(100)-p(2x2) slab.

diffusion step	IS	TS	FS
geometry	bridge	bridge-hollow	bridge
d_{Pt-O} [Å]	1.95×2	1.97, 2.00	1.95×2
E_{tot} [eV]	-144.08	-143.88	-144.08
$G(358.15K)$ [eV]	-143.98	-143.80	-143.98
E_a [eV]		0.19	
$\Delta G^{\ddagger}_{ACT}(358.15K)$ [eV]		0.18	
ν_i [cm^{-1}]	521, 459, 115	485, 372, 67/i	521, 459, 115

/i indicates that a vibrational mode is imaginary

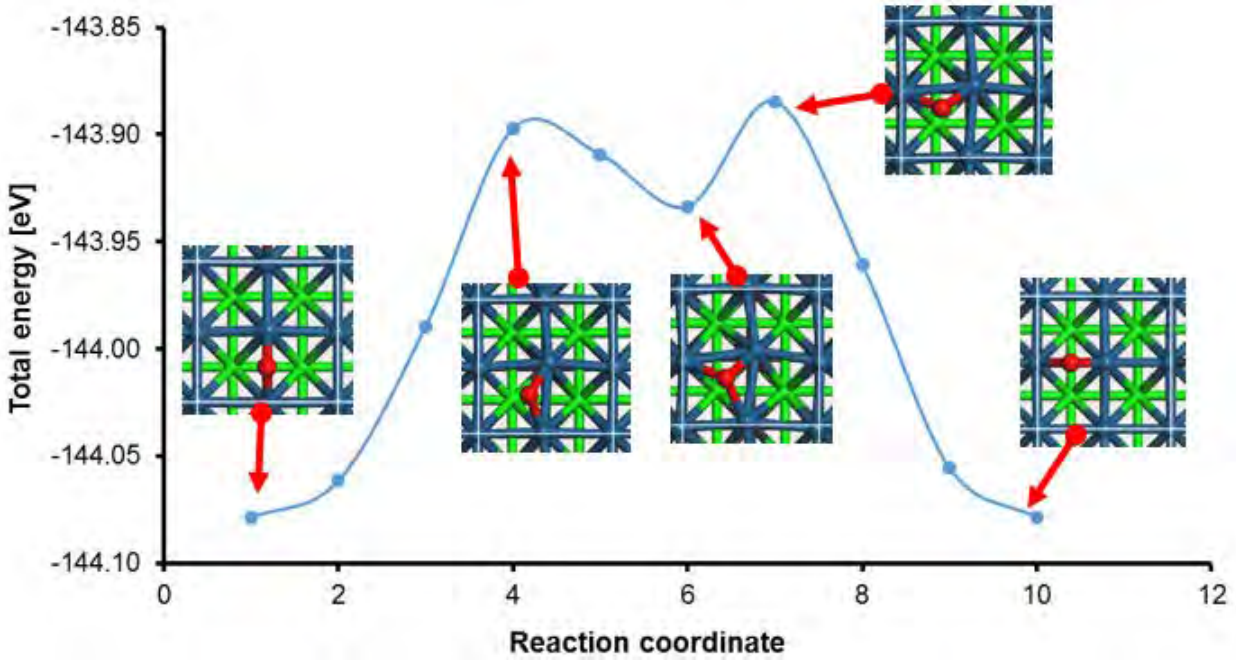

Figure 7.9: Diffusion of atomic O from a Pt(100)-p(2x2) bridge adsorption state to an adjacent bridge adsorption state.

Discussion

Energetic and geometric details of considered diffusion pathways are also given in Appendix D. Each diffusion transition state was seen to have a single imaginary vibrational mode corresponding to a motion in the diffusion path (tangent to the diffusion path). On Pt(111)-p(2x2) the diffusion barrier of atomic O from an fcc to an hcp site was calculated to be 0.55 eV/O, consistent with 0.52 eV/O (USPP−PW91, on a Pt(111)-p(2x2) slab) and 0.58 eV/O (PAW−PBE, on a Pt(111)-p(4x4) slab) reported by Ford *et al.* (2005) and Ogawa *et al.* (2013), respectively. In both literature studies and present study, the transition state was a bridge site separating the fcc and hcp sites. This is consistent with the instability of this adsorption geometry observed in Chapter 5.

For atomic O diffusion on a Pt(100)-p(3x3) slab, Ogawa *et al.* (2013) reported a barrier of 0.51 eV (PAW−PBE) whilst Zyubin *et al.* (2013) reported a barrier of 0.4 eV (PAW−PBE, on a Pt(100)-p(3x4) slab). Both literature studies investigated atomic O diffusion from a bridge site on a Pt(100) slab to the next adjacent bridge site. Although a similar diffusion pathway was investigated in the present study, a lower diffusion barrier was predicted. The diffusion barrier of atomic O from a bridge site to an adjacent bridge site on a Pt(100)-p(2x2) slab was calculated to be 0.19 eV (see Table 7.6). The latter was observed to be inconsistent with the diffusion barriers reported in literature (Zyubin *et al.*, 2013; Ogawa *et al.*, 2013). The potential cause of the latter inconsistency may be attributed to the difference in atomic O coverage−both literature studies consider a relatively low coverage (< 0.11 ML) whilst this study considered a coverage of 0.25 ML. Due to the symmetric nature of the diffusion path, two peaks were observed corresponding to equivalent transition states (a shown in Figure 7.9). Vibrational analysis confirmed one of the peaks to be saddle points (with a single imaginary vibrational mode in the direction of the diffusion path). The investigated atomic O diffusion barriers on near-central terrace sites of the Pt(mNR)-[5(111)×5(100)] nanorod model were found to be in good agreement with the calculated diffusion barriers on extended slab (see summary in Figure 7.10 and Table 7.7). It is worth noting that in all cases studied the vibrational modes of the transition state on a Pt(111) facet were consistent with those on a Pt(111)-p(2x2) slab surface. The latter is also true for the Pt(100) facet and Pt(100)-p(2x2) slab surface.

The interesting observation was the diffusion energy barrier from the EB site towards either the Pt(111) or Pt(100) nanorod facet. This diffusion energy barrier was much higher for diffusion towards the Pt(111) facet (1.05 eV from the EB site towards the fcc1 site) than it was for diffusion towards the Pt(100) facet (0.60 eV from the EB site towards the b1*a site). The atomic O diffusion energy barrier from the EB site of a Pt(211) step-surface towards the first fcc site (fcc1) has been reported to be 0.81 eV (Ogawa *et al.*, 2014). On a 147-atom cuboctahedral nanoparticle a smaller energy barrier (0.42 eV) was reported for atomic O diffusion from an EB site towards the first hcp site (hcp1) (Peng

Table 7.7: Calculated diffusion activation energies (E_a: diffusion energy barrier calculated at -273.15 °C and in a vacuum using DFT, $\Delta G^{\ddagger}_{ACT}(358.15K, 1bar)$: diffusion free energy barrier at 85 °C and 1 bar) for different O diffusion step along a given diffusion path. Vibrational modes of the diffusion transition states are also presented.

diffusion step	E_a [eV]	$\Delta G^{\ddagger}_{ACT}(358.15K, 1bar)$ [eV]	TS $-\nu_i$ [cm^{-1}]
Pt(111)-facet			
EB → fcc1	1.05	1.04	503, 373, 167/i
fcc1 → hcp2	0.55	0.54	500, 394, 141/i
slab: fcc → hcp	0.65	0.64	507, 394, 130/i
Pt(100)-facet			
EB → b1*	0.60	0.58	481, 372, 57/i
b1* → b2*	0.11	0.10	494, 371, 80/i
slab: b → b*	0.18	0.18	485, 372, 67/i

/i indicates that a vibrational mode is imaginary

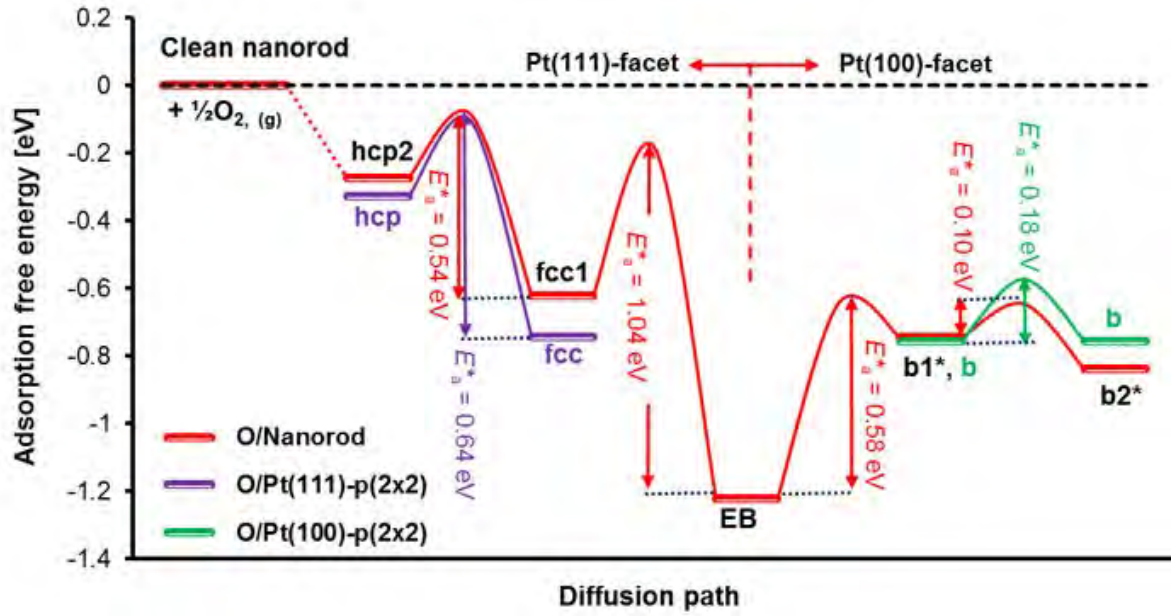

Figure 7.10: Calculated activation free energies ($E_a^* \equiv \Delta G_{ACT}^{\ddagger}$—includes entropic corrections) for diffusion of one atomic O from an EB site towards the Pt(111)-central-fcc site (fcc2) and Pt(100)-near-central-bridge site (b2*) (Figure 7.1). A temperature and pressure correction to 358.15 K and 1 bar, has been considered. All energies are referenced to O_2 in the gas phase and a clean Pt(mNR)-[5(111)×5(100)] nanorod. Also presented are the diffusion barriers of one O atom on Pt(111)-p(2x2) and Pt(100)-p(2x2) extended slab models. All energies are referenced to $\frac{1}{2}O_2$ in the gas phase and a clean Pt(mNR)-[5(111)×5(100)] nanorod.

& Mavrikakis, 2015). Since the transition state geometry reported in the latter study does not match that studied by Ogawa *et al.* (2014) and in the present study (hcp1 site was found to be unstable on the nanorod and on a Pt(211) slab), direct comparison could not be made with the diffusion barrier on 147-atom nanoparticle reported by Peng & Mavrikakis (2015). As stated earlier the calculated diffusion barriers of atomic O from the EB site towards the fcc1 and b1*a sites, were observed to be larger than the energy difference between the EB state and the fcc1 (0.60 eV/O) and b1*a (0.48 eV/O) states, respectively.

The hopping frequencies (k) at 358.15 K were calculated for each diffusion step using the calculated diffusion free energy barriers ($\Delta G_{ACT}^{\ddagger}$) and equation 7.5. The results are summarized in Table 7.8. Based on these frequencies, it was observed that diffusion across the edge atomic row (EB site) limits the rate of atomic O diffusion from one nanorod facet to the next. This limitation was much stronger for diffusion towards the Pt(111) facet by 6 orders of magnitude compared to diffusion towards the Pt(100) facet. When comparing diffusion along the nanorod facets to that on extended slab surfaces, good agreement was observed. The equilibrium constants for diffusion of atomic O from the EB site

Table 7.8: Calculated diffusion frequencies of atomic O from and towards the EB site at 358.15 K and 1 bar.

Away from EB site	k_f $[s^{-1}]$	Towards EB site	k_r $[s^{-1}]$
EB → fcc1	1.88×10^{-2}	EB ← fcc1	5.36×10^{6}
fcc1 → hcp2	2.06×10^{5}	fcc1 ← hcp2	1.68×10^{10}
slab: fcc → hcp	7.35×10^{3}	fcc ← hcp	5.26×10^{9}
EB → b1*	5.27×10^{4}	EB ← b1*	2.66×10^{11}
b1* → b2*	2.84×10^{11}	b1* ← b2*	1.36×10^{10}
slab: b → b*	2.19×10^{11}	b ← b*	2.19×10^{10}

towards the fcc1 and b1*a sites were calculated to be 3.50×10^{-9} and 1.98×10^{-7}, respectively. The latter is a direct indication that at this coverage atomic O diffuse almost irreversibly towards the EB sites from both terrace regions. This is anticipated to continue until the edge sites become saturated with atomic O. Due to the presence of repulsive lateral interactions between co-adsorbed O atoms (Gu & Balbuena, 2007; Madala, 2013), the stability of co-adsorbed states is anticipated to decrease with increasing coverage. Therefore since the edges have been reported to have a high atomic O coverage saturation (Wei & Liu, 2013; Badan *et al.*, 2015), the effect of coverage on diffusion frequency can give an additional insight into the connection between the Pt(111) and Pt(100) facets. This is investigated in the following subsection.

7.2.3 Thermodynamic stability of atomic O at a high coverage limit

Subsection 7.2.1 demonstrated that O atoms (at a coverage of one O atom per Pt(mNR)-[5(111)×5(100)] nanorod model) will preferentially adsorb on an EB site, this subsection investigates the effect of coverage on the adsorption-preference of atomic O and the diffusion free energy barriers at a high coverage limit are considered in Subsection 7.2.4. Starting with a system consisting of a Pt(mNR)-[5(111)×5(100)] nanorod model with one O atom pre-adsorbed on an EB site, the effect of atomic O coverage is investigated by adding a second O atom on various sites along a diffusion pathway as illustrated in Figure 7.2. This results in a set of calculations where various atomic O co-adsorption configurations are investigated. All the investigated co-adsorbed configurations consists of an O atom adsorbed on an EB site of the Pt(mNR)-[5(111)×5(100)] nanorod model and a second O atom on one of various sites along the diffusion path (fcc2, fcc1, EB, b1* and b2*). The different co-adsorption geometries were optimized to find their equilibrium geometries and corresponding ground state energies. Furthermore, vibrational analysis calculations are performed to verify whether the equilibrium geometries were indeed at a minimum of the potential energy surface.

The integral and differential adsorption free energies of atomic O on various nanorod sites were then calculated from the optimized geometries. The integral adsorption free energy ($\Delta G_{2O,ads}(T)|_{int}$) was calculated using equation 7.6,

$$\Delta G_{2O,ads}(T)|_{int} = G_{NR6+2O}(T) - G_{NR6}(T) - G_{O_2,gas}(T) \tag{7.6}$$

where G_{NR6+2O} is the free energy of two co-adsorbed O atoms on the Pt(mNR)-[5(111)×5(100)] nanorod model. Whilst the differential adsorption free energy of atomic O ($\Delta G_{ads,O}(T)|_{diff}$) was given by equation 7.7,

$$\Delta G_{ads,O}(T)|_{diff} = G_{NR6+2O}(T) - G_{NR6+O}(T) - \frac{1}{2}\cdot G_{O_2,gas}(T) \tag{7.7}$$

The difference between the two free energies is the reference state−whilst the zero reference state for the integral free energy is O_2 and a clean Pt(mNR)-[5(111)×5(100)] nanorod model, for the differential free energy the reference state is $\frac{1}{2}O_2$ and a Pt(mNR)-[5(111)×5(100)] nanorod model with atomic O pre-adsorbed on an EB site. The latter free energy is a good indicator of whether increasing coverage is exergonic or endergonic. The geometric and energetic co-adsorption properties of the considered co-adsorption configurations are presented below.

EB-EB co-adsorption state

The geometric and energetic properties of two O atoms co-adsorbed on two adjacent EB sites of the Pt(mNR)-[5(111)×5(100)] nanorod model are presented in Table 7.9 and Figure 7.11. All four Pt-O bonds were calculated to be equal to 1.949 Å (cf. to 1.943 Å at a low coverage limit). The deviation angles from the surface normal vectors of the Pt(111) facet (θ) and Pt(100) facet (β) were calculated to be 33° and 22°, respectively. The O-O separation distance was calculated to be 2.811 Å (equal to the equilibrium Pt-Pt bond length). The addition of a second O atom on an adjacent EB site to an occupied EB site (as shown in Figure 7.11) was observed to be exergonic with a $\Delta G_{2O,ads}|_{diff}$ of -0.27 eV/$\frac{1}{2}O_2$.

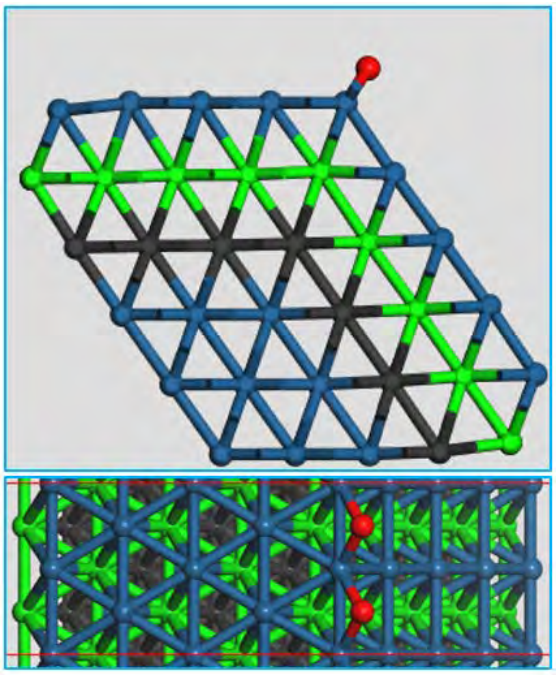

Figure 7.11: Equilibrium geometry of two co-adsorbed O atoms on 2xEB sites of the Pt(mNR)-[5(111)×5(100)] nanorod model. Side view (top) and [111] surface normal view (bottom).

Table 7.9: Equilibrium geometric properties of two co-adsorbed O atoms on 2xEB sites of the Pt(mNR)-[5(111)×5(100)] nanorod model.

site: EB-EB	Pt(mNR)-[5(111)×5(100)]
d_{Pt-O} [Å] O on an EB site	 1.949
d_{O-O} [Å]	2.811
θ β	33° 22°
$\Delta G_{2O,ads}\|_{int}$ [eV/O_2] $\Delta G_{2O,ads}\|_{diff}$ [eV/$\frac{1}{2}O_2$]	-1.49 -0.27[a]

a partial molar free adsorption energy for the addition of an O atom on an EB site at 85°C

EB-fcc1 co-adsorption state

The geometric and energetic properties of two O atoms co-adsorbed on the EB and fcc1 sites of the Pt(mNR)-[5(111)×5(100)] nanorod model are presented in Table 7.10 and Figure 7.12. For the O atom adsorbed on the EB site the equilibrium Pt-O bonds were calculated to be 1.925 Å and 1.969 Å (bonding with an edge Pt atom which is also bonded to the fcc1 bound O atom). The deviation angles from the surface normal vectors of the Pt(111) facet (θ) and Pt(100) facet (β) were calculated to be 39° and 16°, respectively. The equilibrium Pt-O bond lengths for the O atom on the fcc1 site were calculated to be 2.203 Å (bonding to an edge Pt atom), 2.010 Å and 2.013 Å (bonding to non edge Pt atoms). The O-O separation distance was calculated to be 2.8983 Å (larger than the equilibrium Pt-Pt bond length). The addition of a second O atom on the fcc1 site near an occupied EB site (as shown in Figure 7.12) was observed to be exergonic with a $\Delta G_{2O,ads}|_{diff}$ of -0.43 eV/$\frac{1}{2}O_2$.

EB-fcc2 co-adsorption state

The geometric and energetic properties of two O atoms co-adsorbed on the EB and fcc2 sites of the Pt(mNR)-[5(111)×5(100)] nanorod model are presented in Table 7.11 and Figure 7.13. For the O atom adsorbed on the EB site the equilibrium Pt-O bonds were calculated to be 1.939 Å (0.004 Å shorter than the equivalent bond lengths for a single O atom on the EB site). The deviation angles from the surface normal vectors of the Pt(111) facet (θ) and Pt(100) facet (β) were calculated to be

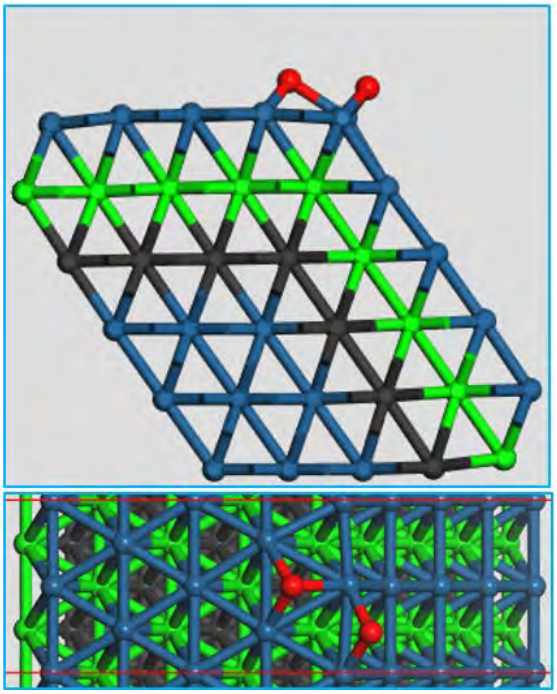

Figure 7.12: Equilibrium geometry of two co-adsorbed O atoms on EB and fcc1 sites of the Pt(mNR)-[5(111)×5(100)] nanorod model. Side view (top) and [111] surface normal view (bottom).

Table 7.10: Equilibrium geometric properties of two co-adsorbed O atoms on EB and fcc1 sites of the Pt(mNR)-[5(111)×5(100)] nanorod model.

site: EB-fcc1	Pt(mNR)-[5(111)×5(100)]
d_{Pt-O} [Å]	
O on an EB site	1.925, 1.969
O on an fcc1 site	2.203, 2.010, 2.013
d_{O-O} [Å]	2.983
θ	39°
β	16°
$\Delta G_{2O,ads}\|_{int}$ [eV/O_2]	-1.65
$\Delta G_{2O,ads}\|_{diff}$ [eV/$\frac{1}{2}O_2$]	-0.43[a]

a partial molar free adsorption energy for the addition of an O atom on an fcc1 site at 85°C

36° and 19°, respectively. The equilibrium Pt-O bond lengths for the O atom on the fcc2 site were calculated to be 2.054 Å (bonding to a second row from the edge Pt atom) and 2.048 Å (bonding to two third row from the edge Pt atoms). The O-O separation distance was calculated to be 5.587 Å. The addition of a second O atom on the fcc2 site (as shown in Figure 7.13) was observed to be exergonic with a $\Delta G_{2O,ads}|_{diff}$ of -0.68 eV/$\frac{1}{2}O_2$.

EB-b1*a co-adsorption state

The geometric and energetic properties of two O atoms co-adsorbed on the EB and b1*a sites of the Pt(mNR)-[5(111)×5(100)] nanorod model are presented in Table 7.12 and Figure 7.14. For the O atom adsorbed on the EB site the equilibrium Pt-O bonds were calculated to be 1.915 Å and 1.992 Å (bonding with an edge Pt atom which is also bonded to the b1*a bound O atom). The deviation angles from the surface normal vectors of the Pt(111) facet (θ) and Pt(100) facet (β) were calculated to be 27° and 28°, respectively. The equilibrium Pt-O bond lengths for the O atom on the b1*a site were calculated to be 2.015 Å (bonding to an edge Pt atom) and 1.931 Å (bonding to non edge Pt atom). The O-O separation distance was calculated to be 2.841 Å (larger than the equilibrium Pt-Pt bond length but shorter than the observed separation for the EB-fcc1 co-adsorption geometry). The addition of a second O atom on the b1*a site near an occupied EB site (as shown in Figure 7.14) was

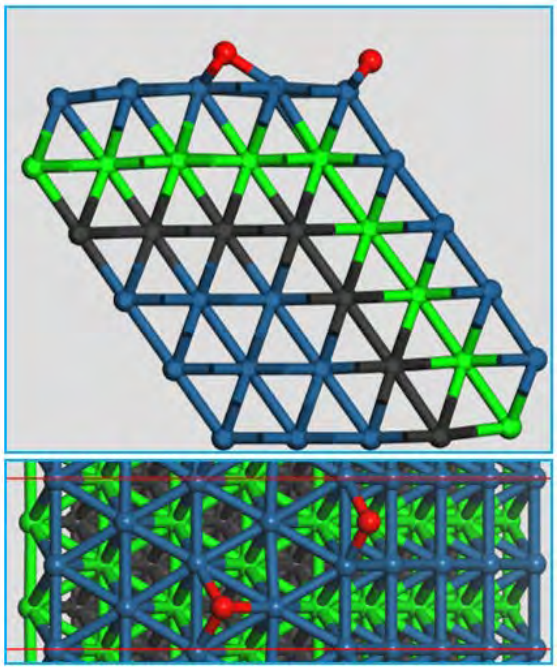

Figure 7.13: Equilibrium geometry of two co-adsorbed O atoms on EB and fcc2 sites of the Pt(mNR)-[5(111)×5(100)] nanorod model. Side view (top) and [111] surface normal view (bottom).

Table 7.11: Equilibrium geometric properties of two co-adsorbed O atoms on EB and fcc2 sites of the Pt(mNR)-[5(111)×5(100)] nanorod model.

site: EB-fcc2	Pt(mNR)-[5(111)×5(100)]
d_{Pt-O} [Å]	
O on an EB site	1.939
O on an fcc2 site	2.048, 2.054
d_{O-O} [Å]	5.587
θ	36°
β	19°
$\Delta G_{2O,ads}\|_{int}$ [eV/O_2]	-1.90
$\Delta G_{2O,ads}\|_{diff}$ [eV/$\frac{1}{2}O_2$]	-0.68[a]

a partial molar free adsorption energy for the addition of an O atom on an fcc2 site at 85°C

observed to be exergonic with a $\Delta G_{2O,ads}|_{diff}$ of -0.26 eV/$\frac{1}{2}O_2$.

EB-b2*a co-adsorption state

The geometric and energetic properties of two O atoms co-adsorbed on the EB and b2*a sites of the Pt(mNR)-[5(111)×5(100)] nanorod model are presented in Table 7.13 and Figure 7.15. Two configurations were investigated−one of these configurations has the two O atoms aligned (see Figure 7.15 middle frame). In both configurations the Pt-O bond lengths of the EB bound O atom were calculated to be ca. 1.940 Å (ca. 0.005 Å shorter than the equivalent bond lengths for a single O atom on the EB site). The deviation angles from the surface normal vectors of the Pt(111) facet (θ) and Pt(100) facet (β) were calculated to be 39° and 16°, respectively. The latter was the same for both configurations in Figure 7.15. The equilibrium Pt-O bond lengths for the O atom on the b1*a site were calculated to be ca. 1.949 Å (ca. 0.005 Å shorter than the equivalent bond lengths for a single O atom on the b2*a site). The O-O separation distance was calculated to be 3.241 Å for the configuration where the two O atoms are aligned and 4.257 Å for the other geometry. The addition of a second O atom on the b2*a site near an occupied EB site (as shown in Figure 7.15) was observed to be exergonic with a $\Delta G_{2O,ads}|_{diff}$ of -0.78 eV/$\frac{1}{2}O_2$ (-0.80 eV/$\frac{1}{2}O_2$ for the misaligned geometry).

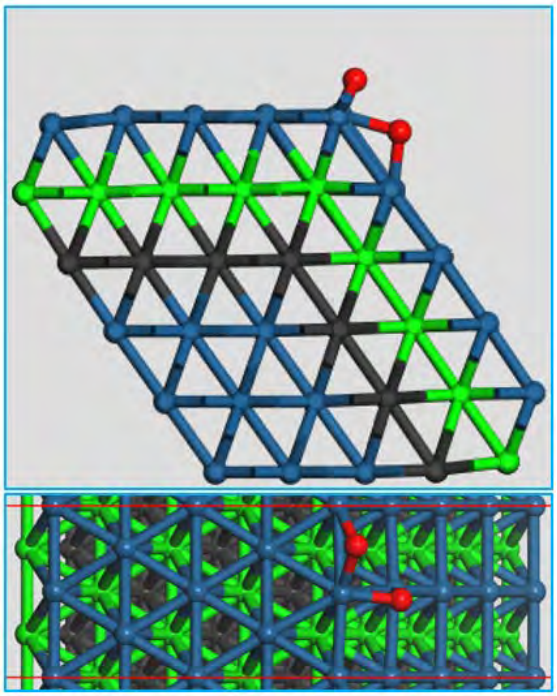

Figure 7.14: Equilibrium geometry of two co-adsorbed O atoms on EB and b1*a sites of the Pt(mNR)-[5(111)×5(100)] nanorod model. Side view (top) and [111] surface normal view (bottom).

Table 7.12: Equilibrium geometric properties of two co-adsorbed O atoms on EB and b1*a sites of the Pt(mNR)-[5(111)×5(100)] nanorod model.

site: EB-b1*a	Pt(mNR)-[5(111)×5(100)]
d_{Pt-O} [Å]	
O on an EB site	1.915, 1.992
O on an b1*a site	2.015, 1.931
d_{O-O} [Å]	2.841
θ	27°
β	28°
$\Delta G_{2O,ads}\|_{int}$ [eV/O_2]	-1.49
$\Delta G_{2O,ads}\|_{diff}$ [eV/$\frac{1}{2}O_2$]	-0.26[a]

a partial molar free adsorption energy for the addition of an O atom on an b1*a site at 85°C

Table 7.13: Equilibrium geometric properties of two co-adsorbed O atoms on EB and b2*a sites of the Pt(mNR)-[5(111)×5(100)] nanorod model.

site: EB-b2*a	Pt(mNR)-[5(111)×5(100)]	
	aligned O atoms	misaligned O atoms
d_{Pt-O} [Å]		
O on an EB site	1.938	1.940
O on an b2*a site	1.946	1.949
d_{O-O} [Å]	3.241	4.257
θ	39°	37°
β	16°	15°
$\Delta G_{2O,ads}\|_{int}$ [eV/O_2]	-2.00	-2.03
$\Delta G_{2O,ads}\|_{diff}$ [eV/$\frac{1}{2}O_2$]	-0.78[a]	-0.80[a]

a partial molar free adsorption energy for the addition of an O atom on an b2*a site at 85°C

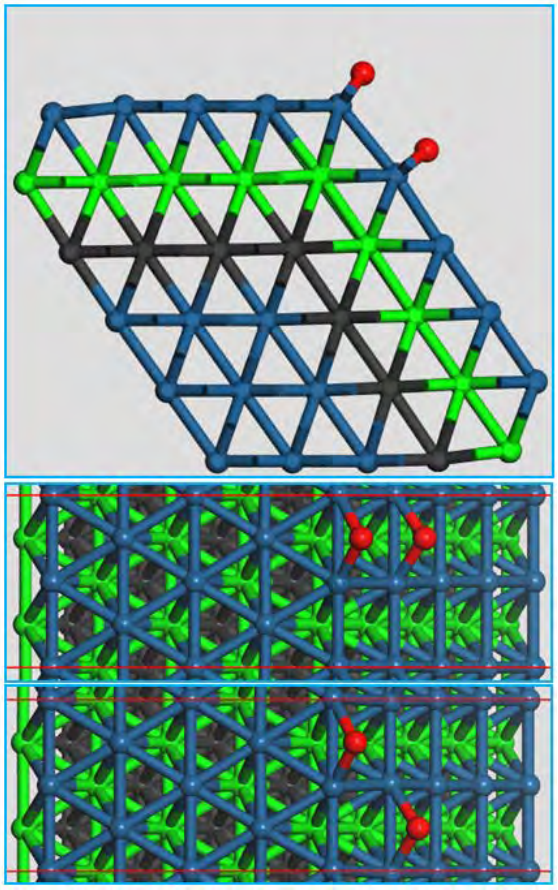

Figure 7.15: Equilibrium geometry of two co-adsorbed O atoms on EB and b2*a sites of the Pt(mNR)-[5(111)×5(100)] nanorod model. Side view (top) and [111] surface normal view (middle: configuration with two O atoms aligned and bottom: configuration with misaligned O atoms).

Discussion

The adsorption of an O atom on an fcc2, fcc1, EB, b1*a and b2*a site of the Pt(mNR)-[5(111)×5(100)] nanorod model pre-covered with an O atom on the EB site was investigated. Figure 7.16 presents the differential (partial molar) free energy of adsorption on the various site along the nanorod model. It was observed that the addition of a second O atom is an exergonic process. Furthermore, unlike where atomic O was adsorbed on various sites of a clean nanorod model, the potential energy surface was observed to be relatively flat for atomic O adsorption on a pre-covered nanorod model. The co-adsorption geometries where an EB bound O atom shared a Pt atom with an fcc1, EB or b1*a bound O atom were observed to result in longer Pt-O bond lengths. For co-adsorption with the O atoms relatively well spaced, EB-fcc2 and EB-b2*a, adsorption geometric properties closely resembled those of equivalent adsorption on clean nanorod model sites (EB, fcc2 and b2*a).

The adsorption free energy of atomic O on the fcc2 and b2*a sites of a clean Pt(mNR)-[5(111)×5(100)] nanorod model was calculated to be -0.60 eV/$\frac{1}{2}O_2$ and -0.84 eV/$\frac{1}{2}O_2$, respectively. Compared to the latter, the differential adsorption of atomic O on the fcc2 and b2*a sites of a Pt(mNR)-[5(111)×5(100)] nanorod model pre-covered with atomic O on an EB site was calculated to be -0.68 eV/$\frac{1}{2}O_2$ and -0.78 eV/$\frac{1}{2}O_2$, respectively (see Figure 7.16). From this observation it can be argued that at the O-O separation possible in the EB-fcc2 and EB-b2*a configurations, the adsorption properties of the co-adsorbed state are approximately equivalent to the adsorption properties of the separated states (where only one O atom is adsorbed on a nanorod). Strong repulsive lateral interactions were observed for the EB-EB, EB-b1*a and EB-fcc1 co-adsorption states. These lateral interaction energies were calculated as a difference between the integral free energy of the co-adsorbed states and the sum of the separated states. The lateral interaction energies therefore decreased in the order EB-EB (0.96 eV) > EB-b1*a (0.48 eV) > EB-fcc1 (0.20 eV) and were observed to be repulsive. An interesting point

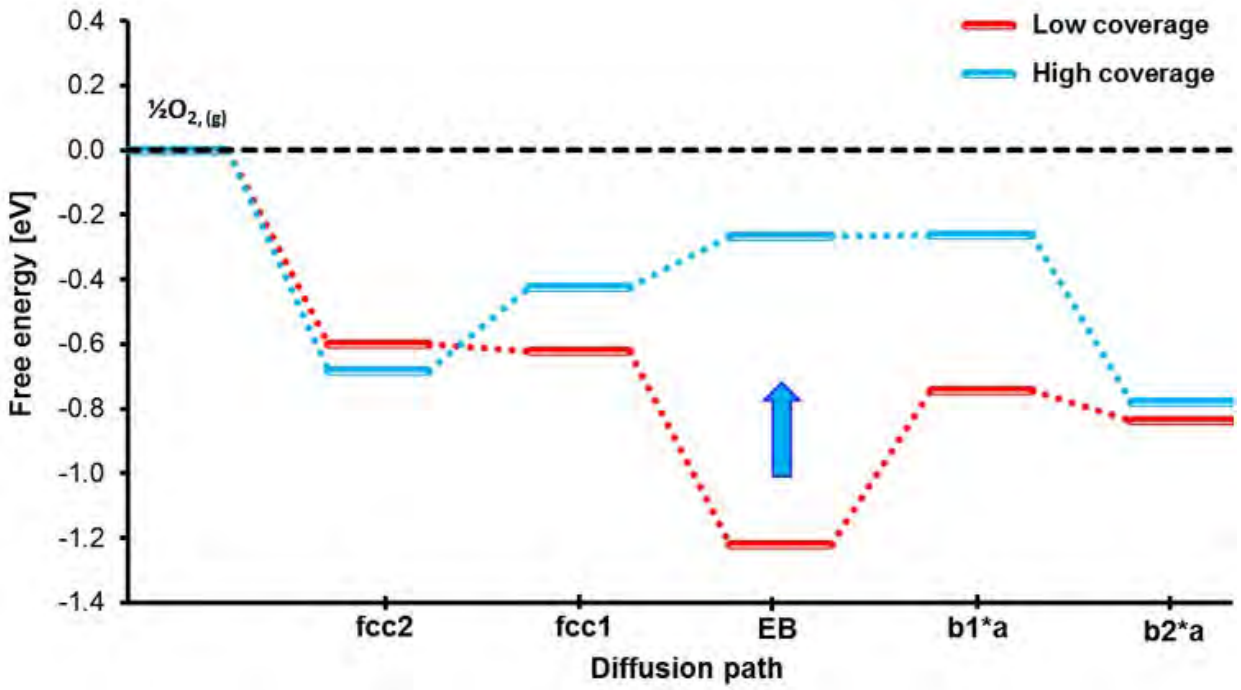

Figure 7.16: Calculated differential adsorption free energy generated for adsorbing a second O atom on a nanorod pre-covered with one O atom on an EB site (High coverage). Also plotted is the profile of atomic O adsorption on a clean nanorod model (Low coverage). All energy value are with respect to $\frac{1}{2}O_2$ in the gas phase and a Pt(mNR)-[5(111)×5(100)] nanorod model (clean: low coverage and pre-covered: high coverage).

of note is the O-O separation in the latter co-adsorption configurations, this separation increases in the reverse order as the lateral interaction energy (2.811 Å < 2.841 Å < 2.983 Å). The observed stabilization of atomic O away from the edge was argued to be due to the decreasing local coverage and the increasing separation between the two co-adsorbed O atoms (Figure 7.16).

7.2.4 Diffusion of O at a high coverage limit

Figure 7.16 demonstrates that a 1 ML O coverage of EB sites is thermodynamically feasible at typical PEMFC conditions, i.e. at 85 °C and 1 bar pressure. However, unlike in the previous case (at a low coverage limit) where there was a deep well in the potential energy surface (see Figure 7.3), at the high coverage limit the potential energy surface is almost flat near the edge. The lowering of the potential energy surface away from the edge is due to the variation in local atomic O coverage. At a low coverage limit it was observed that the activation free energies for diffusion away from an EB geometry were high. This was also compared in terms of hopping frequency where it was found that the diffusion towards the Pt(111) was 6 orders of magnitude slower than diffusion rate towards the Pt(100) facet (when coverage/concentration effect was not considered). The high diffusion barriers were also due to the large adsorption energy differences between the EB adsorbed state and terrace adsorbed states (in Chapter 6 the localized edge effect was demonstrated−this has implications on the change in adsorption energy as a function of distance from the edge). Therefore, an interesting study will be to investigate the diffusion of atomic O at a high coverage limit (where the energy difference between the EB state and the terrace adsorbed states was relatively small, Figure 7.16).

Performing similar calculations as in Subsection 7.2.2, the diffusion barriers of atomic O from EB-EB co-adsorbed states to EB-terrace co-adsorbed states (EB-fcc1 and EB-b1*a) were evaluated. The geometric and energetic properties of the latter diffusion steps are presented below.

EB-EB→EB-fcc1 diffusion step

The transition state for atomic O diffusion from the EB-EB to the EB-fcc1 co-adsorption state was observed to be equivalent to a bridge (b1a) adsorption geometry. The geometric and energetic properties of the latter transition state are presented in Table 7.14 and Figure 7.17. For the O atom adsorbed on the EB site the Pt-O bond lengths were calculated to be 1.935 Å and 1.965 Å (bonding with an edge Pt atom which is also bonded to the b1a bound O atom). The Pt-O bond lengths for the O atom on the b1a site were calculated to be 2.066 Å (bonding to an edge Pt atom) and 1.991 Å (bonding to non-edge Pt atoms). The O-O separation distance was calculated to be 3.092 Å (larger than the equilibrium Pt-Pt bond length). Compared to the transition state of atomic O diffusion from the EB site to the fcc1 site at a low coverage limit, at a high coverage limit the diffusing O atom was observed to have a transition state which was further from the edge atomic row. Figure 7.18 presents the optimized diffusion path of atomic O from the EB-EB to the EB-fcc1 co-adsorption state. The co-adsorption properties of the initial, transition and final states are presented in Table 7.14. Also presented in Table 7.14 are the vibrational frequencies of the transition state. Only one imaginary vibrational mode was observed—in the direction of the diffusion pathway. The activation free energy for this diffusion step was calculated to be 0.53 eV. The corresponding hopping frequency of atomic O diffusion from the EB-EB to the EB-fcc1 adsorption state was calculated to be 2.48×10^{5} s^{-1} at 358 K and 1 bar−typical PEMFC operating conditions.

Table 7.14: Thermodynamic properties of two co-adsorbed O atoms: EB-EB, EB-b1a and EB-fcc1 states.

diffusion step	IS	TS	FS
geometry	EB-EB	EB-b1a	EB-fcc1
d_{Pt-O} [Å]	*a*		*b*
O on an EB site		1.965, 1.938	
O on an b1a/fcc1 site		2.066, 1.991	
d_{O-O} [Å]	*a*	3.092	*b*
E_{tot} [eV]	-390.98	-390.42	-391.13
$G(358.15K)$ [eV]	-390.80	-390.27	-390.96
E_a [eV]		0.56	
$\Delta G^{\ddagger}_{ACT}(358.15K)$ [eV]		0.53	
ν_i [cm^{-1}]	609, 563, 527	536, 511, 477	540, 466, 457
	485, 123, 111	378, 120, 58/*i*	415, 240, 151

a data presented in Table 7.9

b data presented in Table 7.10

/*i* indicates that a vibrational mode is imaginary

EB-EB→EB-b1*a diffusion step

The transition state for atomic O diffusion from the EB-EB to the EB-b1*a co-adsorption state was observed to be equivalent to a bridge (tilted EB state) adsorption geometry. The geometric and energetic properties of the latter transition state are presented in Table 7.15 and Figure 7.19. For the O atom adsorbed on the EB site the Pt-O bond lengths were calculated to be 1.950 Å and 1.952 Å. The Pt-O bond lengths for the O atom on the tilted EB adsorption state (*t*EB) were calculated to be 2.020 Å and 2.036 Å. The O-O separation distance was calculated to be 3.010 Å. Figure 7.20 presents the optimized diffusion path of atomic O from the EB-EB to the EB-b1*a co-adsorption state. The co-adsorption properties of the initial, transition and final states are presented in Table 7.15. Also presented in Table 7.15 are the vibrational frequencies of the transition state. Only one imaginary vibrational mode was observed—in the direction of the diffusion pathway. The activation free energy for this diffusion step was calculated to be 0.36 eV. The corresponding hopping frequency of atomic O diffusion from the EB-EB to the EB-b1*a adsorption state was calculated to be 5.54×10^{7} s^{-1} at 358 K and 1 bar−typical PEMFC operating conditions.

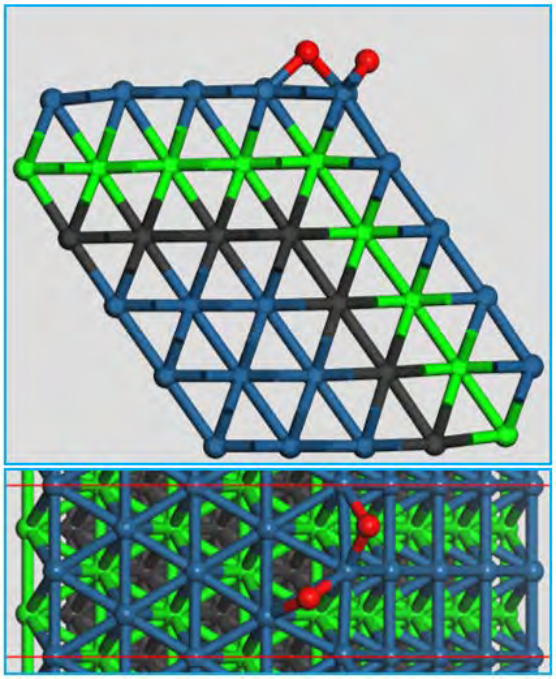

Figure 7.17: Equilibrium geometry of two co-adsorbed O atoms on EB and b1a sites (transition state geometry) of the Pt(mNR)-[5(111)×5(100)] nanorod model. Side view (top) and [111] surface normal view (bottom).

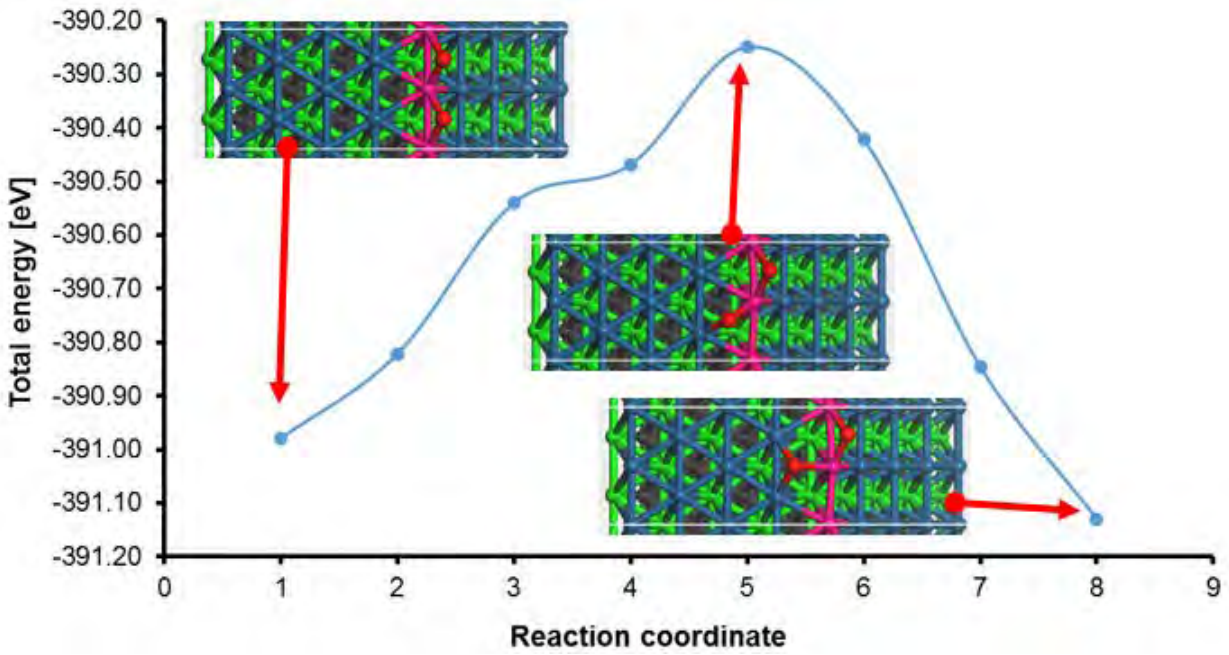

Figure 7.18: Diffusion of atomic O from the EB-EB to the EB-fcc1 co-adsorption state at a high coverage limit.

Discussion

High atomic O coverage at and near edge sites of nanoparticles have been reported (Wei & Liu, 2013). In this study it was demonstrated that a 1 ML atomic O coverage of edge sites is thermodynamically feasible. At this coverage a flat potential energy surface near the edge was observed (see Figure 7.16). For atomic O diffusion from the EB to the fcc1 state, it was observed that both low and high coverage scenarios consisted of a similar transition state (diffusing atomic on a b1a site). Therefore, the reduced diffusion free energy barrier (0.51 eV reduction) was attributed to decrease in the relative stability (0.44 eV) as a result of lateral interaction of the co-adsorbed states (flattening of the potential energy

Table 7.15: Thermodynamic properties of two co-adsorbed O atoms: EB-EB, EB-*t*EB and EB-b1*a states.

diffusion step	IS	TS	FS
geometry	EB-EB	EB-*t*EB	EB-b1*a
d_{Pt-O} [Å]	*a*		*b*
O on an EB site		1.950, 1.952	
O on an b1a/fcc1 site		2.020, 2.036	
d_{O-O} [Å]	*a*	3.010	*b*
E_{tot} [eV]	-390.98	-390.59	-390.96
$G(358.15K)$ [eV]	-390.80	-390.43	-390.80
E_a [eV]		0.39	
$\Delta G^{\ddagger}_{ACT}(358.15K)$ [eV]		0.36	
ν_i [cm^{-1}]	609, 563, 527	549, 488, 450	557, 488, 444
	485, 123, 111	371, 111, 90/*i*	400, 166, 106

a data presented in Table 7.9

b data presented in Table 7.12

/*i* indicates that a vibrational mode is imaginary

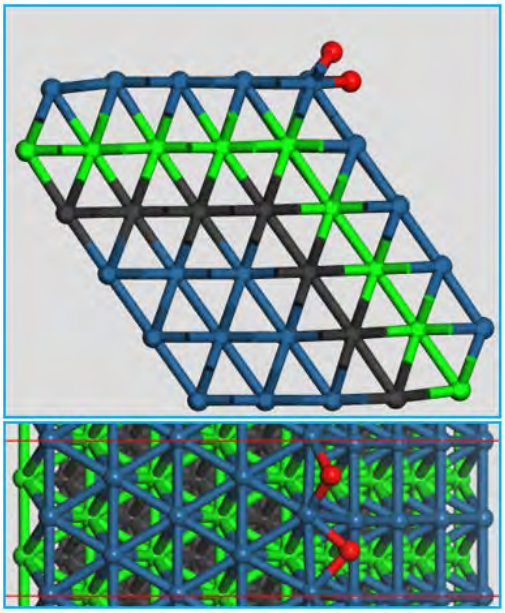

Figure 7.19: Equilibrium geometry of two co-adsorbed O atoms on EB sites ((EB-*t*EB transition state geometry) of the Pt(mNR)-[5(111)×5(100)] nanorod model. Side view (top) and [111] surface normal view (bottom).

surface). For atomic O diffusion from the EB to the b1*a site, it was observed that the transition state geometry at a low coverage was different from that observed at a high coverage−although both geometries were bridge states. The diffusion free energy barrier was lower at a high coverage by 0.22 eV. Figure 7.21 presents a summary of calculated diffusion free energy barriers at a low and high coverage limits. The reduced diffusion free energy barriers as a consequence of high coverage, were comparable to calculated activation energies for ORR rate limiting reaction steps on Pt(111) and Pt(100) terraces (see Tables 1.3 and 1.4 for a comparison with activation energies of ORR reaction steps). The calculated hopping frequency for the movement from the EB-EB co-adsorbed state towards the Pt(111) and Pt(100) nanorod terraces were 2.48×10^5 s^{-1} (EB-EB to EB-fcc1) and 5.54×10^7 s^{-1} (EB-EB to EB-b1*a), respectively. The latter correspond to 7 and 3 orders of magnitude improvements in the diffusion rate from the edge towards the Pt(111) and Pt(100) facets, respectively, compared to diffusion at a low coverage limit.

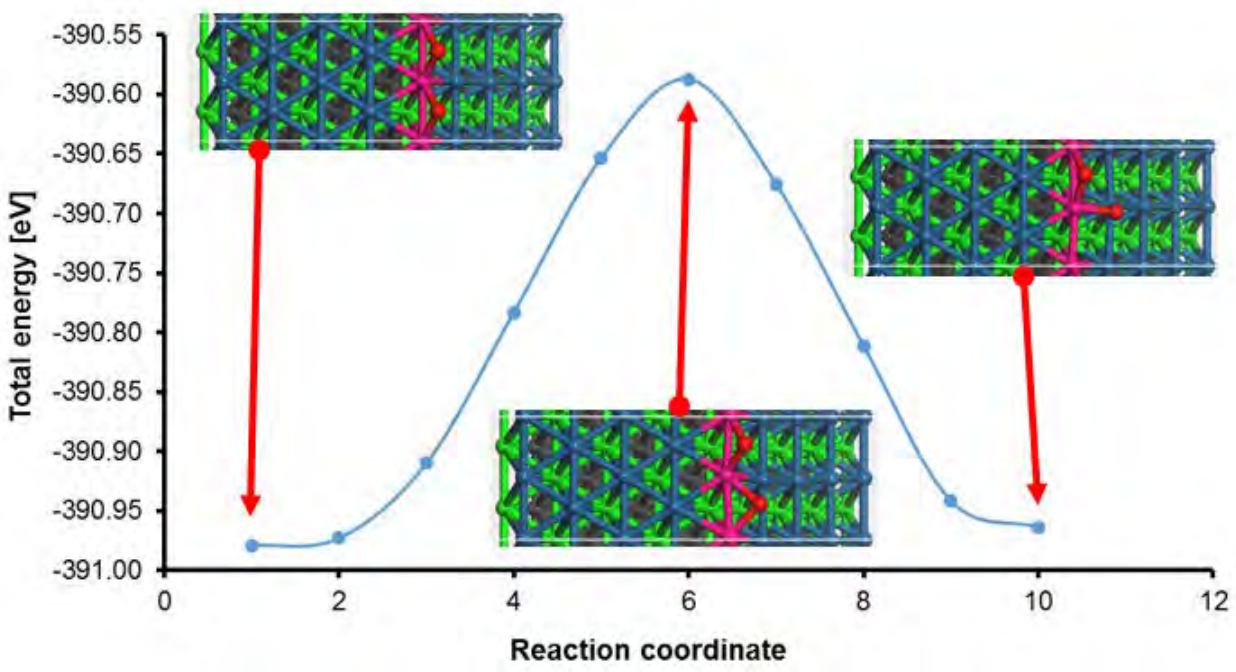

Figure 7.20: Diffusion of atomic O from the EB-EB to the EB-b1*a co-adsorption state at a high coverage limit.

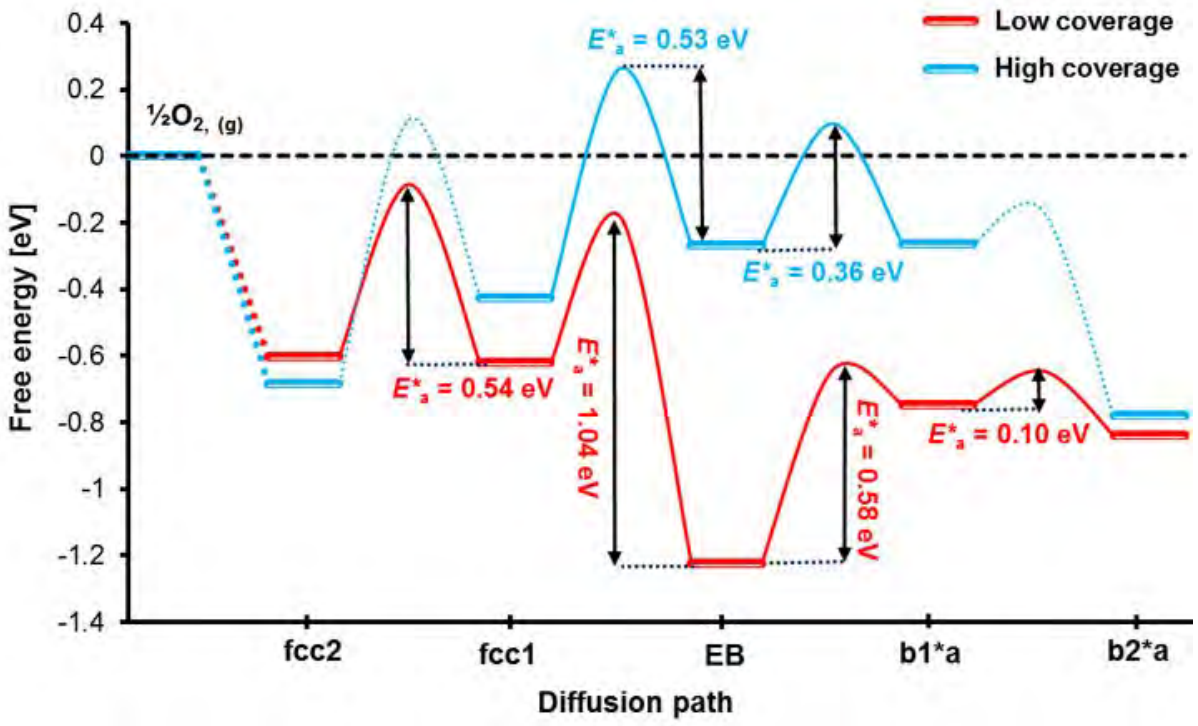

Figure 7.21: Calculated activation free energies ($E_a^* \equiv \Delta G_{ACT}^{\ddagger}$—includes entropic corrections) for diffusion of one atomic O from an EB-EB co-adsorbed state towards the Pt(111)-central-fcc site (fcc2) and Pt(100)-near-central-bridge site (b2*a). A temperature and pressure correction to 85 °C and 1 bar, has been considered. All energies are referenced to $\frac{1}{2}O_2$ in the gas phase and a Pt(mNR)-[5(111)×5(100)] nanorod model (clean: low coverage and pre-covered with atomic O on an EB site: high coverage). The dotted barriers correspond to diffusion at a low coverage limit, Figure 7.10.

7.2.5 Overall diffusion rates

So far multiple diffusion steps between the central terrace sites (fcc2 and b2*a) have been considered. It is of great interest to quantify the overall diffusion rate constant of atomic O from one central terrace

site to another across the edge atomic row. Due to the localization of edge effect on adsorption along the Pt(100) nanorod facet, the b2*a site was considered to be a relatively good approximation of the central terrace region. Furthermore, beyond this site towards the central terrace, it was anticipated that the diffusion energetics of atomic O will be invariant. Along the Pt(111) facet atomic O diffusion was considered upto the fcc2 terrace site. The considered forward and reverse diffusion process can be simplified as illustrated in Figure 7.22. The reciprocal of the rate constant of a diffusion step i, k_i^{-1}, was considered as a diffusion resistance–analogous to the resistance in an electrical circuit (van der Put, 2013). Therefore, the overall hopping frequency was calculated using a equation for resistors in series (equation 7.8).

$$\frac{1}{k_{overall,\,f}} = \frac{1}{k_1} + \frac{1}{k_2} + \frac{1}{k_3} + \frac{1}{k_3} + \frac{1}{k_4} + \frac{1}{k_5} \tag{7.8}$$

Rearranging equation 7.8 result in equation 7.9,

$$k_{overall,\,f} = \frac{1}{\frac{1}{k_1} + \frac{1}{k_2} + \frac{1}{k_3} + \frac{1}{k_3} + \frac{1}{k_4} + \frac{1}{k_5}} \tag{7.9}$$

The overall reverse hopping frequency was also calculated based on the above definition. Using the data presented in Table 7.8 and the above definitions, the overall hopping frequencies, $k_{overall,\,f}$ and $k_{overall,\,r}$ were calculated to be 5.22×10^{4} s^{-1} and 1.88×10^{-2} s^{-1} at a low coverage limit, respectively. At a high coverage limit the overall rate constants were calculated to be 1.40×10^{3} s^{-1} and 1.12×10^{5} s^{-1} for $k_{overall,\,f}$ and $k_{overall,\,r}$, respectively.

Considering the overall diffusion rate constants two observations were made. First, the diffusion of atomic O was more favoured towards the Pt(100) facet at a low coverage limit. Secondly, at a high coverage limit diffusion of atomic O was observed to proceed from the Pt(100) facet towards the Pt(111) facet. Although there are potential coverage effects on the above results, it is interesting to note that at a high coverage limit—a thermodynamically stable state—the hopping frequency of atomic O from the Pt(100) facet towards the Pt(111) nanorod facet is ca. 1.12×10^{5} s^{-1}. This diffusion rate corresponds to a non-zero cell current density. The relationship between the current density (j) and the rate of water production (r_{H_2O}) at the cathode electrode is given by equation 7.10,

$$r_{H_2O} = \frac{j}{nF} \tag{7.10}$$

where n and F are number of charges transferred, 2, and the Faraday's constant. Equation 7.10 and the diffusion rate of atomic O at a high coverage limit (2.48×10^{5} s^{-1}) were equated to calculate the corresponding current density. Assuming a constant site density of 9.92×10^{-5} mole-site.m^{-2} (corresponding to the packing density of a Pt(111) slab surface) a current density of 107 A.cm^{-2} was calculated. Therefore, at a high coverage limit and current density of ca. 100 mA.cm^{-2} the overall hopping frequency of atomic O from a Pt(100) nanorod facet towards a Pt(111) facet (across the edge) would be three orders of magnitude faster than the rate at which a single water molecule is produced (turnover frequency of water production).

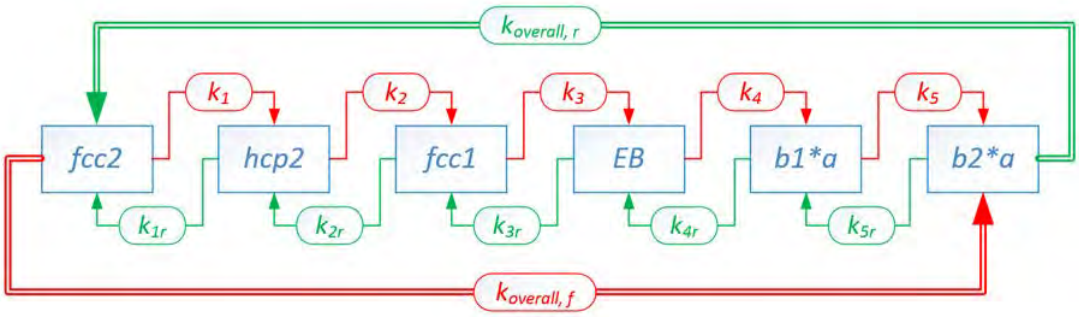

Figure 7.22: Illustration of the overall diffusion of atomic O between the Pt(100) facet and the Pt(111) facet. k_i and k_{ir} are forward and reverse diffusion rate constants for a single diffusion step, respectively.

7.3 Connection of nanorod facets through the bulk

The connection between the nanorod facets can also be through the bulk. This occurs when the behaviour of one facet is influenced by existing coverage on the adjacent facet. If this connection exists then the assumption considered when modelling the ORR overall activity over polycrystalline Pt nanoparticle may not hold. It is generally assumed that each facet would behave as if it were an infinite slab. The latter is tested in the present section by investigating the influence of Pt(100) nanorod facet coverage on the interaction of the Pt(111) nanorod facet with atomic O and vice versa.

Two sets of calculations are conducted; these are interaction of O atoms with each of the two facets separately (i.e. with zero O coverage on the second facet, image A, B, D and E in Figure 7.23) and the interaction of O atoms with each of the facet when the second facet is pre-covered with O atoms image C and F in Figure 7.23). Figure 7.23 illustrates the case studies investigated to determine the degree of interaction between the two nanorod facets through the bulk. It should be noted that in these sets of calculations the EB sites are left unpopulated to eliminate any interactions through the edge coverage.

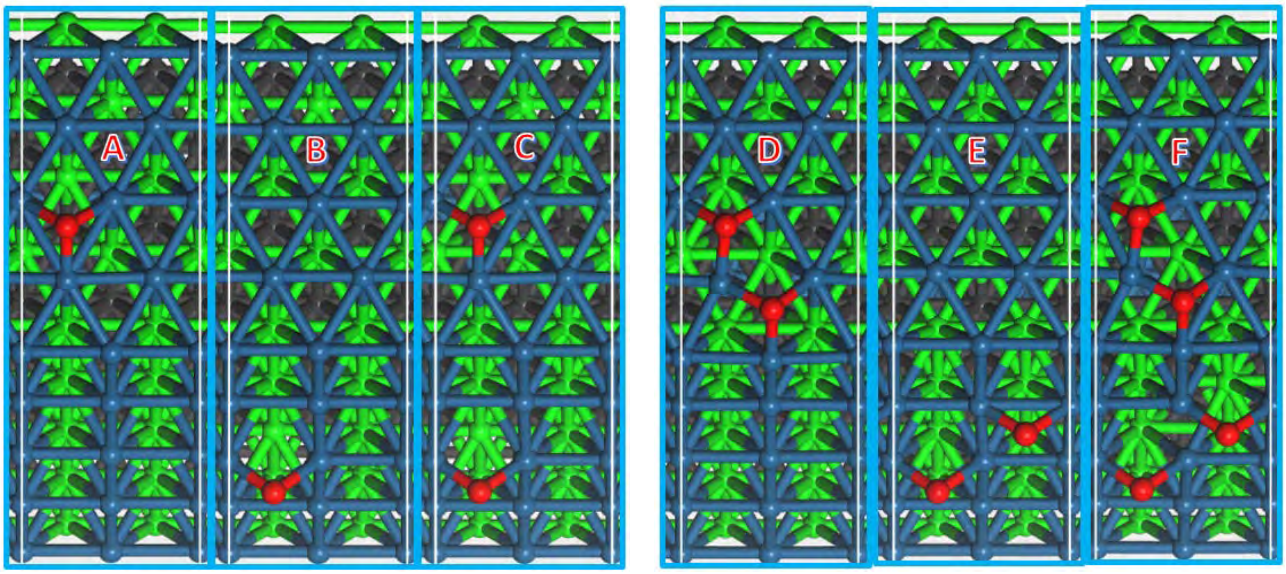

Figure 7.23: Illustration of through bulk interaction of O atoms co-adsorbed on the Pt(111) and Pt(100) nanorod facets. Equilibrium geometries for atomic O co-adsorption on the Pt(111) and Pt(100) nanorod facets—(A-C) at a low local atomic O coverage and (D-F) at a high local atomic O coverage.

It is expected that in the absence of interaction between two O atoms adsorbed on adjacent nanorod facets, the integral adsorption energy of two O atoms on two facets will be equal to the sum of the separate adsorption energies. This is represented by the following expression,

$$\Delta E_{O,bulk} = E_{O,ads}|_{Pt(111)+Pt(100)} - (E_{O,ads}|_{Pt(111)} + E_{O,ads}|_{Pt(111)}) \tag{7.11}$$

where $\Delta E_{O,bulk}$, $E_{O,ads}|_{Pt(111)+Pt(100)}$, $E_{O,ads}|_{Pt(111)}$ and $E_{O,ads}|_{Pt(100)}$ are the interaction energy of O atoms through the bulk, integral adsorption energy of O atoms on both nanorod facets, adsorption energy of O atoms on Pt(111) facet and adsorption energy of O atoms on Pt(100) facet, respectively. Therefore, there is zero through bulk interaction between the Pt(111) and Pt(100) nanorod facets when $\Delta E_{O,bulk} \approx 0$. Table 7.16 presents the adsorption energies corresponding to the geometric structures illustrated in Figure 7.23. A small through bulk interaction between nanorod terrace coverages was observed. Since the adsorbed O atoms for all investigated cases were well separated, it can be argued within reason that the observed interaction energies were due to through bulk interactions and model variation. Although the latter may be true, it should be noted that per O atom the interaction

energies were calculated to be ca. 0.02 eV−which was within the model variation. Therefore, it can be concluded that at the studied coverage at best the through bulk interactions are insignificant.

Table 7.16: Calculated interaction energies of the Pt(111) and Pt(100) nanorod facet coverages.

O coverage	$E_{O,ads}\|_{Pt(111)}$	$E_{O,ads}\|_{Pt(100)}$	$E_{O,ads}\|_{Pt(111)+Pt(100)}$	$\Delta E_{O,bulk}$	
	[eV]	[eV]	[eV]	[eV]	[eV/O]
1×O atom per facet	-1.00[a]	-1.21[a]	-2.25[b]	-0.04	-0.02
2×O atoms per facet	-1.92[b]	-2.42[b]	-4.25[c]	0.08	0.02

a, *b* and *c* are reported with respect to $\frac{1}{2}O_2$, O_2 and $2O_2$ in the gas phase, respectively, and a clean nanorod

Chapter 8

General Conclusions

The present study has used platinum nanorod models to model the edge regions of model nanoparticles. The rhombic nanorod model gives relatively similar adsorption energetic and geometric properties of atomic O and O_2 to what is predicted based on cuboctahedral and truncated octahedral nanoparticles models. Furthermore, this model nanorod has been shown to be in some reasonable agreement with the Pt(211) stepped-surfaces for the adsorption of O_2 whilst for atomic O adsorption on EB sites, a significant deviation was predicted between the nanorod model and the Pt(211) stepped-surface model. The adsorption of both atomic O and O_2 was shown to be much stronger on nanorod edge sites—the Pt(mNR)-[5(111)×5(100)] rhombic nanorod model was found to be sufficiently large to give converged terrace adsorption energies of atomic O and O_2.

The nanorod model was then used to investigate the underlying assumption applied when modelling the overall ORR activity of polycrystalline nanoparticles. This assumption is based on the following conditions:

1. The edge effect is localized and does not influence adjacent terrace sites.
2. The edge sites form a separation barrier that limits the diffusion of reaction intermediates from diffusing across adjacent terraces.

These conditions can be synthesised into one statement which presupposes that the different polycrystalline surface features, i.e. terraces, edges and steps, behave independent of each other (are kinetically isolated) and their respective coverages do not have a connected influence on each other.

Based on the calculated adsorption energies of atomic O and O_2 along the nanorod terraces it can be concluded that, (i) along the Pt(100) nanorod facet the edge effect is localized, i.e. only the EB site exhibit enhanced adsorption energies of atomic O and O_2, and (ii) along the Pt(111) facet the adsorption energies of both atomic O and O_2 are overall weakened (compared to adsorption on equivalent adsorption states on extended slab models) as a result of the presence of edges in the nanorod model. Furthermore, along this terrace, the region between the edge and first atomic row from the edge exhibit enhanced adsorption strengths for O_2 (not true for atomic O). The latter is due to the direct interaction of one O atom with the edge atomic row. Beyond the first atomic row from the edge, the adsorption energy of O_2 is converged. Therefore, along the Pt(111) nanorod facet the edge effect on the adsorption energies of atomic O and O_2 extends across the terrace width (observed as a weakening of the adsorption strength compared to adsorption on extended slab surfaces).

The correlation between the adsorption energy of O_2 and the site properties was also investigated. It was observed that the adsorption energy of O_2 does not correlate well with the site d-band center energies when adsorption on the EB site was considered. Therefore, from the latter observation it can be concluded that the increased stability of O_2 on EB sites is also an effect of the local geometry and degree of relaxation. A good empirical correlation of the same adsorption energies with the site coordination number was observed. The latter is consistent with the present literature, however, no *a*

priori explanation was proposed.

The adsorption studies showed that at low coverage conditions, the edge can be considered as a separation barrier, as the diffusion barriers were found to be high compared to terrace diffusion barriers. However, further calculations revealed that a high edge coverage of 1 ML is thermodynamically feasible. At this coverage it was calculated that the diffusion barriers across the edge were significantly reduced and the hopping frequency was estimated to be improved by 7 orders of magnitude for diffusion from the EB site towards the fcc1 sites (Pt(111) nanorod facet) as a consequence of increased coverage. Therefore, it can be concluded that the edges can no longer be treated as separation barriers between adjacent terraces, this is at least true for the investigated nanorod model. At a current density of 100 mA/cm^2 the overall hopping frequency of atomic O across the edge towards the Pt(111) terrace was calculated to be three orders of magnitude faster than the turnover frequency of water production.

In summary it can therefore be concluded that the proposed hypothesis is not supported by the findings in this study. Although the edge sites were found to adsorb both atomic O and O_2 strongly, their mere existence weakens the adsorption strength on the Pt(111) terrace sites (this effect is however localized for the Pt(100) nanorod facet). Therefore, the Pt(111) slab model results are anticipated to overestimate the adsorption stability of both atomic O and O_2 on model nanoparticle Pt{111} terraces. The connection of the terraces through reaction intermediate diffusion was found to be feasible at typical PEMFC conditions. Therefore the conditions required for the assumption which forms the basis of the overall ORR activity models, are not supported by the findings in this work—it is concluded that this assumption does not hold under the investigated conditions.

Considering other ORR intermediates such as OH may give interesting insight into the connection between the nanorod facets. The next step would be to compile a kinetic model that considers diffusion of key ORR intermediate species and perform sensitivity analyses to investigate the extent by which the connection (or lack of) of different surfaces influence the overall ORR activity. The latter will also highlight the limitation faced when the surfaces are assumed to be kinetically isolated.

Appendix A

Computational methods

A.1 Vibrational analysis

During a vibrational analysis calculations, each relaxed atoms is displaced twice in each direction. Therefore, a system with N number of perturbed atoms, $6N$ displacements will be made to obtain the Hessian matrix. The size of the displacement step was investigated by comparing vibrational frequencies obtained using the commonly used value of 0.02 Å to the results obtained from a smaller displacement step, 0.015Å. The equilibrium adsorption state of O_2 on a Pt(111)-p(2x2) fcc site was used to test the above. Table A.1 presents the calculated vibrational frequencies of O_2 on a Pt(111)-p(2x2) fcc site. No significant difference in calculated vibrational frequencies was observed. Therefore, the commonly used 0.02 Å displacement step was used in this study.

Table A.1: Calulated vibrational frequency modes of O_2 on a Pt(111)-p(2x2) fcc site.

Displacement step	0.01 Å	0.015 Å	0.02 Å
υ_i [cm^{-1}]	811, 509, 368 315, 232, 130	812, 510, 368 318, 230, 138	811, 510, 368 317, 234, 131

A.2 The AM05 functional

The Armiento and Mattssoon functional of 2005 (AM05) (Armiento & Mattsson, 2005) has been reported to give improved equilibrium bulk properties of transitions state metal including platinum. The lattice parameter predicted by this functional are in good agreement with experimental measurements (Mattsson *et al.*, 2008). An attempt to use this LDA based functional resulted in a number of complications. Although, it was observed to give a better prediction of the equilibrium lattice parameter of bulk platinum, 3.917 Å, it was computationally difficult to obtain initial time steps that converged for all gas phase molecules. A number of calculations with varying algorithms and trial time steps were conducted to optimized the geometry of O_2 in a box. A strong dependence of the convergence on the initial time step was observed for different algorithms. Due to the latter and the lack of literatures studies which have used the AM05 functional for investigating the ORR process, this functional was not considered for further investigation.

Appendix B

Interaction of atomic O and O_2 with platinum surfaces

B.1 Unstable geometries

The high-symmetry sites on different platinum surfaces were probed with both atomic O and O_2. Some of the initial geometries on high-symmetry sites were found to be unstable and resulting in converged geometries on different high-symmetry sites. The following subsections presents a few of these geometries, both the starting geometry and the converged geometry after geometric optimization.

B.1.1 Atomic O and O_2 on platinum slab surfaces

Below are the different unstable geometries and their nearest stable states which are obtained during geometry optimization.

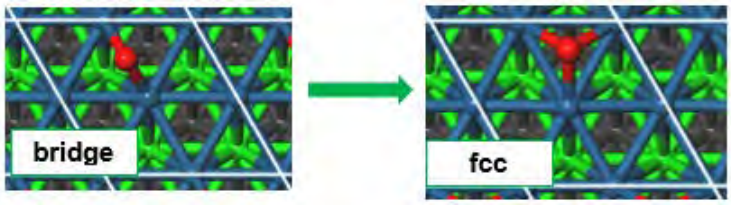

Figure B.1: Adsorption of atomic O on a Pt(111) bridge site.

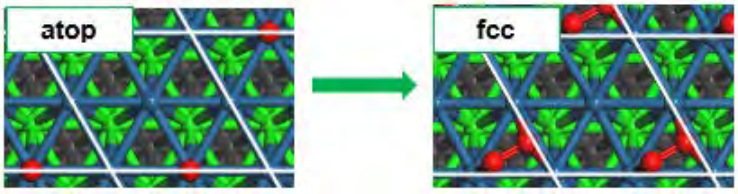

Figure B.2: Adsorption of O_2 on a Pt(111) atop site.

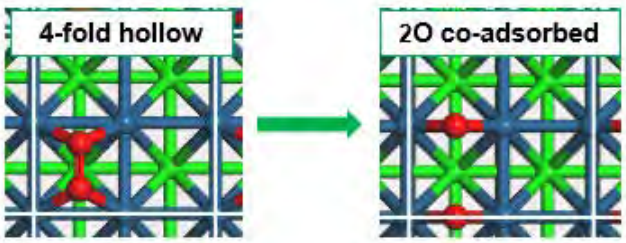

Figure B.3: Adsorption of O_2 on a Pt(100) four-fold hollow site.

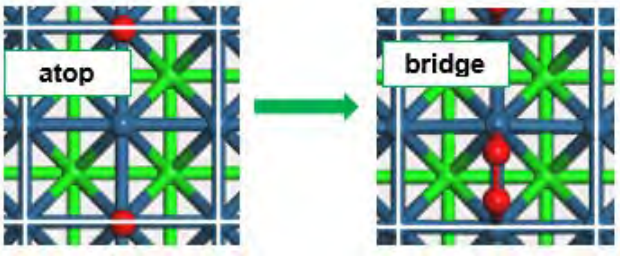

Figure B.4: Adsorption of O_2 on a Pt(100) atop site.

B.1.2 Atomic O and O_2 on a nanorod site

In this subsection the near edge high-symmetry sites which were found to be unstable are presented together with their converged geometries.

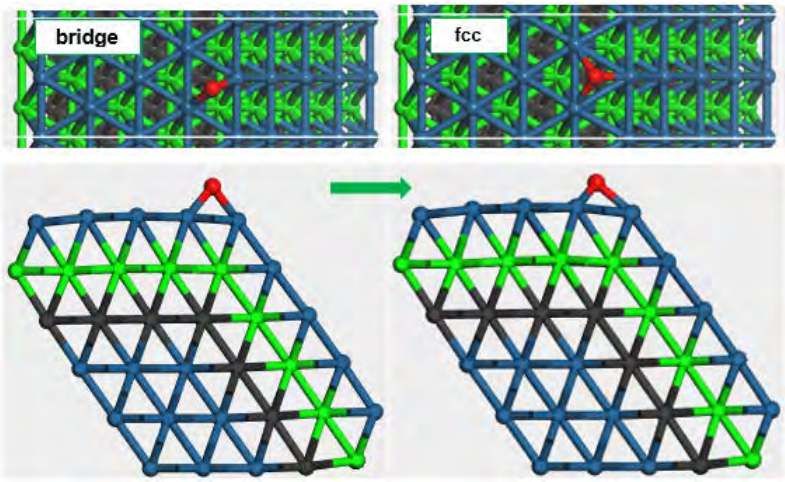

Figure B.5: Adsorption of atomic O on a nanorod near edge bridge site.

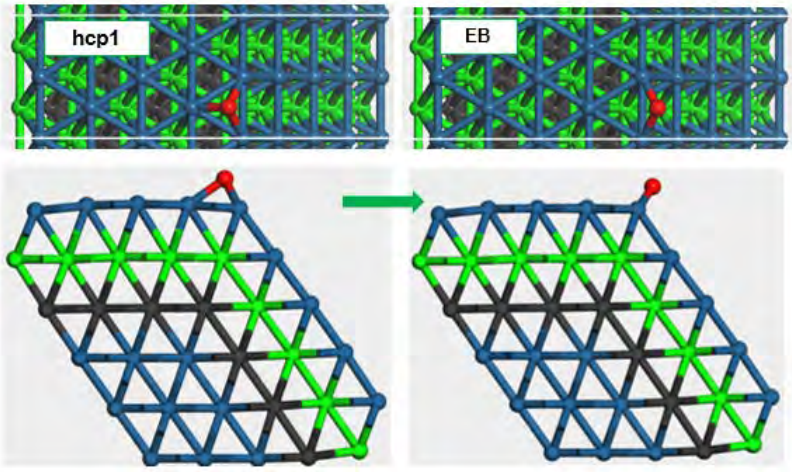

Figure B.6: Adsorption of atomic O on a nanorod near edge hcp site.

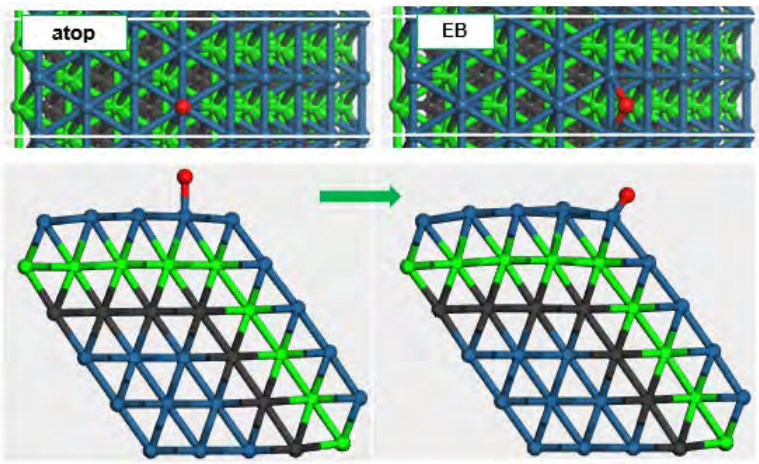

Figure B.7: Adsorption of atomic O on a nanorod near edge Pt(111) facet atop site.

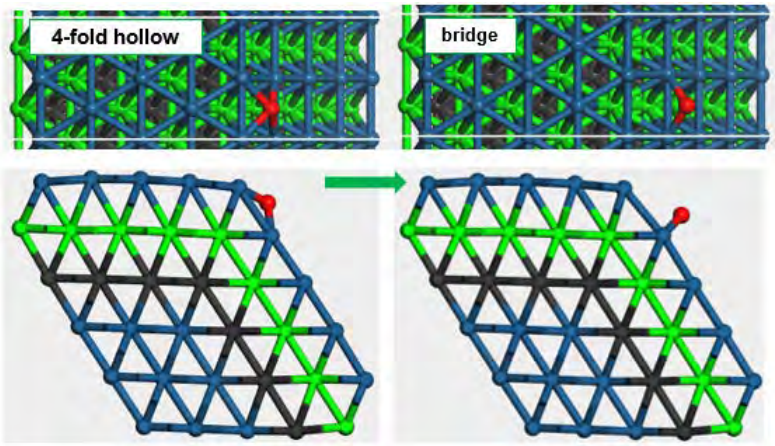

Figure B.8: Adsorption of atomic O on a nanorod near edge four-fold hollow site.

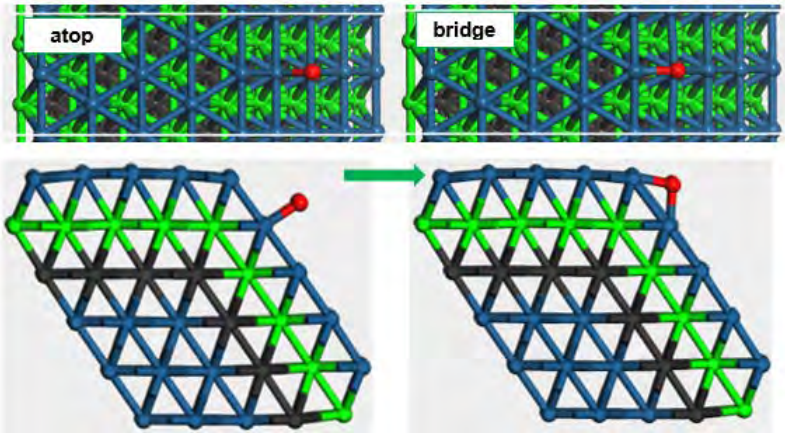

Figure B.9: Adsorption of atomic O on a nanorod near edge Pt(100) facet atop site.

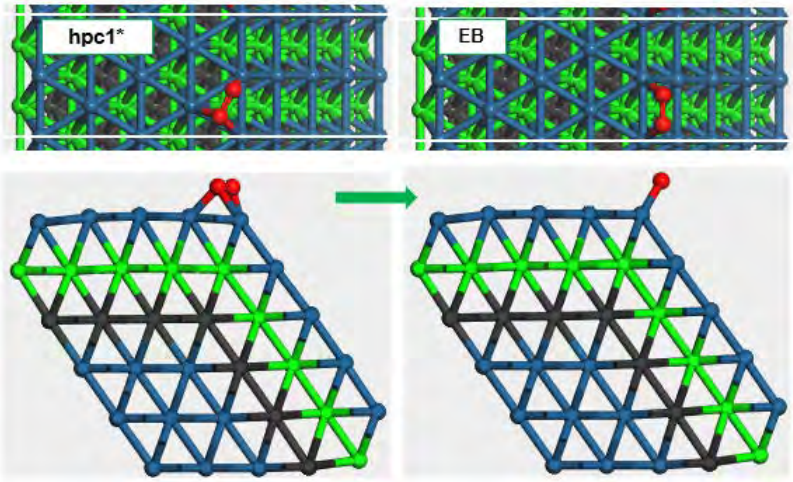

Figure B.10: Adsorption of atomic O on a nanorod near edge hcp1* site.

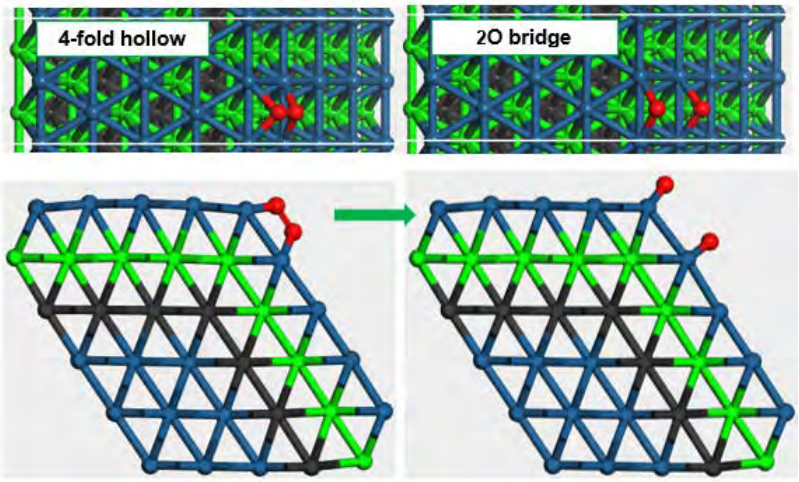

Figure B.11: Adsorption of atomic O on a nanorod near edge four-fold hollow site with O-O bond axis perpendicular to the edge atomic row.

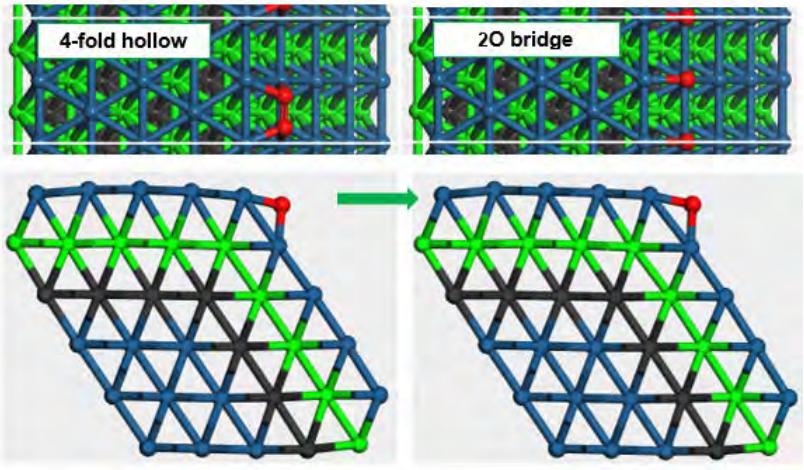

Figure B.12: Adsorption of atomic O on a nanorod near edge four-fold hollow site with O-O bond axis parallel to the edge atomic row.

B.2 Atomic O and O_2 adsorption along nanorod terrace sites

B.2.1 Atomic O along the nanorod terraces

This section presents the calculated adsorption energies of atomic O along different terrace sites on the nanorod. The data here corresponds to Chapter 6. All energies are given with respect to $\frac{1}{2}O_2$ in the gas phase ($eV/\frac{1}{2}O_2$).

Table B.1: Adsorption energies of atomic O along the Pt(111) and Pt(100) facets of the Pt(mNR)-[7(111)×5(100)] and Pt(mNR)-[5(111)×7(100)] nanorod model, respectively.

Nanorod model	Pt(mNR)-[7(111)×5(100)]		Pt(mNR)-[5(111)×7(100)]
facet	Pt(111)		Pt(100)
site	fcc	hcp	bridge
EB+1	-1.08	-	-1.23
EB+2	-1.03	-0.69	-1.21
EB+3	-1.00	-0.65	-1.16

'–' refers to an unstable geometry

Table B.2: Adsorption energies of atomic O along the Pt(mNR)-[5(111)×5(100)] nanorod facets.

Nanorod model	Pt(mNR)-[5(111)×5(100)]		
facet	Pt(111)		Pt(100)
site	fcc	hcp	bridge
EB+1	-1.01	-	-1.23
EB+2	-1.00	-0.66	-1.20

'–' refers to an unstable geometry

B.2.2 O_2 along the nanorod terraces

This section presents the calculated adsorption energies of O_2 along different terrace sites on the nanorod. The data here corresponds to Chapter 6. All energies are given with respect to O_2 in the gas phase (eV/O_2).

Table B.3: Adsorption energies of O_2 along the Pt(111) and Pt(100) facets of a Pt(mNR)-[7(111)×5(100)] and Pt(mNR)-[5(111)×7(100)] nanorod models, respectively.

Nanorod model	Pt(mNR)-[7(111)×5(100)]			Pt(mNR)-[5(111)×7(100)]
facet	Pt(111)			Pt(100)
site	fcc	hcp	bridge	bridge
EB+1	-0.69	-0.91	-0.70	-1.15
EB+2	-0.45	-0.36	-0.53	-1.13
EB+3	-0.42	-0.29	-0.53	-1.13

Table B.4: Adsorption energies of O_2 along the Pt(111) and Pt(100) facets of a Pt(mNR)-[5(111)×5(100)] nanorod model.

Nanorod model	Pt(mNR)-[5(111)×5(100)]			
facet	Pt(111)			Pt(100)
site	fcc	hcp	bridge	bridge
EB+1	-0.63	-0.88	-0.65	-1.15
EB+2	-0.47	-0.32	-0.56	-1.15

Appendix C

Thermodynamic corrections

C.1 Thermodynamic calculations

Since DFT calculated energies are calculated at zero kelvin ($T = 0K$), temperature corrections are required when modelling systems which occur at a different temperature. These corrections are possible with the use of partition functions and statistical thermodynamics. In this section a set of equations which are required to calculate a finite temperature correction are presented. These equations have been adopted from the work of (Hirano, 1993). The Gibbs free energy of adsorption of species i ($G_{i,ads}(T)$) is given by equation C.1,

$$G_i(T) = H_i(T) - TS_i \tag{C.1}$$

where $H_i(T)$ and S_i are the enthalpy and entropy of system i at a finite temperature T, respectively. The enthalpy is then calculated using equation C.2

$$H_i(T) = E_i^{DFT}(T = 0K) + E_i^{vib}(T) + E_i^{rot}(T) + E_i^{trans} + RT \tag{C.2}$$

where $E_i^{DFT}(T = 0K)$ is the DFT-calculated total energy of a system i at $0K$, while $E_i^{vib}(T)$, $E_i^{rot}(T)$ and E_i^{trans} are the vibrational, rotational and translational contributions contributions to the enthalpy of a system i at a finite temperature T, respectively. For an ideal gas these contribution are evaluated, based on statistical thermodynamics using the corresponding partition functions and energy operators, to be as follows (Hirano, 1993)

$$E_i^{vib}(T) = \frac{1}{2}N_A \sum_i h\nu_i + N_A \sum_i \frac{h\nu_i \cdot exp(-\frac{h\nu_i}{k_B T})}{[1 - exp(-\frac{h\nu_i}{k_B T})]} \tag{C.3}$$

$$E_i^{trans}(T) = \frac{3}{2}RT \tag{C.4}$$

$$E_i^{rot}(T) = \frac{n_{rot}}{2}RT \tag{C.5}$$

The entropic term in equation C.1 is given by,

$$S_i(T) = S_i^{vib}(T) + S_i^{rot}(T) + S_i^{trans}(T) + S_i^{degeneracy} \tag{C.6}$$

where $S_i^{vib}(T)$, $S_i^{rot}(T)$ and S_i^{trans} are the vibrational, rotational and translational contributions to the entropy of a system i at a finite temperature T, respectively. The different entropy contributions are calculated as follows,

$$S^{vib} = R\sum \frac{\frac{h\nu_i}{k_B T} exp(-\frac{h\nu_i}{k_B T})}{1 - exp(-\frac{h\nu_i}{k_B T})} - R\sum ln\left\{1 - exp(-\frac{h\nu_i}{k_B T})\right\} \tag{C.7}$$

$$S^{rot}(linear) = Rln\left\{\frac{8\pi^2 I k_B T}{\sigma h^2}\right\} + R \tag{C.8}$$

$$S^{rot}(nonlinear) = \frac{R}{2} ln\left\{\frac{\pi}{\sqrt{\sigma}} \frac{8\pi^2 c I_A}{h} \frac{8\pi^2 c I_B}{h} \frac{8\pi^2 c I_C}{h} \left(\frac{k_B T}{ch}\right)^3\right\} + \frac{3}{2}R \tag{C.9}$$

$$S^{trans} = \frac{5}{2} Rln(T) + \frac{3}{2} Tln(w) - Rln(p) - 2.31482 \tag{C.10}$$

$$S^{degeneracy} = Rln(g) \tag{C.11}$$

where the constants are:
k_B : Boltzmann constant
h : Planck constant
R : Gas constant
ν_i : vibrational mode i
N_A : Avogadro constant
n_{rot} : used to distinguish between linear ($n_{rot} = 3$) and nonlinear ($n_{rot} = 2$) molecules
σ : symmetry number of system i (for a free molecule)
c : speed of light
I_x : moment of inertia about an axis x, where $x = [A, B, C]$
w : molecular weight
p : pressure
g : degeneracy, the number of microscopic arrangements with the same energy

The degeneracy entropy The gas phase and adsorbed state systems are treated differently. For the gas phase all contributions are considered since each gas phase molecule is free to rotate, translate and vibrate. Whilst for adsorbed state systems it was assumed that since all adsorbates are chemically bound on a surface, they are not free to move and rotate. Therefore, only the vibrational contributions were considered. This was also applied for the diffusion transition states, these states were argued to be relatively stable compared to the gas phase and hence there are many vibrational levels they can access before being freely able to rotate and translate.

Appendix D

Diffusion of atomic O along the nanorod

D.1 Adsorption along a diffusion path

The diffusion of atomic O from the EB site towards the Pt(111) and Pt(100) nanorod facets was considered in this study. The data presented below describes, the adsorption strength and vibrational modes of adsorbed states. The total energies of a Pt(111)-p(2x2), Pt(100)-p(2x2) and Pt(mNR)-[5(111)×5(100)] surface models are, -140.18 eV, -138.01 eV and -378.88 eV, respectively.

Table D.1: Thermodynamic properties of initial (IS), transition (TS) and final (FS) states for atomic O diffusion at a low coverage limit (one O atom per nanorod or p(2x2) slab cell.

Diffusion step	IS	TS	FS
EB → fcc1	EB	bridge	fcc1
E_tot [eV]	-385.42	-384.37	-384.82
d_{Pt-O} [Å]	1.94	1.98, 2.00	2.10, 2.04×2
ν_i [cm^{-1}]	532, 464, 138	503, 373, 167/i	444, 377, 316
fcc1 → hcp2	fcc1	bridge	hcp2
E_tot [eV]	-384.82	-384.27	-384.47
d_{Pt-O} [Å]	2.10, 2.04×2	1.99	2.04×2, 2.03
ν_i [cm^{-1}]	444, 377, 316	500, 394, 141/i	445, 376, 317
slab: fcc → hcp	fcc	bridge	hcp
E_tot [eV]	-146.25	-145.59	-145.82
d_{Pt-O} [Å]	2.04	1.99	2.05
ν_i [cm^{-1}]	451, 387, 385	507, 394, 130/i	436, 321, 320
EB → b1*	EB	hollow	b1*
E_tot [eV]	-385.42	-384.82	-384.94
d_{Pt-O} [Å]	1.94	1.99, 2.01	1.96, 1.95
ν_i [cm^{-1}]	532, 464, 138	481, 372, 57/i	507, 446, 118
b1* → b2*	b1*	hollow	b2*
E_tot [eV]	-384.94	-384.82	-385.03
d_{Pt-O} [Å]	1.96, 1.95	2.02, 1.97	1.95
ν_i [cm^{-1}]	507, 446, 118	494, 371, 80/i	518, 454, 114
slab: b → b*	b*	hollow	b*
E_tot [eV]	-144.08	-143.88	-144.08
d_{Pt-O} [Å]	1.95	1.97, 2.00	1.95
ν_i [cm^{-1}]	521, 459, 115	485, 372, 67/i	521, 459, 115

/i indicates that a vibrational mode is imaginary

Table D.2: Thermodynamic properties of initial (IS), transition (TS) and final (FS) states for atomic O diffusion at a high coverage limit (two O atoms per nanorod.

Diffusion step	IS	TS	FS
EB+EB → fcc1+EB	EB+EB	bridge+EB	fcc1+EB
E_tot $[eV]$	-390.98	-390.42	-391.13
d_{Pt-O} [Å]	1.95	2.02^a, 1.97^a	2.20^a, 2.01×2^a
		1.96^b, 1.94^b	1.97^b, 1.93^b
ν_i [cm^{-1}]	609, 563, 527	536, 511, 477	540, 466, 457
	485, 123, 111	378, 120, 58$/i$	415, 240, 151
EB+EB → b1*+EB	EB+EB	bridge+EB	b1*+EB
E_tot $[eV]$	-390.98	-390.59	-390.96
d_{Pt-O} [Å]	1.95	2.04^a, 2.02^a	1.92^a, 1.99^a
		1.95^b	2.02^b, 1.93^b
ν_i [cm^{-1}]	609, 563, 527	549, 488	557, 526, 444
	485, 123, 111	371, 111, 90$/i$	400, 166, 106

a diffusing atomic O

b edge bound atomic O

$/i$ indicates that a vibrational mode is imaginary

D.2 Atomic O diffusion

Table D.3: Atomic O diffusion from an EB site to an fcc1 site.

Images	**EB → fcc1**			**EB+EB → fcc1+EB**		
	E_0 $[eV]$	Force^b $[eV\text{Å}^{-1}]$	NEB-force^b $[eV\text{Å}^{-1}]$	E_0 $[eV]$	Force^b $[eV\text{Å}^{-1}]$	NEB-force^b $[eV\text{Å}^{-1}]$
0	-385.42	0.00	-	-390.98	0.01	-
1	-385.31	0.45	0.09	-390.82	0.04	0.08
2	-385.05	0.55	0.12	-390.54	0.07	0.06
3	-384.83	0.31	0.07	-390.47	0.05	0.06
4	-384.48	0.68	0.12	-390.25	0.01	0.02
5	-384.27	0.01	0.00	-390.42	0.05	0.14
6	-384.49	0.79	0.15	-390.85	0.07	0.24
7	-384.82	0.00	-	-391.13	0.00	-

a single largest absolute force component acting on atomic O

b force perpendicular to the current hyper-tangent

Table D.4: Atomic O diffusion from an EB site to a b1* site.

Images	**EB → b1***			**EB+EB → b1*+EB**		
	E_0 $[eV]$	Force[b] $[eV\text{Å}^{-1}]$	NEB-force[b] $[eV\text{Å}^{-1}]$	E_0 $[eV]$	Force[b] $[eV\text{Å}^{-1}]$	NEB-force[b] $[eV\text{Å}^{-1}]$
0	-385.42	0.00	-	-390.98	0.01	-
1	-385.37	0.25	0.07	-390.97	0.01	0.06
2	-384.95	0.31	0.08	-390.91	0.02	0.06
3	-384.82	0.01	0.03	-390.78	0.04	0.14
4	-384.91	0.13	0.03	-390.65	0.03	0.09
5	-384.94	0.01	-	-390.59	0.01	0.05
6				-390.68	0.04	0.09
7				-390.81	0.08	0.09
8				-390.94	0.06	0.08
9				-390.96	0.01	-

a single largest absolute force component acting on atomic O

b force perpendicular to the current hyper-tangent

Table D.5: Atomic O diffusion from an fcc site to an hcp site.

Images	**fcc1 → hcp2**			**slab: fcc → hcp**		
	E_0 $[eV]$	Force[b] $[eV\text{Å}^{-1}]$	NEB-force[b] $[eV\text{Å}^{-1}]$	E_0 $[eV]$	Force[b] $[eV\text{Å}^{-1}]$	NEB-force[b] $[eV\text{Å}^{-1}]$
0	-384.82	0.00	-	-146.25	0.01	-
1	-384.65	0.72	0.03	-146.21	0.22	0.02
2	-384.38	0.47	0.04	-145.78	0.69	0.03
3	-384.27	0.01	0.02	-145.59	0.00	0.01
4	-384.37	0.52	0.07	-145.67	0.38	0.03
6	-384.47	0.00	-	-145.82	0.00	-

a single largest absolute force component acting on atomic O

b force perpendicular to the current hyper-tangent

Table D.6: Atomic O diffusion from a b site to a b* site.

Images	**b1* → b2***			**slab: b → b***		
	E_0 $[eV]$	Force[b] $[eV\text{Å}^{-1}]$	NEB-force[b] $[eV\text{Å}^{-1}]$	E_0 $[eV]$	Force[b] $[eV\text{Å}^{-1}]$	NEB-force[b] $[eV\text{Å}^{-1}]$
0	-384.94	0.01	-	-144.08	0.02	-
1	-384.91	0.15	0.05	-144.06	0.14	0.02
2	-384.82	0.01	0.07	-143.99	0.25	0.03
3	-385.01	0.16	0.17	-143.90	0.12	0.02
4	-384.98	0.10	0.18	-143.91	0.14	0.01
5	-385.03	0.02	-	-143.93	0.14	0.03
6				-143.88	0.01	0.01
7				-143.96	0.24	0.03
8				-144.06	0.16	0.01
9				-144.08	0.02	-

a single largest absolute force component acting on atomic O

b force perpendicular to the current hyper-tangent

Bibliography

Adamo, C. & Barone, V. (1999). *The Journal of Chemical Physics,* **110** (13), 6158–6170.

Arblaster, J. W. (1997). *Platinum Metals Review,* **41** (1), 12–21.

Armiento, R. & Mattsson, a. E. (2005). *Physical Review B - Condensed Matter and Materials Physics,* **72** (8), 1–5.

Badan, C., Koper, M. T., & Juurlink, L. (2015). *The Journal of Physical Chemistry C,* **119** (211), 13551–13560.

Bandarenka, A. S., Hansen, H. A., Rossmeisl, J., & Stephens, I. E. L. (2014). *Physical Chemistry Chemical Physics,* **16** (27), 13625–13629.

Barteau, M. A., Ko, E. I., & Madix, R. J. (1981). *Surface Science,* **102** (1), 99–117.

Becke, A. (1993). *Journal of Chemical Physics,* **98**, 5648–5652.

Birch, F. (1947). *Physical Review,* **71** (11), 809–824.

Bitzek, E., Koskinen, P., Gähler, F., Moseler, M., & Gumbsch, P. (2006). *Physical Review Letters,* **97** (17), 1–4.

Blöchl, P. E. (1994). *Physical Review B,* **50** (24), 17953–17979.

Bocquet, M.-L., Cerdà, J., & Sautet, P. (1999). *Physical Review B,* **59** (23), 15437–15445.

Calle-Vallejo, F., Loffreda, D., Koper, M. T. M., & Sautet, P. (2015). *Nature Chemistry,* **7** (April), 403–410.

Calle-Vallejo, F., Sautet, P., & Loffreda, D. (2014). *The Journal of Physical Chemistry Letters,* .

Chadi, D. J. & Cohen, M. L. (1973). *Physical Review B,* **8** (12), 5747–5753.

Chen, H. & Zhou, A. (2008). *Numerical Mathamatics: Theory, Methods & Applications,* **1** (1), 1–28.

Da Silva, J. L. F., Stampfl, C., & Scheffler, M. (2006). *Surface Science,* **600** (3), 703–715.

Dirac, P. A. M. (1929). *Proceedings of the Royal Society A: Mathematical, Physical and Engineering Sciences,* **123** (792), 714–733.

Duan, Z. & Wang, G. (2011). *Physical Chemistry Chemical Physics,* **13** (45), 20178–20187.

Duan, Z. & Wang, G. (2013). *The Journal of Physical Chemistry C,* **117** (12), 6284–6292.

Eichler, A. & Hafner, J. (1997). *Physical Review Letters,* **79** (22), 4481–4484.

Feibelman, P., Esch, S., & Michely, T. (1996). *Physical Review Letters,* **77** (11), 2257–2260.

Ford, D. C., Nilekar, A. U., Xu, Y., & Mavrikakis, M. (2010). *Surface Science,* **604** (19-20), 1565–1575.

Ford, D. C., Xu, Y., & Mavrikakis, M. (2005). *Surface Science,* **587** (3), 159–174.

Friebel, D., Viswanathan, V., Miller, D. J., Anniyev, T., Ogasawara, H., Larsen, A. H., O'Grady, C. P., Nørskov, J. K., & Nilsson, A. (2012). *Journal of the American Chemical Society,* **134** (23), 9664–9671.

Gasteiger, H. A., Baker, D. R., Carter, R. N., Gu, W., Liu, Y., Wagner, F. T., & Yu, P. T. (2010). In: *Hydrogen energy*, (Stolten, D., ed) chapter 1. WILEY-VCH Verlag GmbH & Co. Weinheim, Germany.

Gasteiger, H. A., Kocha, S. S., Sompalli, B., & Wagner, F. T. (2005). *Applied Catalysis B: Environmental,* **56** (1-2), 9–35.

Gee, A. T. & Hayden, B. E. (2000). *Journal of Chemical Physics,* **113** (22), 10333–10343.

Gewirth, A. A. & Thorum, M. S. (2010). *Inorganic chemistry,* **49** (8), 3557–66.

Gland, J. L., Sexton, B. A., & Fisher, G. B. (1980). *Surface Science,* **95** (2–3), 587–602.

Gómez-Marín, A. M., Rizo, R., & Feliu, J. M. (2013). *Beilstein Journal of Nanotechnology,* **4** (111), 956–967.

Greeley, B. J., Rossmeisl, J., Hellman, A., & Nørskov, J. K. (2007). *Zeitschrift für Physikalische Chemie-International Journal of Research in Physical Chemistry & Chemical Physics,* **221**, 1209–1220.

Greeley, J., Nørskov, J. K., & Mavrikakis, M. (2002). *Annual Review of Physical Chemistry,* **53**, 319–348.

Gu, Z. & Balbuena, P. (2007). *Journal of Physical Chemistry C,* **111** (27), 9877–9883.

Hammer, B., Hansen, L., & Nørskov, J. (1999). *Physical Review B,* **59** (11), 7413–7421.

Hammer, B., Morikawa, Y., & Nørskov, J. (1996). *Physical Review Letters,* **76** (12), 2141–2144.

Hammer, B., Nielsen, O. H., & Nørskov, J. K. (1997). *Catalysis Letters,* **46**, 31–35.

Hammer, B. & Nørskov, J. (2000). *Advances in Catalysis,* **45**, 71–129.

Hansen, H. A., Viswanathan, V., & Nørskov, J. K. (2014). *The Journal of Physical Chemistry C,* **118** (13), 6706–6718.

Haynes, W. M. (2013). *CRC Handbook of Chemistry and Physics, 94th Edition.* CRC Handbook of Chemistry and Physics. CRC Press, 94th edition.

Hirano, T. (1993). In: *MOPAC Manual*, (Stewart, J. J. P., ed). 7 edition.

Holewinski, A. & Linic, S. (2012). *Journal of the Electrochemical Society,* **159** (11), H864–H870.

Hoshi, N., Nakamura, M., & Hitotsuyanagi, A. (2013). *Electrochimica Acta,* **112**, 899–904.

Jacob, T., Muller, R. P., & Goddard, W. A. (2003). *The Journal of Physical Chemistry B,* **107** (35), 9465–9476.

Jacobse, L., den Dunnen, A., & Juurlink, L. B. F. (2015). *The Journal of Chemical Physics,* **143** (1), 014703.

Janik, M. J., Taylor, C. D., & Neurock, M. (2009). *Journal of The Electrochemical Society,* **156** (1), B126–B135.

Jennings, P. C., Aleksandrov, H. A., Neyman, K. M., & Johnston, R. L. (2014). *Physical Chemistry Chemical Physics,* **16**, 26539–26545.

Jonsson, H., Mills, G., & Jacobsen, K. W. (1998). In: *Classical and Quantum Dynamics in Condensed Phase Simulations - Proceedings of the International School of Physics* pp. 385–404,.

Karlberg, G. S., Rossmeisl, J., & Nørskov, J. K. (2007). *Physical Chemistry Chemical Physics,* **9** (37), 5158–5161.

Keith, J. a. & Jacob, T. (2010). *Angewandte Chemie (International ed. in English),* **49** (49), 9521–9525.

Khein, A., Singh, D. J., & Umrigar, C. J. (1995). *Physical Review B,* **51** (7), 4105–4109.

Kiejna, A., Peisert, J., & Scharoch, P. (1999). *Surface Science,* **432**, 54–60.

Kinoshita, K. (1990). *Journal of The Electrochemical Society,* **137** (3), 845–848.

Kittel, C. (2005). *Introduction to solid state physics.* New York: John Wiley & Sons Inc., 8 edition.

Kohn, W. & Sham, L. J. (1965). *Physical Review,* **140** (4A), A1133–A1138.

Kolb, M. J., Calle-Vallejo, F., Juurlink, L. B. F., & Koper, M. T. M. (2014). *The Journal of Chemical Physics,* **140** (13), 134708.

Kresse, G. & Furthmüller, J. (1996a). *Computational Materials Science,* **6** (1), 15–50.

Kresse, G. & Furthmüller, J. (1996b). *Physical Review B,* **54** (16), 11169–11186.

Kresse, G. & Hafner, J. (1993). *Physical Review B,* **47** (1), 558–561.

Kresse, G. & Hafner, J. (1994a). *Physical Review B,* **49** (20), 14251–14269.

Kresse, G. & Hafner, J. (1994b). *Journal of Physics: Condensed Matter,* **6** (40), 8245–8257.

Kresse, G. & Joubert, D. (1999). *Physical Review B,* **59** (3), 1758–1775.

Kresse, G., Marsman, M., & Jürgen, F. (2014). In: *VASP manual* pp. 1–208.

Kumar, M. (2000). *Physics and Chemistry of Minerals,* **27** (9), 650–655.

Kurth, S., Perdew, J. P., & Blaha, P. (1999). *International Journal of Quantum Chemistry,* **75** (4-5), 889–909.

Lang, B., Joyner, R. W., & Somorjai, G. A. (1972). *Surface Science,* **30** (2), 440–453.

LeSar, R. (2013). *Introduction to Computational Materials Science: Fundamentals to Applications.* Introduction to Computational Materials Science: Fundamentals to Applications. New York: Cambridge University Press.

Lewars, E. G. (2011). *Computational Chemistry.* New York: Springer Science & Business Media, 2 edition.

Li, K., Li, Y., Wang, Y., He, F., Jiao, M., Tang, H., & Wu, Z. (2015a). *Journal of Materials Chemistry A,* **3** (21), 11444–11452.

Li, L., Abild-Pedersen, F., Greeley, J., & Nørskov, J. K. (2015b). *The Journal of Physical Chemistry Letters,* **6** (19), 3797–3801.

Li, L., Larsen, A. H., Romero, N. A., Morozov, V. A., Glinsvad, C., Abild-pedersen, F., Greeley, J., Jacobsen, K. W., & Nørskov, J. K. (2013). *The Journal of Physical Chemistry Letters,* **4**, 222–226.

Liu, D. J. (2010). *Physical Review B,* **81** (3), 035415.

Liu, D.-J. & Evans, J. W. (2010). *Journal of Chemical Physics and Physical Chemistry,* **11** (10), 2174–2181.

Long, N. V., Chien, N. D., Hayakawa, T., Hirata, H., Lakshminarayana, G., & Nogami, M. (2010). *Nanotechnology,* **21** (3), 035605.

Lutz, A. E., Larson, R. S., & Keller, J. O. (2002). *International Journal of Hydrogen Energy,* **27** (10), 1103–1111.

Madala, T. (2013). *Reaction pathways for the formation of hydrogen peroxide in fuel cells: - a DFT study.* M.sc. thesis University of Cape Town.

Markovic, N., Gasteiger, H., Ross, P. N., Berkeley, L., & Division, M. S. (1997). *Journal of the Electrochemical Society,* **144** (5), 1591–1597.

Martínez, J., Hansen, H., Rossmeisl, J., & Nørskov, J. (2009). *Physical Review B,* **79** (4), 045120.

Mattsson, A. E., Armiento, R., Paier, J., Kresse, G., Wills, J. M., & Mattsson, T. R. (2008). *The Journal of Chemical Physics,* **128** (8), 084714.

Mattsson, A. E., Schultz, P. A., Desjarlais, M. P., Mattsson, T. R., & Leung, K. (2005). *Modelling and Simulation in Materials Science and Engineering,* **13** (1), R1–R31.

Mavrikakis, M., Hammer, B., & Nørskov, J. (1998). *Physical Review Letters,* **81** (13), 2819–2822.

McEwen, J.-S., Bray, J. M., Wu, C., & Schneider, W. F. (2012). *Physical Chemistry Chemical Physics,* (111), 16677–16685.

Miller, D. J., Öberg, H., Näslund, L. A., Anniyev, T., Ogasawara, H., Pettersson, L. G. M., & Nilsson, A. (2010). *Journal of Chemical Physics,* **133** (22), 224701.

Miracle-Sole, S. (2013). *arXiv preprint arXiv:1307.5180,* (v1), 1–15.

Monkhorst, H. J. & Pack, J. D. (1977). *Physical Review B,* **16** (12), 1748–1749.

Nesselberger, M., Ashton, S., Meier, J. C., Katsounaros, I., Mayrhofer, K. J. J., & Arenz, M. (2011). *Journal of the American Chemical Society,* **133** (43), 17428–17433.

Nørskov, J. K., Rossmeisl, J., Logadottir, A., Lindqvist, L., Lyngby, D., & Jo, H. (2004). *The Journal of Physical Chemistry Part B,* **108**, 17886–17892.

Norton, P. R., Griffiths, K., & Bindner, P. E. (1984). *Surface Science,* **138** (1), 125–147.

Ogawa, T., Kuwabara, A., Fisher, C. a. J., & Moriwake, H. (2014). *The Journal of Physical Chemistry C,* **118** (41), 23675–23681.

Ogawa, T., Kuwabara, A., Fisher, C. A. J., Moriwake, H., & Miwa, T. (2013). *The Journal of Physical Chemistry C,* **117** (211), 9772–9778.

Panchenko, A., Koper, M. T. M., Shubina, T. E., Mitchell, S. J., & Roduner, E. (2004). *Journal of The Electrochemical Society,* **151** (12), A2016.

Parr, R. G. & Yang, W. (1989). *Density-Functional Theory of Atoms and Molecules.* International Series of Monographs on Chemistry. Oxford University Press, USA.

Payne, M. C., Teter, M. P., Allan, D. C., Arias, T. a., & Joannopoulos, J. D. (1992). *Reviews of Modern Physics,* **64** (4), 1045–1097.

Peng, G. & Mavrikakis, M. (2015). *Nano Letters,* **15** (1), 629–634.

Perdew, J., Kurth, S., Zupan, A., & Blaha, P. (1999). *Physical Review Letters,* **82** (12), 5179–5179.

Perdew, J. P., Burke, K., & Ernzerhof, M. (1996). *Physical Review Letters,* **77**, 3865–3868.

Perdew, J. P., Ruzsinszky, A., Tao, J., Staroverov, V. N., Scuseria, G. E., & Csonka, G. I. (2005). *The Journal of Chemical Physics,* **123** (6), 62201.

Perdew, J. P. & Wang, Y. (1992). *Physical Review B,* **45**, 13244–13249.

Perez-Alonso, F. J., McCarthy, D. N., Nierhoff, A., Hernandez-Fernandez, P., Strebel, C., Stephens, I. E. L., Nielsen, J. H., & Chorkendorff, I. (2012). *Angewandte Chemie (International ed. in English),* **51** (19), 4641–4643.

Puglia, C., Nilsson, a., Hernnäs, B., Karis, O., Bennich, P., & Mårtensson, N. (1995). *Surface Science,* **342** (1-3), 119–133.

Qi, L. & Li, J. (2012). *Journal of Catalysis,* **295**, 59–69.

Qi, L., Qian, X., & Li, J. (2008). *Physical Review Letters,* **101** (14), 1–4.

Sano, M., Seimiya, Y., Ohno, Y., Matsushima, T., Tanaka, S. I., & Kamada, M. (1998). *Applied Surface Science,* **130-132**, 518–522.

Schmidt, T. J., Stamenkovic, V., Ross, P. N., & Markovic, N. M. (2001). *Fuel Celss,* **1** (2), 105–116.

Sha, Y., Yu, T. H., Merinov, B. V., Shirvanian, P., & Goddard, W. A. (2011). *The Journal of Physical Chemistry Letters,* **2** (6), 572–576.

Shao, M., Peles, A., & Shoemaker, K. (2011). *Nano Letters,* **11**, 3714–3719.

Sheppard, D., Terrell, R., & Henkelman, G. (2008). *Journal of Chemical Physics,* **128** (13), 1–10.

Shimojo, F., Kalia, R. K., Nakano, A., & Vashishta, P. (2001). *Computer Physics Communications,* **140** (3), 303–314.

Song, H., Kim, F., Connor, S., Somorjai, G. A., & Yang, P. (2005). *The Journal of Physical Chemistry B,* **109** (1), 188–193.

Springborg, M. (1997). *Density-Functional Methods in Chemistry and Materials Science*. Wiley Series in Theoretical Chemistry. Weinheim, Germany: John Wiley & Sons Ltd.

Stampfl, C., Mannstadt, W., Asahi, R., & Freeman, A. (2001). *Physical Review B,* **63** (15), 155106.

Stephens, I. E. L., Bondarenko, A. S., Grønbjerg, U., Rossmeisl, J., & Chorkendorff, I. (2012). *Energy & Environmental Science,* **5** (5), 6744–6762.

Stroppa, A. & Kresse, G. (2008). *New Journal of Physics,* **10** (6), 063020.

Su, L., Jia, W., Li, C.-M., & Lei, Y. (2014). *ChemSusChem,* **7** (2), 361–378.

Sun, B., Zhang, P., Duan, S., Zhao, X. G., & Xue, Q. K. (2007). *Physical Review B,* **75** (24), 1–11.

Swart, J., van Helden, P., & van Steen, E. (2007). *The Journal of Physical Chemistry C,* **111** (13), 4998–5005.

Tao, J., Perdew, J. P., Staroverov, V. N., & Scuseria, G. E. (2003). *Physical Review Letters,* **91** (October), 146401.

Taylor, P. L., Heinonen, O., & Coleman, P. (2003). *A Quantum Approach to Condensed Matter Physics*, volume 56. Cambridge University Press (Virtual Publishing), USA.

Tripković, V., Cerri, I., Bligaard, T., & Rossmeisl, J. (2014). *Catalysis Letters,* **144** (3), 380–388.

Tritsaris, G. A., Greeley, J., Rossmeisl, J., & Nørskov, J. K. (2011). *Catalysis Letters,* **141** (7), 909–913.

van der Niet, M. J. T. C., den Dunnen, A., Juurlink, L. B. F., & Koper, M. T. M. (2010). *Journal of Chemical Physics,* **132** (17), 174705.

van der Put, P. J. (2013). *The Inorganic Chemistry of Materials: How to Make Things out of Elements.* Springer US.

van Helden, P., van Santen, R. A., & van Steen, E. (2009). *The Journal of Physical Chemistry C,* **113** (2), 644–649.

Vanderbilt, D. (1990). *Physical Review B,* **41** (11), 7892–7895.

Vasić, D., Pašti, I., Gavrilov, N., & Mentus, S. (2013). *Russian Journal of Physical Chemistry A,* **87** (13), 2214–2218.

Viswanathan, V., Hansen, H. A., Rossmeisl, J., & Nørskov, J. K. (2012). *ACS Catalysis,* **2** (8), 1654–1660.

Vitos, L., Ruban, A. V., Skriver, H. L., & Kollar, J. (1998). *Surface Science,* **411**, 186–202.

Šljivančanin, Z. & Hammer, B. (2002). *Surface Science,* **515** (1), 235–244.

Wang, H., Tobin, R., Lambert, D. K., DiMaggio, C. L., & Fisher, G. B. (1997). *Surface Science,* **372** (1-3), 267–278.

Wei, C. & Chou, M. (2002). *Physical Review B,* **66** (23), 1–4.

Wei, G.-F. & Liu, Z.-P. (2013). *Physical Chemistry Chemical Physics,* **15** (42), 18555–18561.

Wright, S. E. (2004). *Renewable Energy,* **29** (2), 179–195.

Xia, P. Y., Xiong, Y., Byungkwon, L., & Skrabalak, S. (2009). *Angewandte Chemie (International ed. in English),* **48** (1), 60–103.

Yamanaka, T., Matsushima, T., Tanaka, S. I., & Kamada, M. (1996). *Surface Science,* **349** (2), 119–128.

Yang, Z., Wang, J., & Yu, X. (2010). *Physics Letters A,* **374** (46), 4713–4717.

Yuan, X. Z. & Wang, H. (2008). In: *PEM Fuel Cell Electrocatalysts and Catalyst Layers: Fundamentals and Applications* pp. 1–87. Vancouver.

Zyubin, A. S., Zyubina, T. S., Dobrovol'skii, Y. A., & Volokhov, V. M. (2013). *Russian Journal of Inorganic Chemistry,* **58** (7), 803–807.